Development of OH Detection and Reactivity Techniques with Applications to Butanol Oxidation

Charlotte Amelia Brumby

Submitted in accordance with the requirements for the degree of Doctor of Philosophy

The University of Leeds

School of Chemistry

March 2017

The candidate confirms that the work submitted is her own, except where work which has formed part of jointly authored publications has been included. The contribution of the candidate and the other authors to this work has been explicitly indicated below. The candidate confirms that appropriate credit has been given within the thesis where reference has been made to the work of others.

The measurements for instrument characterisation presented in Chapter 4 of this thesis are presented in publication as follows:

Stone, D., Whalley, L. K., Ingham, T., Edwards, P. M., Cryer, D. R., Brumby, C. A., Seakins, P. W. and Heard, D. E.: *Measurement of OH reactivity by laser flash photolysis coupled with laser-induced fluorescence spectroscopy*, Atmospheric Measurement Techniques, 9, 2827 – 2844, 2016.

I was responsible for the instrument characterisation measurements with methane and *n*-butanol, and characterisation of the total flow rate and integration time.

Acknowledgements

There were many points along the way that I thought this day would never come and many people have helped me get to this point. Firstly, Paul, thank you for giving me the opportunity to work in the HIRAC lab. Your support and advice over the last four years has been excellent.

Fred and Steph – without you I wouldn't know half of what I do about the running of HIRAC. Thanks also need to go to Dwayne and Lisa for kindly letting me use their OH reactivity instrument, all of the assistance with it and of course, for sending me to Germany for the intercomparison. Dan, you've also been great for helping with instrument problems and talking through the maths when my head gets too confused with it all.

There are so many members of the Seakins and Heard groups who have provided some good entertainment over the years. Hannah, you've always been around for interesting conversations both science and non-science related. Rebecca, a fellow northerner, your energy and commitment to your work is inspiring, and coffee breaks were always appreciated. Ellie and Abbie, you have provided some much needed distractions over the last few months. And of course, Danny, not only did you teach me all I needed to know about the running of the OH reactivity instrument, you have supported me so much during my time in Leeds and I will be forever grateful for your support and confidence in me throughout. Dennis the cat has had a much needed calming effect on me whilst writing this book, always waiting in the window when I get home.

Knitting people, you know who you are, how would I have survived the weeks without the best end to, sometimes, the most difficult day of the week. And I'm sure our excellent discussions over the possibilities of dropped shoulder cardigans and one sleeved jumpers will go on. Maybe one day we will eventually discover who has a spinning wheel?!

I couldn't forget to mention the lovely friends I met at my time in York; Jess, Kirsty, Paul, Mary, we may now all be scattered around the country, but we've always made time to catch up. We are very much due a good get together.

I wouldn't be anywhere without the support of my family. Mum, your kindness and generosity knows no bounds, you may not know how to say many of the words in my

thesis but you've always been interested in what I do. Dad, I'm so close now to being a doctor, I doubt I'd be into science without your encouragement. You've both always had confidence in my abilities and supported the decisions I've made. Sarah, my most favourite sister in the world, you're always there on the end of the phone to reassure me of the bigger picture in life. Jonathan, thanks for all the Python help, you're always there to look at my maths problems. Thomas, I may not see you as often, but you've always been interested in my work when I do see you.

I've met so many wonderful people over the last four years since I've moved to Leeds. I can't name them all here, but you've all played a part in my life here and kept me going through some of the most difficult parts of the PhD.

Abstract

The work presented in this thesis utilises the HIRAC chamber for the development and characterisation of instrumentation for measurements of OH and HO_2 radicals, and OH reactivity. This instrumentation is implemented, alongside other standard measurements, following oxidation of processes of butanol, a potential biofuel, focussing on OH reactivity and ozone formation. Results from further development of calibration methods for determining the sensitivity of a FAGE instrument are presented. Monte Carlo error propagations were used to assess sources of error associated with the N_2O actinometry method for the determination of $F_{184.9\ nm}$, where the variation in the measured [NO] was shown to have the most significant influence (46.1 – 99.1%) on the determined value of $F_{184.9\ nm}$. An alternative calibration method, utilising the HIRAC chamber, for determining the sensitivity of the HO_2 cell, C_{HO2}, of a FAGE instrument as a function of temperature is reported to be $\Delta C_{HO2(HIRAC)} = (0.34 \pm 0.19)\%\ K^{-1}$, in good agreement with previous reported HO_2 cell sensitivity following the conventional "wand" calibration method. Development and characterisation of a LFP-LIF instrument OH reactivity measurements (k'_{OH}) is described, with improved measurements for values of k'_{OH} up to ~150 s^{-1}. The first measurements sampling from the HIRAC chamber are shown to be successful, demonstrated by excellent agreement of $k_{n\text{-butanol + OH}}$ ($(8.21 \pm 0.37) \times 10^{-12}$ cm^3 $molecule^{-1}$ s^{-1}) with the IUPAC recommended value. Anonymised results from an OH reactivity instrument intercomparison at the SAPHIR chamber, are presented. The Leeds LFP-LIF instrument showed good agreement with calculated OH reactivity, where a correlation of 1.032 was observed. Relative rate studies into the temperature dependent rate coefficients of *n*-butanol and *iso*-butanol with Cl atoms are presented, Arrhenius expressions describing the temperature dependencies being $k_{Cl + n\text{-butanol}} = 1.01 \times 10^{-10}$ $\exp((235 \pm 34) / T)$ cm^3 $molecule^{-1}$ s^{-1} over 266 – 343 K and $k_{Cl + iso\text{-butanol}} = 5.53 \times 10^{-10}$ $\exp((367 \pm 76) / T)$ cm^3 $molecule^{-1}$ s^{-1} over 296 – 344 K. Studies following the OH radical and Cl atom initiated oxidation processes of *iso*-butanol and *iso*-butane are presented; ozone formation is observed to be considerably greater for Cl atom initiated processes and greater for *iso*-butane as compared to *iso*-butanol. The first OH reactivity measurements following relatively complex reaction systems are presented, with time profiles showing good agreement between measured and calculated OH reactivities.

Table of Contents

Table of Contents

List of Abbreviations

ACOM	Atmospheric chemistry and observations and modelling
BNC	Berkeley Nucleonics Corporation
BTCA	The British Technical Council for the petroleum and motor industries (calibration gases)
CESAM	Centro de Estudos do Ambiente e do Mar (Centre for environmental and marine studies)
CIMS	Chemical ionisation mass spectrometry
ClearfLo	Clean air for London
CPM	Channeltron photomultiplier
CRDS	Cavity ring down spectroscopy
CRM	Comparative reactivity method
CRM-GC-PID	Comparative reactivity method coupled with gas chromatography with photoionisation detection
CRM-PTR-MS	Comparative reactivity method coupled with proton transfer mass spectrometry
DOAS	Differential optical absorption spectroscopy
EU	European Union
EUPHORE	European photoreactor
FAAM	Facility for airborne atmospheric measurements
FAGE	Fluorescence assay by gas expansion
FAME	Fatty acid methyl ester
FEP	Fluorinated ethylene propylene
FID	Flame ionisation detector
FMI	Finnish meteorological institute
FP-RF	Flash photolysis coupled with resonance fluorescence
FTIR	Fourier transform infrared
FZJ	Forschungszentrum Jülich
GC	Gas chromatography
GC-FID	Gas chromatography coupled with flame ionisation detection
GC-PID	Gas chromatography coupled with photoionisation detection

HIRAC	Highly instrumented reactor for atmospheric chemistry
HO_x	$OH + HO_2$
IISER	Indian institute for science education and research
IR	Infrared
IUPAC	International union of pure and applied chemistry
JPL	Jet propulsion laboratory
LFP-LIF	Laser flash photolysis coupled with laser induced fluorescence
LHV	Lower heating value
LIF	Laser induced fluorescence
LOD	Limit of detection
LSCE	Le laboratoire des sciences du climat et de l'environnement
MACR	Methacrolein
MBL	Marine boundary layer
MCM	Master chemical mechanism
MCP	Multi-channel photomultiplier
MEGAPOLI	Megacities: emissions, urban, regional and global atmospheric and climate effects, and integrated tools for assessment and mitigation
MFC	Mass flow controller
MFM	Mass low metre
MIR	Maximum incremental reactivity
MOPS	Measurement of ozone production sensor
MPI	Max Plank Institute
MPIC	Max Plank Institute für Chemie
MVK	Methyl vinyl ketone
NASA	National aeronautics and space administration
NCAR	National center for atmospheric research
NMVOC	Non methane volatile organic compound
NO_x	$NO + NO_2$
O.D	Outer diameter
ORSUM	OH reactivity specialists unity meeting
PAN	Peroxyacetyl nitrate
PLP-LIF	Puled laser photolysis coupled with laser induced fluorescence
PLP-RF	Pulsed laser fluorescence coupled with resonance fluorescence

POCP	Photochemical ozone creation potential
ppbv	Parts per billion by volume
ppmv	Parts per million by volume
pptv	Parts per trillion by volume
PRF	Pulsed repetition frequency
PR-RA	Pulsed radiolysis coupled with resonance absorption
PSU	Pennsylvania State University
PTR-MS	Proton transfer mass spectrometry
PTR-TOF-MS	Proton transfer time of flight mass spectrometry
RACM	Regional atmospheric chemistry model
RR	Relative rate
SAPHIR	Simulation of atmospheric photochemistry in a large reaction chamber
SI	Spark ignition
SMPS	Scanning mobility particle sizer spectrometer
TOHLM	Total OH loss rate measurement
UHP	Ultra high purity
UK	United Kingdom
US	United States
UV	Ultra violet
VOC	Volatile organic compound
WHO	World Health Organisation
YAG	Yttrium aluminium garnet

List of Figures

List of Tables

Chapter 1. Introduction

1.1 Tropospheric Chemistry

The study of atmospheric chemistry is vital for our understanding of the chemical processes occurring in the troposphere. A comprehensive review of all aspects of atmospheric chemistry is far beyond the scope of this work. With the need for renewable energy sources becoming more apparent as energy usage increases and fossil fuel resources are rapidly declining; this thesis focusses on the development of instrumentation for atmospheric measurements and their implementation for studying the atmospheric oxidation of potential biofuels. This chapter will give an introduction to the relevant tropospheric chemistry of such compounds; a detailed review is given into the current literature on the tropospheric kinetics and oxidation processes of the isomers of butanol (as potential biofuel compounds). A review of the methods for two major types of atmospheric measurements used in this thesis is given, with a comparison of the advantages and disadvantages of both.

Chemical reactions of volatile organic compounds (VOCs) in the troposphere can result in the formation of particles and ozone, both of which are air pollutants that are toxic to human health and can affect the climate (Ellingsen *et al.* 2008). Ambient air pollution was shown to be the cause of three million premature deaths in 2012 (WHO 2016). The study of atmospheric chemistry is typically split into three main areas: laboratory studies, field measurements and computer modelling. Laboratory studies include small scale kinetic measurements to determine rate coefficients of tropospherically relevant reactions as well as more complex studies carried out in atmospheric simulation chambers to investigate the detailed chemical mechanisms of individual reaction schemes. Information determined through kinetic studies is used in the modelling and analysis of both field based and chamber based measurements. Comparisons between modelling studies and field or chamber measurements allow for our current understanding of chemical mechanisms to be probed; where our understanding is lacking, further laboratory studies can be implemented.

The atmosphere is made up of four layers defined by their vertical variations in temperature and pressure; the troposphere, stratosphere, mesosphere and thermosphere.

The troposphere is the lowest layer of the atmosphere, the first ~10 km of the atmosphere and the boundary layer is the lower most ~1 km of the troposphere. The majority of the mass of the atmosphere is found in the troposphere (~90%) and hence most of the reactive trace species, which play a vital role in atmospheric chemistry. Ozone is an important constituent of the atmosphere for a number of reasons; the ozone layer in the stratosphere absorbs UV light ($\lambda < 290$ nm) from the sun, protecting us from its adverse effects. In the troposphere, ozone is toxic to humans, wildlife and crops (Felzer *et al.* 2007, Ellingsen *et al.* 2008, Monks 2009). Tropospheric ozone formation is highly dependent on the presence of nitrogen oxides (NO_x = NO and NO_2) and VOCs. Work in this thesis looks at ozone formation following the oxidation of a potential biofuel (*iso*-butanol) under varying tropospherically relevant NO_x conditions. The hydroxyl radical (OH) is the most abundant oxidising agent in the troposphere, with an average day time concentration of ~10^6 molecule cm^{-3} (Stone *et al.* 2012). In the troposphere, the chemistry of OH radicals is closely related to that of the hydroperoxy radicals (HO_2), collectively referred to as HO_x (= OH + HO_2). Section 1.2 will discuss in detail the tropospheric oxidation of VOCs, focusing on the importance of NO_x concentrations and ozone formation. Measurements of OH reactivity (the pseudo first order loss rate of OH, k'_{OH}) allow for better insights into the oxidation capacity of the troposphere. The potential for the removal of VOCs in the troposphere is vitally important for our understanding of chemical mechanisms and to allow for predictions of climate to be made. High concentrations of NO_x in urban environments are typically mirrored by high concentrations of ozone.

Chlorine atom chemistry can also have an important influence on the chemical reactions occurring in the troposphere and has been seen to have a particular impact on the formation of tropospheric ozone (Simpson *et al.* 2015). The importance of chlorine atom chemistry will be outlined in Section 1.4, and its close connections with tropospheric HO_x and NO_x chemistry.

Details of the development of a laser induced fluorescence (LIF) instrument for the measurement of HO_x within the Highly Instrumented Reactor for Atmospheric Chemistry (HIRAC) chamber are given in Chapter 3, focusing on the development of calibration techniques. Development and characterisation of a laser flash photolysis coupled with laser induced fluorescence (LFP-LIF) instrument for measurement of OH reactivity from the HIRAC chamber are discussed in Chapter 4. This instrument was deployed for an instrument intercomparison at the Simulation of Atmospheric Photochemistry In a large Reaction (SAPHIR) chamber in October 2015, and some of the results from this study

are described in Chapter 5. A kinetic study of the temperature dependent rate coefficients with Cl atoms of two potential biofuels (*iso*-butanol and *n*-butanol) is given in Chapter 6. A detailed product study, of the oxidation of *iso*-butanol under varying NO_x conditions is given in Chapter 7, including comparisons on the formation of ozone with the analogous alkane, *iso*-butane. The first measurements of OH reactivity from the HIRAC chamber following the relatively complex oxidation processes of *iso*-butanol and *iso*-butane are discussed in Chapter 8, with comparisons being made between measured and calculated OH reactivity.

1.2 Tropospheric VOC Oxidation

The chemistry of OH and HO_2 radicals are closely coupled; Figure 1-1 shows a simplified schematic of the HO_x radical related chemical reactions occurring in the troposphere. The very short lifetimes of OH and HO_2 radicals (~1 s and ~100 s, respectively), due to their high reactivity towards VOCs, lead to them having low concentrations in the troposphere (Heard and Pilling 2003). Such low concentrations require the use of extremely sensitive and selective detection techniques (Heard and Pilling 2003). Three main techniques have been developed for the measurement of OH and HO_2 radical concentrations; differential optical absorption spectroscopy (DOAS), chemical ionisation mass spectrometry (CIMS) and laser induced fluorescence (LIF), and will be discussed in Section 1.7.

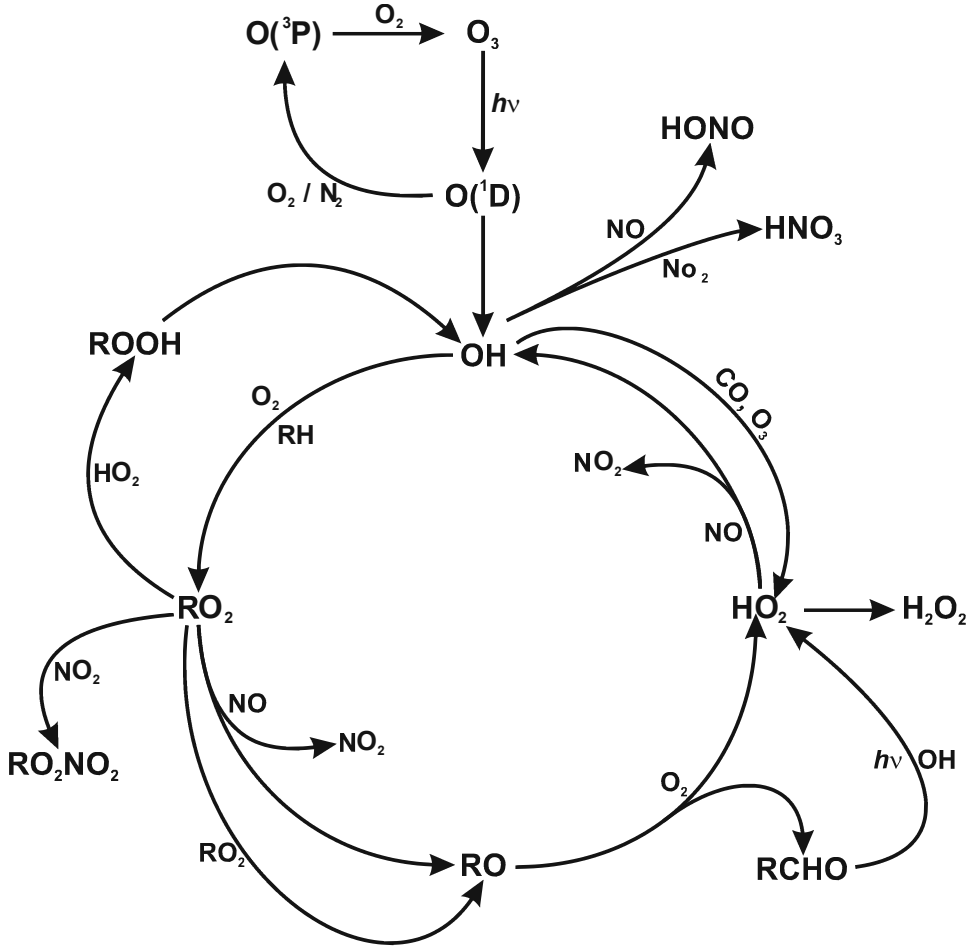

Figure 1-1: Simplified diagram of the HO_x cycle.

OH radicals react with VOCs in the troposphere, which can follow a number of pathways to termination or radical recycling. The majority of OH radicals are formed in the troposphere through the photolysis of O_3 to produce $O(^1D)$, which subsequently reacts with water vapour present in the air to produce two OH radicals (R 1-1 and R 1-2). Collisional quenching of $O(^1D)$ can also occur with O_2 or N_2 to the ground state, $O(^3P)$, (R 1-3) which, in the presence of O_2 will regenerate O_3 (R 1-4), as shown in Figure 1-1.

$$O_3 + h\nu_{(<340\ nm)} \rightarrow O(^1D) + O_2 \qquad \text{R 1-1}$$

$$O(^1D) + H_2O \rightarrow 2OH \qquad \text{R 1-2}$$

$$O(^1D) + M \rightarrow O(^3P) + M \qquad \text{R 1-3}$$

$$O(^3P) + O_2 \rightarrow O_3 \qquad \text{R 1-4}$$

Many reactions can occur with OH radicals, including the reaction with VOCs (RH in Figure 1-1) to produce RO_2 radicals in the presence of O_2, reaction with CO or O_3 to produce HO_2 radicals, reaction with NO to produce HONO and the reaction with NO_2 to produce HNO_3 (R 1-5 to R 1-9).

$OH + RH + O_2 \rightarrow RO_2 + H_2O$ R 1-5

$OH + O_3 \rightarrow HO_2 + O_2$ R 1-6

$OH + CO + O_2 \rightarrow HO_2 + CO_2$ R 1-7

$OH + NO \rightarrow HONO$ R 1-8

$OH + NO_2 \rightarrow HNO_3$ R 1-9

Under environments with high NO_x concentrations, such as urban areas where [NO] = 1 - 100 ppbv, RO_2 radicals react with NO to produce RO radicals and NO_2 (R 1-10). RO radicals subsequently form HO_2 and RCHO in the presence of O_2 in the troposphere. The HO_2 radicals formed through R 1-11 can also react with NO present in high NO_x environments to regenerate OH radicals (R 1-12).

$RO_2 + NO \rightarrow RO + NO_2$ R 1-10

$RO + O_2 \rightarrow HO_2 + RCHO$ R 1-11

$HO_2 + NO \rightarrow OH + NO_2$ R 1-12

The NO_2 formed through R 1-10 and R 1-12 is photolysed ($\lambda > 398$ nm) to produce $O(^3P)$ which can subsequently react with O_2 to form ozone; this is the only known pathway for the formation of O_3 in the troposphere (R 1-13 and R 1-14).

$NO_2 + h\nu_{(\lambda > 398\ nm)} \rightarrow O(^3P) + NO$ R 1-13

$O(^3P) + O_2 \rightarrow O_3$ R 1-14

Under environments with low NO_x concentrations ([NO] < 1 ppbv), such as remote forested areas, RO_2 radicals are lost through reaction with other RO_2 radicals or HO_2 radicals. The HO_2 radicals formed under low NO_x environments by R 1-11 react in the self-reaction, R 1-17, to produce H_2O_2.

$RO_2 + RO_2 \rightarrow 2RO + O_2$ R 1-15

$RO_2 + HO_2 \rightarrow ROOH + O_2$ R 1-16

$HO_2 + HO_2 \rightarrow H_2O_2 + O_2$ R 1-17

OH radicals can also be formed in the troposphere via a number of reactions other than that described by R 1-1 and R 1-2. The photolysis of HONO, H_2O_2, ROOH and HOX (X = Cl, Br, I) all produce OH radicals, R 1-18 to R 1-21 in the troposphere. The importance of chlorine atom chemistry in the troposphere will be discussed in more detail in Section 1.3.

$HONO + h\nu_{(190\ nm < \lambda < 400\ nm)} \rightarrow OH + NO$ R 1-18

$H_2O_2 + h\nu \rightarrow 2OH$ R 1-19

$ROOH + h\nu \rightarrow OH + RO$ R 1-20

$HOX + h\nu \rightarrow OH + X$ R 1-21

Figure 1-2 shows the formation of ozone in the troposphere through the reactions of NO_x with peroxy radicals. As mentioned previously, the reaction of $O(^3P)$ with O_2 is the only known pathway for the formation of ozone in the troposphere. It is therefore crucial to fully understand the oxidation mechanisms of VOCs in the troposphere under tropospherically relevant NO_x conditions.

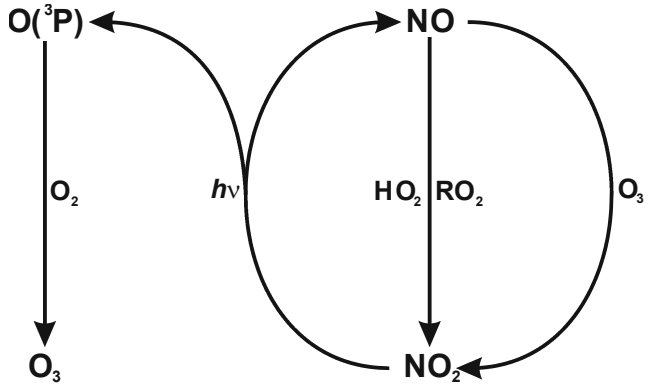

Figure 1-2: Production of ozone through the reaction of NO_x with peroxy radicals, as occurs in the troposphere.

The relationship between [NO_x], [VOC] and ozone production is typically illustrated with an ozone isopleth, an example of which is shown in Figure 1-3, where the coloured contour lines represent the peak ozone concentration. A NO_x limited regime refers to an environment with relatively low NO_x concentration. A small increase in [NO_x] would lead to increased peak ozone formation, however, an increase in [VOC] would only move along the same peak ozone concentration isopleth contour. A VOC limited regime refers to an environment where an increase in [VOC] would lead to an increase in peak ozone concentration, but an increase in [NO_x] would not result in any change.

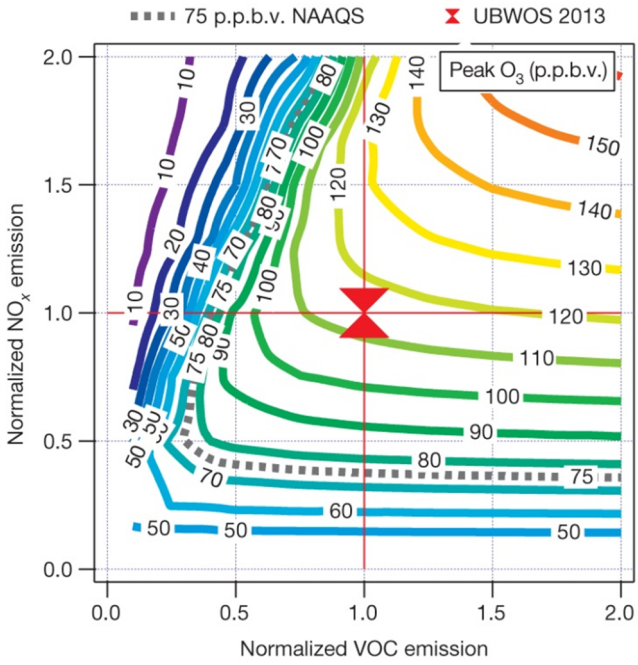

Figure 1-3: Ozone isopleth, adapted from Edwards *et al.* (2014).

Identifying the type of a regime in a specific environment using ozone isopleths, such as that in Figure 1-3 assists in determining the best protocols for controlling ozone; whether it is most appropriate to reduce NO_x concentrations of VOC concentrations.

1.3 Photochemical Ozone Creation Potentials

The reactivity of organic compounds and their production of ozone have been characterised by the use of atmospheric simulation chambers, as well as in estimations with the use of computer models (Carter and Atkinson 1987, Carter and Atkinson 1989). Photochemical ozone creation potentials (POCPs) are used as an indication of the quantity of ozone produced for a specific hydrocarbon, relative to that of ethene (= 100%). Derwent *et al.* (1996) defined the equation Eq. 1-1 for the calculation of POCP values.

$$\mathrm{POCP}_i = \frac{\text{ozone increment with the } i^{th} \text{ hydrocarbon}}{\text{ozone increment with ethene}} \times 100 \qquad \text{Eq. 1-1}$$

It has been demonstrated that the method of calculation and the chemical environment in which the measurements are taken have an important effect on the relative values of POCPs (Carter and Atkinson 1989, Andersson-Sköld *et al.* 1992). Despite this, a general agreement in the ranking of VOCs by their POCP values is observed across the different calculation methods described in the literature. Hundreds of organic compounds are emitted into the atmosphere from a variety of both anthropogenic and biogenic sources. POCP values of a number of different emission sources show that values obtained from road transport exhaust emissions give some of the largest values; Derwent *et al.* (2007)

found road transport exhaust emissions and petrol evaporation emissions to have the highest POCP values (69 and 50, respectively) from a total of 248 different source categories investigated.

The Maximum Incremental Reactivity (MIR) scale was developed for use in urban areas with high NO_x emissions (Carter 1994). The time scale of up to one day is useful for values in such environments, however, in Europe, longer term exposure is of greater interest and importance due to increased influence on climate from long range transportation of emissions. The UK POCP scale, initially developed by Derwent and co-workers, ranks the ability of VOCs to form ozone over longer time scales, typically up to ~5 days (Derwent and Jenkin 1991, Derwent *et al.* 1998).

To better calculate POCP values and predict the effects of alternative fuels on the atmosphere, further research is required to produce better inventories characterising emissions covering a wide range of fuels and engine types. As POCPs are trajectory calculations, calculated for an air mass over a specified timescale (typically about five days), in depth knowledge of weather conditions, atmospheric components and reactions, and biological and anthropogenic emissions is vital. POCP values determined by Derwent *et al.* (1998) are compared to MIR values in Table 1-1 for selected VOCs relevant to the work in this thesis.

A number of comparison studies (Derwent *et al.* 1998, Derwent *et al.* 2001) have been conducted in the literature into the different methods for determining the ozone formation potentials using different methods for a range of environments (POCP and MIR values), in some cases showing a non-linear relationship between the values determined by different methods. Figure 1-4 and Figure 1-5 show the comparisons between MIR and POCP values determined under European and North American conditions, respectively.

Compound	POCP	MIR	Compound	POCP	MIR
Methane	0.6	0.014	*n*-butanol	61.2	2.76
Ethane*	12.3	0.26	*iso*-butanol	37.5	2.41
Propane*	17.6	0.46	*sec*-butanol	40.0	1.30
n-butane*	35.2	1.08	*tert*-butanol	12.3	0.39
iso-butane*	30.7	1.34	3-pentanol	42.2	1.56
n-pentane*	39.5	1.23	Acetylene*	8.5	0.93
iso-pentane*	40.5	1.36	1,3-butadiene*	85.1	12.21
n-octane*	45.3	0.82	Pent-1-ene*	97.7	6.97
Ethene*	100.0	8.76	*Trans*-2-pentene*	111.7	10.25
Propene*	112.3	11.37	Isoprene	109.2	10.28
But-1-ene	107.9	9.42	*n*-hexane*	48.2	1.15
cis-but-2-ene*	114.6	13.89	2-methylpentane*	42.0	1.14
trans-but-2-ene*	113.2	14.79	*n*-heptane*	49.4	0.99
Formaldehyde*	51.9	9.24	Benzene*	21.8	0.69
Acetaldehyde	64.1	6.34	Toluene*	63.7	3.88
Propanal	79.8	6.83	Ethylbenzene	73.0	2.93
Butyraldehyde	79.5	5.75	*m*-xylene*	110.8	9.52
iso-butyraldehyde	51.4	5.05	*p*-xylene*	101.0	5.69
Pentanal	76.5	4.89	*o*-xylene*	105.3	7.44
Acetone	9.4	0.35	1,2,4-trimethylbenzene	127.8	8.64
Methanol	13.1	0.65	1,2,3-trimethylbenzene	126.7	11.66
Ethanol	38.6	1.45	1,3,5-trimethlybenzene	138.1	11.44
n-propanol	54.3	2.38	2,2,4-trimethylpentane	-	1.20
iso-propanol	14.0	0.59			

Table 1-1: Summary of POCP and MIR values for some key VOCs as reported by Derwent *et al.* (1998) and Carter (2009), respectively. *ozone precursor compounds recommended for measurement by EU environmental law (European Parliament and Council of the European Union 2008).

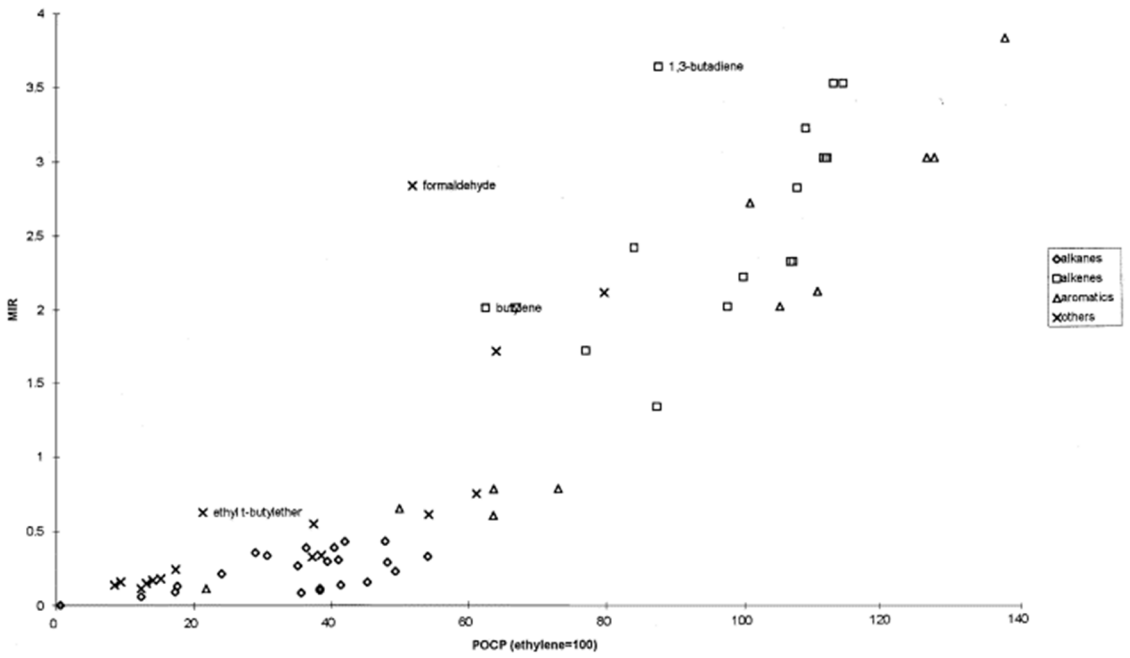

Figure 1-4: Comparison between MIR values determined for North American conditions and POCP values determined for European conditions, reproduced from Derwent *et al.* (1998).

The comparison shown in Figure 1-4 clearly shows a non-linear relationship between the MIR and POCP values, whereas that shown in Figure 1-5 gives a linear relationship between the two sets of values. For both scenarios, the comparisons show that for both MIR and POCP values, alkanes result in relatively low ozone production, with alkanes and aromatics showing increased ozone formation. The distinct non-linear relationship between the MIR and POCP values shown in Figure 1-4 is indicative of the differences in the conditions employed in the determination of ozone formation by each method; the detemination of the POCP values are more depeendent on long range transport than the determination of MIR values. Derwent *et al.* (2001) observed differences in rankings of MIR and POCP values dependent on the conditions used in their determination; noting stark differences in the values for formaldehyde. These differences are attributed to the fate of formaldehyde being highly dependent on the competition between photolysis and oxidation by OH radicals. The comparisons shown in Figure 1-4 and Figure 1-5 demonstrate the importance of the inclusion of relevant environmental factors when determining the potential for ozone production.

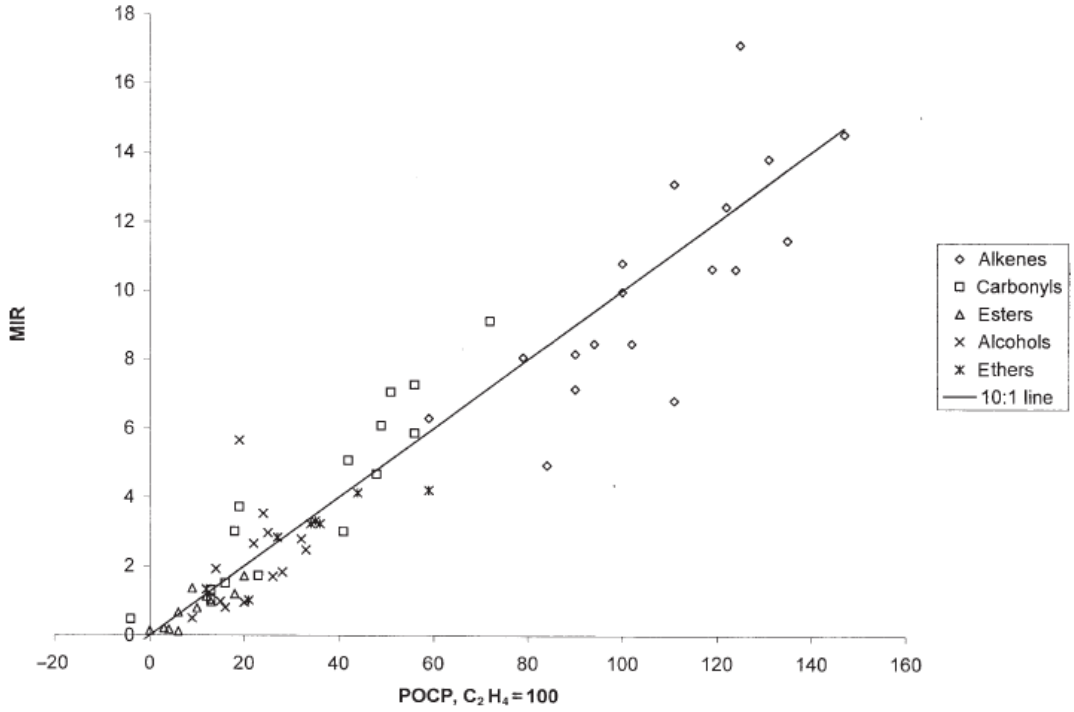

Figure 1-5: Comparison between MIR and POCP values determined for North American conditions, reproduced from Derwent *et al.* (2001).

Tropospheric ozone formation is closely related to the concentrations of VOCs and NO in the troposphere. Ozone formation can be calculated, using:

$$P(O_3) = k_{HO_2+NO}[HO_2][NO] + \sum_i k_i[RO_2]_i[NO] \quad \text{Eq. 1-2}$$

where $P(O_3)$ is the ozone production rate, k_{HO2+NO} can be taken from the literature and $[HO_2]$ and [NO] are measured.

An instrument for the measurement of ozone production in the atmosphere has been developed by Cazorla and Brune (2010); the measurement of ozone production sensor (MOPS). A schematic diagram of the instrument developed by Cazorla and Brune (2010) is shown in Figure 1-6.

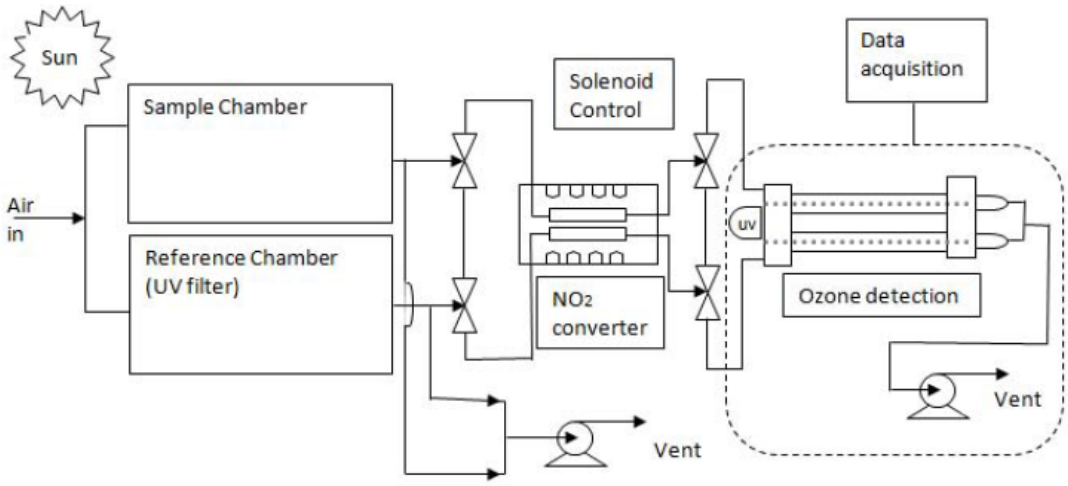

Figure 1-6: Schematic diagram of the MOPS instrument for the measurement of ozone production in the atmosphere, reproduced from Cazorla and Brune (2010).

In the MOPS instrument, ambient air is drawn in to two chambers (11.3 l volume each). The sample chamber is exposed to sunlight allowing for any species present in the air to be processed as they would be in the atmosphere. The reference chamber is covered by a film to prevent its contents from being exposed to UV radiation ($\lambda < 400$ nm) from the sun which would lead to the formation of ozone; still allowing for dark processing of the contents of the chamber to occur. The aim is to measure the difference in the sum of NO_2 and O_3 between the sample chamber and the reference chamber; this is done through the measurement of ozone following the conversion of any NO_2 present in the air sample leaving the two chambers into O_3. The production of ozone is described by:

$$P(O_3) = \Delta O_3/\tau \qquad \text{Eq. 1-3}$$

where $P(O_3)$ is the ozone production rate, ΔO_3 is the difference in the sum of NO_2 and O_3, as measured by the ozone detector following the conversion of NO_2 to O_3, between the two chambers, and τ is the exposure time in the chambers. Cazorla and Brune (2010) have described characterisation of the instrument with respect to the exposure time, radical concentrations and photolysis frequencies within the chambers, and the conversion efficiency of NO_2 to O_3. Preliminary measurements taken at the Pennsylvania State University, US are also reported, indicating that the MOPS instrument for the measurement of ozone production rates in the atmosphere works well. Two studies have since been carried out using MOPS instruments; one measuring the ozone production in Houston in 2009 with the original MOPS instrument, and a second, also measuring in Houston in 2013, with a second version of the MOPS instrument (Cazorla *et al.* 2012, Baier *et al.* 2015). Measurements from 2013 showed good agreement with both

measurements and calculations of ozone production rates from two previous measurement field campaigns (Chen *et al.* 2010, Cazorla *et al.* 2012). A bias due to the production of HONO and its subsequent photolysis in the sample chamber was observed for both versions of the MOPS instrument, and further characterisation of the instrument is required in order to reduce this bias (Baier *et al.* 2015).

1.4 Chlorine Chemistry

While the OH radical is the most abundant oxidising agent in the troposphere, chlorine has been shown to play an important role in the oxidation of VOCs, with significant impact on tropospheric ozone formation under certain conditions (Simpson *et al.* 2015). The role of chlorine in the troposphere has shown increased interest over the last few decades, with many reviews detailing laboratory based studies and field measurements of chlorine containing species (Monks 2005, Saiz-Lopez and von Glasow 2012, Simpson *et al.* 2015).

There are a number of sources of reactive chlorine species in the troposphere; primarily originating from the marine boundary layer (MBL) (Lawler *et al.* 2009, Lawler *et al.* 2011). Reactive chlorine species are known to be produced in a wide range of environments; open ocean sources, coastal regions, emissions from volcanoes, salt lakes and lake beds and heterogeneous chemistry. As the work in this thesis investigates the oxidation processes of biofuels and related compounds, the presence of reactive chlorine species in polluted environments (i.e. high NO_x environments) will be discussed.

A review by Simpson *et al.* (2015) discusses the cycling and activation of halogens in polluted environments; focussing on the oxidation of VOCs and tropospheric ozone production. Activation of reactive chlorine species leads to the formation of chlorine atoms, which subsequently react with VOCs in the atmosphere. One such route leading to the production of Cl atoms, particularly of importance in NO_x environments, is via the night time formation of $ClNO_2$ (Simpson *et al.* 2015).

$NO + O_3 \rightarrow NO_2 + O_2$ R 1-22

$NO_2 + O_3 \rightarrow NO_3 + O_2$ R 1-23

$NO_3 + NO_2 \leftrightarrow N_2O_5$ R 1-24

$N_2O_5 + Cl^-_{(het)} \rightarrow ClNO_2 + NO_3^-_{(het)}$ R 1-25

$ClNO_2 + h\nu \rightarrow Cl + NO_2$ R 1-26

The formation of $ClNO_2$ described by R 1-22 to R 1-26 is now considered to be the major source of reactive chlorine in polluted environments. There are no known night time sinks of $ClNO_2$, and thus it can be transported long distances (Saiz-Lopez and von Glasow 2012). $ClNO_2$ will be photolysed by the morning sunlight (R 1-26) to produce Cl atoms, which can subsequently oxidise VOCs present in the troposphere. In the presence of NO_x, the peroxy radicals formed in the oxidation of VOCs go on to produce ozone. The understanding of NO_y cycling from $ClNO_2$ in the troposphere is crucial, particularly in high NO_x polluted environments, for establishing protocols to reduce the production of ozone in the troposphere.

$ClNO_2$ has been measured in a number of different regions across the globe; measurements at a mountain top in Hong Kong showed that $ClNO_2$ could potentially enhance ozone production by 5 – 16% at the peak ozone (Wang *et al.* 2016). Measurements of $ClNO_2$ have been reported by Bannan *et al.* (2015) during the ClearfLo field campaign in London in 2012. The authors reported, from modelling studies, that when the Cl atom concentration was at its highest, Cl atoms were the dominant oxidising agent for alkanes. Modelling studies by Riedel (2014) and Sarwar *et al.* (2014) both showed an enhancement in ozone formation when $ClNO_2$ was included as a source of Cl atoms, with Sarwar *et al.* (2014) reporting more significant enhancement in winter ozone production than summer ozone production. All of these studies highlight the importance of the inclusion of Cl atom chemistry in assessing the oxidation capacity of the troposphere and its influence on the tropospheric production of ozone.

1.5 Biofuels

A number of recent reviews discuss the current level of research into biofuel production, combustion and the atmospheric implications of the use of such fuels in vehicle engines (Kohse-Höinghaus *et al.* 2010, Naik *et al.* 2010, Westbrook 2013). Two main types of combustion engine exist; spark ignition (SI) petrol engines and compression ignition diesel engines. The work in this thesis is based on the chemistry of butanol in the

troposphere, which has shown potential for its use as an alternative fuel to petrol in SI vehicle engines. Details of the different types of combustion engines will not be given as this is not specifically relevant to the work in this thesis. A brief discussion is given here on the main types of biofuels currently used in vehicle engines, with a more detailed discussion focussing on the production and use of alcohols.

Research has shown that, in most cases, the combustion of biofuels, such as ethanol and methanol, in vehicle engines results in a reduced amount of regulated pollutants being emitted into the atmosphere (Kohse-Höinghaus *et al.* 2010, Wen *et al.* 2010). It is, however, known that biofuels can also lead to an increase in unregulated emissions such as carbonyl compounds (Cardone *et al.* 2002, Fontaras *et al.* 2009, He *et al.* 2009, Lin *et al.* 2009, Chai *et al.* 2013). Despite this, Chai *et al.* (2013), and references therein, note discrepancies between results into research of biodiesel from a number of sources; some studies showing an increase while others showing a decrease in carbonyl emissions. Due to the low number of investigations reported to date, it was concluded that these differences reported in the results most likely arise from the variety of operating conditions employed for the studies.

Biofuels are of great importance for the replacement of traditional fossil fuels. Methanol and ethanol are the most widely used alcohol based fuels, with much interest recently being seen in the potential use of higher alcohols of butanol and propanol (Ratcliff *et al.* 2013, Sarathy *et al.* 2014, Rajesh Kumar and Saravanan 2016). Single component alcohols fuels such as these have fewer problems associated with the characterisation and quantification of their combustion products as compared to the complex mixture of compounds that make up traditional fossil fuels. Typically alcohols replace petrol based vehicle fuels and fatty acid esters replace diesel based vehicle fuels.

Legislation states that by 2020, for all member states of the European Union transport fuels must be made up of at least 10% from renewable sources (European Union 2009). An amendment to the legislation states that only 7% of the total 10% can come from biofuels produced from food crops, i.e. first generation biofuels (European Union 2015).

The production of biofuels can be classed as first or second generation (third generation biofuels have also recently been reported); where first generation biofuels refers to those fuels which are derived from food crops and second generation biofuels are those that are not derived directly from food crops. Second generation biofuels may be produced from food crops, where the crop has already been used as a food source and only waste material

is used in the generation of the biofuel, and from lignocellulosic biomass (Antizar-Ladislao and Turrion-Gomez 2008).

A review of the methods of production for biodiesel has been given by Basha *et al.* (2009). Biodiesel is produced through the transesterification of the fatty acids present in oils, to produce fatty acid methyl esters (FAMEs), shown in Figure 1-7. The long chain methyl esters are similar to the hydrocarbons found in conventional diesel fuel, and so the use of biodiesel in diesel engines is well suited.

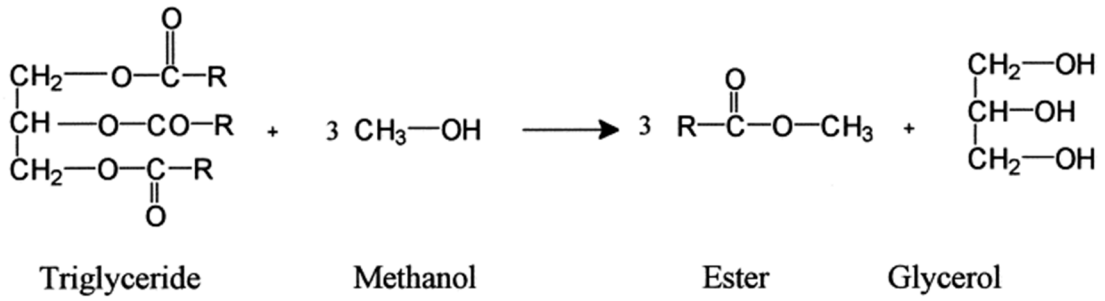

Figure 1-7: The production of biodiesel from oil, reproduced from Alcantara *et al.* (2000).

Biodiesel can be used in diesel engines without the need for any modifications, and can be used neat or blended with diesel. More recent research into the production of biodiesel using microalgae (Schenk *et al.* 2008) shows promising results for its production as a second generation biofuel. A review by Kumar *et al.* (2013) discusses combustion emissions from biodiesel relating to the origin of the fuel itself, highlighting differences in emissions from the combustion of biodiesels dependent on the origin of the biodiesel. The authors conclude that better understanding of emissions dependent of the biodiesel feedstock is required, and that different engine types may also have a significant influence on the combustion emissions.

Butanol has long been produced from biomass, with its production from the fermentation of sugars first being reported by Louis Pasteur in 1861 (Jones and Woods 1986). The four isomers of butanol all have different methods of production; *tert*-butanol is the only isomer that can only be produced via petrochemical methods, *n*-butanol is commonly produced by fermentation of sugars, *sec*-butanol is produced through bacterial fermentation to produce an intermediate product which is subsequently chemically converted to the final butanol product (Nigam and Singh 2011), and *iso*-butanol has more recently seen interest in its production as a biofuel, from the fermentation of the microorganism, Corynebacterium crenatum (Su *et al.* 2015).

Alcohols have long been of interest for use as biofuels in replacing petrol in SI engines; ethanol is currently the most widely used biofuel (Balat *et al.* 2008, Kohse-Höinghaus *et al.* 2010). A chemical kinetic mechanism has been described by Saxena and Williams (2007), shown in Figure 1-8, containing the major reaction sequences of the combustion of ethanol. Acetaldehyde (CH_3CHO) is one of the main combustion emissions of ethanol.

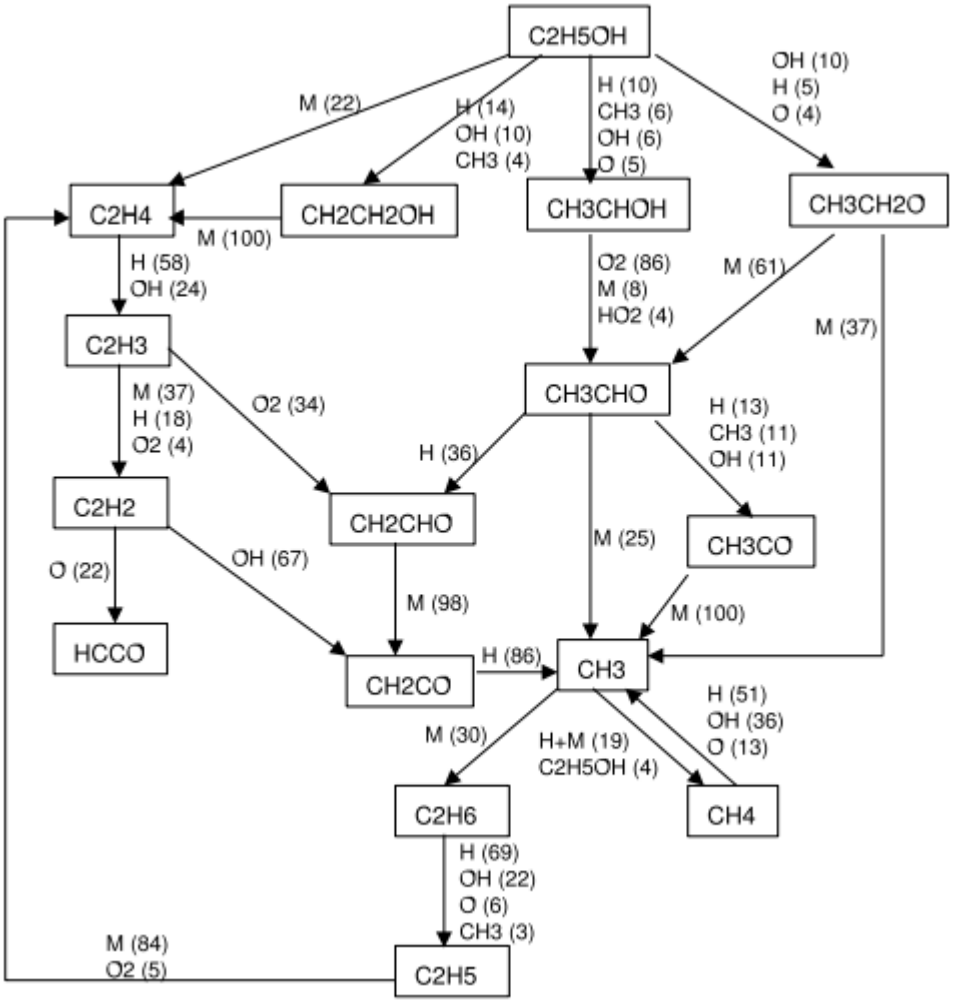

Figure 1-8: Chemical kinetic mechanism for the combustion of ethanol, reproduced from Saxena and Williams (2007).

As the carbon chain of alcohols is increased, the energy density of the alcohols is seen to increase; methanol, ethanol and propanol all have relatively low energy densities whereas the energy density of butanol is more comparable to that of petrol fuel. Because of the higher energy density as compared to smaller chain alcohols, butanols have seen increased research into the suitability as potential biofuels for the replacement of petrol fuel in SI vehicle engines (Grana *et al.* 2010, Kumar and Gayen 2011). Table 1-2 compares the lower heating values (LHVs); it is a measure of the energy content of the fuels, where the LHVs for the isomers of butanol are much closer to that of petrol.

Fuel	**Lower Heating Value (LHV) / MJ L^{-1}**
Petrol	30-33
Diesel	35.66
Methanol	15.8
Ethanol	21.4
n-butanol	26.9
sec-butanol	26.7
iso-butanol	26.6
tert-butanol	25.7

Table 1-2: Comparison of properties for a selection of alcohol fuels and conventional fuels, values taken from Sarathy *et al.* (2014).

The use of higher alcohols as biofuels offer a number of advantages over the currently used ethanol and methanol. Fugitive emissions of fuels are those that are released directly as a vapour or gas of the fuel into the atmosphere. In 2014, 550 kt of non-methane volatile organic compound (NMVOCs) were estimated to be emitted in England, with 13% of those coming from fugitive emissions (Bailey *et al.* 2016). The volatility of fuels is important in determining their potential to be released into the atmosphere as fugitive emissions; with the majority of fugitive emissions coming from spillages during the filling of vehicles at petrol stations. The atmospheric oxidation of alcohols for their potential use as biofuels is therefore extremely important to understand in order to determine their impact on the atmosphere. As the OH radical is the most abundant oxidising species present in the troposphere, the OH initiated atmospheric oxidation of potential alcohol based fuels is discussed.

The work in this thesis focusses on the atmospheric chemistry of butanols; their combustion properties will not be discussed in detail. A review of the current literature on the atmospheric oxidation of the isomers of butanol is detailed in Section 1.5.1, where gaps in the current research are highlighted.

The atmospheric oxidation of ethanol has been investigated by a number of groups, with its rate coefficient for the reaction with OH radicals being well defined (Wallington and Kurylo 1987, Hess and Tully 1988, Jiménez *et al.* 2003, Dillon *et al.* 2005). The IUPAC

recommended rate coefficient for the reaction of ethanol with OH radicals at 298 K is determined from these literature values to be (3.20 ± 0.44) × 10^{-12} cm^3 $molecule^{-1}$ s^{-1} (Atkinson *et al.* 2004). The branching ratios of the OH radical initiated oxidation of ethanol have been studied by Carr *et al.* (2011) and Meier *et al.* (1985), and are both in good agreement that the oxidation occurs predominantly via α-hydrogen abstraction. Carr *et al.* (2011) reported 92 ± 8% α-hydrogen abstraction at 298 K and Meier *et al.* (1985) 75 ± 15% at 298 K. The three possible pathways for the OH radical initiated oxidation of ethanol are represented by reactions R 1-27 to R 1-29, with R 1-28 being the most dominant pathway. These branching ratios were studied over the temperature range 298 - 523 K by Carr *et al.* (2011). The subsequent reaction of the radical produced following the α-hydrogen abstraction is given by R 1-30, leading to the formation of acetaldehyde.

$CH_3CH_2OH + OH \rightarrow CH_2CH_2OH + H_2O$ R 1-27

$\rightarrow CH_3CHOH + H_2O$ R 1-28

$\rightarrow CH_3CH_2O + H_2O$ R 1-29

$CH_3CHOH + O_2 \rightarrow CH_3CHO + HO_2$ R 1-30

The secondary chemistry occurring from the initial oxidation products of ethanol also plays a significant role in the troposphere as further, photolchemically active, carbonyl compounds may be formed. The ß-hydrogen abstraction pathway (R 1-27) leads to the formation of formaldehyde following R 1-31 to R 1-33. The formation of compounds following such secondary chemistry may lead to small molar yields. However, their tropospheric reactivities are typically greater than that of the primary products and therefore can play an important role in subsequent reactions leading to the formation of tropospheric ozone.

$CH_2CH_2OH + O_2 \rightarrow H_2C(OO)CH_2OH$ R 1-31

$H_2C(OO)CH_2OH + NO \rightarrow H_2C(O)CH_2OH$ R 1-32

$H_2C(O)CH_2OH + O_2 \rightarrow 2CH_2O$ R 1-33

1.5.1 Butanols

A number of studies have been reported in the literature on the kinetics and mechanisms of the tropospheric oxidation of small alcohols such as methanol and ethanol. Far fewer studies are reported on the mechanisms, kinetics and products of the tropospheric chemistry of higher alcohols such as the four isomers of butanol. Butanol has seen

increased interest into its production as a potential biofuel, and research into its combustion kinetics and oxidation processes (Kohse-Höinghaus *et al.* 2010, Kumar and Gayen 2011, Oßwald *et al.* 2011, Sarathy *et al.* 2012, Ratcliff *et al.* 2013).

Higher alcohols such as the isomers of butanol lead to more complex tropospheric oxidation mechanisms for their removal via reaction with OH radicals. As for both methanol and ethanol, the OH initiated oxidation predominantly proceeds via hydrogen atom abstraction from the α-carbon position, ultimately resulting in the formation of a carbonyl compound and HO_2. Butanol has four isomeric structures, illustrated in Figure 1-9, where α-hydrogen abstraction is only possible from the *n*-, *sec*- and *iso*-isomers.

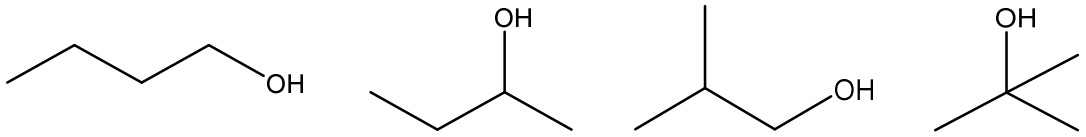

n-butanol *sec*-butanol *iso*-butanol *tert*-butanol

Figure 1-9: The four isomers of butanol.

A number of studies have been reported on the reaction of the isomers of butanol with OH radicals. These include chamber based investigations into the oxidation mechanisms and products of butanols in the presence of NO_x, temperature dependent studies of the rate coefficients with the OH radical and temperature dependent branching ratio studies (Yujing and Mellouki 2001, Cavalli *et al.* 2002, Hurley *et al.* 2009, McGillen *et al.* 2013). As discussed in Section 1.3, chlorine atoms can also play a significant role in the atmospheric oxidation processes of VOCs in the troposphere. The chemical mechanisms and kinetics of butanols for their reaction with Cl atoms have also been studied (Nelson *et al.* 1990, Wu *et al.* 2003). In the following sections, the OH radical and Cl atom initiated tropospheric oxidation and kinetics of the isomers of butanol will be reviewed, with comparisons being drawn between the OH radical and Cl atom oxidation processes. *Tert*-butanol is not to be discussed; it is a solid at room temperature, with a melting point ~25°C, and so is unlikely to be used as a single component biofuel in the future, it is also the only butanol isomer yet to be produced as a biofuel and is currently only a petrochemical product.

1.5.1.1 *n*-butanol

The reaction of *n*-butanol with OH radicals has been studied by a number of groups, investigating the mechanisms, kinetics and products of the reaction. Rate coefficients in the literature for the reaction of *n*-butanol with OH radicals are summarised in Table 1-3.

The room temperature rate coefficients, determined by the relative rate method, reported by Nelson *et al.* (1990), Campbell *et al.* (1976), Cavalli *et al.* (2002), Hurley *et al.* (2009) and Wu *et al.* (2003) are all in good agreement. The value reported by Oh and Andino (2001) is higher than the other relative rate studies, however, it does fall within the IUPAC recommended value of $(8.5 \pm 3.0) \times 10^{-12}$ cm^3 $molecule^{-1}$ s^{-1} (Atkinson *et al.* 2006).

Absolute rate coefficient values at room temperature are all in good agreement. Absolute methods for the determination of OH rate coefficients are prone to influence from OH regeneration within the instruments, and so are likely to under predict the actual rate coefficient values using this method. The study by McGillen *et al.* (2013) also investigated the rate coefficient for the reaction of ^{18}OH radicals with *n*-butanol in order to determine whether OH regeneration was influencing their results. The authors concluded that OH regeneration was ~10% at 296 K for the reaction of OH radicals with *n*-butanol. The numerous OH radical sources employed in the study by McGillen *et al.* (2013), and the absence of OH regeneration for the other isomers of butanol investigated, validate the method used for the determination of the rate coefficients. The authors suggested a number of mechanisms which may lead to the regeneration of OH radicals, however, the exact pathway is unknown.

All the literature rate coefficients given in Table 1-3 are in reasonable agreement within their stated error limits. Two temperature dependent studies have been carried out; those of Yujing and Mellouki (2001) and McGillen *et al.* (2013), which are in good agreement. Both studies, however, have used absolute methods for the determination of the rate coefficient. The relative rate method for the determination of rate coefficients is not influenced by OH regeneration, and so temperature dependent relative rate studies for the determination of the rate coefficient of *n*-butanol with OH radicals would assist in validating those determined by absolute methods.

$k_{OH + n\text{-butanol}}$ / cm^3 molecule^{-1} s^{-1}	Temperature / K	Method	Reference
$(8.31 \pm 0.63) \times 10^{-12}$	296	FP-RF	Wallington and Kurylo (1987)
$(7.80 \pm 0.20) \times 10^{-12}$	298 ± 2	PR-RA	Nelson *et al.* (1990)
$5.30 \times 10^{-12} \exp[(146 \pm 92) / T]$	263 – 372	PLP-LIF	Yujing and Mellouki (2001)
$(8.65 \pm 2.71) \times 10^{-12}$	298	PLP-LIF	Yujing and Mellouki (2001)
$(9.68 \pm 0.75) \times 10^{-12}$	296	PLP-LIF	McGillen *et al.* (2013)*
$(6.8 \pm 1.3) \times 10^{-12}$	292	RR	Campbell *et al.* (1976)
$(7.97 \pm 0.66) \times 10^{-12}$	298 ± 2	RR	Nelson *et al.* (1990)
$(1.03 \pm 0.05) \times 10^{-11}$	298 ± 2	RR	Oh and Andino (2001)
$(7.67 \pm 0.14) \times 10^{-12}$	298 ± 2	RR	Cavalli *et al.* (2002)
$(8.86 \pm 0.85) \times 10^{-12}$	296 ± 2	RR	Hurley *et al.* (2009)
$(8.58 \pm 0.66) \times 10^{-12}$	295 ± 2	RR	Wu *et al.* (2003)
$(8.5 \pm 3.0) \times 10^{-12}$	298	Evaluation†	Atkinson *et al.* (2006)

Table 1-3: Summary of experimentally determined rate coefficients for the reaction of *n*-butanol with OH radicals in the literature. FP-RF = flash photolysis – resonance fluorescence, PR-RA = pulsed radiolysis coupled with resonance absorption, PLP-LIF = pulsed laser photolysis coupled with laser induced fluorescence, RR = relative rate. *Measurements were carried out over the temperature range 220 – 380 K, where non-Arrhenius behaviour was observed. †IUPAC recommended value, determined from the absolute temperature dependent study of Yujing and Mellouki (2001).

Fewer studies have been conducted on the mechanisms and products of the OH initiated oxidation of *n*-butanol. Cavalli *et al.* (2002) and Hurley *et al.* (2009) have both reported on the products of the OH radical initiated oxidation of *n*-butanol in the presence of NO_x. The former study being carried out in the EUPHORE chamber (195 m^3 volume, outdoor, FEP) and the latter in a 0.14 m^3, indoor Pyrex chamber. Molar yields obtained from both of these studies are shown in Table 1-4.

Product	Hurley *et al.* (2009)	Cavalli *et al.* (2002)
Butyraldehyde	44 ± 4%	51.8 ± 7.1%
Propanal	19 ± 2%	23.4 ± 3.5%
Acetaldehyde	12 ± 3%	12.7 ± 2.2%
Formaldehyde	-	43.4 ± 2.4%

Table 1-4: Summary of molar yields determined from the OH radical initiated oxidation of *n*-butanol in the presence of NO_x.

Good agreement between the two studies is observed for the OH radical initiated oxidation of *n*-butanol in the presence of NO_x. Two different OH radical sources were used in the studies; Cavalli *et al.* (2002) used the photolysis of HONO (R 1-37) by UV radiation from the sun, and Hurley *et al.* (2009) used the photolysis of methyl nitrite (CH_3ONO). Both of these OH radical precursors results in relatively high concentrations of NO_x being present in the respective atmospheric simulation chambers. The production of OH radicals from the photolysis of CH_3ONO is described by R 1-34, R 1-35 and R 1-36. Additional NO was added to the initial reaction mixture for the photolysis of CH_3ONO in order to promote the conversion of HO_2 radicals to OH radicals through R 1-36.

$$CH_3ONO + h\nu_{(\lambda \geq 290\ nm)} \rightarrow CH_3O + NO \qquad \text{R 1-34}$$

$$CH_3O + O_2 \rightarrow CH_2O + HO_2 \qquad \text{R 1-35}$$

$$HO_2 + NO \rightarrow OH + NO_2 \qquad \text{R 1-36}$$

The method by which HONO is produced for the studies of Cavalli *et al.* (2002) also results in high levels of NO_x being present in the reaction mixture. The authors reported initial concentrations of NO and NO_2 to be $(1.8 - 2.3) \times 10^{12}$ molecule cm^{-3} (72 - 92 ppbv); similar to that expected in a high NO_x environment. Hurley *et al.* (2009) used

concentrations of NO up to 8.9×10^{14} molecule cm^{-3} (35.6 ppmv) in their studies; far greater than which is typically observed in high NO_x environments.

$$HONO + h\nu_{(\lambda \leq 400\ nm)} \rightarrow OH + NO \qquad \text{R 1-37}$$

Despite the considerable differences in initial NO_x concentrations between the two studies, as seen in Table 1-3, molar yields are in very good agreement. This indicates that the concentration of NO_x present does not have an influence on the products of the OH radical initiated oxidation. Studies under varying NO_x conditions would help to elucidate any dependence on NO_x concentrations. As governments worldwide are enforcing stricter regulations on emissions of NO_x, with emissions in England having declined by ~70% since 1990 (Bailey *et al.* 2016), understanding the potential impact of tropospheric oxidation processes on the environment under varying NO_x conditions is vital.

The OH radical initiated oxidation of *n*-butanol in the absence of NO_x has not been reported in the literature. The use of peroxide photolysis, such as hydrogen peroxide (H_2O_2), would be an ideal low NO_x OH radical source (R 1-38) for such studies.

$$H_2O_2 + h\nu_{(\lambda > 230\ nm)} \rightarrow 2OH \qquad \text{R 1-38}$$

The major disadvantage of the use of peroxides as an OH radical source is that they require shorter wavelengths for their photolysis, at which many of the expected carbonyl products may also be photolysed. Photolysis rates of such carbonyl product compounds can, however, be measured and thus experimental data can be corrected for any photolysis reactions occurring and influencing the product yields.

The kinetics of *n*-butanol with Cl atoms have not been studied as extensively as the reaction with OH radicals. Details of the rate coefficients in the literature for the reaction of *n*-butanol with Cl atoms are summarised in Table 1-5.

$k_{(Cl + n\text{-butanol})}$ / cm^3 molecule^{-1} s^{-1}	Temperature / K	Method	Reference
$(1.96 \pm 0.19) \times 10^{-10}$	298	PLP-RF	Garzón *et al.* (2006)
$3.12 \times 10^{-11}\exp[(548\pm65)/T]$	266 – 382	PLP-RF	Garzón *et al.* (2006)
$(2.14 \pm 0.11) \times 10^{-10}$	298 ± 2	RR	Nelson *et al.* (1990)
$(2.25 \pm 0.11) \times 10^{-10}$	295	RR	Wu *et al.* (2003)
$(2.37 \pm 0.11) \times 10^{-10}$	295	RR	Wu *et al.* (2003)
$(2.21 \pm 0.38) \times 10^{-10}$	296 ± 2	RR	Hurley *et al.* (2009)
$(2.2 \pm 0.4) \times 10^{-10}$	298	Evaluation*	Atkinson *et al.* (2006)

Table 1-5: Summary of experimental literature rate coefficients for the reaction of *n*-butanol with Cl atoms. PLP-RF = pulsed laser fluorescence – resonance fluorescence, RR = relative rate. *IUPAC recommended value, determined from the studies by Garzón *et al.* (2006), Nelson *et al.* (1990) and Wu *et al.* (2003).

All rate coefficients determined by the relative rate method at room temperature are in good agreement. Wu *et al.* (2003) reported two values for the rate coefficient using two different reference compounds; $(2.25 \pm 0.11) \times 10^{-10}$ cm^3 molecule^{-1} s^{-1} was determined using propane as a reference compound and $(2.37 \pm 0.11) \times 10^{-10}$ cm^3 molecule^{-1} s^{-1} using cyclohexane. The rate coefficient reported by Hurley *et al.* (2009) was determined from combining individually determined rate coefficients with three different reference compounds; acetylene, ethane and propene. Cyclohexane was also used as the reference compound in the study by Nelson *et al.* (1990) giving a rate coefficient of $(2.14 \pm 0.11) \times 10^{-10}$ cm^3 molecule^{-1} s^{-1}, which is in good agreement with that determined by Wu *et al.* (2003) using the same reference compound. Garzón *et al.* (2006) have reported the only measurements of the rate coefficient for *n*-butanol with Cl atoms using an absolute method, it is also the only temperature dependent study reported in the literature. The room temperature value reported of $k_{Cl + n\text{-butanol}} = (1.96 \pm 0.19) \times 10^{-10}$ cm^3 molecule^{-1} s^{-1} is in good agreement with the values determined using the relative rate method, however, it is slightly lower. As with the measurement of rate coefficients of compounds with OH radicals by absolute methods, the measurement of Cl atom rate coefficients are also prone to Cl regeneration, influencing the observed rate coefficients,

which result in an underestimation of the rate coefficients, likely to be the cause of the lower value reported by Garzón *et al.* (2006).

As only one temperature dependent study for the determination of the rate coefficient for the reaction of Cl atoms with *n*-butanol has been carried out, by an absolute method which is prone to interferences from Cl atom regeneration, it is concluded that the temperature dependence observed may also be influenced by Cl atom regeneration. McGillen *et al.* (2013) reported that the OH regeneration in their study of the rate coefficient for the reaction of *n*-butanol with OH radicals decreased as temperature increased. Correctly accounting for any interferences from the regeneration of OH radical or Cl atoms in absolute methods for rate coefficient determinations is therefore critical. Non-Arrhenius behaviour was observed for the kinetics of *n*-butanol with OH radicals (McGillen *et al.* 2013). Extending the temperature range and studying the temperature dependence of the rate coefficient for the reaction of *n*-butanol with Cl atoms using the relative rate technique would assist in verifying the temperature dependence observed by Garzón *et al.* (2006) and determining whether, *n*-butanol shows non-Arrhenius behaviour for its reaction with Cl atoms. The relative rate technique is not expected to be influenced by any Cl atom regeneration.

Hurley *et al.* (2009) have presented the only study currently in the literature on the products and mechanism of the Cl atom initiated oxidation of *n*-butanol in the presence and absence of NO_x. The molar yields determined from their study are summarised in Table 1-6.

Product	Molar Yield (with NO)	Molar Yield (without NO)
Butyraldehyde	38 ± 2%	38 ± 2%
Propanal	23 ± 3%	-
Acetaldehyde	12 ± 4%	-
Formaldehyde	33 ± 3%	-

Table 1-6: Molar yields for the Cl atom initiated oxidation of *n*-butanol in the presence and absence of NO as reported by Hurley *et al.* (2009).

The photolysis of Cl_2 was used to produced Cl atoms in the presence and absence of NO_x; studies in the presence of NO_x used initial [NO] = $(1.8 – 3.6) \times 10^{15}$ molecule cm^{-3} (72 - 140 ppmv), again considerably higher concentrations to what would be expected in high NO_x environments. It was concluded that the difference in yields of propanal,

acetaldehyde and formaldehyde in the presence of NO_x is due to the importance of chemical activation in the tropospheric oxidation of *n*-butanol. A review by Orlando *et al.* (2003) discusses the atmospheric chemistry of alkoxy radicals, detailing the importance of chemical activation on the decomposition of alkoxy radicals in oxidation processes in the presence of NO_x. The decomposition of alkoxy radicals in the presence of NO_x can be described by R 1-39 to R 1-45, where the peroxy radical decomposes via a short lived vibrationally excited peroxy nitrite (R 1-39), which is an exothermic reaction. Much of the exothermicity from the reaction of the peroxy radical with NO is transferred to the alkoxy radical, which subsequently decomposes on a short timescale ($<10^{-9}$ s).

$RO_2^{\cdot} + NO \rightarrow ROONO^*$ R 1-39

$ROONO^* \rightarrow RO^{\cdot *} + NO_2$ R 1-40

$ROONO^* + M \rightarrow ROONO + M$ R 1-41

$ROONO \rightarrow RO^{\cdot} + NO_2$ R 1-42

$RO^{\cdot *} \rightarrow$ decomposition of isomerisation R 1-43

$RO^{\cdot *} + M \rightarrow RO^{\cdot} + M$ R 1-44

$RO^{\cdot} \rightarrow$ decomposition, isomerisation or reaction with O_2 R 1-45

None of the yields reported by Hurley *et al.* (2009) following the Cl atom or OH radical initiated oxidation of *n*-butanol in the presence or absence of NO_x were corrected for secondary formation through the oxidation or subsequent reactions of the higher aldehydes, and so are reported as upper limits on the yields. It was determined that the Cl atom initiated oxidation proceeds 38 ± 2% via α-hydrogen abstraction, and the OH radical initiated oxidation proceeds 44 ± 4% via α-hydrogen abstraction for the reaction with *n*-butanol. These percentages reflect the relative kinetics for the Cl atom and OH radical reaction with *n*-butanol and the increased selectivity for the α-hydrogen attack by OH radicals.

1.5.1.2 *sec*-butanol

The kinetics of *sec*-butanol have not been studied as extensively as *n*-butanol under atmospherically relevant conditions. Table 1-7 summarises the rate coefficients in the literature for the reaction of OH radicals with *sec*-butanol. Production of the isomers of butanol for the use as potential biofuels is typically carried out by fermentation processes. However, the production of *sec*-butanol by this method can be expensive as it has a lower

boiling point than water, making it difficult to recover in the fermentation process (Chen *et al.* 2015).

$k_{(OH + sec\text{-butanol})}$ / cm^3 $molecule^{-1}$ s^{-1}	Temperature / K	Method	Reference
$(8.58 \pm 0.49) \times 10^{-12}$	296 ± 2	RR	Chew and Atkinson (1996)
$(8.80 \pm 0.14) \times 10^{-12}$	297 ± 3	RR	Baxley and Wells (1998)
$(7.57 \pm 0.44) \times 10^{-12}$	297 ± 3	RR	Baxley and Wells (1998)
$(8.88 \pm 0.69) \times 10^{-12}$	296	PLP-LIF	McGillen *et al.* (2013)
$(9.01 \pm 1.00) \times 10^{-12}$	298	PLP-LIF	Jiménez *et al.* (2005)
$2.76 \times 10^{-12}\exp[(328\pm124)/T]$	263 – 354	PLP-LIF	Jiménez *et al.* (2005)
$(8.7 \pm 3.1) \times 10^{-12}$	298	Evaluation*	Atkinson *et al.* (2006)

Table 1-7: Summary of experimentally determined rate coefficients for the reaction of Cl atoms with *sec*-butanol. RR = relative rate, PLP-LIF = pulsed laser photolysis – laser induced fluorescence. *IUPAC rate coefficient evaluation determined using measurements made by Chew and Atkinson (1996) and Baxley and Wells (1998).

All of the room temperature rate coefficients for the reaction of OH radicals with *sec*-butanol are in good agreement. The value reported by Jiménez *et al.* (2005) using an absolute method is slightly higher than those determined using the relative rate method; they also determined a slight temperature dependence over the temperature range 263 - 354 K, however, they do note that their obtained results show considerable scatter. Further temperature dependent studies on the kinetics of OH radicals with *sec*-butanol are required to reduce this scatter. Chew and Atkinson (1996) and Baxley and Wells (1998) have reported on the products from the OH radical initiated oxidation of *sec*-butanol, the results from these studies are summarised in Table 1-8.

Product	Chew and Atkinson (1996)	Baxley and Wells (1998)
2-butanone	69.5 ± 0.73%	60 ± 2%
Acetaldehyde	-	29 ± 4%

Table 1-8: Summary of experimentally determined yields for the OH initiated oxidation of *sec*-butanol in the presence of NO_x.

The product yields of 2-butanone from Baxley and Wells (1998) and Chew and Atkinson (1996) are in good agreement, Baxley and Wells (1998) also reported an acetaldehyde yield of 29 ± 4%. Only one study has been reported in the literature on the kinetics of *sec*-butanol with Cl atoms (summarised in Table 1-9), by Ballesteros *et al.* (2007), where a negative temperature dependence was reported over the range 267 – 384 K. The authors also reported the observation of 2-butanone as a major product in the oxidation reaction. No other product studies are available in the literature for the Cl atom initiated oxidation of *sec*-butanol.

$k_{(Cl + sec\text{-butanol})}$ / cm^3 $molecule^{-1}$ s^{-1}	Temperature / K	Method	Reference
$(1.32 \pm 0.14) \times 10^{-10}$	298 ± 2	RR	Ballesteros *et al.* (2007)
$6.16 \times 10^{-11}\exp[(174\pm58)/T]$	267 – 384	PLP-RF	Ballesteros *et al.* (2007)
$(1.10 \pm 0.22) \times 10^{-10}$	298	PLP-RF	Ballesteros *et al.* (2007)

Table 1-9: Summary of experimentally determined rate coefficients for the reaction of *sec*-butanol with Cl atoms. RR = relative rate, PLP-RF = puled laser photolysis – resonance fluorescence.

1.5.1.3 *iso*-butanol

The kinetics, mechanisms and products relating to the atmospheric fate of *iso*-butanol has seen increased interest due to its potential use as a biofuel (Su *et al.* 2015). A summary of the current literature values for the rate coefficient of *iso*-butanol with OH radicals is given in Table 1-10.

$k_{(OH + iso\text{-butanol})}$ / cm^3 $molecule^{-1}$ s^{-1}	Temperature / K	Method	Reference
$3.1 \times 10^{-12} \exp[(352 \pm 82)/T]$	241 – 370	PLP-LIF	Mellouki *et al.* (2004)
$(9.2 \pm 0.4) \times 10^{-12}$	298	PLP-LIF	Mellouki *et al.* (2004)
$(8.8 \pm 0.3) \times 10^{-12}$	295 ± 2	RR	Wu *et al.* (2003)
$(9.2 \pm 0.4) \times 10^{-12}$	295 ± 2	RR	Wu *et al.* (2003)
$(8.5 \pm 0.1) \times 10^{-12}$	298 ± 2	RR	Mellouki *et al.* (2004)
$(8.8 \pm 0.3) \times 10^{-12}$	298 ± 2	RR	Mellouki *et al.* (2004)
$(9.72 \pm 0.72) \times 10^{-12}$	296	PLP-LIF	*McGillen *et al.* (2013)
$(1.14 \pm 0.17) \times 10^{-11}$	296 ± 2	RR	Andersen *et al.* (2010)
$(8.9 \pm 1.7) \times 10^{-12}$	298	†Evaluation	Atkinson *et al.* (2006)

Table 1-10: Summary of experimentally determined rate coefficients for the reaction of *iso*-butanol with OH radicals as described in the literature. PLP-LIF = pulsed lased photolysis – laser induced fluorescence. RR = relative rate. *Temperature dependent studies were also carried out – see text below. †IUPAC evaluated rate coefficient determined from the values reported by Mellouki *et al.* (2004) and Wu *et al.* (2003).

Good agreement is observed between the reported rate coefficients for the reaction of *iso*-butanol with OH radicals. Temperature dependent studies have been carried out by Mellouki *et al.* (2004) and McGillen *et al.* (2013); the former reporting an Arrhenius expression describing the temperature dependence of $3.1 \times 10^{-12} \exp[(352 \pm 82) / T]$ cm^3 $molecule^{-1}$ s^{-1}. The room temperature rate coefficients determined by Mellouki *et al.* (2004) by both the relative rate method and an absolute method are in excellent agreement, indicating no significant influence from OH regeneration in the absolute determination of $k_{OH + iso\text{-butanol}}$. This is in agreement with observations made by McGillen *et al.* (2013) who also reported no OH regeneration. McGillen *et al.* (2013) extended the temperature range to 221 – 381 K, and observed clear non-Arrhenius behaviour. Further temperature dependent studies on the kinetics of *iso*-butanol with OH radicals would assist in verifying the temperature dependence of this reaction.

Only one previous product study of the OH radical initiated oxidation of *iso*-butanol has been reported in the literature by Andersen *et al.* (2010), where the authors reported a

61 ± 4% molar yield of acetone in the presence of NO_x. It would be expected that the OH radical initiated oxidation would predominantly proceed via the α-hydrogen abstraction leading to the formation of *iso*-butyraldehyde. Strong absorptions in the IR by CH_3ONO obscured any evidence of *iso*-butyraldehyde formation in these experiments. Considering the OH radical attack is expected to proceed predominantly via the α-hydrogen, this reported acetone yield of 61 ± 4% is relatively high; the yield however, has not been corrected for any secondary formation of acetone through photolysis or subsequent reaction with OH radicals of *iso*-butyraldehyde, and so should be taken as an upper limit. Similar to the product study of *n*-butanol with OH radicals in the presence of NO_x (Hurley *et al.* 2009), relatively high concentrations of NO were present in the reaction mixture as compared to what would be expected in high NO_x environments. Again it is suggested that the use of a different OH radical precursor, such as H_2O_2, would allow for the products of the reaction with *iso*-butanol to be investigated under more tropospherically relevant concentrations of NO_x, and also allowing for *iso*-butyraldehyde to be observed in the IR.

Only two studies are reported in the literature for the determination of the rate coefficient for the reaction of *iso*-butanol with Cl atoms, their results are summarised in Table 1-11. No temperature dependent studies have been carried out, and both of the room temperature studies have been carried out using the relative rate method.

$k_{(Cl + iso\text{-butanol})}$ / cm^3 $molecule^{-1}$ s^{-1}	Temperature / K	Method	Reference
$(1.82 \pm 0.04) \times 10^{-10}$	295 ± 2	RR*	Wu *et al.* (2003)
$(1.96 \pm 0.11) \times 10^{-10}$	295 ± 2	RR†	Wu *et al.* (2003)
$(2.02 \pm 0.23) \times 10^{-10}$	296 ± 2	RR†	Andersen *et al.* (2010)
$(2.10 \pm 0.33) \times 10^{-10}$	296 ± 2	RR‡	Andersen *et al.* (2010)

Table 1-11: Summary of experimentally determined rate coefficients for the reaction of *iso*-butanol with Cl atoms as reported in the literature. RR = relative rate. *reference compound = propane, †reference compound = cyclohexane, ‡reference compound = ethane.

Both studies employed two different reference compounds; cyclohexane and propane were used by Wu *et al.* (2003), with their results being in very close agreement. Andersen *et al.* (2010) used cyclohexane and ethane as reference compounds, again with excellent agreement between the rate coefficients obtained. The results of the two studies are in

very good agreement, particularly for those where cyclohexane was used as the reference compound. Ambient temperatures vary greatly worldwide, and so it is essential for temperature dependent studies to be carried out for such compounds as *iso*-butanol, in order to fully assess their potential impacts in the troposphere if used as future biofuels. Studies carried out using absolute methods for the measurement of the kinetics for the reaction of *iso*-butanol with Cl atoms would also be greatly beneficial in validating those determined using the relative rate method.

One product study of the Cl atom initiated oxidation of *iso*-butanol in the presence and absence of NO_x is presented in the literature by Andersen *et al.* (2010); the results of which are summarised in Table 1-12.

Product	Yield (with NO)	Yield (without NO)
***Iso*-butyraldehyde**	46 ± 3%	48 ± 3%
Acetone	35 ± 3%	-
Formaldehyde	49 ± 3%	-

Table 1-12: Summary of the molar yields determined by Andersen *et al.* (2010) for the Cl atom initiated oxidation of *iso*-butanol in the presence and absence of NO_x.

Similar to the Cl atom initiated oxidation of *n*-butanol in the absence of NO_x, only the α-hydrogen abstraction product, *iso*-butyraldehyde, was observed as a primary product in the Cl atom initiated oxidation of *iso*-butanol. For small consumptions (<20%) of *iso*-butanol, very small yields (<5%) were observed for acetone and formaldehyde, with considerable formation of these two compounds being observed as secondary products. This is mirrored by a turnover in the production of *iso*-butyraldehyde which, following its production, is subsequently lost due to photolysis and reaction with Cl atoms. Substantial primary yields of acetone and formaldehyde were reported for the Cl atom initiated oxidation in the presence of NO_x; 35 ± 3% and 49 ± 3%, respectively. These yields, however, are likely to be an overestimation as the loss of *iso*-butyraldehyde by OH radicals in the system was assumed to be negligible. Further studies into the OH radical and Cl atom oxidation of *iso*-butanol in the presence of varying, tropospherically relevant NO_x concentrations would assist in developing the understanding of the fate of *iso*-butanol in the troposphere.

Hurley *et al.* (2009) have reported on the kinetics, mechanisms and products of the oxidation of *n*-butanol with Cl atom initiated oxidation in the presence and absence of

NO_x, and OH radical initiated oxidation in the presence of NO_x. This study was carried out in a 140 L Pyrex atmospheric simulation chamber, with the primary carbonyl products from the oxidation processes being presented. The major oxidation product in all cases was seen to be butyraldehyde, following the α-hydrogen abstraction by either Cl atoms or OH radicals. For the Cl atom initiated oxidation in the absence of NO_x, only butyraldehyde was observed as a primary product, however, in the presence of NO_x propanal, acetaldehyde and formaldehyde were also observed as major oxidation products (38%, 23%, 12% and 33% molar yields, respectively). Propanal, acetaldehyde and formaldehyde were also observed for the OH radical initiated oxidation of *n*-butanol in the presence of NO_x, and it was concluded that chemical activation is important in the atmospheric chemistry of the alkoxy radicals formed during the oxidation process.

As the alcohol series is ascended, the tropospheric reactivity of higher alcohols tends towards that of their comparable alkanes. The OH initiated oxidation of the four isomers of butanol has been reported by McGillen *et al.* (2013), with the end product branching ratios discussed.

Product	$k_{(OH + HC)}$ / cm^3 molecule^{-1} s^{-1}	$k_{(Cl + HC)}$ / cm^3 molecule^{-1} s^{-1}
***n*-butanol**	$^{*}8.5 \times 10^{-12}$	$^{*}2.2 \times 10^{-10}$
***sec*-butanol**	$^{*}8.7 \times 10^{-12}$	$^{\dagger}1.32 \times 10^{-10}$
***iso*-butanol**	$^{*}8.9 \times 10^{-12}$	$^{\ddagger}2.06 \times 10^{-10}$
***tert*-butanol**	$^{*}1.1 \times 10^{-12}$	$^{\S}3.15 \times 10^{-11}$

Table 1-13: Comparison of rate coefficients for the reaction of OH radicals and Cl atoms with the four isomers of butanol. *IUPAC recommended rate coefficients taken from Atkinson *et al.* (2006). †taken from Ballesteros *et al.* (2007). ‡taken from Andersen *et al.* (2010). §taken from Wu *et al.* (2003).

As discussed in Section 1.3 the oxidation of VOCs initiated by Cl atoms also plays an important role in tropospheric chemical mechanisms. OH radicals are more abundant in the troposphere, however, VOCs typically have rates of reactions with Cl atoms considerably faster than with OH radicals. Cl atom chemistry has shown increased interest in its importance for VOC oxidation processes particularly in high NO_x polluted environments. Table 1-13 compares the rate coefficients for the reaction of Cl atoms and OH radicals with the four isomers of butanol, showing the difference in reactivity of the isomers of butanol towards OH radicals compared to Cl atoms.

1.5.1.4 Atmospheric Fate of Aldehydes

As has been described in Sections 1.5.1.1, 1.5.1.2 and 1.5.1.3, aldehydes are some of the major products formed during the tropospheric oxidation of alcohols. They are photochemically active, absorbing light in the wavelength range 240 – 360 nm (Wenger 2006). The main fate of aldehydes in the troposphere is their loss through photolysis and reaction with OH radicals. Although alcohols themselves as fuels may have lower atmospheric reactivity as compared to traditional fossil fuels, their major oxidation products (and combustion emissions), aldehydes, typically have much higher reactivity, leading to higher ozone forming potentials (as has been discussed in Section 1.3). It is therefore extremely important to fully understand the mechanisms for both the production and destruction of aldehydes within the troposphere in order to investigate the potential impact on the atmosphere from the use of alcohols as biofuels in vehicle engines. The importance of NO_x chemistry has been described in Section 1.2; the presence of NO_x in the troposphere during the oxidation of VOCs leads to the formation of tropospheric ozone. The studies described above in Sections 1.5.1.1, 1.5.1.2 and 1.5.1.3, into the OH radical and Cl atom initiated oxidation of butanols have all been carried out at extremely high NO_x concentrations. Urban areas typically have high concentrations of NO_x (>100 ppbv) and remote areas such as forested regions typically have low levels of NO_x. In 2014 road transport emissions accounted for 45.1% of total NO_x emissions (Bailey *et al.* 2016).

1.6 Atmospheric Simulation Chambers

Atmospheric simulation chambers are extremely useful in their ability to study many variants in the atmosphere. The Highly Instrumented Reactor for Atmospheric Chemistry (HIRAC) is one such chamber, developed at the University of Leeds (Glowacki *et al.* 2007). There are many atmospheric simulation chambers worldwide, ranging in construction materials, size and available analytical instrumentation. A comprehensive comparison of all of these is far beyond the scope of this work, and so only relevant chambers for comparison with HIRAC will be discussed here. Table 1-14 details a number of atmospheric simulation chambers and their key features.

There are a number of advantages and disadvantages arising from the choice of construction material used in building atmospheric simulation chambers. The use of stainless steel, such as the HIRAC chamber and the CESAM chamber (Wang *et al.* 2011), allows for studies to be conducted under a range of temperatures and pressures. Both of these chambers are constructed to allow either heated or cooled fluid to circulate around

the outside of the chamber, with HIRAC being able to maintain temperatures over the range 253 – 343 K, and CESAM over the range 253 – 323 K. The use of stainless steel as a construction material, however, limits the size achievable for atmospheric simulation chambers.

Fluorinated ethylene propylene (FEP) Teflon chambers, such as SAPHIR, EUPHORE, ACOM and ILMARI (see Table 1-14 for references) can only be operated at ambient temperatures and are typically operated at pressures slightly above ambient (SAPHIR is operated ~80 Pa above ambient pressure and EUPHORE is operated 100 – 200 Pa above ambient). The majority of FEP chambers are large outdoor chambers, such as SAPHIR and EUPHORE, and are able to utilise the UV radiation directly from the sun to initiate chemical reactions. The advantage of this is that the full emission spectrum of the sun is used, and so reactions can be directly linked to those in the atmosphere. Cloud cover, however, can limit the amount of the sun's UV radiation reaching the contents of the chamber. Smaller indoor FEP chambers such as ACOM and ILMARI are often surrounded by UV lamps which can be illuminated to initiate photochemical reactions.

Smaller indoor atmospheric simulation chambers have greater volume to surface area, making wall reactions important to correctly characterise. Such reactions are typically dependent on the construction material. FEP chambers suffer from high background levels of NO_x, and large outdoor FEP chambers such as SAPHIR often utilise the HONO emitted from the chamber walls as a source of OH radicals (Rohrer *et al.* 2005). Details of the HIRAC chamber and its instrumentation will be given in Chapter 2.

Chamber	Location	Construction Material	Volume / m^3	Major Analytical Instrumentation	Light Source	Operating Pressure	Operating Temperature	Reference
HIRAC	Leeds, UK	Stainless Steel	2.25	GC-FID, FTIR, O_3 analyser, NO_x analyser, FAGE, k_{OH}	254 nm 360 nm 310 nm	10 – 1000 mbar	253 – 343 K	Glowacki *et al.* (2007)
SAPHIR	Jülich, Germany	FEP	270	FAGE, DOAS, NO_x analyser. O_3 analyser, k_{OH}, PTR-MS, GC-	Sunlight	80 Pa above ambient	Ambient	Rohrer *et al.* (2005)
EUPHORE	Valencia, Spain	FEP	400	FTIR, PTR-MS, LIF, O_3 analyser, NO_x analyser	Sunlight	100 – 200 above ambient	Ambient	Siese *et al.* (2001)
ACOM	Boulder, CO, USA	FEP	10	GC-FID, PTR-MS, O_3 analyser, CIMS, SMPS	Black Lamps	-	Ambient	(Zhao *et al.* 2013)
CESAM	Paris, France	Stainless Steel	4.2	NO_x analyser, O_3 analyser, GC-MS, FTIR, SMPS	Arc xenon	10^{-7} – 2 atm	253 – 232	Wang *et al.* (2011)
ILMARI	Joensuu, Finland	FEP	29				Ambient	

Table 1-14: Comparison of key features and major analytical instrumentation for selected atmospheric simulation chambers.

1.7 HO_x Measurement Techniques

As has been discussed in Section 1.2, HO_x (= OH + HO_2) plays a vital role in the removal of trace gases and pollutants in the troposphere. The low tropospheric concentrations of OH (~10^6 molecule cm^{-3}) require the use of extremely sensitive detection methods. Three main techniques have been developed for the measurement of HO_x in the troposphere; differential optical absorption spectroscopy (DOAS), chemical ionisation mass spectrometry (CIMS) and laser induced fluorescence (LIF). A brief outline of each of these methods for the measurement of OH and HO_2 radicals in the troposphere is given, with discussion on their main advantages and disadvantages.

1.7.1 Differential Optical Absorption Spectroscopy

Differential optical absorption spectroscopy (DOAS) measures concentrations of species of interest from their absorption at specific wavelengths of light using the Beer-Lambert law:

$$A = \varepsilon c l \qquad \text{Eq. 1-4}$$

where A is the absorption, ε is the cross section of the species of interest at the chosen wavelength, and l is the path length. One of the major draw backs of DOAS instruments is its poor sensitivity, meaning a long path length is needed in order to achieve the signal to noise ratio required to measure low tropospheric concentrations. A DOAS instrument for the measurement of OH radicals is in operation at the SAPHIR chamber in Jülich, Germany, as illustrated in Figure 1-10 (Schlosser *et al.* 2007). Laser light at ~308 nm is used as the light source for the long path for the measurement of OH radicals; in the DOAS set up at the SAPHIR chamber, the 308 nm laser light makes 112 passes, resulting in a total absorption path length of 2240 m.

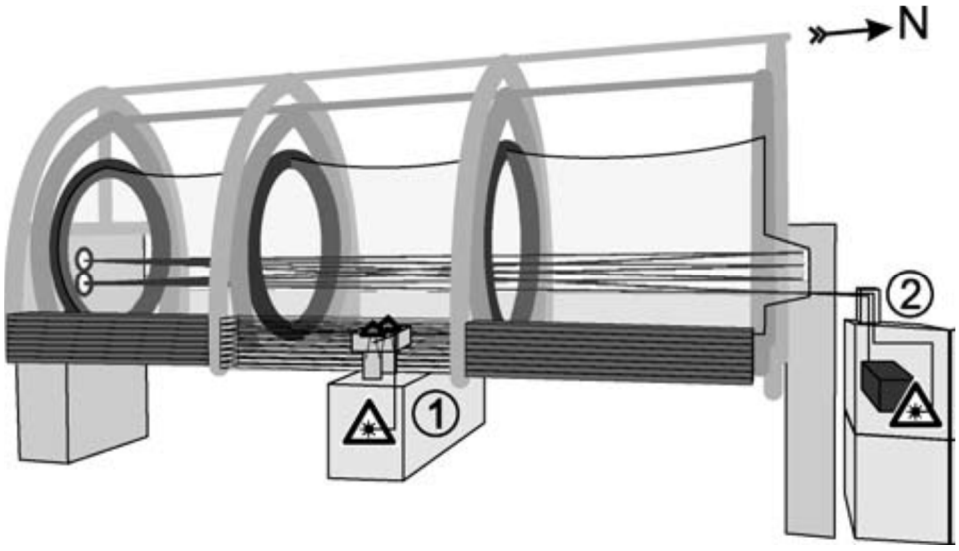

Figure 1-10: Schematic diagram showing positioning of instrumentation for the measurement of HO_x radicals at the SAPHIR chamber at the Jülich Forschungszentrum, Germany. 1 = positioning of LIF FAGE instrument, 2 = DOAS instrument. Reproduced from Schlosser *et al.* (2007).

The method by which OH radical concentrations are measured with DOAS instrumentation means that calibration is not required; but is achieved using data for absorption cross sections that are predetermined in the laboratory using R 1-6. The absorption of other species at the wavelengths used for OH measurements (such as SO_2 and HCHO) need to be subtracted from spectra before the OH absorption spectrum is fitted in order to determine OH concentrations.

1.7.2 Chemical Ionisation Mass Spectrometry

Chemical ionisation mass spectrometry (CIMS) is an indirect method for the measurement of OH radicals. OH radicals are converted into isotopically labelled sulphuric acid (R 1-46 to R 1-48), which does not naturally occur in the troposphere, and so reduces any background interferences. The sulphuric acid can then be measured by quadrupole mass spectrometry of the highly stable anion, following atom abstraction by the nitrate ion, R 1-49 (Berresheim *et al.* 2000).

$$OH + {}^{34}SO_2 + M \rightarrow H^{34}SO_3 + O_2 \qquad \text{R 1-46}$$

$$H^{34}SO_3 + O_2 \rightarrow {}^{34}SO_3 + HO_2 \qquad \text{R 1-47}$$

$${}^{34}SO_3 + H_2O + M \rightarrow H_2{}^{34}SO_4 + M \qquad \text{R 1-48}$$

$$H_2{}^{34}SO_4 + NO_3^-\cdot HNO_3 \rightarrow H^{34}SO_4^-\cdot HNO_3 + HNO_3 \qquad \text{R 1-49}$$

CIMS is not an absolute method for OH radical measurements, and so requires calibration in order to convert signal into OH concentrations. CIMS instrumentation can

also be used for the detection of HO_2 radicals, through its conversion to OH from the reaction with NO:

$$HO_2 + NO \rightarrow OH + NO_2 \qquad \text{R 1-50}$$

1.7.3 Fluorescence Assay by Gas Expansion

Fluorescence assay by gas expansion (FAGE) was first reported by Hard *et al.* (1979) for the *in situ* measurements of OH radicals in the atmosphere. Since then, a number of modifications to the technique have been made, and a number of FAGE instruments are in use globally for ground based, aircraft and chamber based studies of HO_x radicals. Details of the FAGE instrument used in the HIRAC laboratory are given in Chapter 3, including a description of the instrument itself and development of calibration techniques.

In the FAGE method for measuring HO_x radicals, the sampled air is expanded through a pinhole (typically ~1 mm) into a low pressure detection chamber (~3.8 mbar for the HIRAC FAGE instrument). Laser light with a wavelength of ~308 nm is used for both the excitation and detection of fluorescence from OH radicals; this is known as on-resonance detection. HO_2 radicals are converted into OH radicals through their reaction with NO (R 1-50). The OH radicals are then excited and their fluorescence is detected in the same manner.

1.7.4 Overview and Comparison of HO_x Instrumentation

Formal comparisons of the DOAS, CIMS and LIF methods for the measurement of HO_x have been carried out by Schlosser *et al.* (2009) and Fuchs *et al.* (2010). Atmospheric simulation chambers such as SAPHIR and EUPHORE are ideally suited for instrument intercomparison measurements; their large size allows for multiple instruments to sample air of the same chemical composition from within the chamber. One such intercomparison of HO_x instrumentation is the HO_x campaign which was carried out in 2005 at the SAPHIR chamber in Jülich, Germany (Schlosser *et al.* 2009, Fuchs *et al.* 2010). During these measurements, comparisons between LIF, CIMS and DOAS instruments were made for both ambient air samples and air sampled from the SAPHIR chamber. Three LIF instruments and one CIMS instrument were compared for ambient measurements of OH radicals, and three LIF instruments and one DOAS instrument were compared for chamber measurements of OH radicals. Good agreement between the instruments was shown for ambient measurements of OH and excellent agreement was observed for measurements from the SAPHIR chamber. Three LIF instruments were

compared for measurements of HO_2 radicals for both ambient and SAPHIR measurements; with the three instruments showing good agreement with each other. It was, however, observed that the three LIF instruments were influenced by a previously unknown consideration relating to the water vapour concentration within SAPHIR, and it was suggested that this could have also affected ambient measurements where instruments were all sampling from slightly different locations at the site. A number of instrument comparisons have been carried out for ambient measurements of OH radicals, including aircraft based OH radical measurement comparison (Hofzumahaus *et al.* 1998, Schlosser *et al.* 2007, Ren *et al.* 2012).

Measurements of HO_x are typically compared to model simulations; using chemical mechanisms which have been developed through laboratory experiments. The Master Chemical Mechanism (MCM) is a chemical mechanism developed at the University of Leeds for the gas phase chemical reactions occurring in the troposphere; the latest version of the MCM contains the degradation processes of 143 VOCs (MCM 2016). The use of such models, constrained to measurements of VOCs allows for detailed comparisons with measured HO_x concentrations to be made; good agreement, however, does not necessarily mean that all mechanisms within the chemical model are correctly represented. Incorrect estimations for both sources and sinks of HO_x may coincidentally balance with each other. Many comparisons of measurements and modelled HO_x concentrations have been reported in the literature; where modelled OH concentrations often under predict the observed OH concentrations.

A comparison of measured and modelled average diurnal OH concentrations is shown in Figure 1-11 for measurements taken in the Pearl River Delta, China (Hofzumahaus *et al.* 2009). Good agreement between the measured and modelled OH concentrations was observed in the mornings, with the measured OH concentrations being considerably greater than the modelled [OH] and measured HO_2 concentrations being slightly greater than the modelled [HO_2] in the second half of the day. It was concluded that OH sources in the chemical model were not sufficient to match the observed HO_x concentrations at later times in the day.

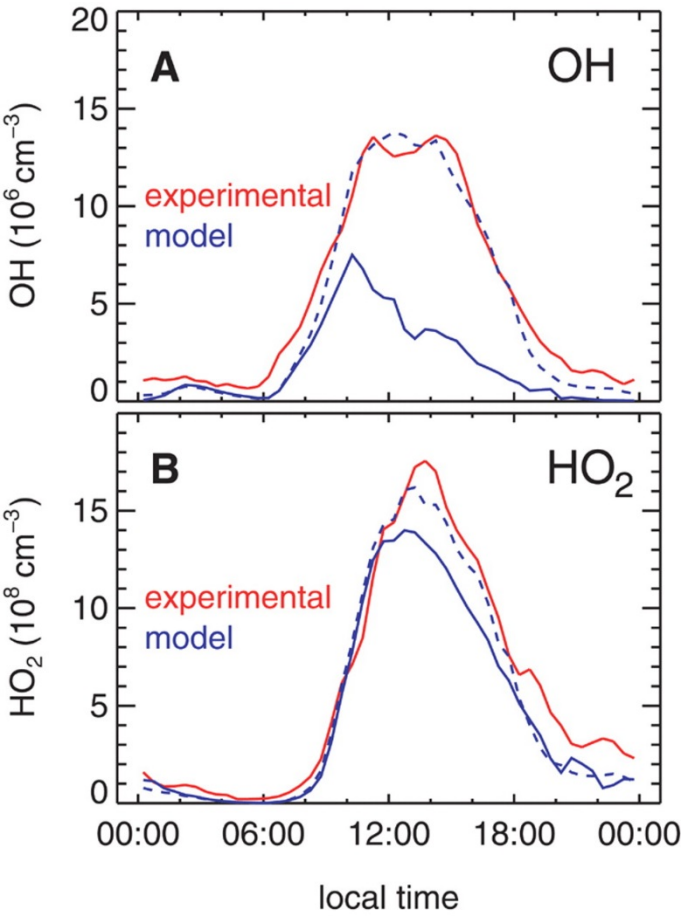

Figure 1-11: Comparison of average diurnal measured and modelled OH and HO_2 concentrations from field measurements take in the Pearl River Delta, China. Solid red lines represent measured concentrations, solid blue lines represent Regional Atmospheric Chemistry Mechanism (RACM) base case modelled concentrations, dashed blue lines represent extended RACM modelled concentrations. Reproduced from Hofzumahaus *et al.* (2009).

1.8 OH Reactivity Measurement Techniques

Three different types of instrument have been developed and are widely used for measuring total OH reactivity; the total OH loss rate measurement (TOHLM), the comparative reactivity method (CRM) and laser flash photolysis coupled with laser induced fluorescence (LFP-LIF). A description of each of the three methods will be given here (a detailed description of the Leeds LFP-LIF instrument is given in Chapter 4).

1.8.1 Comparative Reactivity Method

The comparative reactivity method for the measurement of OH reactivity was first described by Sinha *et al.* (2008) and has since been developed by a number of groups (Table 1-15). CRM instruments consist of a glass reaction cell, as illustrated in Figure 1-12, in which a sequence of flows are introduced, coupled to a detector (PTR-MS or GC-PID) in order to measure the total OH loss rate. The CRM relies on the measurement of a reactive species, typically pyrrole, during a three step measurement

procedure, described by Figure 1-13. The concentration of pyrrole is highest in the first step (C1 in Figure 1-13). In this step, pyrrole is introduced into the reaction cell with dry zero air, and should only be lost to any reaction with impurities present in the dry zero air, loss to the walls of the reaction cell or photolysis of pyrrole by the mercury pen ray lamp ($\lambda = 184.9$ nm). The pyrrole concentration decreases in the second step (C2 in Figure 1-13), where OH radicals are generated in the reaction cell, following R 1-51, as humidified zero air is introduced into the reaction cell. The decrease in pyrrole concentration in the second step is due to the reaction of pyrrole with the OH radicals present in the reaction cell.

$$H_2O + h\nu_{(\lambda = 184.9\ nm)} \rightarrow H + OH \qquad \text{R 1-51}$$

$$H + O_2 + M \rightarrow HO_2 + M \qquad \text{R 1-52}$$

In the third step (C3 in Figure 1-13) an increase in pyrrole concentration from the C2 step is observed. Ambient air is drawn into the reaction cell through "Arm A" as shown in Figure 1-12. OH radicals are also generated following R 1-51 from an addition of humidified air into the reaction cell. The increase in pyrrole concertation in this step is due to the OH reactive species present in the sampled ambient air competing with the pyrrole for the reaction with OH radicals present in the reaction cell. From these three steps, the OH reactivity (k'_{OH}) can be calculated following Eq. 1-5:

$$k'_{OH} = \frac{(C3\text{-}C2)}{(C1\text{-}C3)} k_{OH+pyrrole} C1 \qquad \text{Eq. 1-5}$$

where $k_{OH + pyrrole}$ is the rate constant for the reaction of pyrrole with OH radicals, taken as 1.28×10^{-10} cm^3 molecule^{-1} s^{-1} from Dillon *et al.* (2012). Several criteria have been described by Sinha *et al.* (2008) for choosing an appropriate reference compound, most importantly the compound must not be present in ambient air and must have a well-defined rate coefficient for its reaction with OH radicals. The authors also noted that the method could employ other suitable reference species, such as labelled isotopes of isoprene, where suitable compounds with a lower rate coefficient with OH than that of pyrrole would improve the sensitivity at lower values of OH reactivity.

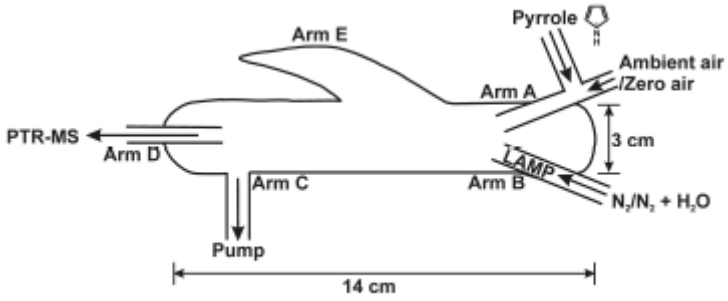

Figure 1-12: Schematic of the glass reaction cell used in CRM instruments for the measurement of OH reactivity, reproduced from Sinha *et al.* (2008).

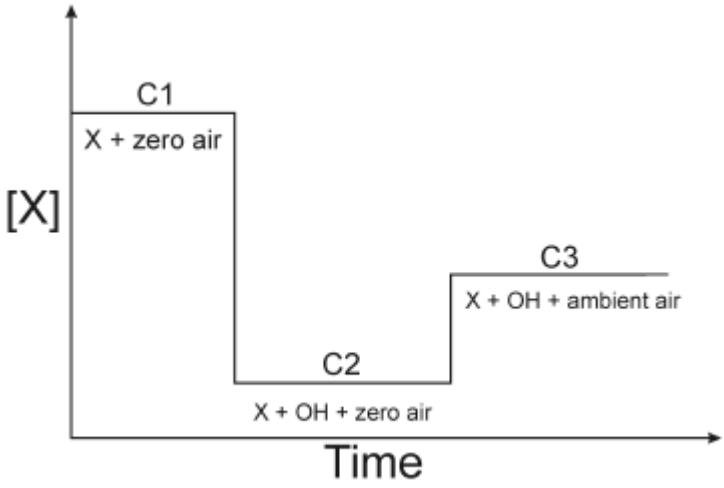

Figure 1-13: Schematic of the three step measurement procedure used in the measurement of OH reactivity with CRM instruments, where [x] is pyrrole. Reproduced from Sinha *et al.* (2008).

During all three steps in the measurement procedure, a mercury pen ray lamp is switched on (placed in "Arm B", as illustrated in Figure 1-13), in order to produce OH radicals in the presence of humidified air, following R 1-51. Characterisation of a number of CRM instruments has been reported by several groups (Sinha *et al.* 2008, Hansen *et al.* 2015, Michoud *et al.* 2015). Full details on the of the characterisation of CRM instruments is beyond the scope of this work, however, it should be noted that numerous correction factors are required during the data analysis procedure, including corrections for changes in relative humidity within the reactor during the three step measurement procedure, corrections for NO and NO_2 which leads to increased formation of OH by reaction of NO with HO_2 (HO_2 is produced within the reaction cell by R 1-52), and correction for deviations from pseudo first order conditions.

Since the CRM technique was first described in the literature, a number of groups have also developed instruments based on the original glass reaction cell design, with many

of them using glass reaction cells built by the Max-Planck-Institut für Chemie (Mainz, Germany). Table 1-15 gives details of a number of CRM instruments that have been developed to date. Sinha *et al.* (2008) first described the CRM instrument for OH reactivity measurements, with Nölscher *et al.* (2012) describing an alternative method for monitoring the pyrrole concentration by GC-PID. The use of GC-PID as a detector for pyrrole in CRM instruments provides a number of advantages over the PTR-MS, mainly its reduced cost, reduced running costs and that it is considerably smaller than the PTR-MS systems, making it easier to transport for field measurements. A summary of the use of the CRM-GC-PID system is given by Nölscher *et al.* (2012), where measurements were compared to, and shown to be in good agreement with, a CRM-PTR-MS instrument system. This comparison of the two detector systems included laboratory, plant chamber and boreal forest measurements. A CRM-GC-PID system is also in development at the Finnish Meteorological Institute (FMI), Finland.

Group	Instrument Detector	Limit of detection / s^{-1}	References
MPI, Mainz, Germany	GC-PID	3	(Nölscher *et al.* 2012)
MPI, Mainz, Germany	PTR-MS	3 (3σ)	Williams *et al.* (2016)
NCAR, Boulder CO, USA	PTR-MS	15 (3σ)	(Kim *et al.* 2011)
FMI, Finland	GC-PID	Not Available	Not Available
Mines Douai, France	PTR-MS	3 (3σ)	Michoud *et al.* (2015)
LSCE, France	PTR-MS	3 (3σ)	Zannoni *et al.* (2016)
IISER, India	PTR-MR	4.5	Kumar and Sinha (2014)

Table 1-15: Comparison of CRM instruments for the measurements of OH reactivity. GC-PID = Gas Chromatography photoionisation detector, PTR-MS = proton transfer mass spectrometry.

1.8.2 Total OH Loss rate Measurement

The total OH loss rate measurement (TOHLM) for measuring OH reactivity was first described by Kovacs and Brune (2001). A schematic of a TOHLM instrument is shown in Figure 1-14. In this method, OH radicals are generated in the flow tube of the instrument via the photolysis of water vapour by a mercury pen ray lamp (R 1-51 and

R 1-52), housed within a moveable injector. Reactive species sampled from ambient air react with the OH radicals within the flow tube, with the OH radicals being detected by LIF.

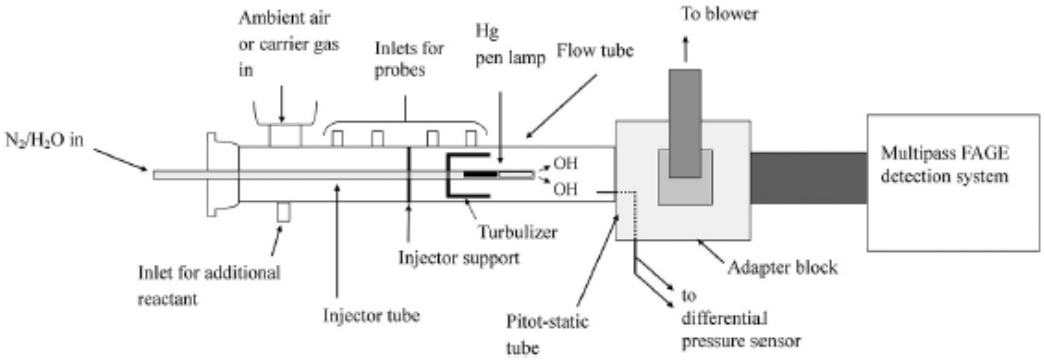

Figure 1-14: Schematic of a TOHLM instrument for the measurement of OH reactivity, reproduced from Hansen *et al.* (2014).

The injector is moved forwards and backwards within the flow tube in order to alter the time for the reaction of the OH radicals with OH reactive species present in the sampled gas. The OH radical signal is measured continuously over the forwards and backwards movement of the injector in order to build up a decay.

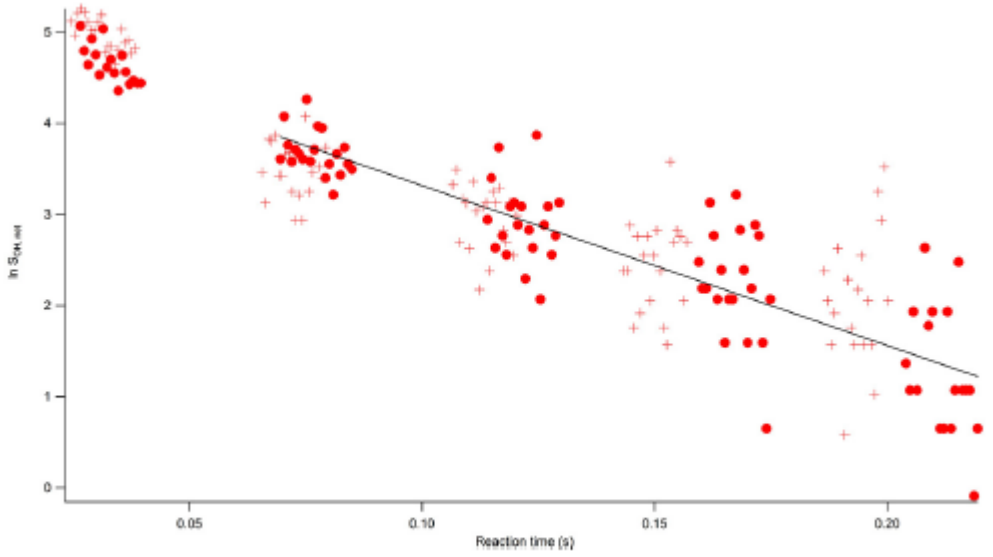

Figure 1-15: Example of data recorded by the Indiana University TOHLM instrument for the measurement of OH reactivity, reproduced from Hansen *et al.* (2014). Red crosses show data from the injector moving in the forwards direction and red circles show data from the injector moving in the backwards direction.

An example of data recorded from a TOHLM instrument is given in Figure 1-15. A linear fit to the natural logarithm of the data yields and OH reactivity value, in this case a value of 16.4 s^{-1} was obtained (Hansen *et al.* 2014). The reaction time (*x*-axis) correlates to the

injector position within the instrument. The first set of data points in this plot are not used in the analysis as the OH in the flow tube is not completely mixed at these short reaction times (<50 – 60 ms).

Group	OH Detection Method	Limit of Detection / s^{-1}	$k'_{OH(physical)}$ / s^{-1}	References
Pennsylvania State University, USA	LIF	0.3 (2σ)	2.0 ± 0.3	Mao *et al.* (2009)
Indiana University, Bloomington IN, USA	LIF	0.7 (1σ)	3.6 ± 0.2	Hansen *et al.* (2014)
University of Leeds, UK*	LIF	2	1.6 ± 0.4	Ingham *et al.* (2009)
German Weather Service	CIMS	Not Available	Not Available	Not Available

Table 1-16: Comparison of a number of TOHLM instruments for the measurement of OH reactivity. *Instrument no longer in use.

1.8.3 Laser Flash Photolysis coupled with Laser Induced Fluorescence

The laser flash photolysis coupled with laser induced fluorescence (LFP-LIF) method for measuring OH reactivity was first described by Sadanaga *et al.* (2004). In this method, OH radicals are produced in a flow tube via ozone photolysis (R 1-53). $O(^1D)$, produced in R 1-53, and subsequently reacts with water vapour present in the sampled gas flow to give two OH radicals, R 1-54.

$$O_3 + h\nu_{(\lambda = 266\ nm)} \rightarrow O_2 + O(^1D) \qquad \text{R 1-53}$$

$$O(^1D) + H_2O \rightarrow 2OH \qquad \text{R 1-54}$$

The OH radicals produced in the flow tube of the instrument react with any OH reactive species present in the sampled gas flow; the OH decay signal is detected by LIF and recorded in real time. A more detailed description of the LFP-LIF method for the measurements of OH reactivity, and specific details on the Leeds LFP-LIF instrument will be given in Chapter 4.

Group	Limit of Detection / s^{-1}	Instrument zero / s^{-1}	References
Tokyo Metropolitan University, Japan	Not reported	2.8	Sadanaga *et al.* (2004)
University of Lille, France	0.9 – 3.6 (3σ)	6.6 ± 1.2	Hansen *et al.* (2015)
University of Leeds, UK	0.4 – 1.0 (1σ)	2.25 ± 0.21	Stone *et al.* (2016) Cryer (2016)
Jülich Forschungszentrum, Germany*	0.9 (3σ)	1.4 ± 0.3	Lou *et al.* (2010)
Jülich Forschungszentrum, Germany†	0.3 (1σ)	3.1	Fuchs *et al.* (2017)

Table 1-17: Comparison of LFP-LIF OH reactivity instruments. *Mobile instrument developed for field measurements. †Instrument developed for measurements sampling from the SAPHIR chamber.

1.8.4 Overview and Comparison of OH Reactivity Instruments

A brief description has been given here of the three techniques that have been developed for the measurement of OH reactivity. Further details of the LFP-LIF instrument developed at Leeds are given in Chapter 4. Each of the three techniques have distinct advantages and disadvantages. Both the LFP-LIF and TOHLM instruments use 308 nm laser light to detect OH radicals by LIF. These instruments have been developed by groups who already have existing laser set ups for the measurement of OH and HO_2 radicals by LIF at 308 nm. CRM instruments have typically been developed by groups already using PTR-MS instruments for the measurements of VOCs.

The main advantage of the LFP-LIF technique over the TOHLM is that it is the only instrument able to measure OH reactivity in real time. This is especially advantageous for measurements in places where concentrations of OH reactive species present in the sampled air are changing on a relatively short time scale, such as in urban environments. The averaging time of the LFP-LIF is mainly dependent on the initial signal observed (as described in Chapter 4), whereas the averaging time of the TOHLM instruments is dependent on the time required to move the injector backwards and forwards to build up an OH decay, typically being ~200s.

The major disadvantage of the LFP-LIF instruments is that the instrument requires the use of two lasers; one at 266 nm for the generation of OH radicals in the photolysis flow tube, and one at 308 nm for the excitation and detection of fluorescence of OH radicals in the FAGE cell, which incurs high costs. LFP-LIF instruments have high time resolution, typically 30 – 120 s.

CRM instruments have a much lower time resolution, typically taking one OH reactivity measurement every 10 minutes, due the three step procedure required for the measurements. The GC-PID instrument described by Nölscher *et al.* (2012) offers a low cost alternative for the measurements of OH reactivity. A major disadvantage of the CRM instruments is that they require a large number of corrections in the data analysis procedures in order to determine the value of k'_{OH}, which can lead to greater uncertainties. Extensive characterisation is required in order to apply appropriate correction factors to the raw data (Michoud *et al.* 2015).

A number of instrument comparisons have recently been described in the literature for the measurement of OH reactivity using the different instrument techniques. Zannoni *et al.* (2015) described a comparison of two CRM OH reactivity instruments; one from LSCE, France and one from Mines Douai, France. In results from an intercomparison in the Mediterranean basin of these two instruments, good agreement between the two instruments was observed for measurements of OH reactivity in a low NO_x, terpene rich environment (Zannoni *et al.* 2015). A correlation plot of the raw OH reactivity measurements for values up to 50 s^{-1} gave a gradient of 0.74 ± 0.07 and $R^2 = 0.667$. When all correction factors had been applied to OH reactivity measurements from the two instruments, the correlation of the final values increased to give a gradient of 0.96 ± 0.12, however, the scatter was also significantly increased, with $R^2 = 0.543$. Measurements of OH reactivity made with TOHLM and CRM instruments require corrections to be made to the raw data to account for any reaction of HO_2 (produced simultaneously in the instruments from the method of OH radical production) with NO present in the sampled gas.

Similar to measurements of OH and HO_2 radical concentrations, OH reactivity measurements are often compared to modelled and calculated OH reactivity, using measurements of VOC concentrations. One such example is a detailed modelling study carried out by Whalley *et al.* (2016), where numerous model scenarios were compared with measurements of OH reactivity from the ClearfLo field campaign in London 2012,

as illustrated by Figure 1-16. A recent review by Yang *et al.* (2016) discusses a wide range of both experimental and modelling studies of OH reactivity, which the reader is referred to for further details.

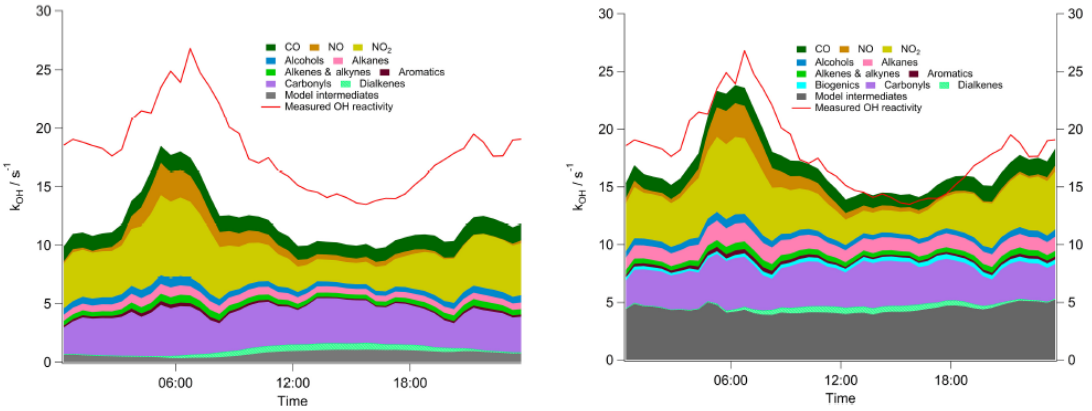

Figure 1-16: Comparison of modelled and measured OH reactivity for two different model scenarios. Left: model constrained to a standard set of measured VOC concentrations including C_2 – C_8 hydrocarbons and a small number of OVOCs Right: model constrained to an extended set of measured VOC concentrations including species up to C_{12} hydrocarbons. Reproduced from Whalley *et al.* (2016).

The inclusion of modelled intermediate species and an extended set of VOC concentration measurements for modelling the OH reactivity significantly reduces the gap between measured and modelled OH reactivity for measurements from the ClearfLo campaign. These results clearly show the importance of comprehensive VOC measurements in order to improve our understanding of chemical mechanisms and processes occurring in the troposphere. An extensive OH reactivity instrument comparison was carried out at the SAPHIR chamber in Jülich, Germany in October 2015. Results from some of the experiments carried out during this intercomparison are discussed in Chapter 5.

1.9 Summary

This chapter has given an introduction to the tropospheric chemistry relevant to the work presented in this thesis, highlighting the importance of atmospheric simulation chamber studies. A review of current literature into the atmospheric chemistry of the isomers of butanol has been given, focussing on those of importance for their potential use as biofuels. The different measurement techniques for the measurements of HO_x concentrations and OH reactivity have been compared. Details of an instrument for the measurement of HO_x concentrations will be given in Chapter 3, focussing on the development of calibration techniques. The development of an OH reactivity instrument

for measurements with the HIRAC chamber is given in Chapter 4, and results from an instrument intercomparison are given in Chapter 5. Results from temperature dependent relative rate studies for the reaction of *n*-butanol and *iso*-butanol with Cl atoms are given in Chapter 6. Results from the Cl atom and OH radical initiated oxidation processes of *iso*-butanol in the presence of varying initial NO concentrations are given Chapter 7, with a comparison of the products given for the different scenarios, including measurements of HO_x. Chapter 8 presents the first measurements of OH reactivity from the HIRAC chamber, following the relatively complex systems of the Cl atom and OH radical initiated oxidation of *iso*-butanol in the presence of varying initial NO concentrations, with comparisons being made to OH reactivity calculated from the measured species within HIRAC.

1.10 Project Aims

Atmospheric simulation chambers are an extremely important tool in the investigation of tropospheric chemistry, where specific chemical reactions can be studied in isolation. They are also extremely useful as they can provide a controlled environment in which analytical instrumentation can be developed and characterised. A major aim of this thesis was to further develop a FAGE instrument for the measurement of OH and HO_2 radicals and a LFP-LIF instrument for the measurement of OH reactivity, utilising the HIRAC chamber. Development of calibration methods, including the determination of the FAGE HO_2 cell sensitivity as a function of temperature, studied using the HIRAC chamber, and investigation into the errors associated with the N_2O actinometry experiment, are presented in Chapter 3.

Measurements of OH reactivity give valuable information relating to the oxidation capacity of an environment. Ambient measurements are typically compared to OH reactivity calculated from co-measured OH sinks; where the OH reactivity measurements are often greater than the calculations. These discrepancies are commonly attributed to unmeasured OH sinks and intermediate species. Measurements of OH reactivity following chamber studies enables measurements to be taken under a controlled environment, where known concentrations of reactants are present, and products of chemical reactions can be monitored. Comparison between calculated and measured OH reactivity following chamber studies is extremely useful as it can assist in highlighting areas in our understanding of specific chemical reactions that may be less well understood. The development of a LFP-LIF instrument to allow measurements from the

HIRAC chamber was another aim of this work. Chapter 4 details results from the development of this instrument and characterisation experiments whilst sampling from the HIRAC chamber. Results from an OH reactivity instrument intercomparison which was carried out at the SAPHIR chamber in Jülich, Germany, are presented in Chapter 5. These results assist in the validation of the measurement technique, with comparisons to two other instrument types and calculated OH reactivity.

Finally the work in this thesis aimed to bring together the development and improvement of both the FAGE instrument for OH and HO_2 radical measurements and the LFP-LIF instrument for OH reactivity measurements from the HRIAC chamber. There is increasing demand for research into potential biofuels as a renewable energy source. The isomers of butanol have shown potential as biofuels, with most studies having been presented on the production of *n*-butanol and *iso*-butanol. Chapter 7 and Chapter 8 present results following the oxidation of *iso*-butanol; with Chapter 8 reporting the first OH reactivity measurements from the HIRAC chamber following relatively complex oxidation processes. The aim of studying the oxidation processes of *iso*-butanol was to investigate the ozone formation under tropospherically relevant NO_x conditions and follow the changes in OH reactivity throughout the oxidation processes.

1.11 References

Alcantara, R., Amores, J., Canoira, L., Fidalgo, E., Franco, M. J. and Navarro, A. (2000). "Catalytic production of biodiesel from soy-bean oil, used frying oil and tallow." Biomass and Bioenergy **18**(6): 515-527.

Andersen, V. F., Wallington, T. J. and Nielsen, O. J. (2010). "Atmospheric Chemistry of *i*-Butanol." The Journal of Physical Chemistry A **114**(47): 12462-12469.

Andersson-Sköld, Y., Grennfelt, P. and Pleijel, K. (1992). "Photochemical Ozone Creation Potentials: A study of Different Concepts." Journal of the Air & Waste Management Association **42**(9): 1152-1158.

Antizar-Ladislao, B. and Turrion-Gomez, J. L. (2008). "Second-generation biofuels and local bioenergy systems." Biofuels Bioproducts & Biorefining-Biofpr **2**(5): 455-469.

Atkinson, R., Baulch, D. L., Cox, R. A., Crowley, J. N., Hampson, R. F., Hynes, R. G., Jenkin, M. E., Rossi, M. J. and Troe, J. (2004). "Evaluated kinetic and photochemical data for atmospheric chemistry: Volume I - gas phase reactions of O_x, HO_x, NO_x and SO_x species." Atmospheric Chemistry and Physics **4**(6): 1461-1738.

Atkinson, R., Baulch, D. L., Cox, R. A., Crowley, J. N., Hampson, R. F., Hynes, R. G., Jenkin, M. E., Rossi, M. J., Troe, J. and Subcommittee, I. (2006). "Evaluated kinetic and photochemical data for atmospheric chemistry: Volume II - gas phase reactions of organic species." Atmospheric Chemistry and Physics **6**(11): 3625-4055.

Baier, B. C., Brune, W. H., Lefer, B. L., Miller, D. O. and Martins, D. K. (2015). "Direct ozone production rate measurements and their use in assessing ozone source and receptor regions for Houston in 2013." Atmospheric Environment **114**: 83-91.

Bailey, R., Claxton, R., Jones, L., Kilroy, E., Misselbrook, T., Pang, Y., Passant, N., Salisbury, E., Smith, H., Thistlethwaite, G., Wakeling, D. and Walker, C. (2016). Air Quality Pollutant Inventories, for England, Scotland, Wales and Northern Ireland: 1990-2014. N. A. E. Inventory.

Balat, M., Balat, H. and Öz, C. (2008). "Progress in bioethanol processing." Progress in Energy and Combustion Science **34**(5): 551-573.

Ballesteros, B., Garzon, A., Jimenez, E., Notario, A. and Albaladejo, J. (2007). "Relative and absolute kinetic studies of 2-butanol and related alcohols with tropospheric Cl atoms." Physical Chemistry Chemical Physics **9**(10): 1210-1218.

Bannan, T. J., Booth, A. M., Bacak, A., Muller, J. B. A., Leather, K. E., Le Breton, M., Jones, B., Young, D., Coe, H., Allan, J., Visser, S., Slowik, J. G., Furger, M., Prévôt, A. S. H., Lee, J., Dunmore, R. E., Hopkins, J. R., Hamilton, J. F., Lewis, A. C., Whalley, L. K., Sharp, T., Stone, D., Heard, D. E., Fleming, Z. L., Leigh, R., Shallcross, D. E. and Percival, C. J. (2015). "The first UK measurements of nitryl chloride using a chemical ionization mass spectrometer in central London in the summer of 2012, and an investigation of the role of Cl atom oxidation." Journal of Geophysical Research: Atmospheres **120**(11): 2014JD022629.

Basha, S. A., Gopal, K. R. and Jebaraj, S. (2009). "A review on biodiesel production, combustion, emissions and performance." Renewable and Sustainable Energy Reviews **13**(6–7): 1628-1634.

Baxley, J. S. and Wells, J. R. (1998). "The hydroxyl radical reaction rate constant and atmospheric transformation products of 2-butanol and 2-pentanol." International Journal of Chemical Kinetics **30**(10): 745-752.

Berresheim, H., Elste, T., Plass-Dulmer, C., Eisele, F. L. and Tanner, D. J. (2000). "Chemical ionization mass spectrometer for long-term measurements of atmospheric OH and H_2SO_4." International Journal of Mass Spectrometry **202**(1-3): 91-109.

Campbell, I. M., McLaughlin, D. F. and Handy, B. J. (1976). "Rate constants for reactions of hydroxyl radicals with alcohol vapours at 292 K." Chemical Physics Letters **38**(2): 362-364.

Cardone, M., Prati, M. V., Rocco, V., Seggiani, M., Senatore, A. and Vitolo, S. (2002). "Brassica carinata as an Alternative Oil Crop for the Production of Biodiesel in Italy: Engine Performance and Regulated and Unregulated Exhaust Emissions." Environmental Science & Technology **36**(21): 4656-4662.

Carr, S. A., Blitz, M. A. and Seakins, P. W. (2011). "Site-Specific Rate Coefficients for Reaction of OH with Ethanol from 298 to 900 K." The Journal of Physical Chemistry A **115**(15): 3335-3345.

Carter, W. P. L. (1994). "Development of Ozone Reactivity Scales for Volatile Organic-Compounds." Journal of the Air & Waste Management Association **44**(7): 881-899.

Carter, W. P. L. (2009). "Updated Maximum Incremental Reactivity Scale and Hydrocarbon Bin Reacvities for Regulatory Applications." 2017, from https://www.arb.ca.gov/research/reactivity/mir09.pdf.

Carter, W. P. L. and Atkinson, R. (1987). "An experimental study of incremental hydrocarbon reactivity." Environmental Science & Technology **21**(7): 670-679.

Carter, W. P. L. and Atkinson, R. (1989). "Computer modeling study of incremental hydrocarbon reactivity." Environmental Science & Technology **23**(7): 864-880.

Cavalli, F., Geiger, H., Barnes, I. and Becker, K. H. (2002). "FTIR Kinetic, Product, and Modeling Study of the OH-Initiated Oxidation of 1-Butanol in Air." Environmental Science & Technology **36**(6): 1263-1270.

Cazorla, M. and Brune, W. H. (2010). "Measurement of Ozone Production Sensor." Atmospheric Measurement Techniques **3**(3): 545-555.

Cazorla, M., Brune, W. H., Ren, X. and Lefer, B. (2012). "Direct measurement of ozone production rates in Houston in 2009 and comparison with two estimation methods." Atmospheric Chemistry and Physics **12**(2): 1203-1212.

Chai, M., Lu, M., Liang, F., Tzillah, A., Dendramis, N. and Watson, L. (2013). "The use of biodiesel blends on a non-road generator and its impacts on ozone formation potentials based on carbonyl emissions." Environmental Pollution **178**(0): 159-165.

Chen, S., Ren, X., Mao, J., Chen, Z., Brune, W. H., Lefer, B., Rappenglück, B., Flynn, J., Olson, J. and Crawford, J. H. (2010). "A comparison of chemical mechanisms based on TRAMP-2006 field data." Atmospheric Environment **44**(33): 4116-4125.

Chen, Z., Wu, Y., Huang, J. and Liu, D. (2015). "Metabolic engineering of Klebsiella pneumoniae for the de novo production of 2-butanol as a potential biofuel." Bioresource Technology **197**: 260-265.

Chew, A. A. and Atkinson, R. (1996). "OH radical formation yields from the gas-phase reactions of O_3 with alkenes and monoterpenes." Journal of Geophysical Research: Atmospheres **101**(D22): 28649-28653.

Cryer, D. R. (2016). Measurements of hydroxyl radical reactivity and formaldehyde in the atmosphere. PhD, Leeds.

Derwent, R. G. and Jenkin, M. E. (1991). "Hydrocarbons and the long-range transport of ozone and PAN across Europe." Atmospheric Environment. Part A. General Topics **25**(8): 1661-1678.

Derwent, R. G., Jenkin, M. E., Passant, N. R. and Pilling, M. J. (2007). "Photochemical ozone creation potentials (POCPs) for different emission sources of organic compounds under European conditions estimated with a Master Chemical Mechanism." Atmospheric Environment **41**(12): 2570-2579.

Derwent, R. G., Jenkin, M. E. and Saunders, S. M. (1996). "Photochemical ozone creation potentials for a large number of reactive hydrocarbons under European conditions." Atmospheric Environment **30**(2): 181-199.

Derwent, R. G., Jenkin, M. E., Saunders, S. M. and Pilling, M. J. (1998). "Photochemical ozone creation potentials for organic compounds in northwest Europe calculated with a master chemical mechanism." Atmospheric Environment **32**(14-15): 2429-2441.

Derwent, R. G., Jenkin, M. E., Saunders, S. M. and Pilling, M. J. (2001). "Characterization of the Reactivities of Volatile Organic Compounds Using a Master Chemical Mechanism." Journal of the Air & Waste Management Association **51**(5): 699-707.

Dillon, T. J., Holscher, D., Sivakumaran, V., Horowitz, A. and Crowley, J. N. (2005). "Kinetics of the reactions of HO with methanol (210-351 K) and with ethanol (216-368 K)." Physical Chemistry Chemical Physics **7**(2): 349-355.

Dillon, T. J., Tucceri, M. E., Dulitz, K., Horowitz, A., Vereecken, L. and Crowley, J. N. (2012). "Reaction of Hydroxyl Radicals with C_4H_5N (Pyrrole): Temperature and Pressure Dependent Rate Coefficients." The Journal of Physical Chemistry A **116**(24): 6051-6058.

Edwards, P. M., Brown, S. S., Roberts, J. M., Ahmadov, R., Banta, R. M., deGouw, J. A., Dube, W. P., Field, R. A., Flynn, J. H., Gilman, J. B., Graus, M., Helmig, D., Koss, A., Langford, A. O., Lefer, B. L., Lerner, B. M., Li, R., Li, S.-M., McKeen, S. A., Murphy, S. M., Parrish, D. D., Senff, C. J., Soltis, J., Stutz, J., Sweeney, C., Thompson, C. R., Trainer, M. K., Tsai, C., Veres, P. R., Washenfelder, R. A., Warneke, C., Wild, R. J., Young, C. J., Yuan, B. and Zamora, R. (2014). "High winter ozone pollution from carbonyl photolysis in an oil and gas basin." Nature **514**(7522): 351-354.

Ellingsen, K., Gauss, M., Van Dingenen, R., Dentener, F. J., Emberson, L., Fiore, A. M., Schultz, M. G., Stevenson, D. S., Ashmore, M. R., Atherton, C. S., Bergmann, D. J., Bey, I., Butler, T., Drevet, J., Eskes, H., Hauglustaine, D. A., Isaksen, I. S. A., Horowitz, L. W., Krol, M., Lamarque, J. F., Lawrence, M. G., van Noije, T., Pyle, J., Rast, S., Rodriguez, J., Savage, N., Strahan, S., Sudo, K., Szopa, S. and Wild, O. (2008). "Global ozone and air quality: a multi-model assessment of risks to human health and crops." Atmospheric Chemistry and Physics Discussions **2008**: 2163-2223.

European Parliament and Council of the European Union (2008). Directive 2008/50/EC of the European Parliament and the Council of 21 May 2008 on ambient air quality and cleaner air for Europe.

European Union (2009). Directive 2009/28/EC of the European Parliament and of the Council of 23 April 2009 on the promotion of the use of energy from renewable sources and amending subsequently repealing Directives 2001/77/EC and 2003/30/EC. Official Journal of European Union**:** 16-62.

European Union (2015). Directive (EU) 2015/1513 of the European Parliament and of the Council of 9 September 2015 amending Directive 98/70/EC relating to the quality of petrol and diesel fuels and amending Directive 2009/28/EC on the promotion of the use of energy from renewable sources**:** 1-29.

Felzer, B. S., Cronin, T., Reilly, J. M., Melillo, J. M. and Wang, X. (2007). "Impacts of ozone on trees and crops." Comptes Rendus Geoscience **339**(11–12): 784-798.

Fontaras, G., Karavalakis, G., Kousoulidou, M., Tzamkiozis, T., Ntziachristos, L., Bakeas, E., Stournas, S. and Samaras, Z. (2009). "Effects of biodiesel on passenger car fuel consumption, regulated and non-regulated pollutant emissions over legislated and real-world driving cycles." Fuel **88**(9): 1608-1617.

Fuchs, H., Brauers, T., Dorn, H. P., Harder, H., Häseler, R., Hofzumahaus, A., Holland, F., Kanaya, Y., Kajii, Y., Kubistin, D., Lou, S., Martinez, M., Miyamoto, K., Nishida, S., Rudolf, M., Schlosser, E., Wahner, A., Yoshino, A. and Schurath, U. (2010). "Technical Note: Formal blind intercomparison of HO_2 measurements in the atmosphere simulation chamber SAPHIR during the HOxComp campaign." Atmospheric Chemistry and Physics **10**(24): 12233-12250.

Fuchs, H., Tan, Z., Lu, K., Bohn, B., Broch, S., Brown, S. S., Dong, H., Gomm, S., Häseler, R., He, L., Hofzumahaus, A., Holland, F., Li, X., Liu, Y., Lu, S., Min, K. E., Rohrer, F., Shao, M., Wang, B., Wang, M., Wu, Y., Zeng, L., Zhang, Y., Wahner, A. and Zhang, Y. (2017). "OH reactivity at a rural site (Wangdu) in the North China Plain: contributions from OH reactants and experimental OH budget." Atmospheric Chemistry and Physics **17**(1): 645-661.

Garzón, A., Cuevas, C. A., Ceacero, A. A., Notario, A., Albaladejo, J. and Fernández-Gómez, M. (2006). "Atmospheric reactions $Cl+CH_3–(CH_2)_n–OH(n=0–4)$: A kinetic and theoretical study." The Journal of Chemical Physics **125**(10): 104305.

Glowacki, D. R., Goddard, A., Hemavibool, K., Malkin, T. L., Commane, R., Anderson, F., Bloss, W. J., Heard, D. E., Ingham, T., Pilling, M. J. and Seakins, P. W. (2007). "Design of and initial results from a Highly Instrumented Reactor for Atmospheric Chemistry (HIRAC)." Atmospheric Chemistry and Physics **7**(20): 5371-5390.

Grana, R., Frassoldati, A., Faravelli, T., Niemann, U., Ranzi, E., Seiser, R., Cattolica, R. and Seshadri, K. (2010). "An experimental and kinetic modeling study of combustion of isomers of butanol." Combustion and Flame **157**(11): 2137-2154.

Hansen, R. F., Blocquet, M., Schoemaecker, C., Léonardis, T., Locoge, N., Fittschen, C., Hanoune, B., Stevens, P. S., Sinha, V. and Dusanter, S. (2015). "Intercomparison of the comparative reactivity method (CRM) and pump–probe technique for measuring total OH reactivity in an urban environment." Atmospheric Measurement Techniques **8**(10): 4243-4264.

Hansen, R. F., Griffith, S. M., Dusanter, S., Rickly, P. S., Stevens, P. S., Bertman, S. B., Carroll, M. A., Erickson, M. H., Flynn, J. H., Grossberg, N., Jobson, B. T., Lefer, B. L. and Wallace, H. W. (2014). "Measurements of total hydroxyl radical reactivity during CABINEX 2009 - Part 1: field measurements." Atmospheric Chemistry and Physics **14**(6): 2923-2937.

Hard, T. M., Obrien, R. J., Cook, T. B. and Tsongas, G. A. (1979). "Interference Suppression in HO Fluorescence Detection." Applied Optics **18**(19): 3216-3217.

He, C., Ge, Y., Tan, J., You, K., Han, X., Wang, J., You, Q. and Shah, A. N. (2009). "Comparison of carbonyl compounds emissions from diesel engine fueled with biodiesel and diesel." Atmospheric Environment **43**(24): 3657-3661.

Heard, D. E. and Pilling, M. J. (2003). "Measurement of OH and HO_2 in the Troposphere." Chemical Reviews **103**(12): 5163-5198.

Hess, W. P. and Tully, F. P. (1988). "Catalytic conversion of alcohols to alkenes by OH." Chemical Physics Letters **152**(2–3): 183-189.

Hofzumahaus, A., Aschmutat, U., Brandenburger, U., Brauers, T., Dorn, H.-P., Hausmann, M., Heßling, M., Holland, F., Plass-Dülmer, C. and Ehhalt, D. H. (1998). "Intercomparison of Tropospheric OH Measurements by Different Laser Techniques during the POPCORN Campaign 1994." Journal of Atmospheric Chemistry **31**(1): 227-246.

Hofzumahaus, A., Rohrer, F., Lu, K., Bohn, B., Brauers, T., Chang, C.-C., Fuchs, H., Holland, F., Kita, K., Kondo, Y., Li, X., Lou, S., Shao, M., Zeng, L., Wahner, A. and Zhang, Y. (2009). "Amplified Trace Gas Removal in the Troposphere." Science **324**(5935): 1702-1704.

Hurley, M. D., Wallington, T. J., Laursen, L., Javadi, M. S., Nielsen, O. J., Yamanaka, T. and Kawasaki, M. (2009). "Atmospheric Chemistry of *n*-Butanol: Kinetics, Mechanisms, and Products of Cl Atom and OH Radical Initiated Oxidation in the Presence and Absence of NO_x." The Journal of Physical Chemistry A **113**(25): 7011-7020.

Ingham, T., Goddard, A., Whalley, L. K., Furneaux, K. L., Edwards, P. M., Seal, C. P., Self, D. E., Johnson, G. P., Read, K. A., Lee, J. D. and Heard, D. E. (2009). "A flow-tube based laser-induced fluorescence instrument to measure OH reactivity in the troposphere." Atmospheric Measurement Techniques **2**(2): 465-477.

Jiménez, E., Gilles, M. K. and Ravishankara, A. R. (2003). "Kinetics of the reactions of the hydroxyl radical with CH_3OH and C_2H_5OH between 235 and 360 K." Journal of Photochemistry and Photobiology A: Chemistry **157**(2–3): 237-245.

Jiménez, E., Lanza, B., Garzón, A., Ballesteros, B. and Albaladejo, J. (2005). "Atmospheric Degradation of 2-Butanol, 2-Methyl-2-butanol, and 2,3-Dimethyl-2-butanol: OH Kinetics and UV Absorption Cross Sections." The Journal of Physical Chemistry A **109**(48): 10903-10909.

Jones, D. T. and Woods, D. R. (1986). "Acetone-butanol fermentation revisited." Microbiological Reviews **50**(4): 484-524.

Kim, S., Guenther, A., Karl, T. and Greenberg, J. (2011). "Contributions of primary and secondary biogenic VOC tototal OH reactivity during the CABINEX (Community Atmosphere-Biosphere INteractions Experiments)-09 field campaign." Atmospheric Chemistry and Physics **11**(16): 8613-8623.

Kohse-Höinghaus, K., Oßwald, P., Cool, T. A., Kasper, T., Hansen, N., Qi, F., Westbrook, C. K. and Westmoreland, P. R. (2010). "Biofuel Combustion Chemistry: From Ethanol to Biodiesel." Angewandte Chemie International Edition **49**(21): 3572-3597.

Kovacs, T. A. and Brune, W. H. (2001). "Total OH loss rate measurement." Journal of Atmospheric Chemistry **39**(2): 105-122.

Kumar, M. and Gayen, K. (2011). "Developments in biobutanol production: New insights." Applied Energy **88**(6): 1999-2012.

Kumar, N., Varun and Chauhan, S. R. (2013). "Performance and emission characteristics of biodiesel from different origins: A review." Renewable and Sustainable Energy Reviews **21**: 633-658.

Kumar, V. and Sinha, V. (2014). "VOC–OHM: A new technique for rapid measurements of ambient total OH reactivity and volatile organic compounds using a single proton transfer reaction mass spectrometer." International Journal of Mass Spectrometry **374**: 55-63.

Lawler, M. J., Finley, B. D., Keene, W. C., Pszenny, A. A. P., Read, K. A., von Glasow, R. and Saltzman, E. S. (2009). "Pollution-Enhanced Reactive Chlorine Chemistry in the Eastern Tropical Atlantic Boundary Layer." Geophysical Research Letters **36**: L08810.

Lawler, M. J., Sander, R., Carpenter, L. J., Lee, J. D., von Glasow, R., Sommariva, R. and Saltzman, E. S. (2011). "HOCl and Cl_2 observations in marine air." Atmospheric Chemistry and Physics **11**(15): 7617-7628.

Lin, Y.-C., Wu, T.-Y., Ou-Yang, W.-C. and Chen, C.-B. (2009). "Reducing emissions of carbonyl compounds and regulated harmful matters from a heavy-duty diesel engine

fueled with paraffinic/biodiesel blends at one low load steady-state condition." Atmospheric Environment **43**(16): 2642-2647.

Lou, S., Holland, F., Rohrer, F., Lu, K., Bohn, B., Brauers, T., Chang, C. C., Fuchs, H., Häseler, R., Kita, K., Kondo, Y., Li, X., Shao, M., Zeng, L., Wahner, A., Zhang, Y., Wang, W. and Hofzumahaus, A. (2010). "Atmospheric OH reactivities in the Pearl River Delta – China in summer 2006: measurement and model results." Atmospheric Chemistry and Physics **10**(22): 11243-11260.

Mao, J., Ren, X., Brune, W. H., Olson, J. R., Crawford, J. H., Fried, A., Huey, L. G., Cohen, R. C., Heikes, B., Singh, H. B., Blake, D. R., Sachse, G. W., Diskin, G. S., Hall, S. R. and Shetter, R. E. (2009). "Airborne measurement of OH reactivity during INTEX-B." Atmospheric Chemistry and Physics **9**: 163-173.

McGillen, M. R., Baasandorj, M. and Burkholder, J. B. (2013). "Gas-Phase Rate Coefficients for the OH + *n*-, *i*-, *s*-, and *t*-Butanol Reactions Measured Between 220 and 380 K: Non-Arrhenius Behavior and Site-Specific Reactivity." The Journal of Physical Chemistry A **117**(22): 4636-4656.

MCM. (2016). "Master Chemical Mechanism Version 3.3.1." 2016.

Meier, U., Grotheer, H. H., Riekert, G. and Just, T. (1985). "Temperature dependence and branching ratio of the C_2H_5OH+OH reaction." Chemical Physics Letters **115**(2): 221-225.

Mellouki, A., Oussar, F., Lun, X. and Chakir, A. (2004). "Kinetics of the reactions of the OH radical with 2-methyl-1-propanol, 3-methyl-1-butanol and 3-methyl-2-butanol between 241 and 373 K." Physical Chemistry Chemical Physics **6**(11): 2951-2955.

Michoud, V., Hansen, R. F., Locoge, N., Stevens, P. S. and Dusanter, S. (2015). "Detailed characterizations of the new Mines Douai comparative reactivity method instrument via laboratory experiments and modeling." Atmospheric Measurement Techniques **8**(8): 3537-3553.

Monks, P. (2009). "Atmospheric Composition Change—Global and Regional Air Quality." Atmospheric Environment **43**: 5268.

Monks, P. S. (2005). "Gas-phase radical chemistry in the troposphere." Chemical Society Reviews **34**(5): 376-395.

Naik, S. N., Goud, V. V., Rout, P. K. and Dalai, A. K. (2010). "Production of first and second generation biofuels: A comprehensive review." Renewable & Sustainable Energy Reviews **14**(2): 578-597.

Nelson, L., Rattigan, O., Neavyn, R., Sidebottom, H., Treacy, J. and Nielsen, O. J. (1990). "Absolute and relative rate constants for the reactions of hydroxyl radicals and chlorine atoms with a series of aliphatic alcohols and ethers at 298 K." International Journal of Chemical Kinetics **22**(11): 1111-1126.

Nigam, P. S. and Singh, A. (2011). "Production of liquid biofuels from renewable resources." Progress in Energy and Combustion Science **37**(1): 52-68.

Nölscher, A. C., Sinha, V., Bockisch, S., Klüpfel, T. and Williams, J. (2012). "Total OH reactivity measurements using a new fast Gas Chromatographic Photo-Ionization Detector (GC-PID)." Atmospheric Measurement Techniques **5**(12): 2981-2992.

Oh, S. and Andino, J. M. (2001). "Kinetics of the gas-phase reactions of hydroxyl radicals with C1–C6 aliphatic alcohols in the presence of ammonium sulfate aerosols." International Journal of Chemical Kinetics **33**(7): 422-430.

Orlando, J. J., Tyndall, G. S. and Wallington, T. J. (2003). "The Atmospheric Chemistry of Alkoxy Radicals." Chemical Reviews **103**(12): 4657-4690.

Oßwald, P., Güldenberg, H., Kohse-Höinghaus, K., Yang, B., Yuan, T. and Qi, F. (2011). "Combustion of butanol isomers – A detailed molecular beam mass spectrometry investigation of their flame chemistry." Combustion and Flame **158**(1): 2-15.

Rajesh Kumar, B. and Saravanan, S. (2016). "Use of higher alcohol biofuels in diesel engines: A review." Renewable and Sustainable Energy Reviews **60**: 84-115.

Ratcliff, M. A., Luecke, J., Williams, A., Christensen, E., Yanowitz, J., Reek, A. and McCormick, R. L. (2013). "Impact of Higher Alcohols Blended in Gasoline on Light-Duty Vehicle Exhaust Emissions." Environmental Science & Technology **47**(23): 13865-13872.

Ren, X., Mao, J., Brune, W. H., Cantrell, C. A., Mauldin, R. L., Hornbrook, R. S., Kosciuch, E., Olson, J. R., Crawford, J. H., Chen, G. and Singh, H. B. (2012). "Airborne intercomparison of HO_x measurements using laser-induced fluorescence and chemical ionization mass spectrometry during ARCTAS." Atmospheric Measurement Techniques **5**(8): 2025-2037.

Riedel, T. P. (2014). "An MCM Modeling Study of Nitryl Chloride ($ClNO_2$) Impacts on Oxidation, Ozone Production and Nitrogen Oxide Partitioning in Polluted Continental Outflow." Atmospheric Chemistry and Physics **14**: 3789.

Rohrer, F., Bohn, B., Brauers, T., Bruning, D., Johnen, F. J., Wahner, A. and Kleffmann, J. (2005). "Characterisation of the photolytic HONO-source in the atmosphere simulation chamber SAPHIR." Atmospheric Chemistry and Physics **5**: 2189-2201.

Sadanaga, Y., Yoshino, A., Watanabe, K., Yoshioka, A., Wakazono, Y., Kanaya, Y. and Kajii, Y. (2004). "Development of a measurement system of OH reactivity in the atmosphere by using a laser-induced pump and probe technique." Review of Scientific Instruments **75**(8): 2648-2655.

Saiz-Lopez, A. and von Glasow, R. (2012). "Reactive halogen chemistry in the troposphere." Chemical Society Reviews **41**(19): 6448-6472.

Sarathy, S. M., Oßwald, P., Hansen, N. and Kohse-Höinghaus, K. (2014). "Alcohol combustion chemistry." Progress in Energy and Combustion Science **44**: 40-102.

Sarathy, S. M., Vranckx, S., Yasunaga, K., Mehl, M., Oßwald, P., Metcalfe, W. K., Westbrook, C. K., Pitz, W. J., Kohse-Höinghaus, K., Fernandes, R. X. and Curran, H. J. (2012). "A comprehensive chemical kinetic combustion model for the four butanol isomers." Combustion and Flame **159**(6): 2028-2055.

Sarwar, G., Simon, H., Xing, J. and Mathur, R. (2014). "Importance of tropospheric $ClNO_2$ chemistry across the Northern Hemisphere." Geophysical Research Letters **41**(11): 2014GL059962.

Saxena, P. and Williams, F. A. (2007). "Numerical and experimental studies of ethanol flames." Proceedings of the Combustion Institute **31**(1): 1149-1156.

Schenk, P. M., Thomas-Hall, S. R., Stephens, E., Marx, U. C., Mussgnug, J. H., Posten, C., Kruse, O. and Hankamer, B. (2008). "Second Generation Biofuels: High-Efficiency Microalgae for Biodiesel Production." BioEnergy Research **1**(1): 20-43.

Schlosser, E., Bohn, B., Brauers, T., Dorn, H.-P., Fuchs, H., Häseler, R., Hofzumahaus, A., Holland, F., Rohrer, F., Rupp, L., Siese, M., Tillmann, R. and Wahner, A. (2007). "Intercomparison of Two Hydroxyl Radical Measurement Techniques at the Atmosphere Simulation Chamber SAPHIR." Journal of Atmospheric Chemistry **56**(2): 187-205.

Schlosser, E., Brauers, T., Dorn, H. P., Fuchs, H., Häseler, R., Hofzumahaus, A., Holland, F., Wahner, A., Kanaya, Y., Kajii, Y., Miyamoto, K., Nishida, S., Watanabe, K., Yoshino, A., Kubistin, D., Martinez, M., Rudolf, M., Harder, H., Berresheim, H., Elste, T., Plass-Dülmer, C., Stange, G. and Schurath, U. (2009). "Technical Note: Formal blind intercomparison of OH measurements: results from the international campaign HOxComp." Atmospheric Chemistry and Physics **9**(20): 7923-7948.

Siese, M., Becker, K. H., Brockmann, K. J., Geiger, H., Hofzumahaus, A., Holland, F., Mihelcic, D. and Wirtz, K. (2001). "Direct measurement of OH radicals from ozonolysis of selected alkenes: A EUPHORE simulation chamber study." Environmental Science & Technology **35**(23): 4660-4667.

Simpson, W. R., Brown, S. S., Saiz-Lopez, A., Thornton, J. A. and Glasow, R. v. (2015). "Tropospheric Halogen Chemistry: Sources, Cycling, and Impacts." Chemical Reviews **115**(10): 4035-4062.

Sinha, V., Williams, J., Crowley, J. N. and Lelieveld, J. (2008). "The Comparative Reactivity Method - a new tool to measure total OH Reactivity in ambient air." Atmospheric Chemistry and Physics **8**(8): 2213-2227.

Stone, D., Whalley, L. K. and Heard, D. E. (2012). "Tropospheric OH and HO_2 radicals: field measurements and model comparisons." Chemical Society Reviews **41**(19): 6348-6404.

Stone, D., Whalley, L. K., Ingham, T., Edwards, P. M., Cryer, D. R., Brumby, C. A., Seakins, P. W. and Heard, D. E. (2016). "Measurement of OH reactivity by laser flash photolysis coupled with laser-induced fluorescence spectroscopy." Atmospheric Measurement Techniques **9**(7): 2827-2844.

Su, H., Jiang, J., Lu, Q., Zhao, Z., Xie, T., Zhao, H. and Wang, M. (2015). "Engineering Corynebacterium crenatum to produce higher alcohols for biofuel using hydrolysates of duckweed (Landoltia punctata) as feedstock." Microbial Cell Factories **14**(1): 16.

Wallington, T. J. and Kurylo, M. J. (1987). "The gas phase reactions of hydroxyl radicals with a series of aliphatic alcohols over the temperature range 240–440 K." International Journal of Chemical Kinetics **19**(11): 1015-1023.

Wang, J., Doussin, J. F., Perrier, S., Perraudin, E., Katrib, Y., Pangui, E. and Picquet-Varrault, B. (2011). "Design of a new multi-phase experimental simulation chamber for atmospheric photosmog, aerosol and cloud chemistry research." Atmospheric Measurement Techniques **4**(11): 2465-2494.

Wang, T., Tham, Y. J., Xue, L., Li, Q., Zha, Q., Wang, Z., Poon, S. C. N., Dubé, W. P., Blake, D. R., Louie, P. K. K., Luk, C. W. Y., Tsui, W. and Brown, S. S. (2016). "Observations of nitryl chloride and modeling its source and effect on ozone in the planetary boundary layer of southern China." Journal of Geophysical Research: Atmospheres **121**(5): 2476-2489.

Wen, L.-b., Xin, C.-Y. and Yang, S.-C. (2010). "The effect of adding dimethyl carbonate (DMC) and ethanol to unleaded gasoline on exhaust emission." Applied Energy **87**(1): 115-121.

Wenger, J. (2006). Chamber Studies on the Photolysis of Aldehydes Environmental. Environmental Simulation Chambers: Application to Atmospheric Chemical Processes. I. Barnes and K. Rudzinski, Springer Netherlands. **62:** 111-119.

Westbrook, C. K. (2013). "Biofuels Combustion." Annual Review of Physical Chemistry **64**(1): 201-219.

Whalley, L. K., Stone, D., Bandy, B., Dunmore, R., Hamilton, J. F., Hopkins, J., Lee, J. D., Lewis, A. C. and Heard, D. E. (2016). "Atmospheric OH reactivity in central London: observations, model predictions and estimates of in situ ozone production." Atmospheric Chemistry and Physics **16**(4): 2109-2122.

WHO (2016). Ambient air pollution: A global assessment of exposure and burden of disease. W. H. ORganization.

Williams, J., Keßel, S. U., Nölscher, A. C., Yang, Y., Lee, Y., Yáñez-Serrano, A. M., Wolff, S., Kesselmeier, J., Klüpfel, T., Lelieveld, J. and Shao, M. (2016). "Opposite OH reactivity and ozone cycles in the Amazon rainforest and megacity Beijing: Subversion of biospheric oxidant control by anthropogenic emissions." Atmospheric Environment **125, Part A**: 112-118.

Wu, H., Mu, Y., Zhang, X. and Jiang, G. (2003). "Relative rate constants for the reactions of hydroxyl radicals and chlorine atoms with a series of aliphatic alcohols." International Journal of Chemical Kinetics **35**(2): 81-87.

Yang, Y., Shao, M., Wang, X., Nölscher, A. C., Kessel, S., Guenther, A. and Williams, J. (2016). "Towards a quantitative understanding of total OH reactivity: A review." Atmospheric Environment **134**: 147-161.

Yujing, M. and Mellouki, A. (2001). "Temperature dependence for the rate constants of the reaction of OH radicals with selected alcohols." Chemical Physics Letters **333**(1–2): 63-68.

Zannoni, N., Dusanter, S., Gros, V., Sarda Esteve, R., Michoud, V., Sinha, V., Locoge, N. and Bonsang, B. (2015). "Intercomparison of two comparative reactivity method instruments in the Mediterranean basin during summer 2013." Atmospheric Measurement Techniques **8**(9): 3851-3865.

Zannoni, N., Gros, V., Lanza, M., Sarda, R., Bonsang, B., Kalogridis, C., Preunkert, S., Legrand, M., Jambert, C., Boissard, C. and Lathiere, J. (2016). "OH reactivity and concentrations of biogenic volatile organic compounds in a Mediterranean forest of downy oak trees." Atmospheric Chemistry and Physics **16**(3): 1619-1636.

Zhao, J., Ortega, J., Chen, M., McMurry, P. H. and Smith, J. N. (2013). "Dependence of particle nucleation and growth on high-molecular-weight gas-phase products during ozonolysis of α-pinene." Atmospheric Chemistry and Physics **13**(15): 7631-7644.

Chapter 2. Highly Instrumented Reactor for Atmospheric Chemistry

2.1 Introduction

An introduction to tropospheric chemistry relevant to the work in this thesis has been given in Chapter 1. Atmospheric simulation chambers play a pivotal role in the study of chemical reactions occurring in the troposphere. A comparison of a number of different chambers has been given in Chapter 1; here a description of the Highly Instrumented Reactor for Atmospheric Chemistry (HIRAC) is given, detailing the commercial instruments coupled to the chamber for measurements, including Fourier Transform Infrared spectroscopy (FTIR), gas chromatography (GC), ozone and NO_x analysers. The custom built FAGE instrument for the measurement of HO_x radicals will be described in Chapter 3 and a LFP-LIF instrument for OH reactivity measurements will be described in Chapter 4.

HIRAC has been developed in order to carry out a wide range of atmospheric measurements and investigations Glowacki *et al.* (2007a). It is a 2.25 m^3 cylindrical atmospheric simulation chamber constructed from 304 grade stainless steel, allowing for both pressure and temperature dependent studies to be carried out. The internal surface area of the chamber is ~13 m^2, including all internal instrumental surfaces. The stainless steel construction of HIRAC allows experiments to be carried out over a range of pressure (15 – 1000 mbar).

Stainless steel tubes welded to the outside of the chamber enable the circulation of heated or cooled fluid in order to carry out experiments over the temperature range 253 – 343 K. The stainless steel tubing is connected to a temperature control unit (Huber thermostat Model 690W), filled with thermo fluid (DW-Therm). The temperature control unit circulates the thermo fluid through the stainless steel tubing, allowing for even temperature regulation of the chamber. Temperature gradients across the chamber have been measured previously, showing very small gradients, within 1 K, with small deviations of ± 4 K observed close to the flanges of the chamber where no thermo fluid is circulated (Farrugia 2013).

HIRAC has many flanges through which numerous analytical instrumentation can be connected. Two large flanges on one side of the chamber, which could potentially support several instrument inlet ports. Two smaller flanges on the other side of the chamber allow for more analytical instruments to be coupled; one of which is permanently dedicated for sampling by the FAGE instrument (as described in Chapter 3). A cutaway diagram of the HIRAC chamber is shown in Figure 2-1, where the FAGE instrument can be seen through one of the smaller flanges on one side of the chamber.

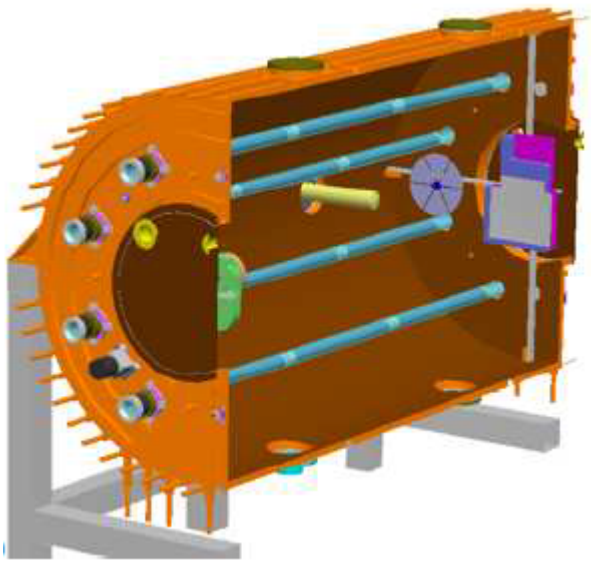

Figure 2-1: Schematic cutaway diagram of the HIRAC chamber showing the arrangement of the quartz tubes inside the chamber in which photolysis lamps are housed. One of the mixing fans is visible. The supports for the FTIR multipass mirrors at one end of the chamber are visible. The FAGE instrument can also be seen. Adapted from Glowacki *et al.* (2007a).

Eight quartz tubes spanning the full length of the chamber are designed to house photolysis lamps which initiate chemical reactions within the chamber. Three types of lamps are available to be mounted within the quartz tubes, with different maximum output wavelengths; Philips TL-K 40W/05 (λ_{max} = 360 nm), GE G55T8 / OH 7G UVC (λ_{max} = 254 nm) and Philips TL 40W/12 RS SLV (λ_{max} = 300 nm). The photolysis lamps have an optimum operating temperature of ~35 - 39°C, and so the quartz tubes are continually flushed with a flow of laboratory nitrogen in order to maintain the temperature. The flush of nitrogen also ensures no water vapour is present in the air surrounding the photolysis lamps which would freeze at low temperatures. A thermocouple is placed approximately half way along each lamp to allow the temperature of the lamps within the quartz tubes to be monitored, and the nitrogen flush can be

adjusted accordingly. Figure 2-2 shows the output of the three sets of photolysis lamps available for use within HIRAC.

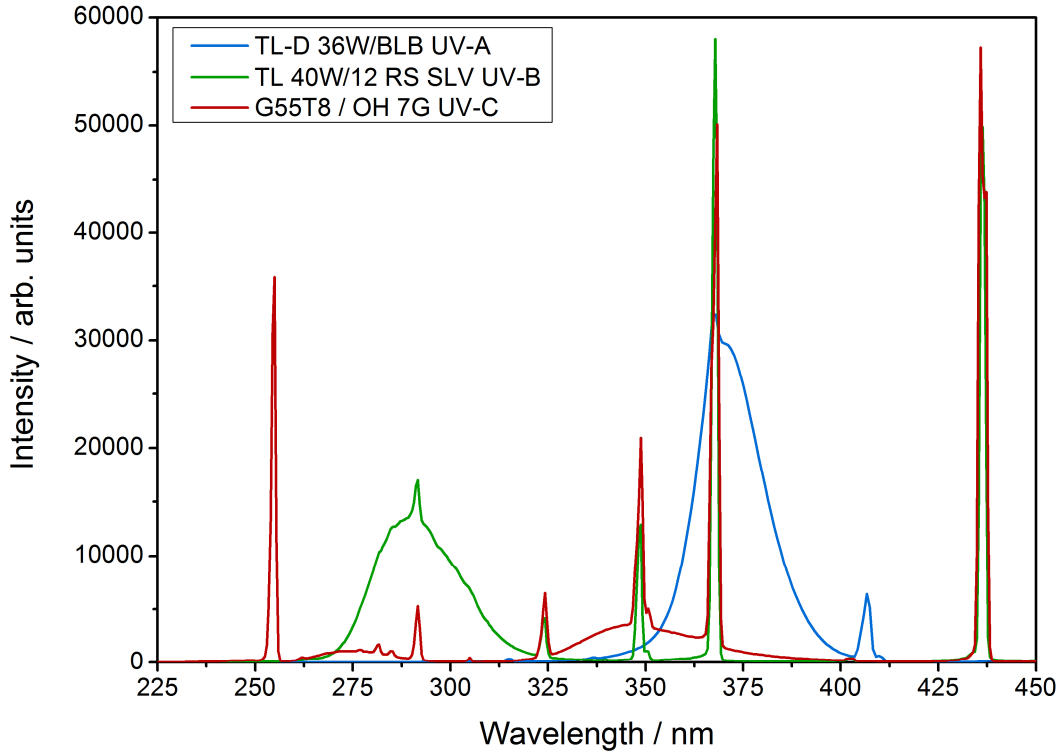

Figure 2-2: Emission spectra of the three different photolysis lamps available for use within HIRAC. Reproduced from Winiberg (2014).

Between experiments, HIRAC is evacuated to <1 mbar in ~60 minutes using a rotary pump backed roots blower (Leybold Trivac D40B with Leybold Ruvac WAU251). This ensures maximum removal of trace species from the chamber. The internal pressure of HIRAC is monitored with a pressure transducer (Lybold Ceravac, 0 – 1000 Torr).

For general operation of HIRAC, the chamber is filled to the desired pressure with 80% UHP N_2 (BOC, 99.998% purity) and 20% O_2 (BOC, 99.999% purity). Known concentrations of the VOCs of interest are added to the chamber; either via a vacuum line as a gas or by direct injection as a liquid, over a flow of N_2. Experiments are typically initiated through the photolysis of a precursor (to generate OH radicals or Cl atoms), or by the ozonolysis of an alkene. Concentrations of compounds of interest are then monitored via a range of analytical instruments, which will be described in more detail in the following sections.

Four mixing fans (two at either end inside the chamber) ensure good mixing of compounds within the chamber. Mixing times within HIRAC have been investigated by Glowacki *et al.* (2007a), where it was shown that with all four mixing fans running at

1500 rpm and 30000 rpm, the mixing times were ~70 s and ~60 s, respectively. For routine operation of HIRAC, all four mixing fans are set to 1500 rpm.

In house written LabVIEW software monitors and records temperatures (six thermocouples inside the chamber and one thermocouple connected to each photolysis lamp), chamber pressure, [O_3] and [NO_x]. Due to the large potential sampling output from HIRAC from the numerous analytical instruments available for measurements, a counter flow system has been set up in order to maintain the desired total pressure. The internal chamber pressure is monitored using LabVIEW software, and controls adjustment of flow settings of two MFCs (one for N_2 and one for O_2) in order to maintain the desired pressure.

2.2 HIRAC Instrumentation

Numerous analytical instrumentation can be coupled to the HIRAC chamber for measurements of a wide range of species. These include two GC instruments for the detection of a range of VOCs, an FTIR multipass set up for the measurement of VOCs and commercial O_3 and NO_x analysers; all of which will be described in the following sections. A LIF FAGE instrument is also available for the measurement of OH and HO_2 radicals from the HIRAC chamber, which will be described in Chapter 3, with results from development of calibration techniques being presented. A LFP-LIF instrument for the measurement of OH reactivity has been modified for measurements from HIRAC, the development and characterisation of this instrument with HIRAC will be given in Chapter 4.

2.2.1 Fourier Transform Infrared Spectroscopy

Fourier transform infrared (FTIR) spectroscopy is widely used in atmospheric simulation chambers for the detection of a range of species. FTIR measurements are made through the absorption of IR radiation by IR active species present in a sample. A significant advantage of FTIR measurements over other analytical techniques, such as GC measurements, is that is an *in situ* detection method. A sample is not required to be taken from the chamber, and so the exact composition of species present in the chamber are monitored; there are no sampling lines or detectors for the sample to pass through, and so eliminating any interferences that may arise from processing of compounds within such sampling lines. An interferometer allows for the simultaneous measurement of all IR frequencies.

The Beer-Lambert law (Eq. 2-1) can be used to calculate the concentration of the absorbing species from their absorption cross sections:

$$I/I_0 = e^{-\sigma cl} \qquad \text{Eq. 2-1}$$

where I is the measured intensity at a specific wavelength, I_0 is the initial intensity, c is the concentration of the absorbing species, l is the total path length and σ is the absorption cross section of the absorbing species. The sensitivity can be increased through the use of a long path length, achievable with the use of a multipass system. The optimum number of passes for the HIRAC FTIR set up has been described by Glowacki *et al.* (2007b).

HIRAC is coupled to a Bruker IFS/66 FTIR spectrometer. A modified Chernin type multipass matrix system has been developed for measurements within the HIRAC chamber, and is described in detail by Glowacki *et al.* (2007b). A diagram of the multipass set up of the light from the FTIR to the detector, as set up for measurements from the HIRAC chamber, is illustrated in Figure 2-3.

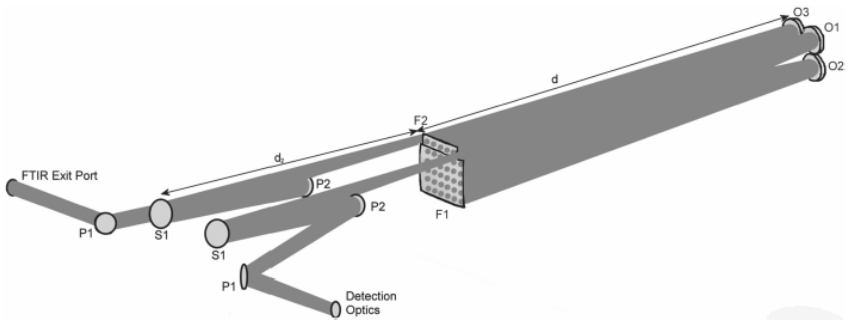

Figure 2-3: Schematic showing the multipass of the light from the FTIR to the detection optics. F1 and F2 are the field mirrors, mounted at one end inside the chamber. O1, O2 and O3 are the objective mirrors mounted at the other end inside the chamber. P1, P2 and S1 are transfer optics housed within a box external to HIRAC. Reproduced from Glowacki *et al.* (2007a).

The multipass set up consists of the FTIR spectrometer, the transfer optics, the field and objective mirrors mounted to either end of the inside of the chamber, and an external detector. Light from the FTIR spectrometer enters and exits the chamber through wedged KBr windows (75 + 0/-0.2 mm diameter, (5.0 ± 0.1) mm (min) width, with 0.5° wedge). The field mirrors, objective mirrors and transfer optics make up the modified Chernin type multipass matrix system. The transfer optics (P1, P2 and S1) are housed within a box external to the chamber, which is constantly purged with a flow of nitrogen in order

to ensure minimal interference from compounds, such as water, present within the external pass of the light from the FTIR.

The field and objective mirrors (F1 and F2, and O1, O2 and O3, respectively), making up the multipass set up within the chamber, are illustrated in Figure 2-4. This set up allows for 72 passes through HIRAC of the light from the FTIR spectrometer, resulting in a total path length of 128.5 m. A significant advantage of the modified Chernin cell is that it allows for ease of alignment through careful adjustment of the screws on each of the three objective mirrors, which can be easily accessed through the removal of the large flange at the end of the chamber.

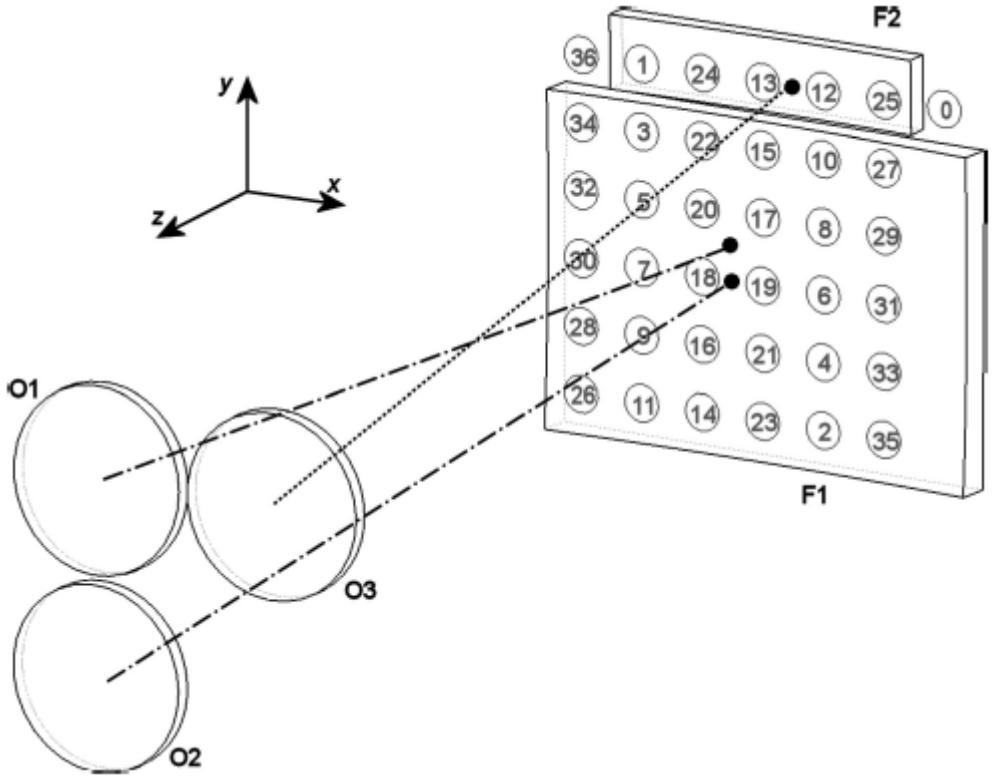

Figure 2-4: Schematic showing the modified Chernin type multipass matrix system designed for use within the HIRAC chamber. F1 and F2 are the field mirrors and O1, O2 and O3 are the objective mirrors. The set up shown allows for 72 passes of the light through the HIRAC chamber, giving a total path length of 128.5 m. Reproduced from Glowacki *et al.* (2007b).

FTIR spectra are used for the identification and quantification of compounds present in the HIRAC chamber throughout the course of experiments. Prior to any compounds being added to the chamber, with only N_2 (80%) and O_2 (20%) present in the chamber, an FTIR background spectrum is recorded. The background spectrum is subtracted from subsequent spectra in order to remove any absorptions from impurities such as CO and H_2O present in the bath gas. Reference spectra of the compounds of interest are recorded,

for known concentrations of those compounds. These reference spectra can then be fitted to the experimental spectra in order to determine concentrations.

2.2.2 Gas Chromatography

Gas chromatography (GC) is an analytical technique used for the separation and characterisation of VOCs. It is used to separate compounds in a sample to enable both qualitative and quantitative analysis. All commercial GC instruments consist of the same basic components; an injector port for sample introduction, a column which is fixed inside an oven, and a detector. A sample is injected onto a column; the different compounds present in the sample travel through the column at different rates. The rate at which each compound passes through the column is primarily dependent on the physical properties of the compounds. Compound separation can be optimised through altering a range of operating parameters, including the column and oven temperature. As each compound exits (elutes) the column, it passes through a detector. The signal produced as the compounds reach the detector is recorded as a peak on a chromatogram, representative of the time spent on the column and the total concentration of each compound. Identification of compounds within a sample is determined by their retention time, dependent on the specific operating conditions for the GC.

Two GC instruments (GC-FID, Agilent Technologies, 6890N) are connected to the HIRAC chamber for the detection and quantification of a wide range of VOCs. Online sampling is used to monitor the concentration of compounds throughout experiments. This is achieved with the use of a series of valves in order to draw a sample from the chamber and inject it onto the GC column typically every 1 – 5 minutes, dependent on the separation of compounds in the GC. A schematic of the online sampling set up for the two GCs is illustrated in Figure 2-5. A gas sample is drawn from the chamber into two sample loops (5 ml volume). The sample is then injected onto the columns via a 6-way valve, as the carrier gas (Helium, He) is flushed through the sample loops.

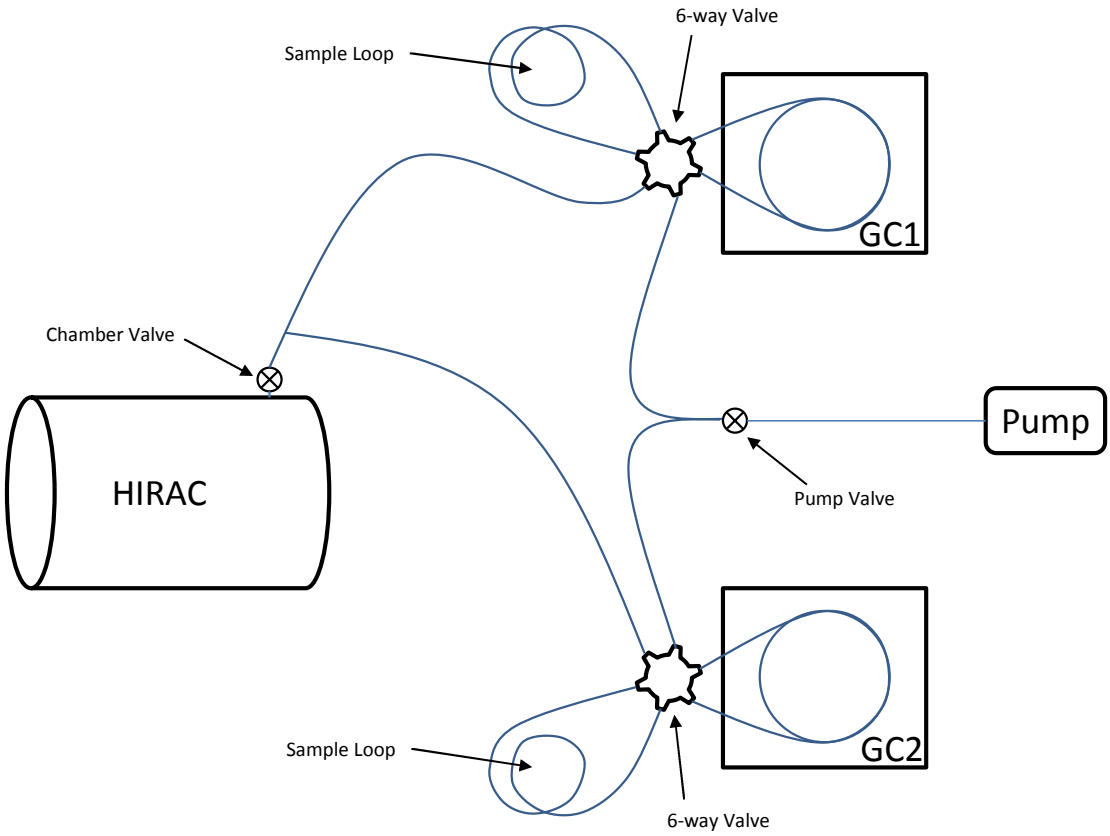

Figure 2-5: Schematic diagram illustrating the valve set up for the online sampling of two GC instruments from the HIRAC chamber.

Once the sample has been injected onto the columns, the 6-way valve is then switched so that the sample loop and the sample line up to the chamber valve are evacuated by a pump (Leybold 4B). Figure 2-6 illustrates the timings for the online sapling of the GCs from HIRAC.

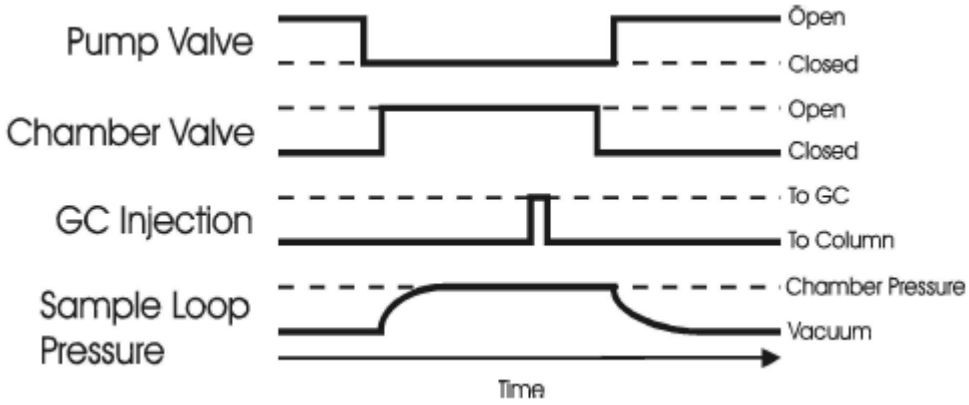

Figure 2-6: Schematic showing the relative timings of the online sampling of the two GCs from the HIRAC chamber. Adapted from Glowacki *et al.* (2007a).

The two HIRAC GC instruments use flame ionisation detectors (FIDs) for the detection of compounds as they are eluted from the column. The sample burns as it passes through

the flame, creating ions, of which their signal is recorded as a peak in the chromatogram. Calibration is required as the sizes of the peaks are dependent on the functionality of the individual compounds. GC calibration is achieved through the sampling of known concentrations of compounds from the HIRAC chamber. A range of concentrations are sampled, produced either through multiple additions of the compound into the chamber, or by the dilution of the chamber (the chamber is evacuated to a known pressure and refilled to 1000 mbar with air). This allows for a calibration plot to be produced, an example of which is shown in Figure 2-7, for the GC calibration of *iso*-butanol sampled from HIRAC at 298 K and 1000 mbar.

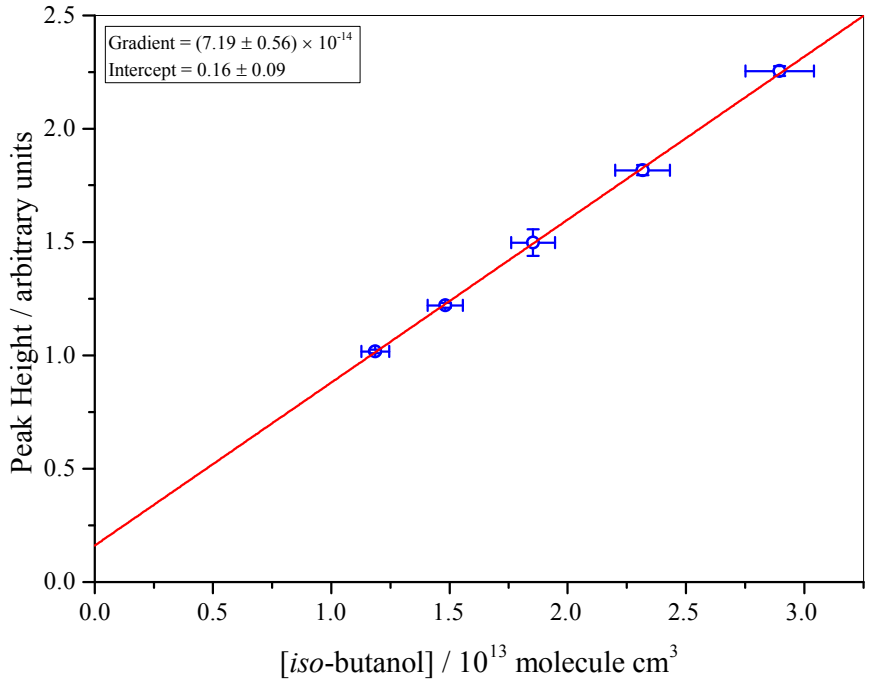

Figure 2-7: GC calibration plot for *iso*-butanol. Calibration produced by sampling from the HIRAC chamber at 298 K and 1000 mbar.

It is also important to carry out both temperature and pressure dependent calibration for compounds for such experiments as the total amount of each compound collected in the sample loop and injected onto the GC column will vary with both of these parameters.

GC columns vary in a number of ways including their length, column diameter, stationary phase and film thickness. There are two main types of GC columns; packed columns and capillary columns. Capillary columns are the most commonly used type of GC columns. For the work in this thesis, two different GC columns were used; a CP-Sil 5CB column (50 m length, 0.32 mm i.d., 5 μm film thickness) and a DB-WAX column

(15 m length, 0.32 mm i.d., 0.25 µm film thickness). The CP-Sil 5CB column is a low polarity column, suitable for the separation and detection of C_2 – C_6 hydrocarbons as compounds are separated primarily by their boiling points. The DB-WAX column is a polar column suitable for the separation and detection of highly polar compounds. Figure 2-8 shows an example of compound separation in a GC, using the CP-Sil 5CB column to separate *iso*-butanol, *iso*-butyraldehyde and acetone.

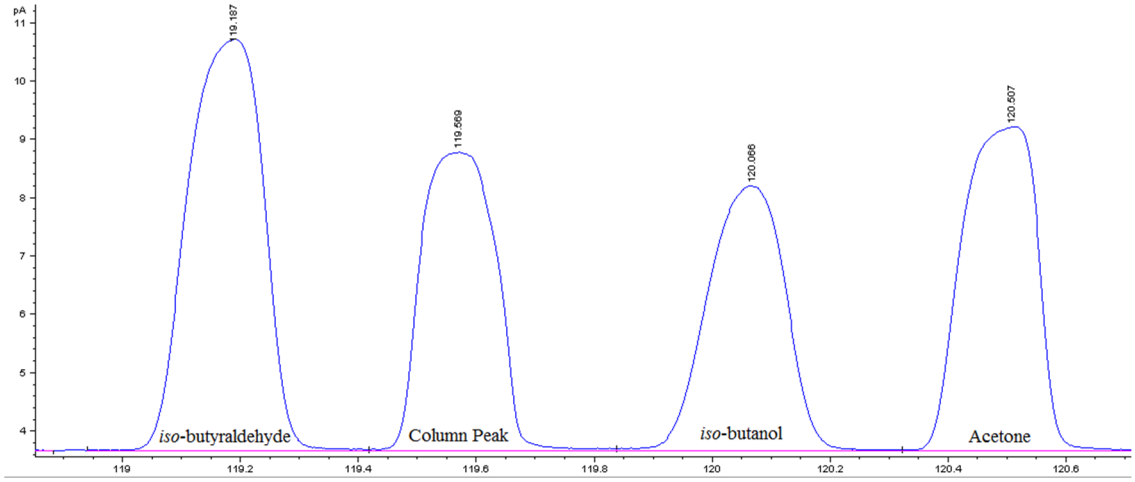

Figure 2-8: Example GC chromatogram showing the peak separation of *iso*-butanol, *iso*-butyraldehyde and acetone. Separation achieved for the CP-Sil 5 CB column, sampling from the HIRAC chamber filled to ~1000 mbar with 80% UHP N_2 and 20% O_2.

2.2.3 Commercial Gas Analysers

Commercial analysers for the measurement of ozone and NO_x (= NO + NO_2) are also connected to HIRAC; a UV photometric O_3 analyser (Thermo Electron Corporation, Model 49C, LOD = 1.0 ppbv) and a chemiluminescence NO-NO_2-NO_x analyser (Thermo Environmental Instruments Inc., Model 42C, LOD = 50 pptv at 120 s averaging time).

NO_x concentrations are measured by chemiluminescence, with a ~1 l min^{-1} sample being taken from the chamber. NO in the sampled gas reacts with O_3 to produce electronically excited NO_2^* (R 2-1). The light emitted as the NO_2^* relaxes to the ground state NO_2 is measured; it is proportional to the concentration of NO present in the sample. NO_2 concentrations can also be measured; the NO_2 is first converted to NO using a molybdenum NO_2 to NO converter, before reacting with O_3 to produce NO_2^*.

$$NO + O_3 \rightarrow NO_2^* + O_2 \qquad \text{R 2-1}$$

$$NO_2^* \rightarrow NO_2 + h\nu \qquad \text{R 2-2}$$

As the NO produced from the conversion of NO_2 in the sampled air cannot be distinguished from the NO present in the sampled air, the sum of NO_2 and NO (NO_x) is recorded, with the NO_2 concentration being determined by subtracting the [NO] from the total NO_x concentration.

It is known that measurements of NO_2 concentrations using chemiluminescence NO_x analysers are prone to interferences; Villena *et al.* (2012) have reported on the observation of strong interferences from chemiluminescence NO_x measurements in an urban environment, a road traffic tunnel and in measurements from an atmospheric simulation chamber. The authors reported strongly positive interferences in measurements from an urban environment, and strongly negative interferences in measurements from a road traffic tunnel. It was determined, through chamber studies, that the observed negative interferences arose from the photolysis of VOCs within the photolytic converter and the subsequent reaction of the peroxy radicals produced with NO present in the sampled air. It was concluded that the positive interferences were due to the presence of NO_y species (e.g. PAN and HONO). A number of studies in the literature have reported on the interference from organic nitrates in the measurement of NO_2 concentrations; the molybdenum NO_2 to NO converter used in chemiluminescence NO_x analysers is not specific to the conversion of NO_2, with organic nitrates also being converted to NO, and hence included in the total measurement (Demerjian 2000, Dunlea *et al.* 2007, Steinbacher *et al.* 2007). With the interferences described, measurements of [NO_2] and [NO_x] should be considered with caution as to avoid misinterpretation of results.

Chemiluminescence NO_x boxes are used for the measurement of [NO] whilst sampling from HIRAC and in the N_2O actinometry procedure (described in Chapter 3). Calibration of the chemiluminescence NO_x analyser for the measurement of NO concentrations and its response to N_2O in the sampled gas flow is detailed in Chapter 3.

Ozone concentrations within HIRAC are measured with a UV photometric O_3 analyser (Thermo Electron Corporation, Model 49C, LOD = 1.0 ppbv). The O_3 analyser is connected to HIRAC with ¼" Teflon tubing, sampling through a flange at the top of the chamber. Whilst sampling from the chamber, the O_3 analyser draws a sample of ~1 l min^{-1}. The ozone analyser measures ozone concentrations through its absorption of

UV light at 254 nm, using the Beer-Lambert law (Eq. 2-1). Calibration of the UV O_3 analyser should not be required. The instrument splits the intake flow of sampled gas into two; one flow is passed through an ozone scrubber to act as a reference (I_0 in R 2-1) and then to a detector, the second gas flow is passed straight to a detector. The ozone concentration is determined through the difference in UV absorption between the two gas flows.

2.2.4 Other Instrumentation

The relatively large size of HIRAC and number of available inlet ports allows for the coupling of numerous instruments to the chamber for measuring a range of species. A number of permanently couple instruments have been described here; the dedicated FAGE instrument is discussed in Chapter 3, and a newly interfaced LFP-LIF OH reactivity instrument is discussed in Chapter 4. A cavity ring down spectroscopy (CRDS) set up has been previously used for the detection of NO_3 (Malkin 2010), and a new version is currently under construction for the measurement of peroxy radicals.

2.3 References

Demerjian, K. L. (2000). "A review of national monitoring networks in North America." Atmospheric Environment **34**(12–14): 1861-1884.

Dunlea, E. J., Herndon, S. C., Nelson, D. D., Volkamer, R. M., San Martini, F., Sheehy, P. M., Zahniser, M. S., Shorter, J. H., Wormhoudt, J. C., Lamb, B. K., Allwine, E. J., Gaffney, J. S., Marley, N. A., Grutter, M., Marquez, C., Blanco, S., Cardenas, B., Retama, A., Ramos Villegas, C. R., Kolb, C. E., Molina, L. T. and Molina, M. J. (2007). "Evaluation of nitrogen dioxide chemiluminescence monitors in a polluted urban environment." Atmospheric Chemistry and Physics **7**(10): 2691-2704.

Farrugia, L. (2013). Kinetics and mechanistic studies in the HIRAC chamber. PhD, University of Leeds.

Glowacki, D. R., Goddard, A., Hemavibool, K., Malkin, T. L., Commane, R., Anderson, F., Bloss, W. J., Heard, D. E., Ingham, T., Pilling, M. J. and Seakins, P. W. (2007a). "Design of and initial results from a Highly Instrumented Reactor for Atmospheric Chemistry (HIRAC)." Atmospheric Chemistry and Physics **7**(20): 5371-5390.

Glowacki, D. R., Goddard, A. and Seakins, P. W. (2007b). "Design and performance of a throughput-matched, zero-geometric-loss, modified three objective multipass matrix system for FTIR spectrometry." Applied Optics **46**(32): 7872-7883.

Malkin, T. L. (2010). Detection of Free-Radicals and Other Species to Investigate Atmospheric Chemistry in the HIRAC Chamber. PhD, University of Leeds.

Steinbacher, M., Zellweger, C., Schwarzenbach, B., Bugmann, S., Buchmann, B., Ordóñez, C., Prevot, A. S. H. and Hueglin, C. (2007). "Nitrogen oxide measurements at rural sites in Switzerland: Bias of conventional measurement techniques." Journal of Geophysical Research: Atmospheres (1984–2012) **112**(D11).

Villena, G., Bejan, I., Kurtenbach, R., Wiesen, P. and Kleffmann, J. (2012). "Interferences of commercial NO_2 instruments in the urban atmosphere and in a smog chamber." Atmospheric Measurement Techniques **5**(1): 149-159.

Winiberg, F. (2014). Characterisation of FAGE apparatus for HO_x detection and application in an environmental chamber. PhD, University of Leeds.

Chapter 3. Fluorescence Assay by Gas Expansion – Instrument Development and Characterisation

3.1 Introduction

Measurements of OH and HO_2 radicals have been discussed in Chapter 1, with comparison of the different measurement techniques used. The fluorescence assay by gas expansion (FAGE) method has seen considerable development since it was first reported as a technique for the detection of OH and HO_2 radicals by Hard *et al.* (1979). There are many FAGE instruments used globally for the detection of HO_x radicals for ground based, aircraft, and chamber studies (Kanaya *et al.* 2001, Dusanter *et al.* 2009, Amedro *et al.* 2012). The HIRAC FAGE instrument, which is the focus of this chapter, has been described in detail elsewhere (Glowacki *et al.* 2007, Winiberg *et al.* 2015).

Here a description of the HIRAC FAGE instrument is given, focussing in particular on the calibration procedure. As FAGE is not an absolute method for measuring OH and HO_2 radical concentrations, calibration is required in order to convert the experimental measurement signal into concentrations. Low concentrations and the short lifetime of HO_x in the troposphere require sensitive and selective detection techniques. A detailed description of the conventional calibration method for FAGE instrumentation is given, with discussion on the sources of error associated with it. The major source of error in the conventional FAGE instrumentation calibration method arises from the N_2O actinometry procedure required for determining the output flux, $F_{184.9\,nm}$, of a mercury pen ray lamp. In order to gain a better understanding of the error associated with the determination of $F_{184.9\,nm}$, an in depth study into the N_2O actinometry experimental procedure and the apparatus used is given. Comparisons are given on a range of experimental apparatus available for measurements.

Total uncertainty, as discussed in Section 3.4.3, can be determined from the sum in quadrature of the accuracy and precision of the measurements. This total uncertainty typically does not represent the systematic error associated with the measurements in the

function used in calculating $F_{184.9\,nm}$. To gain further insight into the breakdown of errors associated with all parameters required in the determination of $F_{184.9\,nm}$, Monte Carlo error propagation is discussed in Section 3.4.3, with examples given from experimental data.

HIRAC is ideally suited for carrying out alternative methods for FAGE instrumentation calibration. The HIRAC chamber has previously been utilised for pressure dependent calibration of both the OH and HO_2 cells of the HIRAC FAGE instrument (Winiberg *et al.* 2015). Section 3.5 details further use of the HIRAC chamber to determine the sensitivity of the HIRAC FAGE instrument as a function of temperature. Comparison is made between the conventional and alternative calibration methods, with discussion of the errors associated with each method. The alternative HIRAC calibration methods provide validation for the conventional FAGE instrumentation calibration method.

3.2 Instrumentation

A cross sectional schematic of the HIRAC FAGE instrument is shown in Figure 3-1. The instrument is constructed from black anodised aluminium with an internal diameter of 50 mm for the sampling flow tube.

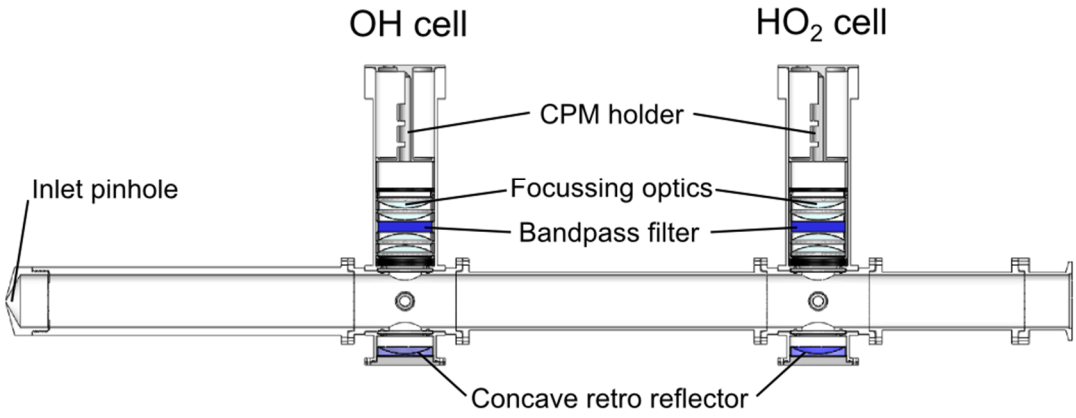

Figure 3-1: Side view cross sectional schematic of the FAGE instrument, reproduced from Winiberg (2014).

A sample is expanded through a pinhole of 1.0 mm diameter at the end of the inlet. The instrument uses an inlet length of 280 mm to ensure sampling from within HIRAC is far enough away from the chamber walls and out of the region where radical gradients are observed, as has been described by Malkin (2010), where a small radical gradient was

observed from the chamber walls to 200 mm within HIRAC. A Baratron (MKS, 10 Torr) is positioned between the OH and HO_2 detection cells in order to measure the internal pressure of the instrument during experiments. The internal pressure of the HIRAC FAGE instrument is typically ~2.7 Torr during routine operation, maintained by a rotary-backed roots blower (Leybold, trivac D40B and ruvac WAU251). The low pressure within FAGE instruments is used in order to extend the fluorescence lifetime of OH radicals allowing temporal isolation of the scattered light at 308 nm from the resonant fluorescence light at the same wavelength. The NO injection port is also situated between the OH and HO_2 detection cells. HO_2 radicals are titrated by NO:

$$HO_2 + NO \rightarrow OH + NO_2 \qquad \text{R 3-1}$$

and the resulting OH radicals are detected to enable measurement of HO_2 radicals. ~0.005 l min^{-1} of NO (BOC, high purity, N2.5 nitric oxide) was introduced prior to the HO_2 detection cell, via 1/8" stainless steel tubing by a MFC. RO_2 radicals may also be measured through conversion to OH radicals following their reaction with NO within the FAGE instrument:

$$RO_2 + NO \rightarrow RO + NO_2 \qquad \text{R 3-2}$$

$$RO + O_2 \rightarrow HO_2 + RCHO \qquad \text{R 3-3}$$

$$HO_2 + NO \rightarrow OH + NO_2 \qquad \text{R 3-4}$$

Whalley *et al.* (2013) reported on an enhancement of HO_2 signal in the presence of RO_2 radicals. The interference reported by the authors was determined to be dependent on the design of the FAGE cell and the operating conditions. Studies by Whalley *et al.* (2013) reported on enhancement of HO_2 signal from RO_2 radicals derived from isoprene, alkenes and aromatics. Careful characterisation of the concentration of NO used in FAGE instrumentation is required; lower NO concentrations are more selective towards the conversion of HO_2 to OH (rather than RO_2 to OH), but are less sensitive.

A scavenger injection system has been installed, allowing for a scavenger species (e.g. *iso*-butane) to be injected into the inlet in order to quantify any OH generated by the laser light, as described by Winiberg *et al.* (2015). The authors observed OH interferences during the hydrocarbon decay method of OH calibration, which were characterised through the injection of *iso*-butane into the FAGE instrument during the experiments. The scavenger injection system will not be discussed further as it was not used for this work.

In the measurements described throughout this work, the detector refers to either a Channel Photo-Multiplier (CPM, Perkin Elmer, C943P) detector or a Multi-Channel Photomultiplier detector (MCP, Photek PMT 325) for the detection of OH fluorescence. The gating and data acquisition described here refers specifically to the CPM detector, however, it should be noted that gating and data acquisition are very similar, with the major advantage of using the new MCP detectors over the CPM detectors being the improved sensitivity (sensitivity was observed to be increased by approximately an order of magnitude for both the OH and HO_2 FAGE cells).

The fluorescence collection optics are lenses used to focus the OH fluorescence through the narrow bandpass filter, which only allows light at wavelengths of ~308 nm to pass through (Barr Associates, 308.75 mm, 5.0 mm bandwidth, 50% transmission). The concave retro-reflectors at the bottom of the detection cells are used to roughly double the sensitivity of the instrument by reflecting the fluorescence light back up the cell towards the detector.

A 5 kHz laser system (JDSU Nd:YAG pumped Sirah Credo-dye-N dye laser) was used to generate the 308 nm laser light required for the excitation and detection of OH radicals. The 308 nm laser light was introduced into the detection cells via optical fibres; with the laser power entering the OH cell typically 6 – 10 mW and 2 – 3 mW in the HO_2 detection cell. Two photodiodes (UDT-555UV, Laser Components, UK) were used to measure variation in the laser power through each detection cell during experiments, positioned at the exit of each of the detection cells.

3.2.1 Data Acquisition

The use of on-resonance fluorescence detection requires the use of a gating system in order to distinguish between the OH fluorescence and the laser light, both at ~308 nm. Figure 3-2 shows the gate timings used in the detection cells of the FAGE instrument when using the CPM detectors. The start time of the gating system is indicated by t_0, which is given by a trigger, in the form of an electrical pulse, from the JDSU laser to the gating box. At t_0 + 100 ns the laser pulse is generated; at this time both the photon counting card (Becker and Hickl PMS-400A) and the CPM detector are switched off. The photon counting card is then triggered after the laser pulse, followed by the CPM detector after ~100 ns. This 100 ns wait is to allow for the photon counting card warm up time. The A bin of 1 μs is when the photons are collected and counted from the OH fluorescence, followed by a 9 μs wait bin to ensure that the fluorescence is complete, and finally the B bin of 20 μs measures any background dark counts.

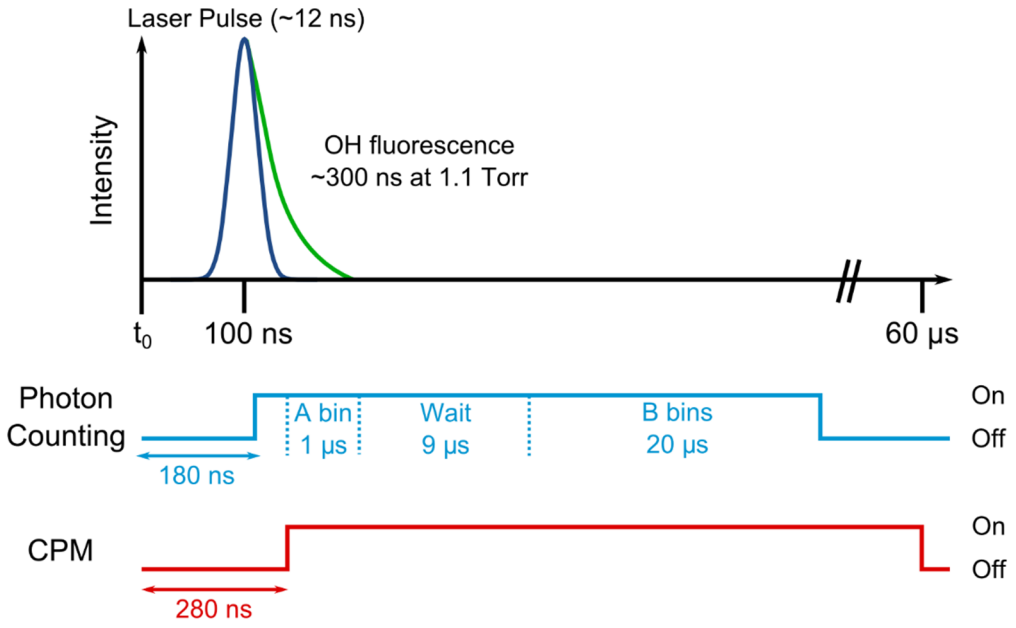

Figure 3-2: Gating system used for HIRAC FAGE instrument, reproduced from Winiberg (2014).

3.2.2 Reference Cell

A reference cell is required in order to aid tuning of the wavelength of the laser for the excitation of OH radicals, and to ensure it remains at 308 nm. The reference cell design used for the HIRAC FAGE instrument is based on that described by Wennberg *et al.* (1994), where OH radicals are formed continuously by flowing water saturated air over a hot wire filament. Ambient air is drawn through a water bubbler, for humidification, and into the reference cell. The humidified air passes over a hot wire filament in order to produce OH radicals, which are excited by passing <1 mW of the 308 nm laser power through the cell. Fluorescence of the OH radicals is then detected perpendicular to the laser beam by an un-gated CPM detector.

3.3 Conventional "wand" Calibrations

The conventional FAGE instrument calibration method employs the use of a flow tube calibration source, known as the "wand", for producing a known concentration of OH and HO_2 radicals, through R 3-5 and R 3-6:

$$H_2O + h\nu_{(\lambda = 184.9\ nm)} \rightarrow OH + H \qquad \text{R 3-5}$$

$$H + O_2 + M \rightarrow HO_2 + M \qquad \text{R 3-6}$$

Alternative methods are also possible for calibration of FAGE instrumentation, which can be used to determine the accuracy of the "wand" calibration method. Alternative FAGE calibration methods will be discussed in more detail in Section 3.5.

A schematic of the "wand" calibration set up for the conventional calibration of FAGE instrumentation is shown in Figure 3-3. Water photolysis is commonly used for the calibration of FAGE instruments for the measurements of OH and HO_2 radical concentrations, and has been described by a number of groups (Faloona *et al.* 2004, Commane *et al.* 2010). It is possible to use the "wand" calibration method to determine the sensitivity of the FAGE instrument as a function of both temperature and pressure. The use of different sized pinholes on the inlet of the FAGE instrument alters the pressure within the FAGE cells. Temperature dependent "wand" calibrations can be performed by heating or cooling both the instrument inlet and calibration source.

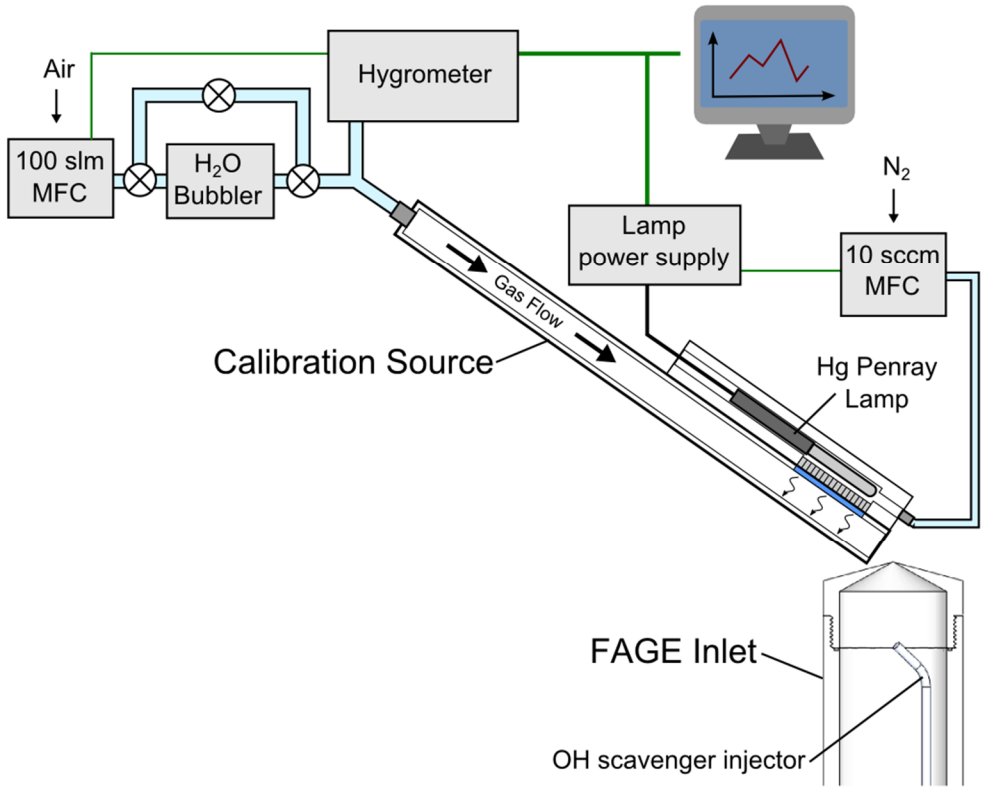

Figure 3-3: "Wand" calibration set up for conventional FAGE calibration, taken from Winiberg *et al.* (2015).

During the "wand" calibration experiments, air (40 l min^{-1}, BTCA) is passed through a water bubbler, in order to humidify it, and into the calibration source. A small portion of the humidified air is sampled by a hygrometer (Buck Research Instruments CR-4 Chilled Mirror Hygrometer) to measure the water concentration in order to determine the concentration of OH and HO_2 radicals being formed within the "wand". The water vapour present in the air is photolysed by light from a mercury pen ray lamp ($\lambda = 184.9$ nm), collimated into the end of the main flow tube of the "wand". The concentration of OH and HO_2 radicals can be determined following Eq. 3-1:

$$[OH] = [HO_2] = [H_2O]_{vap}\, \sigma_{H2O}\, \phi_{OH}\, F_{184.9\,nm}\, \Delta t \qquad \text{Eq. 3-1}$$

where ϕ_{OH} is the quantum yield for the photolysis of OH, $F_{184.9\,nm}$ is the actinic flux of the output from the mercury pen ray lamp, σ_{H2O} is the absorption cross section for water vapour at 184.9 nm and Δt is the irradiation time. The value of σ_{H2O} is taken as $(7.22 \pm 0.22) \times 10^{-20}$ molecule^{-1} cm^2 from the literature (Cantrell *et al.* 1997) and ϕ_{OH} is generally taken to be unity ($= \phi_{HO2} = 1$) (Fuchs *et al.* 2011). The lamp flux, $F_{184.9\,nm}$, can be determined by actinometrical methods (N_2O or O_2), which will be discussed in Section 3.4. The output of the mercury pen ray lamp is dependent on the power supplied

to it, and hence, it is possible to alter the concentration of OH and HO_2 radicals produced during the "wand" calibration by altering the power of the lamp. A calibration factor, C_{OH} or C_{HO2}, can be determined following Eq. 3-2 or Eq. 3-3:

$$C_{OH} = S_{OH} / [OH] \quad \text{Eq. 3-2}$$

$$C_{HO2} = S_{HO2} / [HO_2] \quad \text{Eq. 3-3}$$

where S_{OH} and S_{HO2} are the OH and HO_2 signals, respectively.

Figure 3-4 and Figure 3-5 show example calibration plots for the OH and HO_2 HIRAC FAGE cells, respectively.

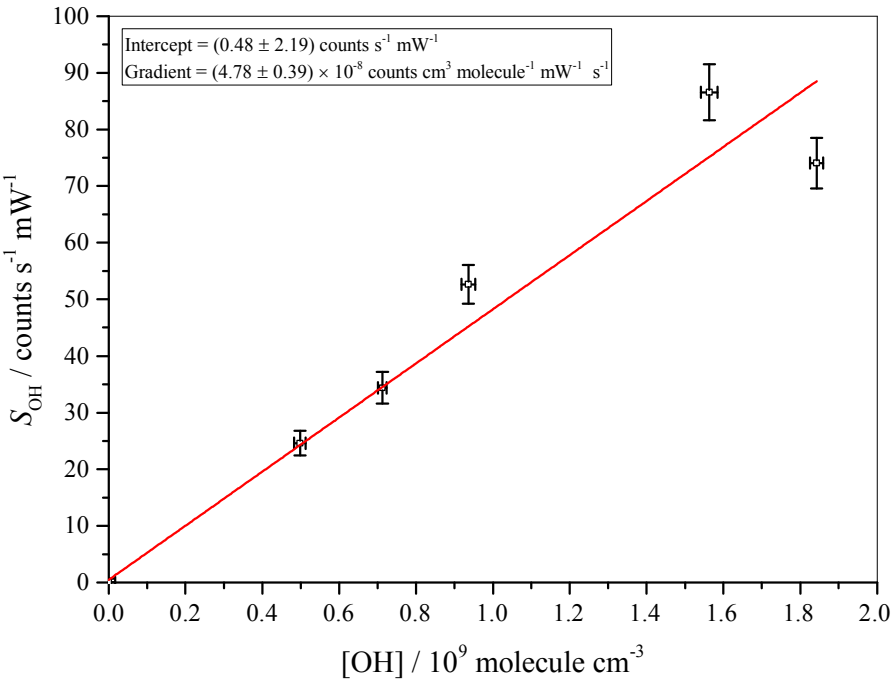

Figure 3-4: Calibration plot of the HIRAC FAGE OH cell using the "wand" calibration method. Error bars represent the 1σ standard deviation to the 60 second data. Measurements carried out with MCP detectors. $C_{OH} = (4.78 \pm 1.11) \times 10^{-8}$ counts cm^3 $molecule^{-1}$ s^{-1} mW^{-1}, where the error is determined from the sum in quadrature of the error in the gradient and the uncertainty in the measurements. Cell pressure = 2.71 Torr, laser power = 5.7 mW through the OH cell and $[H_2O]_{vap}$ = 2770 ppmv.

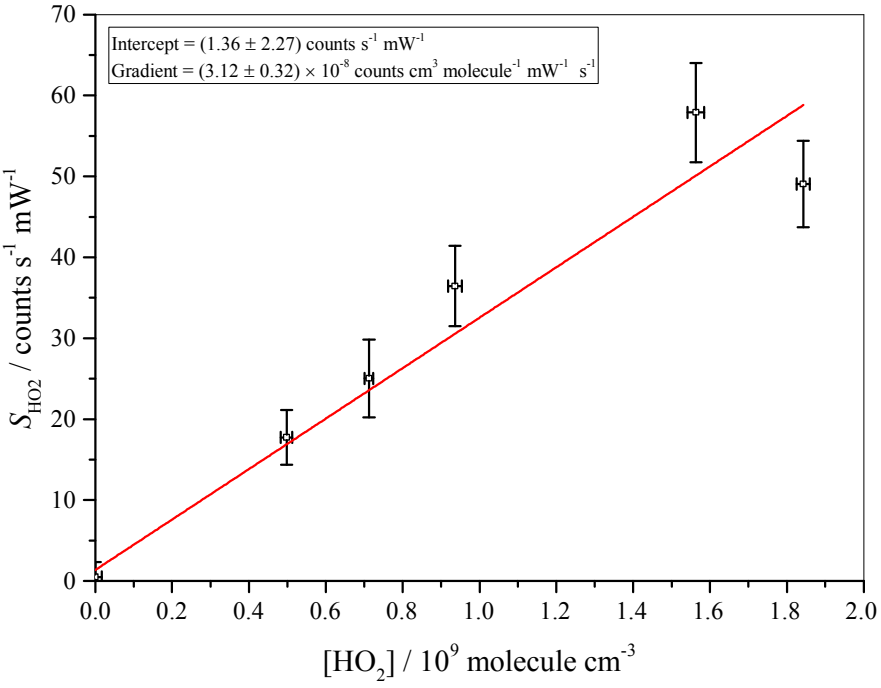

Figure 3-5: Calibration plot of the HIRAC FAGE HO_2 cell using the "wand" calibration method. Error bars represent the 1σ standard deviation to the 60 second data. Measurements carried out with MCP detectors. C_{HO2} = (3.12 ± 0.85) × 10^{-8} counts cm^3 $molecule^{-1}$ s^{-1} mW^{-1}, where the error is determined from the sum in quadrature of the error in the gradient and the uncertainty in the measurements. Cell pressure = 2.71 Torr, laser power = 2.8 mW through the HO_2 cell and $[H_2O]_{vap}$ = 2770 ppmv.

Pressure dependant calibrations are achieved with the use of different sized pinholes (0.5 - 1.0 mm) on the inlet in order to create a range of pressures (1.38 – 3.25 Torr) within the FAGE instrument inlet. A major disadvantage to using this method to produce different pressures within the instrument is that the flow rate within the instrument is dictated by the size of the pinhole, and hence, flow dynamics may be also altered by altering the pinhole size. The sensitivity of the HIRAC FAGE instrument has been determined previously, as a function of instrument cell pressure by Winiberg (2014), shown in Figure 3-6. A slight positive dependence was observed with an increase in internal cell pressure for the sensitivity of the HIRAC FAGE instrument towards both OH and HO_2, whilst the sharper increase in sensitivity observed in the HO_2 cell was attributed to a decrease in reaction time and mixing of the NO at the lower pressures.

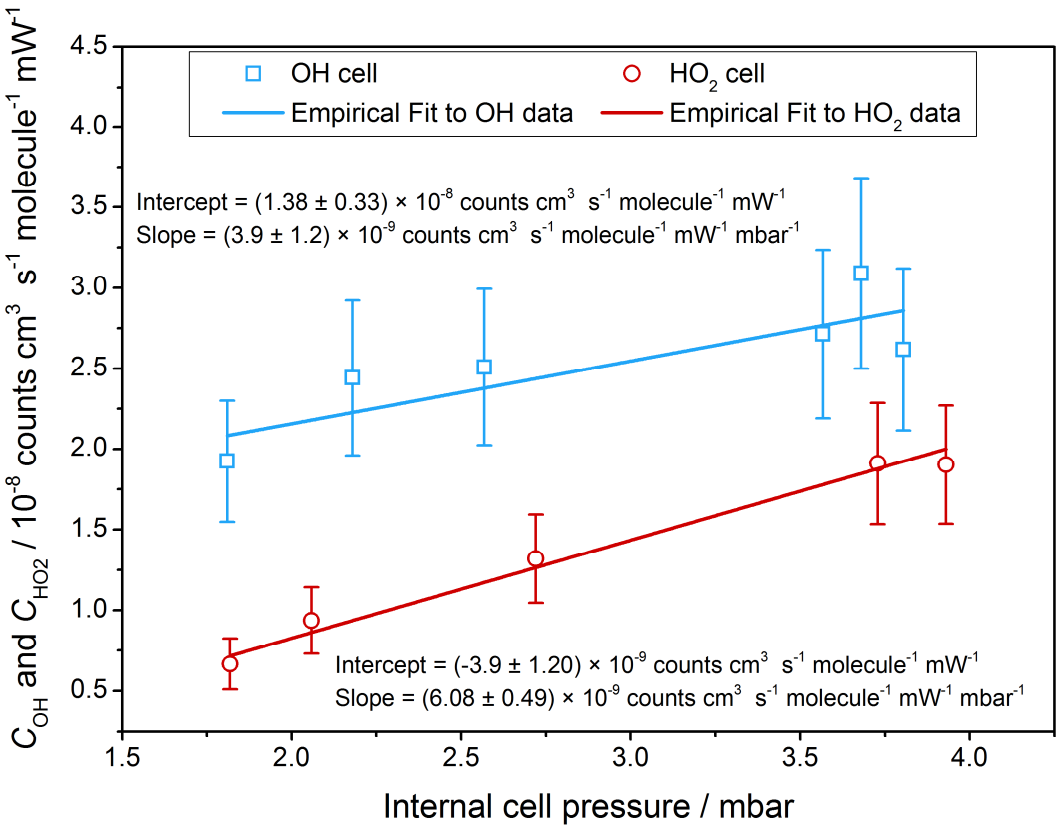

Figure 3-6: HIRAC FAGE "wand" calibration as a function of internal cell pressure, taken from Winiberg (2014).

The observed pressure dependence of the sensitivity of the FAGE instrument towards both OH and HO_2 radicals shows the importance of maintaining and recording a constant pressure within the instrument. Accurately characterising FAGE instrumentation sensitivity as a function of pressure and temperature is essential for accurately measuring [OH] and [HO_2] across different areas of the globe where temperatures vary considerably, and for aircraft measurements where the ambient pressure outside the aircraft varies with altitude. It is also vital for correctly determining HO_x concentrations in HIRAC for experiments carried out over a range of temperatures and pressures.

3.3.1 Error Analysis

Uncertainty in the conventional "wand" calibration method is determined from the sum in quadrature of the accuracy and precision in the calibration procedure. Parameters contributing to the total overall uncertainty in the "wand" calibration are listed in Table 3-1; the largest uncertainty coming from the N_2O actinometry procedure for the determination of $F_{184.9\ nm}$.

Parameter	Typical Uncertainty
$F_{184.9\ nm}$	20%
$[H_2O]$	1%
σ_{H2O}	3%
ϕ_{OH}	negligible
t	2%
OH power	3%
HO_2 power	8%
Online position	4%

Table 3-1: Summary of uncertainties contributing to the total overall uncertainty in the conventional "wand" calibration.

The uncertainty in $[H_2O]$ is taken from the hygrometer accuracy, the uncertainty in σ_{H2O} is taken from the literature (Cantrell *et al.* 1997), uncertainty in t comes from the uncertainties in the MFCs used. Uncertainty in OH and HO_2 power is taken from the laser power meter uncertainties. The uncertainty in the online position comes from the method for finding the online wavelength positions, where the laser wavelength is scanned until it reaches 98% of the maximum signal. The total uncertainty associated with the "wand" calibration method was estimated to be 21%.

As is shown here, the largest uncertainty in the "wand" calibration procedure arises from the determination of $F_{184.9\ nm}$ by N_2O actinometry. The following section (3.4) discusses the N_2O actinometry procedure, with focus on the breakdown of errors and their percentage contribution to the total overall variation in the determination of $F_{184.9\ nm}$.

3.4 N_2O Actinometry

The water vapour photolysis "wand" calibration method relies on accurate knowledge of the flux, $F_{184.9\ nm}$, of the pen ray lamp used in the calibration procedure. N_2O actinometry is used to determine the lamp flux, $F_{184.9\ nm}$, for the mercury pen ray lamp. This has been described numerous times (Faloona *et al.* 2004, Whalley *et al.* 2007, Dusanter *et al.* 2008). There are many known errors associated with N_2O actinometry. The work presented in this section aims to better understand the main sources of error when

determining $F_{184.9\,nm}$ using N_2O actinometry. The availability of three separate FAGE instruments; one ground based (Whalley *et al.* 2010), one aircraft based (Commane *et al.* 2010) and one chamber based (Winiberg *et al.* 2015), at Leeds, allowed for detailed comparison to be made between their calibration apparatus to gain further insight into the sources of error. With a better understanding of the error in measuring $F_{184.9\,nm}$, improvement in the calibration procedure can be made. Reducing the error in calibrating FAGE instrumentation will allow for more accurate HO_x measurements.

The use of O_2 actinometry may also be used for the determination $F_{184.9\,nm}$, and has been previously described Commane (2009). Winiberg (2014) described a comparison of O_2 and N_2O actinometry for the determination of $F_{184.9\,nm}$, showing good agreement between the two methods. There are a number of disadvantages associated with the O_2 actinometry method as compared to the N_2O actinometry method for $F_{184.9\,nm}$ determination; greater uncertainties (~20%, 1σ compared to ~16%, 1σ for N_2O actinometry), much lower flow rates and the necessity to measure the O_2 cross section which is dependent on the mercury pen ray lamp emission spectrum. The lower flow rates used in the O_2 actinometry method, 30 l min^{-1}, mean that the flow conditions are not comparable to those used in the "wand" calibration. Due to the larger uncertainties, differing operating conditions and the requirement to measure the O_2 cross section, O_2 actinometry is not routinely used in the calibration procedure for the HIRAC FAGE instrument, and so only the method of N_2O actinometry for the determination of $F_{184.9\,nm}$ will be discussed further from herein.

3.4.1 Experimental

The apparatus used for the determination of $F_{184.9\,nm}$ by N_2O actinometry is shown in Figure 3-7, taken from Winiberg (2014), where the calibration source is the same "wand" as is used for the conventional FAGE calibration, and the trace gas analyser is a chemiluminescence NO_x analyser (Thermo Electron Corporation Model 42C, LOD = 50 pptv at 120 s averaging time). A total flow of 40 l min^{-1} was flowed through the "wand" using a range of N_2O (BOC, medical grade) percentages of up to 10% in high purity air (BOC, BTCA-178). The flows from the three mass flow controllers (MFCs) were set and monitored with the use of in house written LabVIEW software. The lamp power and [NO] are also read and logged by this same software. The N_2O gas is flowed through a Sofnofil Trap, as shown in Figure 3-7, in order to oxidise any $NO_{x/y}$ impurities present in the N_2O gas cylinder. Sofnofil is used as a chemical absorbent, with the active

ingredient of aluminium oxide. It has, however, been shown that the use of the Sofnofil Trap has little influence on the determination of $F_{184.9\,nm}$ (Figure 3-10).

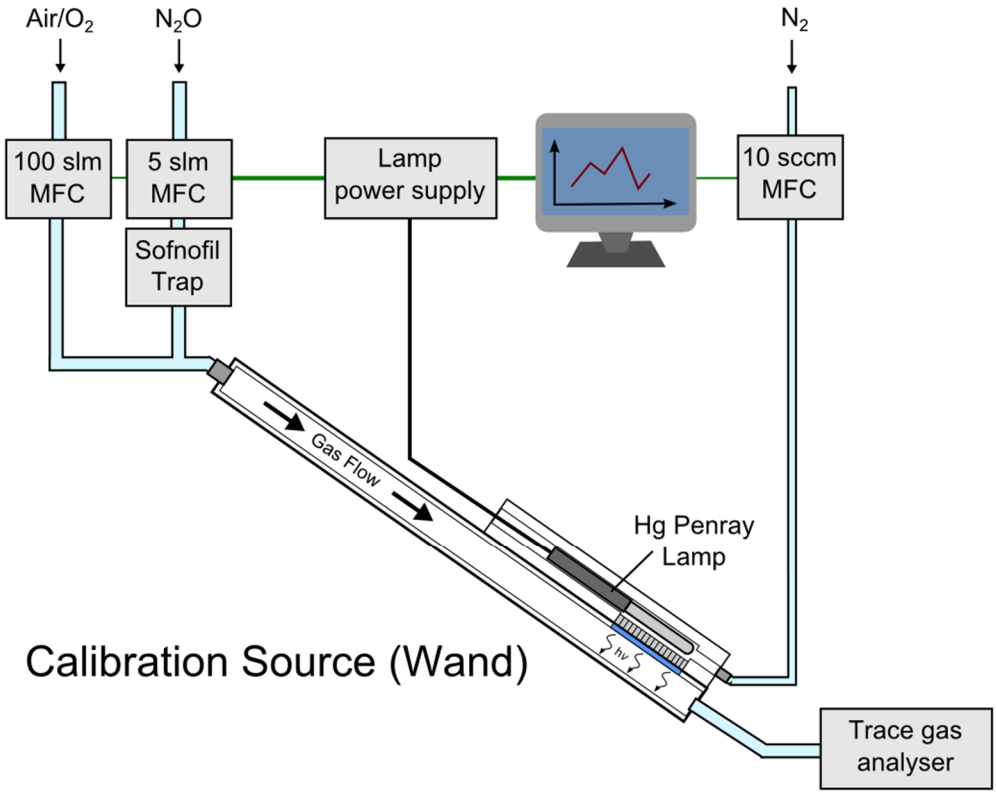

Figure 3-7: Schematic of the N_2O actinometry set up for determining the lamp flux, $F_{184.9\,nm}$, of a mercury pen ray lamp used in the conventional FAGE "wand" calibration. For $F_{184.9\,nm}$ determination by the N_2O actinometry method, a mixture of N_2O in air (40 l min^{-1} total flow) is flowed through the "wand" and the trace gas analyser used is a chemiluminescence NO_x analyser. Taken from (Winiberg 2014).

Reactions R 3-7 to R 3-13 describe the reactions involved in the N_2O actinometry experiment. A known concentration of N_2O is photolysed by the mercury pen ray lamp (R 3-7), producing $O(^1D)$, which in turn reacts with a further molecule of N_2O to give NO (R 3-12). The NO produced following these reactions is then measured by the chemiluminescence NO_x analyser. It is also possible for the $O(^1D)$ produced via R 3-7 to be removed by a number of other reactions, described by R 3-8 to R 3-13.

$$N_2O + h\nu \xrightarrow{k_{R\,3\text{-}7}} N_2 + O(^1D) \quad \text{R 3-7}$$

$$O(^1D) + O_2 \xrightarrow{k_{R\,3\text{-}8}} O(^3P) + O_2 \quad \text{R 3-8}$$

$$O(^1D) + N_2 \xrightarrow{k_{R\,3\text{-}9}} O(^3P) + N_2 \quad \text{R 3-9}$$

$$O(^1D) + N_2O \xrightarrow{k_{R\,3\text{-}10}} O(^3P) + N_2O \quad \text{R 3-10}$$

$$O(^3P) + O_2 + M \xrightarrow{k_{R\,3\text{-}11}} O_3 + M \quad \text{R 3-11}$$

$$O(^1D) + N_2O \xrightarrow{k_{R\,3\text{-}12}} 2NO \quad \text{R 3-12}$$

$$O(^1D) + N_2O \xrightarrow{k_{R\,3\text{-}13}} N_2 + O_2 \quad \text{R 3-13}$$

Following the reactions described above, $F_{184.9\,nm}$ can be determined following Eq. 3-4:

$$F_{184.9\,nm}\Delta t = \frac{(k_{R\,3\text{-}8}[O_2] + k_{R\,3\text{-}9}[N_2] + (k_{R\,3\text{-}13} + k_{R\,3\text{-}12})[N_2O])[NO]}{2\left(k_{R\,3\text{-}12}\,\sigma_{N_2O}\,\Phi_{O(^1D)}[N_2O]^2\right)} \quad \text{Eq. 3-4}$$

where Δt is the irradiation time which can be calculated from the known dimensions of the "wand" as a function of the total flow rate of gas through the "wand", $\phi_{O(1D)}$ is the quantum yield for the photodissociation $O(^1D)$ (~1) and σ_{N2O} is the absorption cross section of N_2O at 184.9 nm. σ_{N2O} is taken from the literature as $(1.43 \pm 0.02) \times 10^{-19}$ cm^2 molecule^{-1} (Creasey *et al.* 2000). All the concentrations of species in Eq. 3-4 are in molecule cm^{-3}.

The rate coefficients, $k_{R\,3\text{-}8}$, $k_{R\,3\text{-}9}$, $k_{R\,3\text{-}13}$ and $k_{R\,3\text{-}12}$ used in Eq. 3-4 are given in Table 3-2, where the values taken from Sander *et al.* (2011) are those which have been used here for determination of $F_{184.9\,nm}$ following Eq. 3-4. A comparison of rate coefficients taken from Sander *et al.* (2011) is given to those from Atkinson *et al.* (2004). It should be noted that these rate coefficients are evaluations from values in the literature, carried out by NASA/JPL and IUPAC, respectively. Slight differences in reported values are evident, indicating that the choice of values for rate coefficients to be used may have an influence on the final determination of $F_{184.9\,nm}$ from the N_2O actinometry procedure.

Both sets of rate coefficients are given in Table 3-2, based on evaluations of studies which have been reported in the literature. Evaluations by IUPAC were last updated in 2001 for $k_{R\,3\text{-}8}$, 2009 for $k_{R\,3\text{-}9}$ and 2007 for $k_{R\,3\text{-}13}$ and $k_{R\,3\text{-}12}$, whereas all evaluations reported by JPL were most recently updated in June 2011.

The errors associated with the recommended IUPAC rate coefficients are decided upon by the evaluators themselves, based on the knowledge of the measurement techniques used in the literature values used in determining the recommended values (Atkinson *et al.* 2004). Eq. 3-5 represents the error determination for JPL recommended rate coefficients (Sander *et al.* 2011) and Eq. 3-6 represents the error determination for IUPAC recommended rate coefficients (Atkinson *et al.* 2004). Errors associated with the JPL recommended rate coefficients are also determined by the evaluators to best represent the errors in the individual measurements used in the evaluation (Sander *et al.* 2011).

$$\mathrm{f}(T)=\mathrm{f}(298\ \mathrm{K})\exp\left|\mathrm{g}\left(\frac{1}{T}-\frac{1}{298}\right)\right| \qquad \text{Eq. 3-5}$$

$$\Delta\log k(T)=\Delta\log k(298\ \mathrm{K})+0.4343\left\{\Delta E/R\left(\frac{1}{T}-\frac{1}{298}\right)\right\} \qquad \text{Eq. 3-6}$$

Rate Coefficients	JPL Value* / molecule^{-1} cm^3 s^{-1}	JPL Value at 293 K / molecule^{-1} cm^3 s^{-1}	IUPAC Value† / molecule^{-1} cm^3 s^{-1}	IUPAC Value at 293 K / molecule^{-1} cm^3 s^{-1}	Reaction
$k_{R\ 3\text{-}8}$	$3.3 \times 10^{-11}\ e^{(55\ /\ T)}$	$(3.98 \pm 0.36) \times 10^{-11}$	$3.2 \times 10^{-11}\ e^{(67\ /\ T)}$	$(4.0 \pm 0.46) \times 10^{-11}$	$O(^1D) + O_2 \rightarrow O(^3P) + O_2$
$k_{R\ 3\text{-}9}$	$2.15 \times 10^{-11}\ e^{(110\ /\ T)}$	$(3.13 \pm 0.25) \times 10^{-11}$	$2.15 \times 10^{-11}\ e^{(110\ /\ T)}$	$(3.13 \pm 0.36) \times 10^{-11}$	$O(^1D) + N_2 \rightarrow O(^3P) + N_2$
$k_{R\ 3\text{-}12}$	$7.25 \times 10^{-11}\ e^{(20\ /\ T)}$	$(7.76 \pm 0.79) \times 10^{-11}$	7.6×10^{-11}	$(7.6 \pm 0.88) \times 10^{-11}$	$(O^1D) + N_2O \rightarrow N_2 + O_2$
$k_{R\ 3\text{-}13}$	$4.63 \times 10^{-11}\ e^{(20\ /\ T)}$	$(4.96 \pm 0.50) \times 10^{-11}$	4.3×10^{-11}	$(4.3 \pm 0.50) \times 10^{-11}$	$O(^1D) + N_2O \rightarrow 2NO$

Table 3-2: Rate coefficients used for determining the product of lamp flux using Eq. 3-4, *values and errors taken from Sander et al. (2011), †values and errors taken from Atkinson et al. (2004).

During an actinometry experiment the mercury pen ray lamp current was varied between ~0.8 mA and ~4.0 mA, this is the same procedure used for producing a range of HO_x concentrations in the conventional FAGE "wand" calibration method. Two main calibration racks were used for this comparison study; one routinely used for the calibration of the HIRAC FAGE instrument, and another routinely used for the calibration of a FAGE instrument employed on the FAAM BAe-146-301 aircraft. Both calibration racks include a MFC for the main air flow and another for the flow of N_2O into the wand (a third MFC is used to control a flow of N_2 past the mercury pen ray lamp in order to remove any impurities surrounding it and to maintain a constant temperature), a chemiluminescence NO_x analyser, a lamp power supply and in-house written software for controlling, monitoring and recording flows, temperatures, lamp power and [NO]. A third chemiluminescence NO_x analyser was also available for comparison, usually employed for field measurements within the ground based FAGE shipping container. Herein, the different apparatus employed will be referred to as HIRAC-, aircraft- and container-. A full calibration of all apparatus has been carried out, including calibration of all chemiluminescence NO_x analysers and all MFCs with appropriate gases.

3.4.1.1 NO_x Analyser Calibration

In the chemiluminescence NO_x analysers, the NO is titrated to NO_2 with ozone, which produces the electronically excited NO_2^* molecule. This electronically excited NO_2^* molecule can then relax to the ground state either via collisional quenching or radiative decay, emitting infrared light where the intensity of this light, is proportional to the concentration of NO. The excited state NO_2^* may be relaxed to the ground state following collisional quenching; N_2O is a more efficient quencher of NO_2^* than air, and so it is necessary to take this into account by carrying out the calibration of the NO_x analyser over a range of N_2O concentrations similar to that used for the N_2O actinometry procedure. An excess flow of air is passed across the sampling inlet of the NO_x analyser, where the NO_x analyser draws in a sample of ~1 l min^{-1} and the remaining air flow goes through an exhaust line and into a fume cupboard. A flow of NO (BOC, 450 ppbv in N_2) is added to the air flow in order to produce a range of NO concentrations; a zero measurement is taken where no flow of NO is added in order to correct for any offset of the NO_x analyser.

$$NO + O_3 \rightarrow NO_2^* + O_2 \qquad \text{R 3-14}$$

$$NO_2^* \rightarrow NO_2 + h\nu \qquad \text{R 3-15}$$

Figure 3-8 and Figure 3-9 show the calibration plot of the HIRAC chemiluminescence NO_x analyser and its response to N_2O, respectively. The gradient of the linear least squares fit from the plot of measured [NO] against calculated [NO] gives a calibration factor, C_{NO}. The procedure is repeated for a range of N_2O percentages up to ~10%, and the resultant C_{NO} values are plotted against the N_2O percentage (Figure 3-9). The gradient from the linear least squares fit to the plot of C_{NO} against N_2O% gives the NO_x analyser response to N_2O; the sensitivity of the NO_x analyser decreases as the N_2O percentage is increased.

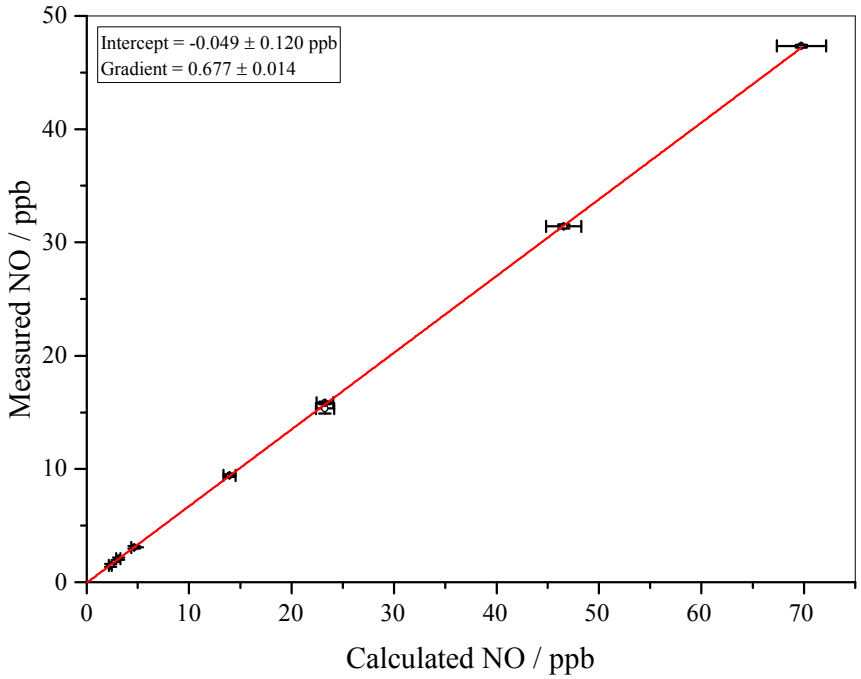

Figure 3-8: NO_x box calibration plot for HIRAC chemiluminescence NO_x analyser (zero [N_2O]). Error bars are total errors in measured and calculated [NO] to 1σ. Errors in the intercept and gradient are the standard error in the fitting procedure.

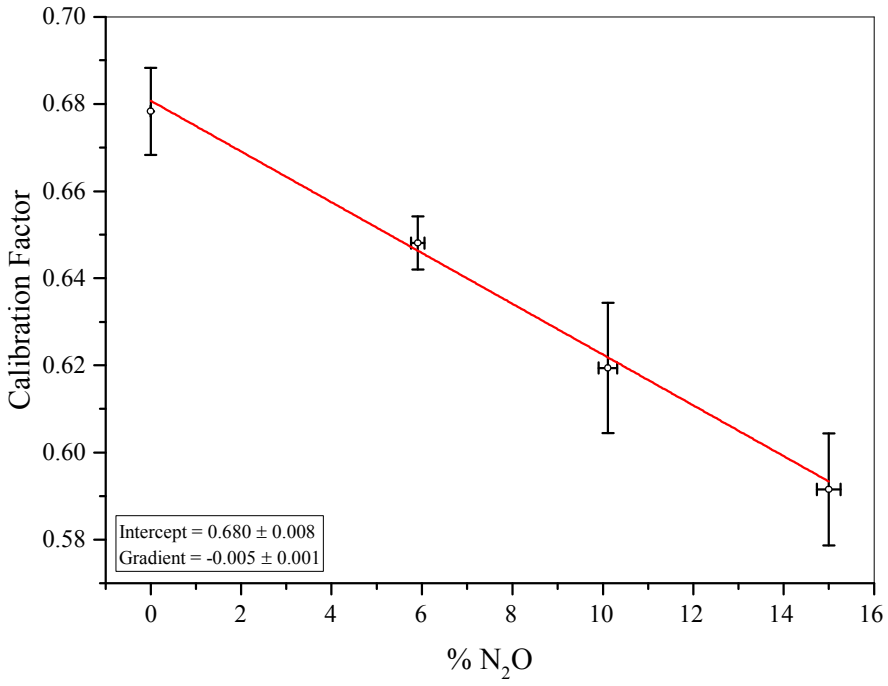

Figure 3-9: NO_x box response to N_2O for HIRAC chemiluminescence NO_x analyser. Error bars are total errors to 1σ. Errors in the intercept and gradient are the standard error in the fitting procedure.

A comparison of NO_x analyser calibration factors and response to N_2O is given in Table 3-3 for the three chemiluminescence NO_x analysers used in this study. The HIRAC and the aircraft NO_x analysers are in excellent agreement for the calibration factors and response to N_2O; the FAGE container NO_x analyser has a lower calibration factor (gradient 0.575 ± 0.012 compared to 0.677 ± 0.014 for the HIRAC NO_x analyser and 0.672 ± 0.014 for the aircraft NO_x analyser). It is not surprising that the sensitivity of the container NO_x analyser is lower than both the HIRAC and aircraft NO_x analysers considering its extended usage in a wide range of environments, often in urban areas where NO_x and aerosol concentration are high, which can lead to reduced sensitivity from fittings and tubing becoming dirty.

NO_x Analyser	NO Calibration		N_2O Response	
	Gradient	Intercept	Gradient	Intercept
HIRAC	0.677 ± 0.014	-0.049 ± 0.120	-0.005 ± 0.001	0.680 ± 0.008
Aircraft	0.672 ± 0.013	-0.026 ± 0.135	-0.005 ± 0.001	0.666 ± 0.005
Container	0.575 ± 0.012	-0.234 ± 0.106	-0.005 ± 0.001	0.578 ± 0.004

Table 3-3: Comparison of chemiluminescence NO_x analyser calibrations and NO_x box response to N_2O for three NO_x analysers. Errors are standard error from linear least squares fitting procedure.

3.4.2 Reproducibility of Results

A number of comparisons were carried out between the apparatus available from the two different calibration racks and the additional NO_x analyser. A comparison of various apparatus is given here, with discussion on major sources of error in the determined lamp flux, $F_{184.9\,nm}$. A summary of values determined from linear regression analysis, weighted to both the *x* and *y* error bars, is given in Table 3-4. The gradient obtained from the linear regression analysis represents the change in lamp flux, $F_{184.9\,nm}$, as a function of lamp current, and is used in the FAGE HO_x calibration data analysis process.

All data were corrected for the relevant MFC and NO_x box calibrations, and it was observed that all measurements for the determination of $F_{184.9\,nm}$ produced plots of $F_{184.9\,nm}$ against lamp current where values of the gradient agree to within their stated errors.

Run	Intercept / photon cm^{-2} s^{-1}	Gradient / photon cm^{-1} s^{-1} mA^{-1}	N_2O / %
1	$(-6.8 \pm 14.4) \times 10^{11}$	$(1.2 \pm 0.1) \times 10^{13}$	6
2*	$(-2.4 \pm 1.5) \times 10^{12}$	$(1.2 \pm 0.1) \times 10^{13}$	6
3†	$(2.5 \pm 14.7) \times 10^{11}$	$(1.1 \pm 8.1) \times 10^{13}$	7
4‡	$(1.6 \pm 12.4) \times 10^{11}$	$(9.9 \pm 0.7) \times 10^{13}$	7
5	$(1.2 \pm 13.0) \times 10^{11}$	$(1.0 \pm 0.1) \times 10^{13}$	7
6§	$(-1.6 \pm 1.2) \times 10^{12}$	$(9.7 \pm 0.7) \times 10^{12}$	8
7**	$(-5.7 \pm 15.6) \times 10^{11}$	$(1.0 \pm 0.1) \times 10^{13}$	7
8	$(3.0 \pm 23.3) \times 10^{11}$	$(1.1 \pm 0.1) \times 10^{13}$	7

Table 3-4: Comparison of the results from N_2O actinometry carried out for the determination of the flux of a mercury pen ray lamp, F184.9 nm, using the HIRAC calibration rack. *Measurements carried out with N2O flowed through a Sofnofil Trap. †MCF for N_2O from Aircraft calibration rack used for measurements. ‡Measurements carried out with the lamp power supply from the Aircraft calibration rack. §MFC for air from Aircraft calibration rack used for measurements. **Software from Aircraft calibration rack used for measurements. Errors reported are the standard error from the linear least squares fitting procedure.

A comparison of $F_{184.9\,nm}$ determination carried out with and without the N_2O gas flow passing through a Sofnofil trap is shown in Figure 3-10. Excellent agreement was observed between the two sets of data, where the gradients obtained from the linear least squares fitting to *x* and *y* errors agree perfectly. A difference in the data sets was observed in the intercept obtained, however, they are within error of each other. A larger intercept was observed for the data set following N_2O actinometry where the N_2O gas flow was not passed through a Sofnofil trap, indicating that some impurities within the N_2O may be influencing the determination of $F_{184.9\,nm}$, however, the excellent agreement of the gradients would imply that these impurities do not have a significant influence on the results.

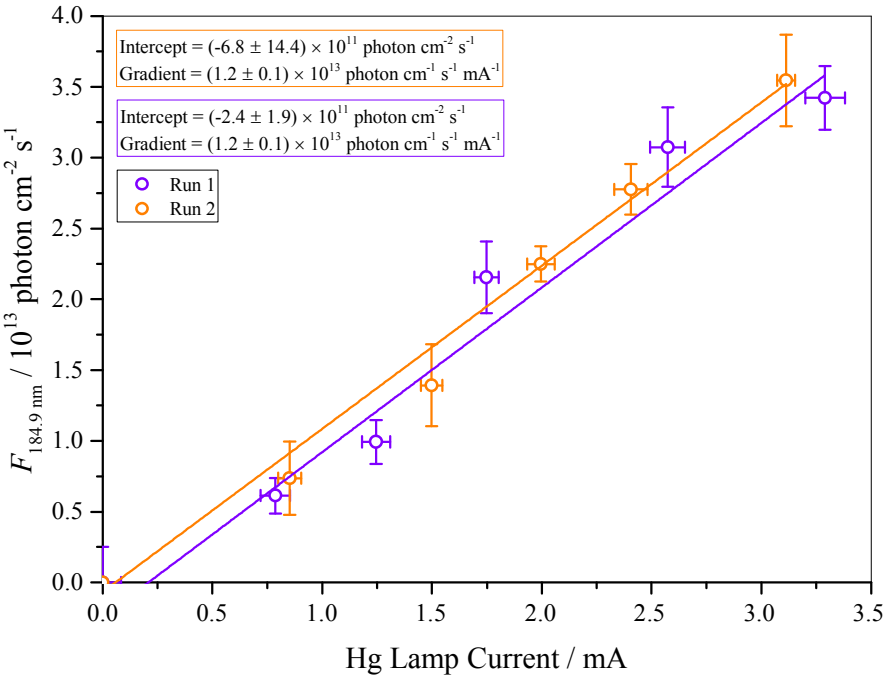

Figure 3-10: Hg lamp flux, $F_{184.9\,nm}$, as a function of lamp current, determined by N_2O actinometry. Comparison of results taken with (Run 1) and without (Run 2) the N_2O flow passing through a Sofnofil Trap. Measurements taken with and without the Sofnofil trap were at a flow of 5.7% N_2O in air through the HIRAC calibration "wand". Errors in the *x*-axis represent the standard deviation in the lamp current measurement to 1σ, and errors in the *y*-axis represent the total error propagated from the errors associated with other measurements required for the determination of $F_{184.9\,nm}$. Solid lines represent linear least squares fit to the data weighted to errors in the *x* and *y* axis. Errors in the gradients and intercepts are the standard error in the fitting procedure.

Figure 3-11 shows a comparison of N_2O actinometry plots for measurements carried out using two different lamp power supplies. Both power supplies are (Oriel Model 6060), and so should come with the same error associated with them. Very good agreement is observed between the two sets of data, with the gradient obtained using the HIRAC lamp

power supply, Run 5, being (1.0 ± 0.1) × 10^{11} photon cm^{-2} s^{-1} mA^{-1} and (9.9 ± 0.7) × 10^{11} photon cm^{-2} s^{-1} mA^{-1} for measurements carried out with the aircraft lamp power supply, Run 4. The larger error in the gradient obtained from Run 4 is likely associated with the measurement of the lamp current, as seen by the error bars in Figure 3-11. Although the two lamp power supplies are technically identical, many other factors may influence the errors associated with them, including age and usage.

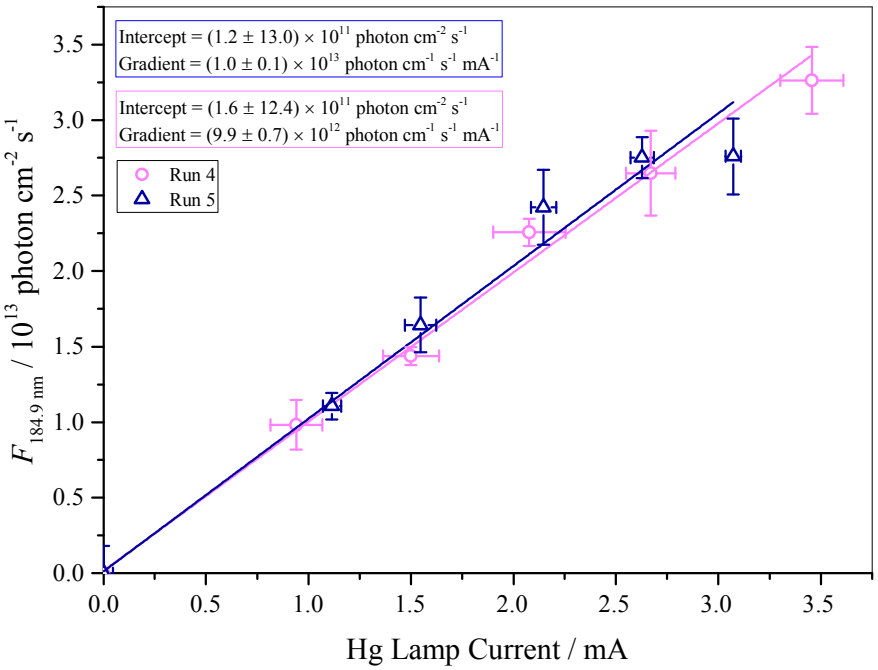

Figure 3-11: Hg lamp flux, $F_{184.9\,nm}$, as a function of lamp current, determined by N_2O actinometry. Comparison of results taken with two different lamp power supply units. Run 4 was carried out with the aircraft lamp power supply and Run 5 was carried out with the HIRAC lamp power supply. Measurements with the two lamp power supplies were at a flow of 6.98% N_2O in air through the HIRAC calibration "wand". Errors in the *x*-axis represent the standard deviation in the lamp current measurement to 1σ, and errors in the *y*-axis represent the total error propagated from the errors associated with other measurements required for the determination of $F_{184.9\,nm}$. Solid lines represent the linear least squares fit to the data, weighted to errors in the *x* and *y* axis. Errors in the gradients and intercepts are the standard error in the fitting procedure.

A comparison of N_2O actinometry results carried out with measurements being recorded on two different software systems is given in Figure 3-12. The measurements, again, are in excellent agreement, with the gradient for measurements carried out using the HIRAC software, Run 7, being (1.1 ± 0.1) × 10^{11} photon cm^{-2} s^{-1} mA^{-1} and (1.0 ± 0.1) × 10^{11} photon cm^{-2} s^{-1} mA^{-1}. Although the N_2O software has been written in-house in two different programs (the HIRAC software being written in LabVIEW and the aircraft software being written in Delphi), both sets of software are written to set and record all of the same experimental parameters.

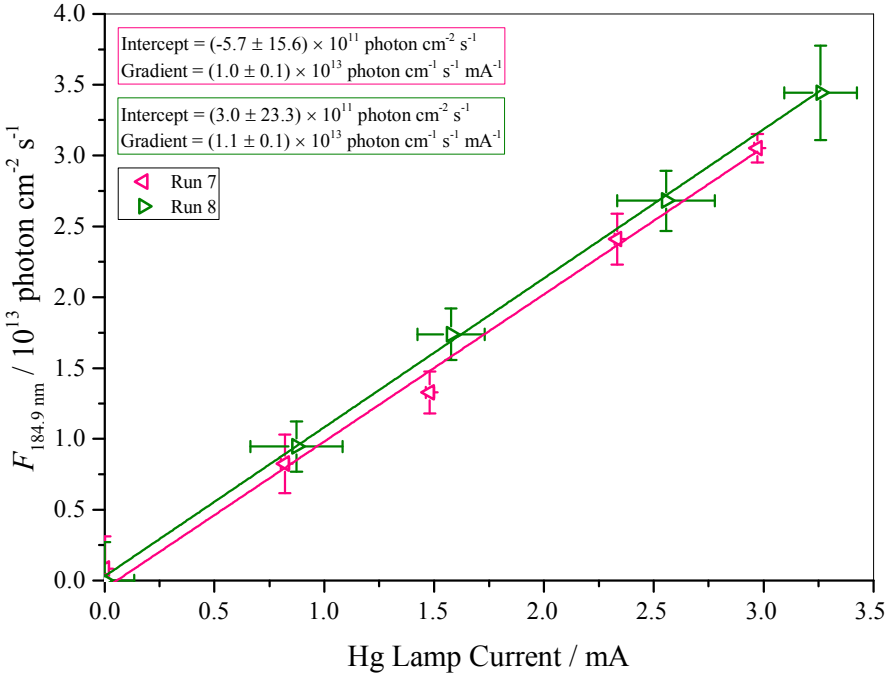

Figure 3-12: Hg lamp flux, $F_{184.9\,nm}$, as a function of lamp current, determined by N_2O actinometry. Comparison of results recorded with software from two different calibration racks. Run 7 was recorded using the software from the aircraft calibration rack, obtained using a total flow of 6.98% N_2O in air, and Run 8 was recorded using the software from the HIRAC calibration rack, obtained using a total flow of 6.81% N_2O in air. Errors in the *x*-axis represent the standard deviation in the lamp current measurement to 1σ, and errors in the *y*-axis represent the total error propagated from the errors associated with other measurements required for the determination of $F_{184.9\,nm}$. Solid lines represent the linear least squares fit to the data, weighted to errors in both the *x* and *y* axis. Errors in the gradients and intercepts are the standard error in the fitting procedure.

The comparisons described here show little variation in the determination of $F_{184.9\,nm}$ following N_2O actinometry experiments carried out using numerous apparatus. It is interesting to observe that the errors in the lamp current vary considerably. It should be noted, however, that the error in the determined $F_{184.9\,nm}$ is independent of the error in the lamp current.

3.4.3 Error Analysis

3.4.3.1 Summary of Errors

The errors shown in Figure 3-10, Figure 3-11 and Figure 3-12 are derived from the standard deviation in the measured lamp current to 1σ in the *x*-axis, and the *y*-axis errors are calculated from the propagation of the errors associated with each of the values used in the calculation of $F_{184.9\,nm}$ (Eq. 3-4). Errors in the flow rates are typically ~1%, calculated following Eq. 3-7:

$$\sigma_{flow} = (0.007 \times \text{flow rate}) + (0.002 \times \text{full scale}) \quad \text{Eq. 3-7}$$

Errors in rate coefficients are taken from the literature (Sander *et al.* 2011), and are given in Table 3-2. Error in temperature is taken from the standard deviation of the measurements.

Parameter	**Typical Uncertainty**
Flow Rate	1%
Temperature	1%
Pressure	1%
$k_{R\ 3\text{-}8}$*	9%
$k_{R\ 3\text{-}9}$*	8%
$k_{R\ 3\text{-}13}$*	10%
$k_{R\ 3\text{-}12}$*	10%
$F_{184.9\ nm}$	20%

Table 3-5: Typical uncertainties from parameters used in the determination of $F_{184.9\ nm}$. *uncertainties for JPL (Sander *et al.* 2011) evaluated rate coefficients at 293 K. Uncertainty in $F_{184.9\ nm}$ is taken as the sum in quadrature of the overall accuracy and precision.

Accurate determination of $F_{184.9\ nm}$ is essential in order to accurately calibrate the HIRAC FAGE instrument using the traditional "wand" calibration method. The results described above on the reproducibility of results when using numerous different apparatus for the determination of $F_{184.9\ nm}$ show no discernible differences between the different apparatus used. The value of $F_{184.9\ nm}$, determined through N_2O actinometry, is the largest source of error in the FAGE "wand" calibration procedure. Total uncertainty in $F_{184.9\ nm}$ can be propagated from the given uncertainties in the individual values used in the calculation, as has been carried out for the results described thus far. This uncertainty does not represent systematic errors well; errors arising from unrepresentative samples or errors arising from the function used in the determination of the final value. To gain a better insight into the sources of this error from the N_2O actinometry, the method of Monte Carlo error propagation was used in order to more accurately determine an error in the value of $F_{184.9\ nm}$. The Monte Carlo method was first described by Metropolis and Ulam

(1949) and has since been widely used and reported for the propagation of random error arising from input parameters of which their variance is known. This method is typically used when the determination of a value comes from numerous parameters, all with errors associated with them.

3.4.3.2 Monte Carlo

In the Monte Carlo error propagation method, large sets of random numbers are generated with similar statistical properties to the real data, such as the spread of the data and its distribution. Therefore, it is important to know the spread and distribution of the individual raw data measurements in order to generate appropriate randomly generated number sets. Normality tests were carried out on the raw data, and it was determined that all measurements were well represented by a normal distribution.

A simulation was set up in order to investigate the random error associated with the determination of the value of $F_{184.9\,nm}$ from N_2O actinometry. As described for the N_2O actinometry method for the determination of $F_{184.9\,nm}$, the current of the mercury pen ray lamp is altered in order to achieve a range of different values of $F_{184.9\,nm}$, over a range of N_2O percentages, in order to ensure that the N_2O quenching effect in the chemiluminescence NO_x analyser is correctly accounted for. For experimental measurements, each measurement point (each set lamp current) was recorded for 120 s. Initial values inputted to the simulation were taken as the averages for each raw data value, and the spread was taken as the standard deviation.

Once $F_{184.9\,nm}$ has been determined for each lamp current over a range of N_2O percentages, the gradient of the straight line fit to the plot of $F_{184.9\,nm}$ vs. lamp current was used for the HO_x calibration procedure. The error in the *x*-axis is only dependent on the error in the lamp current; determined from the 1σ standard deviation of the measurement. As this work is investigating the error of $F_{184.9\,nm}$, the error in the lamp current is excluded from the following discussion.

The standard deviation for measurements of gas flows, temperatures and NO concentration were determined for each measurement point at a different lamp current. These standard deviations were then used to generate large sets of numbers for each parameter, over a normal distribution, from the average values. For each set of random numbers generated, the lamp flux, $F_{184.9\,nm}$, was calculated. Figure 3-13 shows a plot of $F_{184.9\,nm}$ against the lamp current for 10000 samples generated for each parameter at each lamp current, taken from a normal distribution from the average and standard deviation of each parameter; this figure shows the plot where the lamp current is also varied.

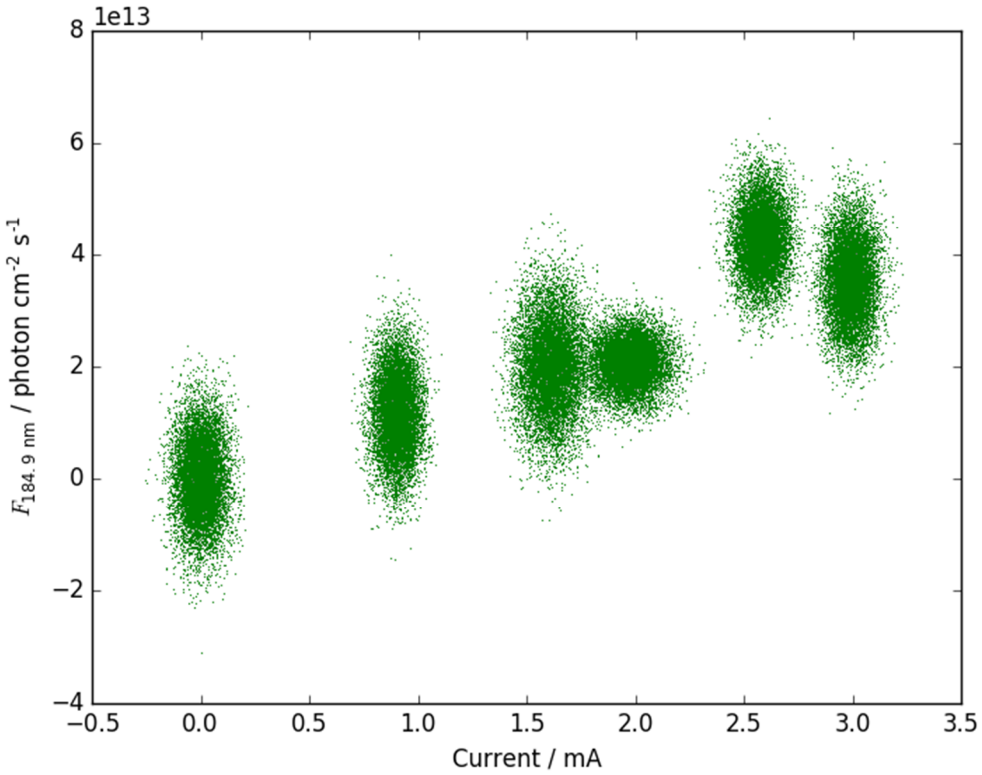

Figure 3-13: Example N_2O actinometry plot generated from 10000 random samples over error input range for each parameter included in the calculation of $F_{184.9\ nm}$.

As discussed, the variation in lamp current, at a given setting, does not influence the determination of $F_{184.9\ nm}$; Figure 3-14 and Figure 3-15 show plots of $F_{184.9\ nm}$ against lamp current where only the parameters used for the determination of $F_{184.9\ nm}$ were generated from the average and standard deviation of each parameter from a normal distribution for 10000 samples. As discussed in Section 3.4.1, the choice of rate coefficients used in the determination of $F_{184.9\ nm}$ may influence the final value of $F_{184.9\ nm}$. Figure 3-14 was generated using recommended rate coefficients and their errors from JPL (Sander *et al.* 2011), and Figure 3-15 was generated using the IUPAC recommended rate coefficients (Atkinson *et al.* 2004). The gradients obtained from the linear least squares fitting to the data (solid red line in Figure 3-14 and Figure 3-15) agree well; $(1.35 \pm 0.03) \times 10^{13}$ photon cm^{-1} s^{-1} mA^{-1} from Figure 3-14 and $(1.39 \pm 0.04) \times 10^{13}$ photon cm^{-1} s^{-1} mA^{-1} from Figure 3-15, where the error is the standard error from the fitting procedure. The error in the gradient from data produced using the IUPAC rate coefficient values is slightly greater (2.88%) than from using the JPL rate coefficient values (2.22%), which can be attributed to the larger errors associated with the IUPAC rate coefficient values (Table 3-2).

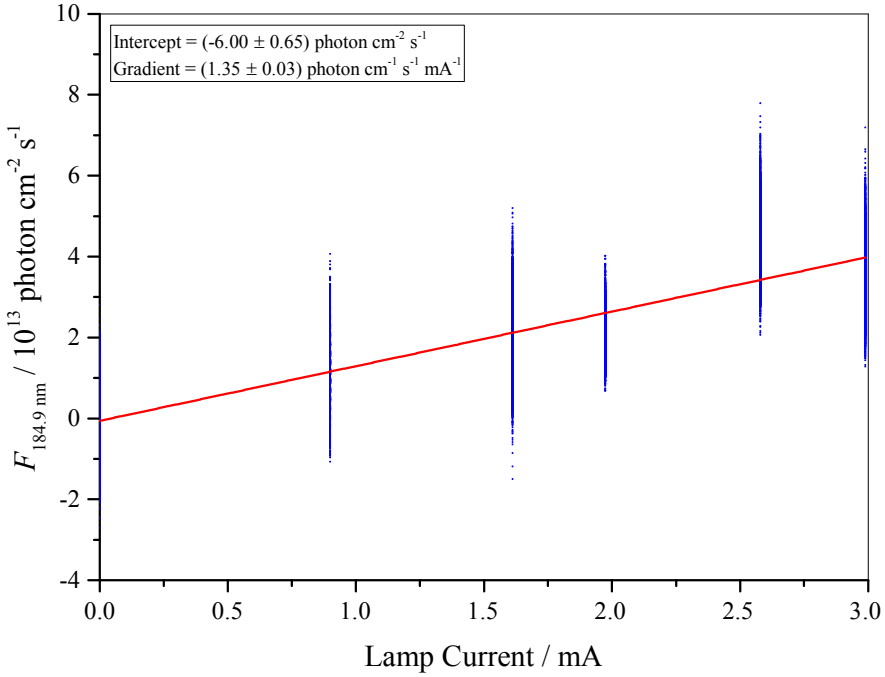

Figure 3-14: Plot of $F_{184.9\ nm}$ against lamp current where all parameters used in the determination of $F_{184.9\ nm}$ are varied from their average between the standard deviation, taken from a normal distribution for 10000 samples. k values used are those from JPL evaluation (Sander *et al.* 2011). The lamp current was kept constant, using the average value determined for each lamp current. Error in the intercept and gradient is the standard error from the fitting procedure.

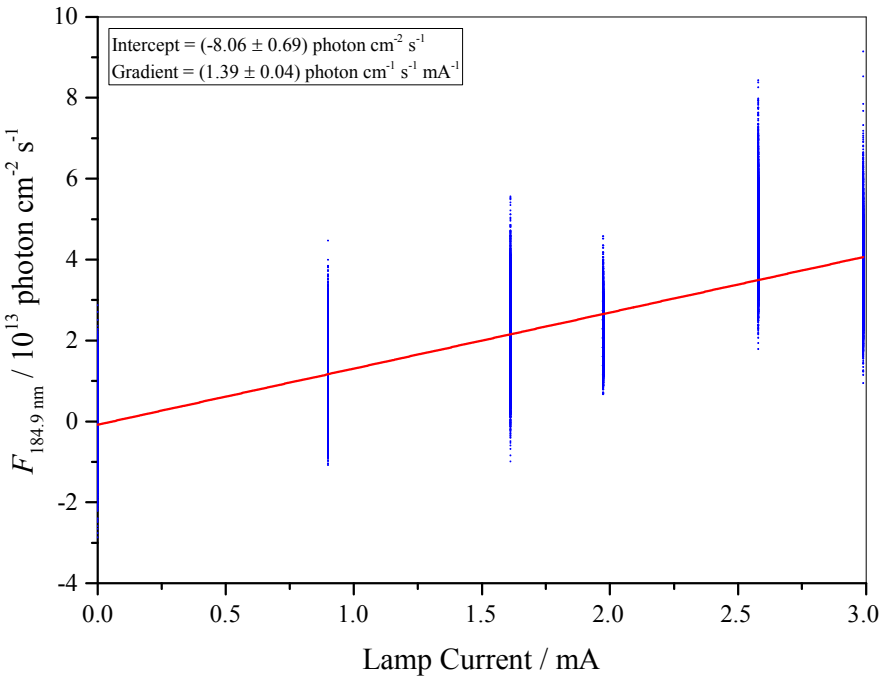

Figure 3-15: Plot of $F_{184.9\,nm}$ against lamp current where all parameters used in the determination of $F_{184.9\,nm}$ are varied from their average between the standard deviation, taken from a normal distribution for 10000 samples. *k* values used are those from IUPAC evaluation (Atkinson *et al.* 2004). The lamp current was kept constant, using the average value determined for each lamp current. Error in the intercept and gradient is the standard error from the fitting procedure.

In order to investigate the influence of individual parameters on the determined $F_{184.9\,nm}$, correlation plots for $F_{184.9\,nm}$ against each parameter were produced. Correlation plots of $F_{184.9\,nm}$ against all parameters required in the determination of $F_{184.9\,nm}$ are shown in Figure 3-16 and Figure 3-17 for JPL (Sander *et al.* 2011) rate coefficient values and IUPAC (Atkinson *et al.* 2004) rate coefficient values, respectively, where the value for the lamp current was kept constant at 1.65 mA in both cases. From the correlation plots, it is clear that the value of [NO] has the most significant influence on the determined $F_{184.9\,nm}$ for determinations carried out using both the JPL evaluated rate coefficients (Sander *et al.* 2011) and the IUPAC evaluated rate coefficients (Atkinson *et al.* 2004).

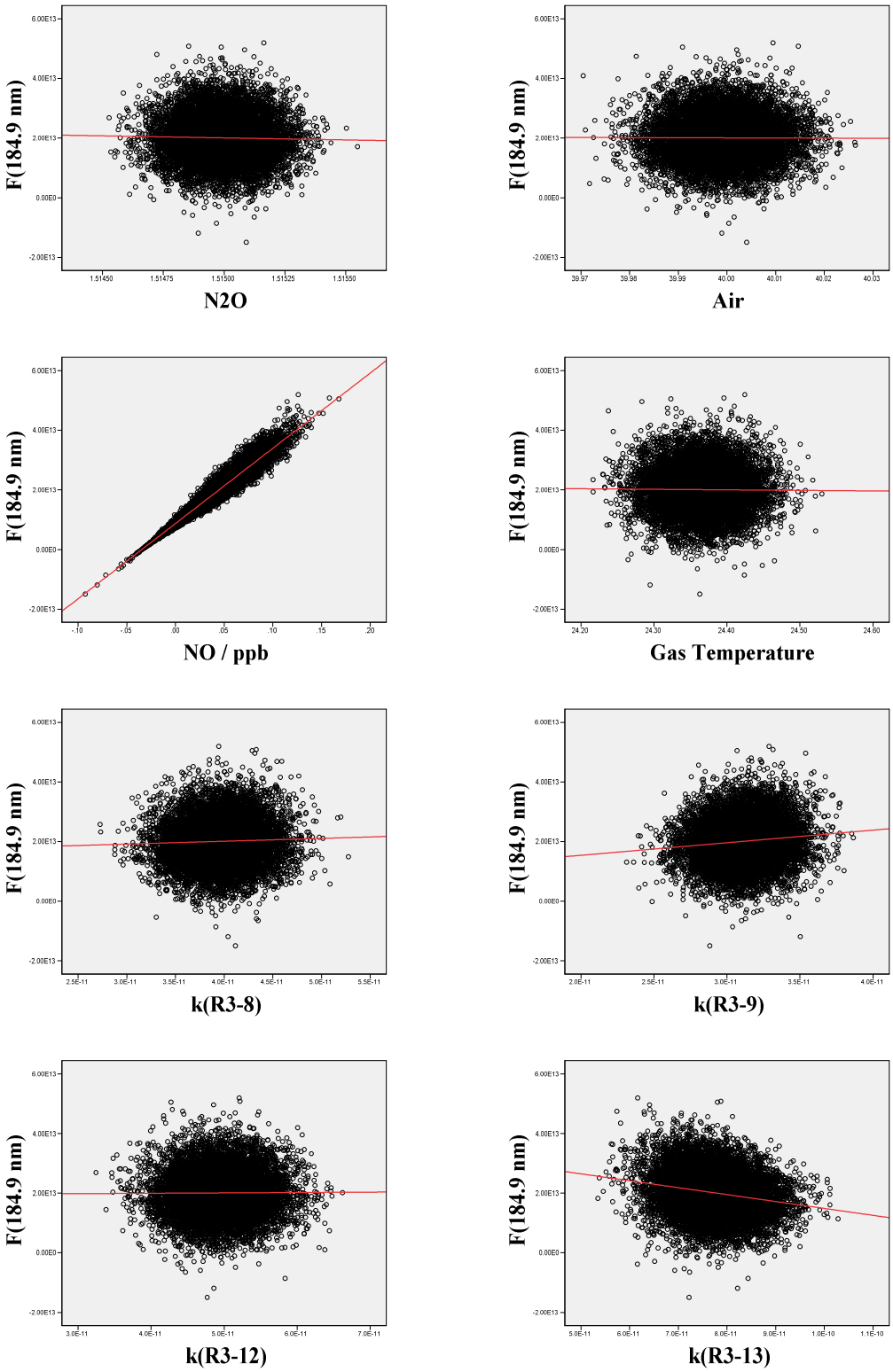

Figure 3-16: Correlation plots for $F_{184.9\ nm}$ against all parameters used for the determination of $F_{184.9\ nm}$. Lamp current was kept constant at 1.65 mA. $F_{184.9\ nm}$ was determined using JPL evaluated rate coefficients (Sander *et al.* 2011). Experimental measurements were carried out at 3.7% N_2O. Solid red lines represent linear least squares fit to the data. $R^2(N_2O)$ = 0.001, R^2(Air) = 0.000, R^2(NO) = 0.930, R^2(Gas Temperature) = 0.000, $R^2(k_{R\ 3\text{-}8})$ = 0.002, $R^2(k_{R\ 3\text{-}9})$ = 0.013, $R^2(k_{R\ 3\text{-}12})$ = 0.000, $R^2(k_{R\ 3\text{-}13})$ = 0.043.

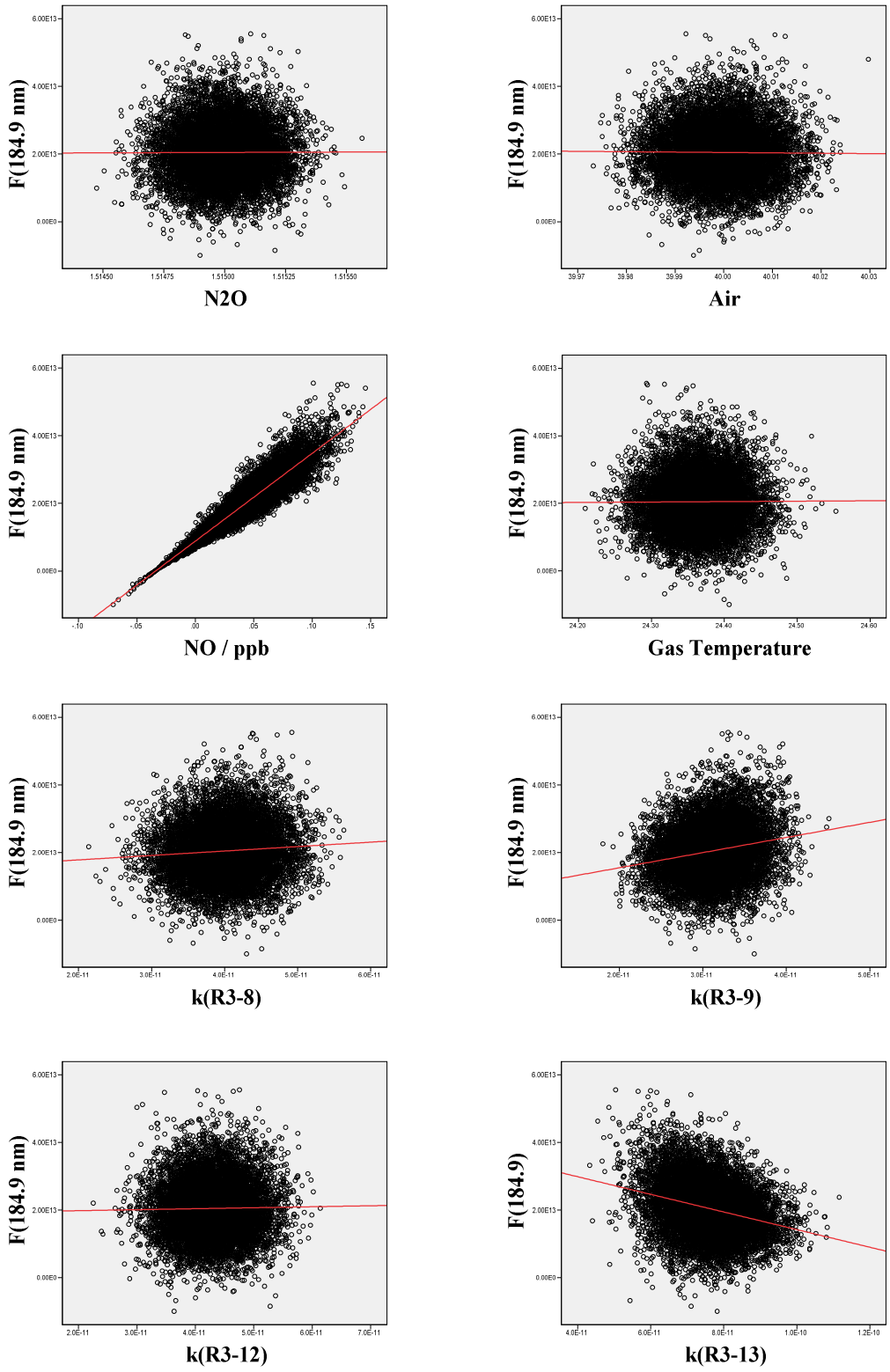

Figure 3-17: Correlation plots for $F_{184.9\,nm}$ against all parameters used for the determination of $F_{184.9\,nm}$. Lamp current was kept constant at 1.65 mA, $F_{184.9\,nm}$ was determined using IUPAC evaluated rate coefficients (Atkinson *et al.* 2004). Experimental measurements were carried out at 3.7% N_2O. Solid red lines represent linear least squares fit to the data. $R^2(N_2O) = 0.000$, $R^2(Air) = 0.000$, $R^2(NO) = 0.859$, $R^2(Gas\ Temperature) = 0.000$, $R^2(k_{R\,3\text{-}8}) = 0.006$, $R^2(k_{R\,3\text{-}9}) = 0.040$, $R^2(k_{R\,3\text{-}12}) = 0.000$, $R^2(k_{R\,3\text{-}13}) = 0.081$.

The R^2 values obtained from linear least squares fitting to the data gives an estimate to the contribution of each parameter to the variation in $F_{184.9\,nm}$, where an R^2 value of 0.843 would indicate that the variation in that specific parameter contributes roughly 84.3% to the variation in the determined value of $F_{184.9\,nm}$. A comparison of all R^2 values over a full range of lamp current values for $F_{184.9\,nm}$ determined with both JPL evaluated rate coefficients (Sander *et al.* 2011) and IUPAC evaluated rate coefficients (Atkinson *et al.* 2004) is given in Table 3-6, where measurements were carried out at a total of 3.7% N_2O in air. In all cases, the correlation between the NO and $F_{184.9\,nm}$ was greatest, $R^2 = 0.461$ - 0.991. For values of $F_{184.9\,nm}$ determined using the IUPAC evaluated rate coefficients (Atkinson *et al.* 2004) the correlation between $F_{184.9\,nm}$ and NO is typically lower as compared to those determined using the JPL evaluated rate coefficients (Sander *et al.* 2011); with the correlation between the four rate coefficients used in the determination of $F_{184.9\,nm}$ observed to be greater for the IUPAC values than the JPL values. The greatest correlation between $F_{184.9\,nm}$ and the rate coefficients is seen for $k_{R\ 3\text{-}12}$, for both IUPAC and JPL evaluated rate coefficients, this is unsurprising considering the error in $k_{R\ 3\text{-}12}$ is greatest for both the JPL and IUPAC values (~12% error in $k_{R\ 3\text{-}12}$ for IUPAC recommended value at 293 K and ~10% error in $k_{R\ 3\text{-}12}$ for JPL recommended value at 293 K).

The contribution to the variation in $F_{184.9\,nm}$ from NO, $k_{R\ 3\text{-}8}$, $k_{R\ 3\text{-}9}$ and $k_{R\ 3\text{-}12}$ was seen to increase to a maximum at a lamp current of 2.62 mA and then decrease slightly at the maximum lamp current. This indicates that at the maximum lamp current here, the error in $F_{184.9\,nm}$ is becoming influenced more significantly by some other factor or factors. It is known that at lamp currents greater than ~3 mA, that the lamp flux no longer follows a linear trend.

	R^2 (JPL)	R^2 (IUPAC)	R^2 (JPL)	R^2 (IUPAC)	R^2 (JPL)	R^2 (IUPAC)	R^2 (JPL)	R^2 (IUPAC)	R^2 (JPL)	R^2 (IUPAC)	R^2 (JPL)	R^2 (IUPAC)
Lamp Current / mA	0.004 ± 0.06		0.94 ± 0.06		1.65 ± 0.08		2.02 ± 0.09		2.62 ± 0.07		3.03 ± 0.06	
Lamp Temperature / °C	37.33 ± 0.02		39.71 ± 0.08		40.32 ± 0.15		41.16 ± 0.06		42.28 ± 0.04		42.82 ± 0.14	
Gas Temperature / ° C	24.56 ± 0.08		24.23 ± 0.06		24.37 ± 0.04		24.05 ± 0.04		24.12 ± 0.05		24.34 ± 0.07	
N_2O	0.001	0.000	0.000	0.000	0.001	0.000	0.000	0.000	0.000	0.000	0.000	0.000
Air	0.000	0.000	0.000	0.000	0.000	0.000	0.000	0.000	0.000	0.000	0.000	0.000
NO	0.991	0.981	0.962	0.927	0.930	0.859	0.722	0.626	0.629	0.461	0.773	0.605
Gas Temperature	0.000	0.000	0.000	0.000	0.000	0.000	0.000	0.000	0.000	0.000	0.000	0.000
$k_{R\ 3\text{-}8}$	0.000	0.000	0.001	0.003	0.002	0.006	0.007	0.016	0.015	0.018	0.005	0.010
$k_{R\ 3\text{-}9}$	0.000	0.000	0.006	0.019	0.013	0.040	0.049	0.121	0.076	0.165	0.043	0.108
$k_{R\ 3\text{-}12}$	0.000	0.000	0.000	0.000	0.000	0.000	0.000	0.001	0.001	0.000	0.001	0.001
$k_{R\ 3\text{-}13}$	0.000	0.000	0.019	0.039	0.043	0.081	0.177	0.216	0.262	0.343	0.164	0.149

Table 3-6: Comparison of R^2 values taken from correlation plots of $F_{184.9\,nm}$ against all parameters required for the determination of $F_{184.9\,nm}$ using both the JPL evaluate rate coefficients (Sander *et al.* 2011) and the IUPAC evaluate rate coefficients (Atkinson *et al.* 2004) for a full range of lamp currents, where the lamp current was kept at a constant value for the error analysis. Lamp current, lamp temperature and gas temperature values are all taken from the average experimental measurement values, where the error is the standard deviation in the measurements. Measurements were taken at 3.7% N_2O.

The Monte Carlo method of error propagation has demonstrated its potential in the investigation into the sources of error associated with the N_2O actinometry method for the determination of $F_{184.9\,nm}$. The variation in the measurement of [NO] has been shown to have the most significant influence on the variation of the determined value of $F_{184.9\,nm}$. The error in the measurement of [NO] in the N_2O actinometry method for the determination of $F_{184.9\,nm}$ is dependent on the calibration of the chemiluminescence NO_x analyser employed. Three chemiluminescence NO_x analysers have been used here in the determination of $F_{184.9\,nm}$ (Section 3.4.2), showing no discernible difference in the gradient of the linear least squares fit to the determined $F_{184.9\,nm}$ against the measured lamp current. Differences in the calibration factors for the three NO_x analysers were observed, with the container NO_x analyser having a lower C_{NO} than the HIRAC and aircraft NO_x analysers (Table 3-3). Further Monte Carlo simulations, with random number sets generated from the averages and standard deviations taken from measurements using the three different chemiluminescence NO_x analysers would give further insight into the influence of variance from the measured [NO] on the variation in the determination of $F_{184.9\,nm}$.

The Monte Carlo error simulations described here are generated from only one set of averaged experimental parameters and their standard deviations. In order to fully determine whether the variation in the determined value of $F_{184.9\,nm}$ is most significantly influenced by the variation in measured [NO] across a range of N_2O percentages, further simulations would be required, with correlations being made between $F_{184.9\,nm}$ and all the parameters used in its determination.

3.5 Alternative HIRAC Calibrations

The HIRAC chamber is ideally suited for carrying out alternative methods for the calibration of FAGE instrumentation; allowing for both pressure and temperature dependent calibrations to be investigated. Pressure dependent calibrations of the HIRAC FAGE instrument have been previously reported (Winiberg *et al.* 2015), where an increase in sensitivity in both the OH and HO_2 cells of the instrument was observed; ΔC_{OH} = (17 ± 11)% and ΔC_{HO2} = (31.6 ± 4.4)% increase per mbar air pressure over an external pressure range of 440 – 1000 mbar, giving an internal cell pressure of 1.42 - 3.8 mbar. This pressure dependence of the HIRAC FAGE instrument was also compared to a pressure dependent “wand” calibration, where the internal pressure of the instrument was altered with the use of different sized pinholes on the inlet. As mentioned previously, changing the pinhole size may alter the flow dynamics within the flow tube

of the instrument, and hence influence the sensitivity of the instrument for the detection of OH and HO_2 radicals. Good agreement was observed between the calibrations for the FAGE instrument sensitivity as a function of pressure; $C_{OH(\text{“wand”})}/C_{OH(HIRAC)} = 1.19 \pm 0.26$ and $C_{HO2(\text{“wand”})} / C_{HO2(HIRAC)} = 0.96 \pm 0.18$, implying that the flow within the instrument was not significantly influenced by the size of the pinhole (Winiberg *et al.* 2015). Within the HIRAC chamber, OH calibrations were carried out using the hydrocarbon decay method as previously described (Hard *et al.* 1995, Bloss *et al.* 2004, Dusanter *et al.* 2008), following the decay of cyclohexane, *n*-pentane and *iso*-butene from their reaction with OH radicals. A comparison of the pressure dependence for the OH cell calibration of the HIRAC FAGE instrument is given in Figure 3-18.

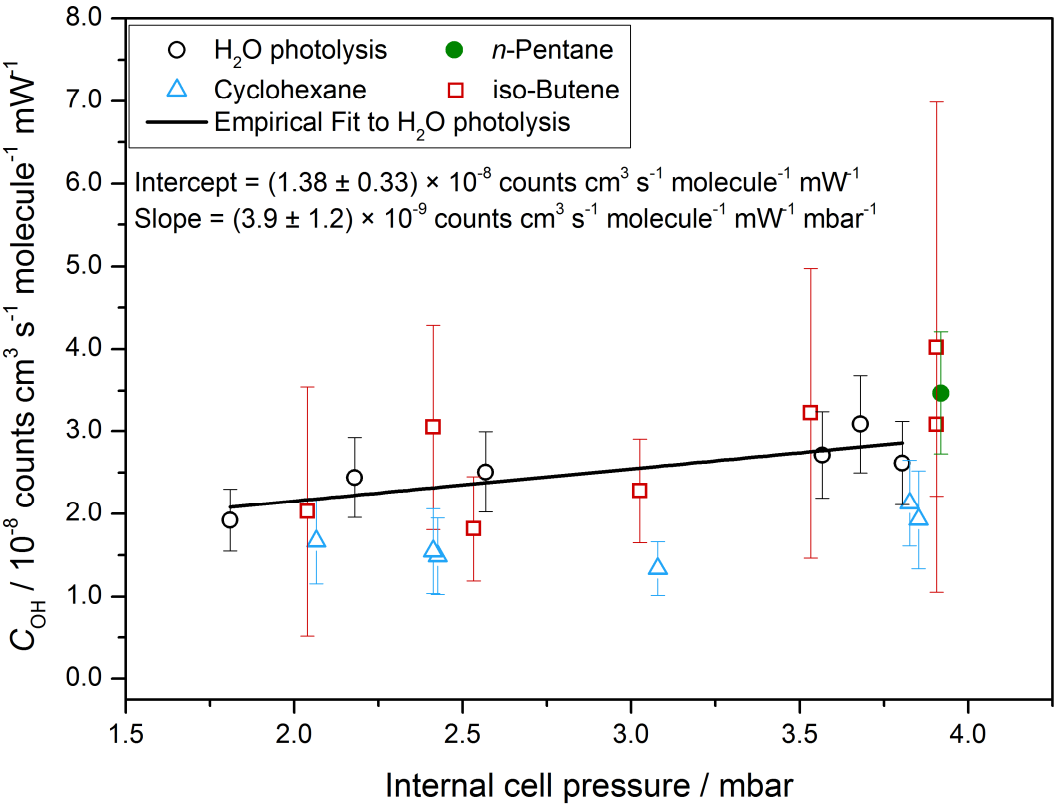

Figure 3-18: Comparison of internal cell pressure dependence of conventional “wand” calibration with HIRAC hydrocarbon decay calibration for the OH cell of the HIRAC FAGE instrument, taken from Winiberg et al. (2015).

Calibration of the FAGE HO_2 cell within HIRAC can be achieved using the well-defined self-reaction of HO_2. HCHO is photolysed to produce HO_2 radicals in a steady state, once the photolysis lamps are switched off, the HO_2 recombination reaction can be followed from the loss of HO_2 within the chamber. Comparison of the pressure dependence for the HO_2 cell calibration of the HIRAC FAGE instrument between the conventional “wand” calibration method and the HCHO photolysis method is given in Figure 3-19.

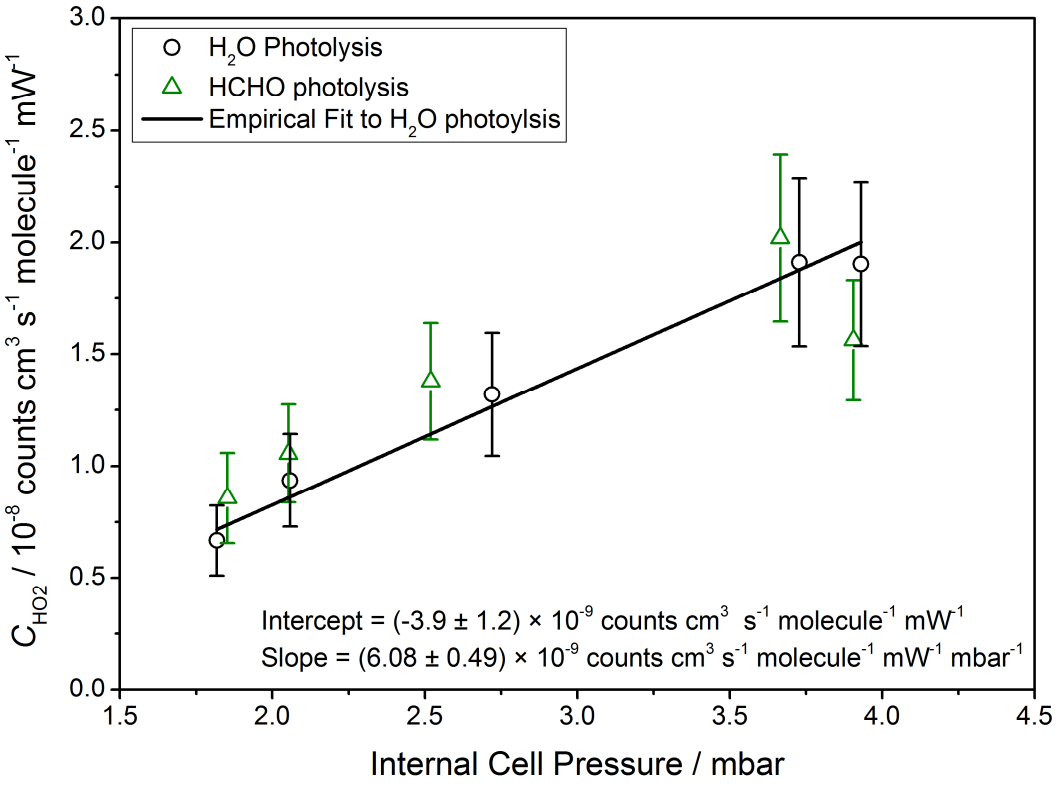

Figure 3-19: Comparison of internal cell pressure dependence of conventional "wand" calibration with HIRAC HCHO photolysis calibration method for the HO_2 cell of the HIRAC FAGE instrument, taken from Winiberg *et al.* (2015).

Good agreement between the HIRAC calibration methods and the conventional "wand" method for calibrating the HIRAC FAGE instrument gives further validation to the suitability of the conventional "wand" calibration method. In the following section (3.5.1), results from temperature dependent calibrations of the HIRAC FAGE HO_2 cell are described following the HO_2 self-reaction utilising the HIRAC chamber. These results are compared with those previously reported by Winiberg (2014) for the sensitivity of the HO_2 cell as a function of temperature as determined with the conventional "wand" calibrations.

3.5.1 HO_2 Temperature Dependent Calibration

The temperature dependence of the sensitivity of the HO_2 cell was investigated following the HCHO photolysis method for the HIRAC FAGE calibration. The sensitivity of the HO_2 cell as a function of temperature has been reported previously by Winiberg (2014) using the conventional "wand" method, where an increase of $\Delta C_{HO2} = (0.29 \pm 0.42)\%$ per Kelvin was observed, shown in Figure 3-20.

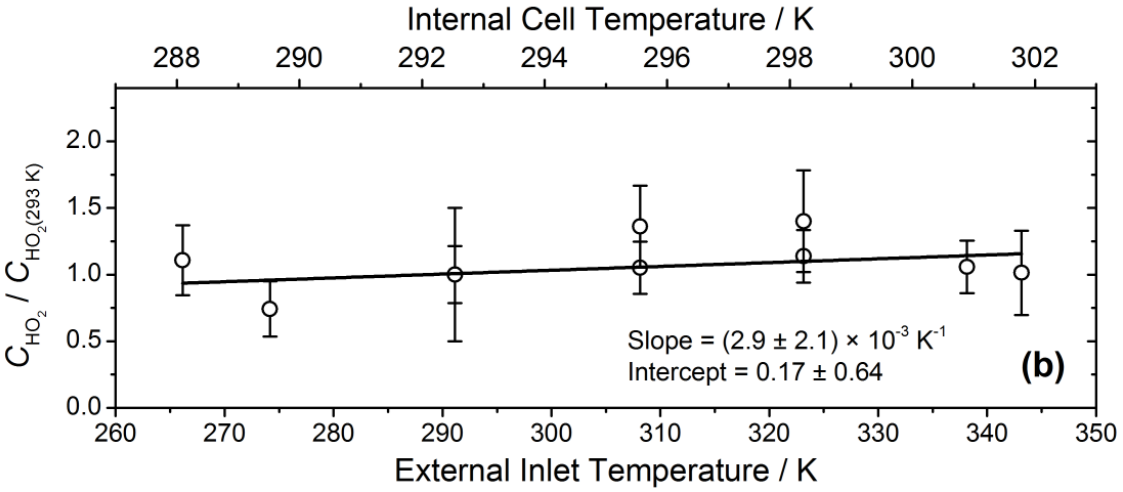

Figure 3-20: Sensitivity of the HIRAC FAGE OH cell as a function of temperature following the conventional "wand" calibration method, at a constant internal cell pressure of 3.81 ± 0.02 mbar and $[H_2O]_{vap}$ of 2000 ± 300 ppmv, adapted from Winiberg (2014). Internal cell temperature was determined through temperature profile experiments within the HO_2 cell prior to the calibrations.

HIRAC was set to the desired temperature using the Huber temperature control system as described in Chapter 2 and the temperature range 273 – 343 K was studied. For each experiment, HIRAC was filled with 800 mbar N_2 (BOC, 99.998% purity) and 200 mbar O_2 (BOC, 99.999% purity). HCHO, (1.10 – 2.20) × 10^{13} molecule cm^{-3}, was introduced into the chamber by the heating of paraformaldehyde powder (Sigma Aldrich, 99% purity). Photolysis lamps (Philips, TL40W/12 RS) with a maximum output at ~300 nm were repeatedly switched on and off in order to record several HO_2 decay profiles for one fill of chamber. Upon irradiation of the chamber, HO_2 was rapidly formed; once a stable concentration was reached, the photolysis lamps were switched off and the resultant decay of HO_2 radicals was monitored using the HIRAC FAGE instrument for approximately three minutes until near background levels of HO_2 signal were observed. This process was repeated three times with the mixing fans switched on and three times with the mixing fans switched off for each fill of the chamber; allowing for C_{HO2} to be determined six times for each chamber fill.

Reactions R 3-16 to R 3-22 describe the processes occurring in the HCHO photolysis for the HO_2 calibration of FAGE within the HIRAC chamber. Photolysis of HCHO produces H and HCO (R 3-16) and H_2 and CO (R 3-17) in approximately 60:40 ratio (Carbajo *et al.* 2008). In the presence of O_2, H subsequently reacts with O_2 to produce HO_2 radicals (R 3-19). Once the photolysis lamps have been switched off, the HO_2 radicals can be lost via their self-reaction (R 3-20 and R 3-21), or by loss to the walls of the chamber and dilution of HIRAC (R 3-22).

$HCHO + h\nu \rightarrow H + HCO$ R 3-16

$HCHO + h\nu \rightarrow H_2 + CO$ R 3-17

$HCO + O_2 \rightarrow HO_2 + CO$ R 3-18

$H + O_2 + M \rightarrow HO_2 + M$ R 3-19

$HO_2 + HO_2 \rightarrow H_2O_2 + O_2$ R 3-20

$HO_2 + HO_2 + M \rightarrow H_2O_2 + O_2 + M$ R 3-21

$HO_2 \rightarrow$ Loss R 3-22

The rate of loss of HO_2 radicals can be described by Eq. 3-8:

$$\frac{d[HO_2]}{dt} = -\left(k_{loss}[HO_2] + 2k_{HO_2+HO_2}[HO_2]^2\right) \quad \text{Eq. 3-8}$$

where $k_{HO2+HO2}$ is the sum of the pressure dependent (R 3-21) and pressure independent (R 3-20) rate coefficients for the HO_2 recombination reaction, as defined by Atkinson *et al.* (2004). k_{loss} is the combined dilution and wall loss rate of HO_2 from HIRAC. Integrating Eq. 3-8 with respect to time, t, gives Eq. 3-9:

$$\frac{1}{[HO_2]_t} = \left(\frac{1}{[HO_2]_{t_0}} + \frac{2k_{HO_2+HO_2}}{k_{loss}}\right) e^{(k_{loss}t)} - \left(\frac{2k_{HO_2+HO_2}}{k_{loss}}\right) \quad \text{Eq. 3-9}$$

As described previously by Eq. 3-3, the $[HO_2]$ is related to the normalised HO_2 signal, S_{HO2}, measured with the FAGE instrument, and the HO_2 sensitivity, C_{HO2}. It is not necessary to know $[HO_2]$ as Eq. 3-3 can be substituted into Eq. 3-9:

$$\left(S_{HO_2}\right)_t = \left\{\left(\frac{1}{\left(S_{HO_2}\right)_{t_0}} + \frac{2k_{HO_2+HO_2}}{k_{loss}C_{HO_2}}\right) e^{(k_{loss}t)} - \left(\frac{2k_{HO_2+HO_2}}{k_{loss}C_{HO_2}}\right)\right\}^{-1} \quad \text{Eq. 3-10}$$

where $(S_{HO2})_t$ is the HO_2 signal at time t and $(S_{HO2})_{t0}$ is the HO_2 signal at t_0; Eq. 3-10 can be fitted to the normalised HO_2 signal measured by the FAGE instrument in order to determine a value of C_{HO2} and of k_{loss}. The value of k_{loss} is dependent on the daily conditions of the chamber walls and temperature of the chamber, and so is determined by the fitting process. The value of k_{loss} can be constrained by the use of global fitting for each different temperature measurement where the HO_2 decay profiles were fitted using a global fitting routine in order for k_{loss} to be kept constant for all fits to Eq. 3-10. With the mixing fans off, the decay of HO_2 can be described by a linear fit, Eq. 3-11:

$$\left(S_{HO_2}\right)_t = \frac{1}{\left(S_{HO_2}\right)_{t0}} + \left(\frac{2k_{HO_2+HO_2}t}{C_{HO_2}}\right)^{-1} \quad \text{Eq. 3-11}$$

The measurements described here for the HO_2 recombination are from experiments carried out with the chamber mixing fans switched on as this is representative of typical experimental chamber conditions.

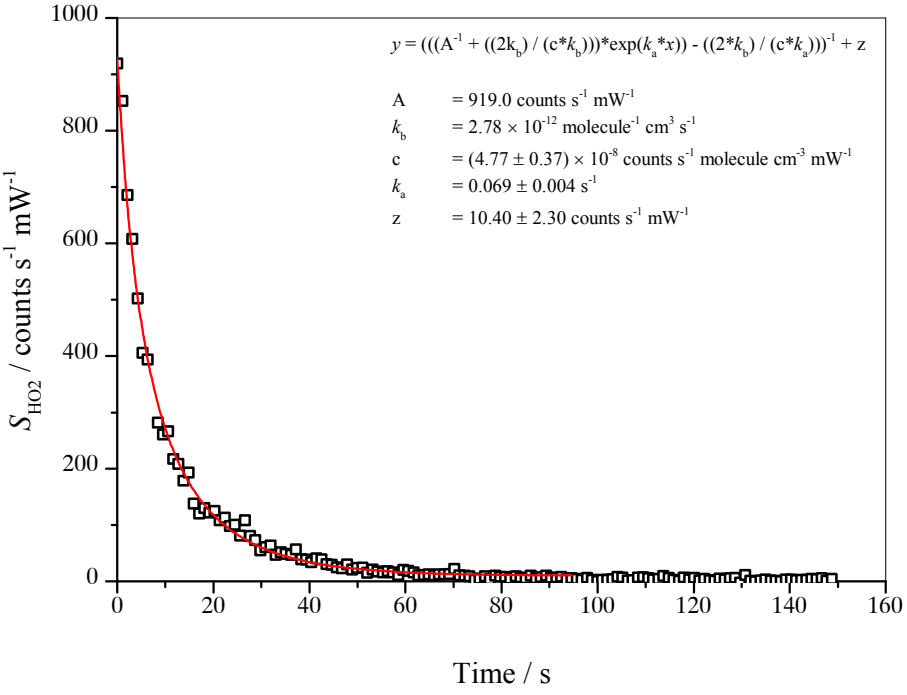

Figure 3-21: Normalised S_{HO2} decay following the HO_2 recombination reaction at 1000 mbar total chamber pressure and ~293K. Data were fitted using Eq. 3-10 to determine C_{HO2}, where $A = (S_{HO2})_{t0}$, $k_b = k_{HO2+HO2}$, c = C_{HO2}, $k_a = k_{loss}$ and z = offset, with uncertainties given to ±1σ. Parameters with no errors were fixed in the fitting procedure.

It was not possible to carry out the HIRAC FAGE HO_2 temperature dependent calibrations at the same time as the HO_2 "wand" temperature dependent calibrations were carried out, and so, for comparison, calibration factors have been scaled so that C_{HO2} determined at 293 K from both methods are in agreement. "Wand" calibrations carried out immediately following the HO_2 HIRAC FAGE temperature dependent studies were seen to be in excellent agreement with the HCHO photolysis method for determining C_{HO2}, $C_{HO2("wand")} = (3.38 \pm 1.18) \times 10^{-8}$ counts cm^3 molecule^{-1} mW^{-1} s^{-1} at 293 K as compared to $C_{HO2(HIRAC)} = (3.69 \pm 1.50) \times 10^{-8}$ counts cm^3 molecule^{-1} mW^{-1} s^{-1} at 293 K. The corresponding internal HO_2 cell temperatures to the HIRAC temperatures, determined from temperature profiles determined previously during the study of the

"wand" calibration as a function of temperature, are shown on the bottom *x*-axis, and the HIRAC temperatures are shown on the top *x*-axis.

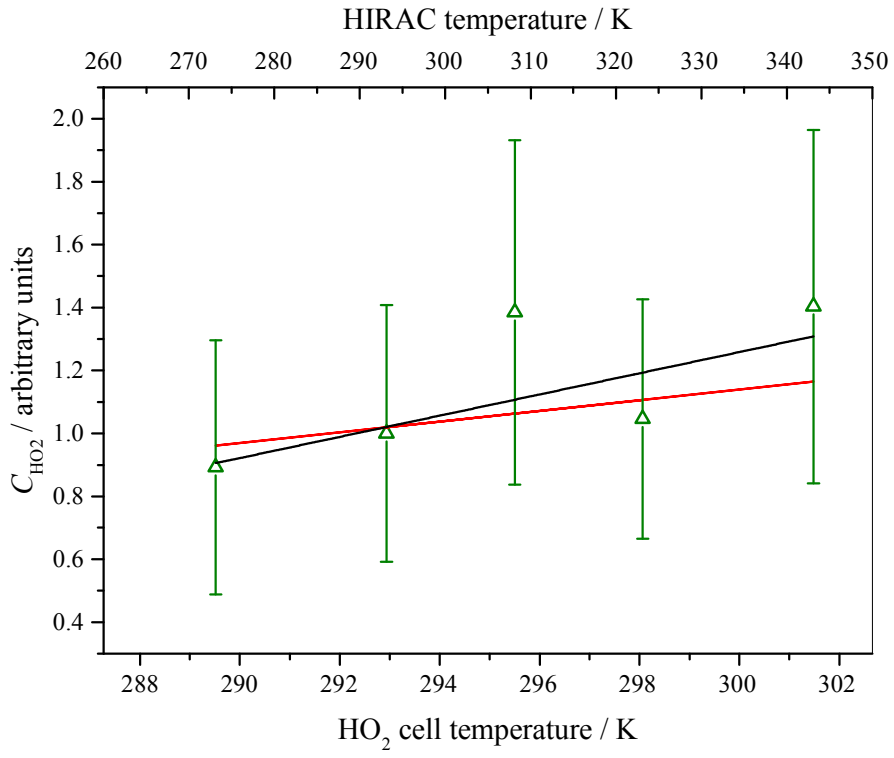

Figure 3-22: Comparison of HO_2 cell sensitivity as a function of temperature. Green triangles represent HO_2 sensitivity as a function of temperature as determined following the HO_2 recombination reaction, where error bars represent the total uncertainty to 1σ. The black line represents the linear least squares fit to the data, where the gradient is $(3.37 \pm 1.89) \times 10^{-2}$ K^{-1} for HO_2 cell temperature and $(5.76 \pm 3.23) \times 10^{-3}$ K^{-1} for HIRAC temperature. The red line represents the HO_2 cell sensitivity as a function of temperature as determined from the "wand" calibration method, reported by Winiberg (2014).

Good agreement between the "wand" and alternative methods for determining the sensitivity of the HO_2 cell as a function of temperature was observed; $\Delta C_{HO2(HIRAC)} = (0.34 \pm 0.19)$ % and $\Delta C_{HO2("wand")} = (0.29 \pm 0.42)$ % increase per Kelvin for the internal HO_2 cell temperature. It should be noted that the internal HO_2 cell temperature was determined from temperature profiles carried out at the time of the HO_2 "wand" calibration temperature dependence experiments; temperature profiles of the HO_2 cell should be measured whilst sampling from HIRAC at different temperatures in order to determine whether the temperature profiles used here are appropriate. The agreement between the two methods of calibration would indicate that the HO_2 cell temperature profile during HIRAC temperature dependent studies is similar to that determined for "wand" calibrations.

3.5.2 Error Analysis

Each data point in Figure 3-22 is an average of several C_{HO2} values determined through global fitting of Eq. 3-10 to the data at each temperature. The error bars represent the standard deviation of the averages, and the total uncertainty in the calibration. The factors contributing to the total uncertainty of the calibration are given in Table 3-7.

Parameter	**Uncertainty**
$k_{HO2 + HO2(273\ K)}$	31%
$k_{HO2 + HO2(293\ K)}$	27%
$k_{HO2 + HO2(308\ K)}$	24%
$k_{HO2 + HO2(323\ K)}$	21%
$k_{HO2 + HO2(343\ K)}$	19%
$S_{(HO2)t0}$	30%
Laser power	8%
Online position	2%

Table 3-7: Summary of uncertainties contributing to the total overall uncertainty in the HCHO photolysis method for HO_2 calibrations using the HIRAC chamber.

The error in $k_{HO2 + HO2}$ was taken from the IUPAC recommended temperature dependent values (Atkinson *et al.* 2004), the error in $S_{(HO2)t0}$ was determined, as described by Winiberg (2014) from the standard deviation of the offline signal, uncertainty in laser power and online position are taken as described in Section 3.3.1. The total uncertainty in the HCHO photolysis calibration method was estimated to be 36 – 44%.

The HCHO calibration method is extremely useful in validating the conventional "wand" calibration method for the temperature dependent calibration of FAGE instrumentation. The experimental procedure is relatively quick to carry out, and the ability to measure $C_{HO2(HIRAC)}$ several times in one experimental run is highly advantageous. Further temperature dependence of the HO_2 cell calibration, particularly at lower temperatures would help to refine the sensitivity to HO_2 as a function of temperature, still within a tropospherically relevant range of temperatures.

3.6 Conclusions and Future Work

A detailed study into the reproducibility and errors associated with the N_2O actinometry method for the determination of $F_{184.9\ nm}$, which is required in the conventional "wand" calibration of FAGE instrumentation, has been given. No discernible difference was observed between any of the apparatus used in the comparison study, giving increased confidence in the experimental procedure for the determination of $F_{184.9\ nm}$. It has been shown that the variation in the measured [NO] during the N_2O actinometry experiment is most significant in the variation of the final calculated value of $F_{184.9\ nm}$ following Monte Carlo simulation for the error propagation. Some trend is observed between the lamp current and the influence on the variation of $F_{184.9\ nm}$ from the error in $k_{R3\text{-}9}$ and $k_{R3\text{-}13}$ when using both the IUPAC and JPL recommended values of the rate coefficients; an increase in the influence from the rate coefficient error on the variation in the determined $F_{184.9\ nm}$ was seen with increasing lamp current. Further Monte Carlo simulations taken from a wider range of experimental measurements would assist in determining the relationship between the errors in the rate coefficients and the variation in the determined value of $F_{184.9\ nm}$. Increasing the percentage N_2O in the total gas flow for the experimental procedure typically shows no discernible difference to the determination of $F_{184.9\ nm}$; Monte Carlo simulations of the errors over a range of N_2O percentages would verify whether the variation in N_2O flow at different N_2O percentages has any influence on the variation in the determination of $F_{184.9\ nm}$.

As the variation in the measurement of [NO] is seen to have the most significant influence on the variation in the determined $F_{184.9}$ nm, alternative methods of measuring [NO] in the N_2O actinometry procedure may give rise to smaller errors in the determination of $F_{184.9\ nm}$. The use of an instrument for the measurement of [NO] able to measure lower concentrations with higher accuracy would reduce the influence of the variation from [NO] measurements on the determination of $F_{184.9\ nm}$.

The N_2O actinometry experimental procedure is routinely carried out at room temperature (~298 K). Determination of $F_{184.9\ nm}$ over a range of temperatures, similar to those studied for the temperature dependent calibrations, would give further validation of the temperature dependence observed for the sensitivity of the HIRAC FAGE instrument.

Similar error analysis to that done here for the N_2O actinometry experimental procedure would assist in determining which parameters have the most significant influence on the variation in the determination of C_{HOx}.

The first temperature dependent calibration of a FAGE instrument for HO_2 has been carried out using an alternative calibration method, with excellent agreement between the conventional "wand" calibration method and the alternative HIRAC HCHO photolysis method. Work is ongoing into the temperature dependent OH calibration of the HIRAC FAGE instrument for comparison between the alternative hydrocarbon decay method with the conventional "wand" method for calibration. Very good agreement, $\Delta C_{HO2(HIRAC)}$ = (0.34 ± 0.19) % and $\Delta C_{HO2("wand")}$ = (0.29 ± 0.42) % increase per Kelvin, was observed between the two methods for determining the sensitivity of the HO_2 cell as a function of temperature. The small temperature dependence observed following the HCHO photolysis method of calibration is within the uncertainty of the conventional "wand" calibration method, of 22% for the HO_2 cell calibration, and can be considered to be insignificant for the temperature range studied here (273 – 343 K). Temperature profiles for both the OH and HO_2 cells should be determined whilst sampling from the HIRAC chamber over a similar range of temperatures as has been described here for the HCHO photolysis calibration method, and for the previous "wand" calibration study. This would provide validation of the temperature profiles used in this work, and further validation of the HCHO method for determining the sensitivity of the HO_2 FAGE cell as a function of temperature. Work on the sensitivity of the OH FAGE cell as a function of temperature, determined by alternative HIRAC calibration methods is ongoing.

3.7 References

Amedro, D., Miyazaki, K., Parker, A., Schoemaecker, C. and Fittschen, C. (2012). "Atmospheric and kinetic studies of OH and HO_2 by the FAGE technique." Journal of Environmental Sciences **24**(1): 78-86.

Atkinson, R., Baulch, D. L., Cox, R. A., Crowley, J. N., Hampson, R. F., Hynes, R. G., Jenkin, M. E., Rossi, M. J. and Troe, J. (2004). "Evaluated kinetic and photochemical data for atmospheric chemistry: Volume I - gas phase reactions of O_x, HO_x, NO_x and SO_x species." Atmospheric Chemistry and Physics **4**(6): 1461-1738.

Bloss, W. J., Lee, J. D., Bloss, C., Heard, D. E., Pilling, M. J., Wirtz, K., Martin-Reviejo, M. and Siese, M. (2004). "Validation of the calibration of a laser-induced fluorescence instrument for the measurement of OH radicals in the atmosphere." Atmospheric Chemistry and Physics **4**(2): 571-583.

Cantrell, C. A., Zimmer, A. and Tyndall, G. S. (1997). "Absorption cross sections for water vapor from 183 to 193 nm." Geophysical Research Letters **24**(17): 2195-2198.

Carbajo, P. G., Smith, S. C., Holloway, A.-L., Smith, C. A., Pope, F. D., Shallcross, D. E. and Orr-Ewing, A. J. (2008). "Ultraviolet Photolysis of HCHO: Absolute HCO Quantum Yields by Direct Detection of the HCO Radical Photoproduct." The Journal of Physical Chemistry A **112**(48): 12437-12448.

Commane, R. (2009). Understanding Radical Chemistry Throughout the Troposphere using Laser-Induced Fluorescence Spectroscopy. PhD, The University of Leeds.

Commane, R., Floquet, C. F. A., Ingham, T., Stone, D., Evans, M. J. and Heard, D. E. (2010). "Observations of OH and HO_2 radicals over West Africa." Atmospheric Chemistry and Physics **10**(18): 8783-8801.

Creasey, D. J., Heard, D. E. and Lee, J. D. (2000). "Absorption cross-section measurements of water vapour and oxygen at 185 nm. Implications for the calibration of field instruments to measure OH, HO_2 and RO_2 radicals." Geophysical Research Letters **27**(11): 1651-1654.

Dusanter, S., Vimal, D. and Stevens, P. S. (2008). "Technical note: Measuring tropospheric OH and HO_2 by laser-induced fluorescence at low pressure. A comparison of calibration techniques." Atmospheric Chemistry and Physics **8**(2): 321-340.

Dusanter, S., Vimal, D., Stevens, P. S., Volkamer, R. and Molina, L. T. (2009). "Measurements of OH and HO_2 concentrations during the MCMA-2006 field campaign – Part 1: Deployment of the Indiana University laser-induced fluorescence instrument." Atmospheric Chemistry and Physics **9**(5): 1665-1685.

Faloona, I., Tan, D., Lesher, R., Hazen, N., Frame, C., Simpas, J., Harder, H., Martinez, M., Di Carlo, P., Ren, X. and Brune, W. (2004). "A Laser-induced Fluorescence Instrument for Detecting Tropospheric OH and HO_2: Characteristics and Calibration." Journal of Atmospheric Chemistry **47**(2): 139-167.

Fuchs, H., Bohn, B., Hofzumahaus, A., Holland, F., Lu, K. D., Nehr, S., Rohrer, F. and Wahner, A. (2011). "Detection of HO_2 by laser-induced fluorescence: calibration and interferences from RO_2 radicals." Atmospheric Measurement Techniques **4**(6): 1209-1225.

Glowacki, D. R., Goddard, A., Hemavibool, K., Malkin, T. L., Commane, R., Anderson, F., Bloss, W. J., Heard, D. E., Ingham, T., Pilling, M. J. and Seakins, P. W. (2007). "Design of and initial results from a Highly Instrumented Reactor for Atmospheric Chemistry (HIRAC)." Atmospheric Chemistry and Physics **7**(20): 5371-5390.

Hard, T. M., George, L. A. and O'Brien, R. J. (1995). "FAGE Determination of Tropospheric HO and HO_2." Journal of the Atmospheric Sciences **52**(19): 3354-3372.

Hard, T. M., Obrien, R. J., Cook, T. B. and Tsongas, G. A. (1979). "Interference Suppression in HO Fluorescence Detection." Applied Optics **18**(19): 3216-3217.

Kanaya, Y., Sadanaga, Y., Hirokawa, J., Kajii, Y. and Akimoto, H. (2001). "Development of a Ground-Based LIF Instrument for Measuring HO_x Radicals: Instrumentation and Calibrations." Journal of Atmospheric Chemistry **38**(1): 73-110.

Malkin, T. L. (2010). Detection of Free-Radicals and Other Species to Investigate Atmospheric Chemistry in the HIRAC Chamber. PhD, University of Leeds.

Metropolis, N. and Ulam, S. (1949). "The Monte Carlo Method." Journal of the American Statistical Association **44**(247): 335-341.

Sander, S. P., Friedl, R. R., Abbatt, J. P. D., Barker, J., Golden, D. M., Kolb, C. E., Kurylo, M. J., Moortgat, G. K., Wine, P. H., Huie, R. E. and Orkin, V. L. (2011). Chemical kinetics and photochemical data for use in atmospheric studies - Evaluation 17. Pasadena CA, Jet Propulsion Laboratory. **17**.

Wennberg, P. O., Cohen, R. C., Hazen, N. L., Lapson, L. B., Allen, N. T., Hanisco, T. F., Oliver, J. F., Lanham, N. W., Demusz, J. N. and Anderson, J. G. (1994). "Aircraft-borne, laser-

induced fluorescence instrument for the in situ detection of hydroxyl and hydroperoxyl radicals." Review of Scientific Instruments **65**(6): 1858-1876.

Whalley, L. K., Blitz, M. A., Desservettaz, M., Seakins, P. W. and Heard, D. E. (2013). "Reporting the sensitivity of laser-induced fluorescence instruments used for HO_2 detection to an interference from RO_2 radicals and introducing a novel approach that enables HO_2 and certain RO_2 types to be selectively measured." Atmospheric Measurement Techniques **6**(12): 3425-3440.

Whalley, L. K., Furneaux, K. L., Goddard, A., Lee, J. D., Mahajan, A., Oetjen, H., Read, K. A., Kaaden, N., Carpenter, L. J., Lewis, A. C., Plane, J. M. C., Saltzman, E. S., Wiedensohler, A. and Heard, D. E. (2010). "The chemistry of OH and HO_2 radicals in the boundary layer over the tropical Atlantic Ocean." Atmospheric Chemistry and Physics **10**(4): 1555-1576.

Whalley, L. K., Furneaux, K. L., Gravestock, T., Atkinson, H. M., Bale, C. S. E., Ingham, T., Bloss, W. J. and Heard, D. E. (2007). "Detection of iodine monoxide radicals in the marine boundary layer using laser induced fluorescence spectroscopy." Journal of Atmospheric Chemistry **58**(1): 19-39.

Winiberg, F. (2014). Characterisation of FAGE apparatus for HO_x detection and application in an environmental chamber. PhD, University of Leeds.

Winiberg, F. A. F., Smith, S. C., Bejan, I., Brumby, C. A., Ingham, T., Malkin, T. L., Orr, S. C., Heard, D. E. and Seakins, P. W. (2015). "Pressure-dependent calibration of the OH and HO_2 channels of a FAGE HO_x instrument using the Highly Instrumented Reactor for Atmospheric Chemistry (HIRAC)." Atmospheric Measurement Techniques **8**(2): 523-540.

Chapter 4. OH Reactivity Instrument Development

4.1 Introduction

The importance of OH reactivity measurements has been discussed in Chapter 1, with a comparison of the different types of instrumentation used for such measurements. This chapter is focussed on a detailed description of a laser flash photolysis coupled with laser induced fluorescence (LFP-LIF) instrument for the measurement of OH reactivity (k'_{OH}). Development of the LFP-LIF OH reactivity instrument is described in Section 4.3, where considerable improvement on the measurement capability is observed. Characterisation of instrument performance as a function of a range of parameters (photolysis flow tube pressure, cell pressure, $[O_3]$ and flow rate) is given, showing no discernible dependence on any of the parameters investigated under normal operating conditions.

Section 4.4 describes the development of the LFP-LIF OH reactivity instrument that was necessary to couple the instrument to the HIRAC chamber. This is the first time an OH reactivity instrument has been coupled to the HIRAC chamber for measurements of k'_{OH}. Validation of measurements taken whilst sampling from the HIRAC chamber are discussed through the measurement of the bimolecular rate coefficients of hydrocarbons with well-defined rate coefficients in the literature. The first measurements following a series of complex reactions within the HIRAC chamber are given in Chapter 8.

4.2 Instrumentation

4.2.1 Instrument Overview

A LFP-LIF instrument has been developed, based on the design first described by Sadanaga *et al.* (2004), at the University of Leeds as a field instrument. Previously a total OH loss rate method (TOHLM) instrument was used for the measurement of OH reactivity, described by Ingham *et al.* (2009). Full details of the LFP-LIF instrument have been given recently by Stone *et al.* (2016); a description of the instrument and measurement technique will be given here, focussing on its development and characterisation. A schematic of the LFP-LIF instrument is shown in Figure 4-1.

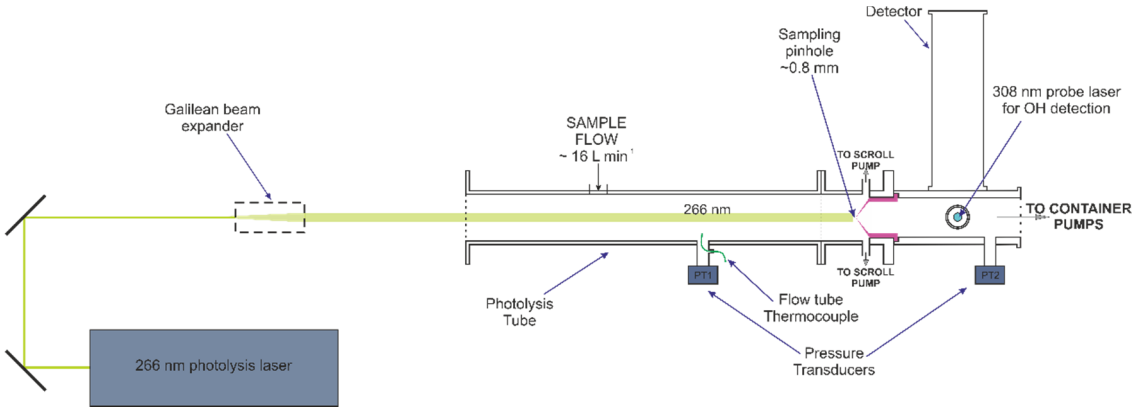

Figure 4-1: Schematic of the Leeds LFP-LIF OH reactivity instrument. The detector used is a channel photomultiplier (CPM). PT1 and PT2 are pressure transducers to measure the photolysis flow tube pressure and the FAGE cell pressure, respectively. The Galilean beam expander is a telescope used to expand the photolysis laser beam to ~1 cm diameter.

For field measurements, OH radicals are produced in the photolysis flow tube via the photolysis of ambient O_3 at 266 nm, which produces $O(^1D)$ in R 4-1. The $O(^1D)$ subsequently reacts with water vapour present in the air to produce two OH radicals, R 4-2. In laboratory experiments, O_3 is added to the sample flow, produced by the photolysis of O_2 in air (R 4-3 and R 4-4).

$$O_3 + h\nu_{(\lambda = 266\ nm)} \rightarrow O_2 + O(^1D) \qquad \text{R 4-1}$$

$$O(^1D) + H_2O \rightarrow 2OH \qquad \text{R 4-2}$$

$$O_2 + h\nu_{(\lambda = 184.9\ nm)} \rightarrow 2O(^3P) \qquad \text{R 4-3}$$

$$O(^3P) + O_2 \rightarrow O_3 \qquad \text{R 4-4}$$

The OH radicals then react with any OH reactive species present in the gas being sampled by the instrument, and the decay of the OH radical signal is detected in real time by LIF at 308 nm. The OH reactivity (k'_{OH}) can then be determined from the decay of the OH LIF signal, as will be described in Section 4.3.

A photolysis laser (Big Sky Laser CFR 200, Quantel USA) is used to produce the 266 nm laser light required to photolyse O_3 (R 4-1). A Nd:YAG pumped Ti:Sapphire laser (Photonics Industries), situated in the FAGE shipping container, was used to produce the 308 nm laser light used for the excitation of OH radicals and the subsequent detection of their fluorescence at 308 nm. During laboratory experiments, the HIRAC FAGE laser (Nd:YAG pumped dye laser at 308 nm) may also be used as the probe laser for the detection of OH radicals with the OH reactivity instrument. For measurements carried out in this work, the 308 nm laser light was taken from the ground based FAGE shipping container, which is described here. The HIRAC FAGE laser has been described in

Chapter 3. The 308 nm laser light (~20 mW) is directed through the FAGE detection cell via an anti-reflective coated optical fibre (Oz Optics, QMMJ-55-UVVIS-200/240-3-30-ARZ-SP).

The photolysis flow tube is constructed from stainless steel, with an internal diameter of 50 mm and length of 85 cm. Air sampled by the photolysis flow tube, enters via a ½" Teflon line, perpendicular to the photolysis flow tube. The OH FAGE detection cell used in the LFP-LIF OH reactivity instrument measures OH radicals by the on-resonance LIF detection method, as described by Ingham *et al.* (2009) for the old TOHLM instrument. The OH radicals produced, following reactions R 4-1 and R 4-2 react with species present in the flow of air being sampled (typically ~16 – 20 l min^{-1} drawn through the air intake port into the photolysis flow tube). A flow of ~16 l min^{-1} of air is drawn through the photolysis flow tube, with ~3.6 l min^{-1} being sampled by the FAGE cell, which is held at a low pressure of ~1 Torr by a roots blower backed rotary pump (Leybold Vacuum SV200/WAU1001). The remaining ~12.4 l min^{-1} of the sampled gas flow is drawn out of the photolysis flow tube by a scroll pump (Agilent Technologies, IDP3). Absolute laser power, provided it does not fluctuate significantly during the time it takes to record a single decay, is not required to be measured for OH reactivity measurements, as it is a relative method based on the decay of OH radicals from the initial [OH] produced. The 308 nm laser light has not been observed to fluctuate significantly, and can be monitored by a photodiode measuring the laser power through a reference cell in the FAGE shipping container.

4.2.2 Data Acquisition

The LFP-LIF OH reactivity instrument requires the use of two delay generators in order to control the timings of the laser pulse and the data acquisition. One delay generator (SRS-DG535) is used to distinguish between the scattered probe laser light and the OH fluorescence, which are both at the same wavelength of ~308 nm. A second delay generator is required in order to control the timings of the 266 nm photolysis laser and photon counting card for the generation of OH radicals in the photolysis flow tube.

The gating timings for the operation of the LFP-LIF OH reactivity instrument are given in Figure 4-2. t_0 is set by a third, external delay generator which triggers the 308 nm laser inside the FAGE shipping container.

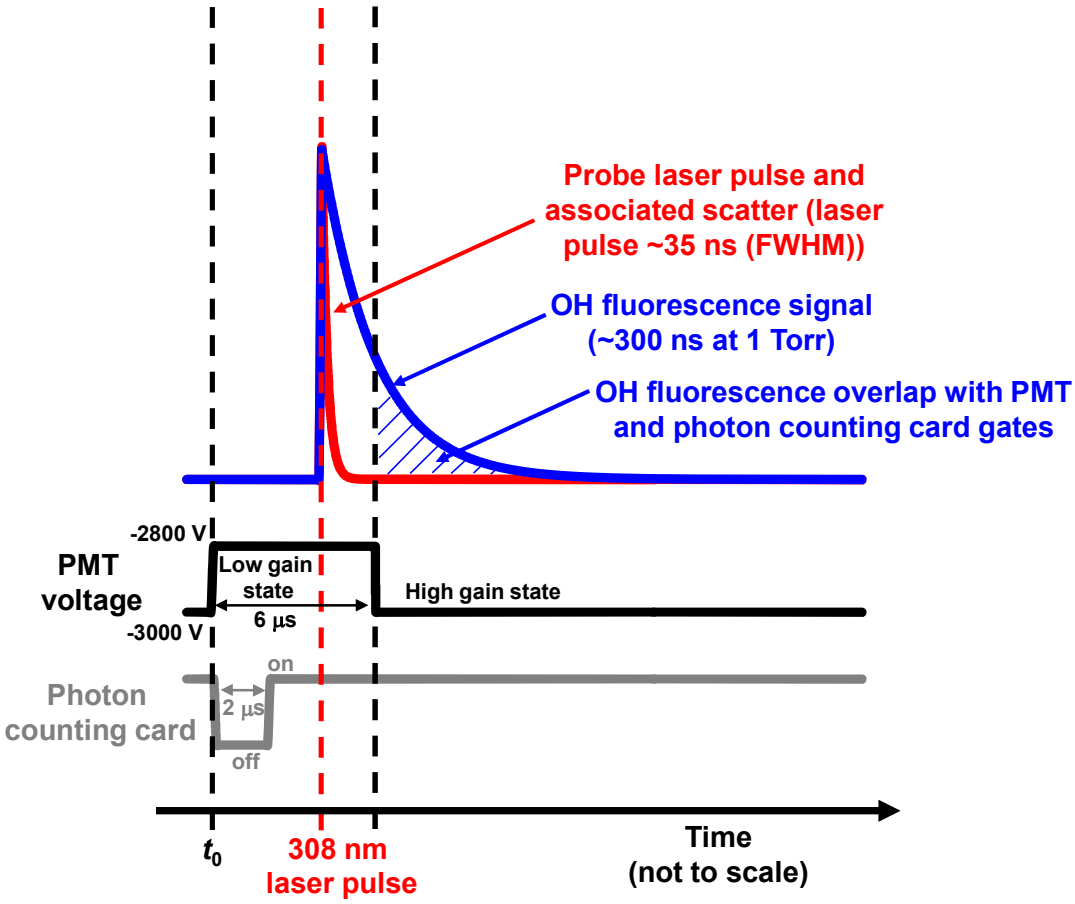

Figure 4-2: Schematic of the gating timings used in the measurement of OH signal during routine operation of the LFP-LIF instrument. Adapted from Stone *et al.* (2016). The blue shaded region indicates the overlap between the OH fluorescence and the photon counting.

The gating timings of the second delay generator (BNC-555) for the control of the 266 nm photolysis laser and photon counting card trigger are shown in Figure 4-3. A photon counting card (Becker and Hickl, PMS200A) is triggered on at the beginning of every measurement period, 0.1 s prior to the 266 nm photolysis laser being triggered, allowing for background signal in the FAGE cell to be recorded. The timings sequence shown in Figure 4-2 for the 308 nm probe laser is repeated every 200 µs for each photolysis pulse and the OH decay is constructed from each of these individual OH measurements.

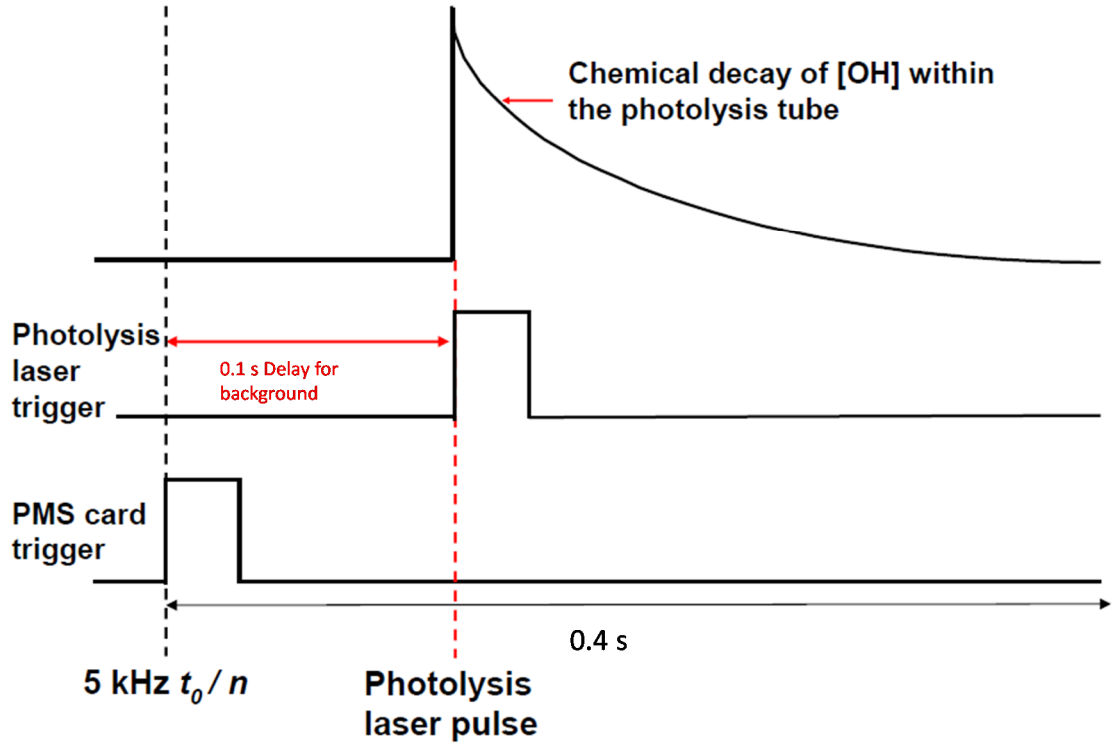

Figure 4-3: Schematic diagram showing the timings of the 266 nm photolysis laser, adapted from Edwards (2011).

4.2.3 Determination of $k'_{OH(raw)}$

$k'_{OH(raw)}$ refers to the loss rate of the decays recorded by the instrument, this value consists of the true OH reactivity value (k'_{OH}) and $k'_{OH(physical)}$, that arises from physical losses of OH within the instrument. The value of $k'_{OH(physical)}$ is required to be known in order to determine a value of k'_{OH} from the $k'_{OH(raw)}$ values. As discussed in Section 4.2.2, the measurement timings for the LFP-LIF OH reactivity instrument are controlled by two delay generators. Figure 4-4 shows a schematic diagram of the structure of the data acquired by the photon counting card for one decay of OH following irradiation of the gas sample with 266 nm light.

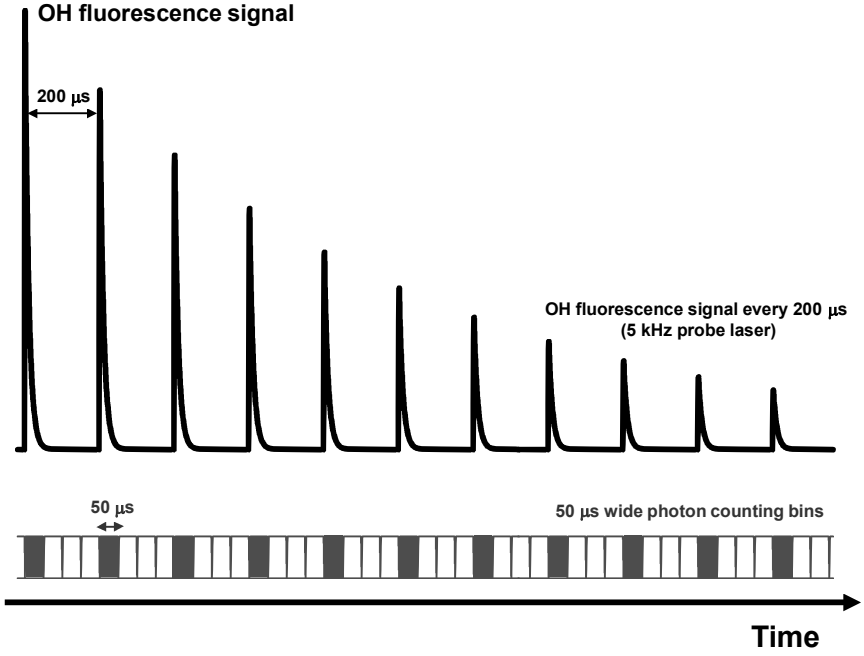

Figure 4-4: Schematic of the photon counting used to collect data on the OH fluorescence during the LPF-LIF OH reactivity instrument operation. Reproduced from Stone *et al.* (2016).

The 308 nm probe laser light had a pulse repetition frequency (PRF) of 5 kHz and so the time between each pulse was 200 μs. Fluorescence is collected in 50 μs bins. The OH fluorescence lifetime is on the order of a few 100 ns and so only the first 50 μs bin, in each set of four, contain any OH fluorescence signal, with three empty fluorescence bins between each. An analysis programme, written by D. R. Cryer in Python 2.7, was used to extract a value of $k'_{OH(raw)}$ from the measurement data through the fitting of an exponentially decaying function. The non-fluorescence bins are removed, giving only data from the OH fluorescence. The background signal recorded prior to the 266 nm photolysis laser pulse is averaged and subtracted from each remaining data point. Following this, every five data points are summed and assigned the time of the first data point in each sum. The resulting decay is then fitted to yield a value of $k'_{OH(raw)}$. Two different fitting functions have been used to determine $k'_{OH(raw)}$; a bi-exponential function and a single exponential function. These will be discussed in Section 4.3 in relation to development of the instrument.

4.2.4 Determination of $k'_{OH(physical)}$

In order to determine $k'_{OH(physical)}$, measurements of $k'_{OH(zero)}$ are carried out, where 15 l min^{-1} synthetic air (BOC, BTCA 178) is passed through a water bubbler and combined with 1 l min^{-1} of synthetic air passed over a mercury pen ray lamp, in order to produce O_3. The total flow of 16 l min^{-1} is sampled by the instrument. The resultant

$k'_{OH(raw)}$ is equal to $k'_{OH(zero)}$, which is the sum of $k'_{OH(physical)}$ plus any contribution to the measured OH reactivity by contaminants present in the air and water used. In order to extract a value of $k'_{OH(physical)}$ from the $k'_{OH(zero)}$ value, the contributions from contaminants present need to be quantified. Better still would be for the determination of $k'_{OH(physical)}$ with the use of extremely pure synthetic air, where contributions from any contaminants are negligible, and well within the error of the measurements.

Details on the determination of $k'_{OH(physical)}$ have been given by Cryer (2016), for both the old and new inlet configurations, which are described in this chapter. For the new inlet configuration determination of the value of $k'_{OH(physical)}$ was carried out during the OH reactivity instrument comparison at the SAPHIR chamber (Chapter 5), where access to a supply of very clean synthetic air was available. It was assumed that this was the purest air that has ever been available for the measurement of $k'_{OH(physical)}$, and that the value of $k'_{OH(raw)}$ would be equal to that of $k'_{OH(physical)}$. The synthetic air available for use at the SAPHIR chamber was produced from the boil off of liquid nitrogen (80%) and liquid oxygen (20%). The value of $k'_{OH(physical)}$ determined through these experiments was reported to be (2.25 ± 0.21) s^{-1} (1σ standard deviation), and this is the value that has been subtracted from all field measurements of $k'_{OH(raw)}$ for the new inlet configuration. Cryer (2016) also described the determination of $k'_{OH(physical)}$ for the old inlet configuration, determined to be (1.25 ± 0.42) s^{-1}.

4.2.5 Effect of NO Recycling

The effects of NO recycling on the measurement of OH reactivity in LFP-LIF instrumentation have been discussed in the literature (Sadanaga *et al.* 2004, Stone *et al.* 2016). Sadanaga *et al.* (2004) reported that the error arising, from the influence of recycled OH from the reaction of HO_2 with NO on the measured OH reactivity was <5% at concentrations of NO up to 20 ppbv. Stone *et al.* (2016) also reported no significant influence on the measurement of OH reactivity from the production of HO_2 within the photolysis flow tube of the instrument described here. A modelling study was conducted by Stone *et al.* (2016) to investigate the potential interferences arising from both HO_2 and RO_2 radicals generated within the photolysis flow tube; HO_2 radicals can be generated from the reaction of CO with OH radicals, and RO_2 radicals can be generated through the reaction of VOCs with NO within the photolysis flow tube. It was concluded that, over a range of conditions investigated, recycled OH has no significant influence on the measurement of OH reactivity using the LFP-LIF instrument described here.

Interferences from OH recycling by a very high concentration of NO, arising from a very specific VOC mixture (CO and CH_4), sampled form the SAPHIR chamber will be discussed in Chapter 5. This is, however, an unrepresentative mixture of VOCs that would unlikely be sampled under ambient conditions or that have been measured in HIRAC for this work.

4.3 Instrument Development and Characterisation

A new inlet and photolysis flow tube pump-out system was designed by Dr. Trevor Ingham. Figure 4-5 and Figure 4-7 show the old and new instrument inlet configurations, respectively. The old inlet is considerably longer than the new inlet (~110 mm compared to ~12 mm). The new inlet has a conical pinhole (0.8 mm) whereas the old inlet has a flat pinhole (0.8 mm), which is held in position by an o-ring and the suction from the vacuum pumps connected to the FAGE cell.

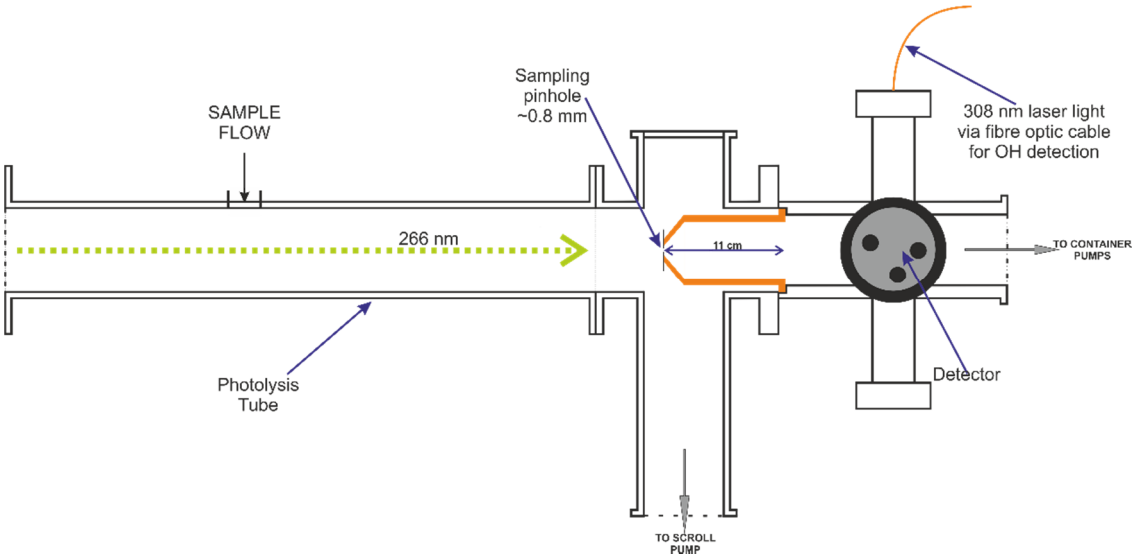

Figure 4-5: Schematic of the old inlet and photolysis flow tube pump-out configuration. Inlet length ~110 mm with side arm photolysis flow tube pump-out system.

With the previous instrument configuration (Figure 4-5), bi-exponential decay profiles were observed, with data being fitted using Eq. 4-1:

$$\frac{(S_{OH})_t}{(S_{OH})_0} = C\ exp\left(-k'_{OH(fast)}\right) + \ (1 - C)\ exp\left(-k'_{OH(raw)}\right) \qquad \text{Eq. 4-1}$$

where $(S_{OH})_0$ is the OH signal at time zero, $(S_{OH})_t$ is the OH signal at time t, $k'_{OH(fast)}$ is the fast component of the bi-exponential decay, C is a constant parameter relating to the proportion of the decay accounted for by either $k'_{OH(fast)}$ or $k'_{OH(raw)}$. The Python 2.7 analysis programme outputs all of the parameters determined from the fit to Eq. 4-1 as well as the standard error to 1σ for each parameter. A bi-exponential OH decay profile

measured with the old inlet configuration is shown in Figure 4-6, where the solid red line represents the fit to Eq. 4-1, giving a value of $k'_{OH(raw)} = (6.9 \pm 0.3)\ s^{-1}$. The exact reasoning for the observation of bi-exponential OH decay profiles observed in the measurements of OH reactivity with LFP-LIF instrumentation is not known, however, it is suggested that it likely arises due to the method of gas sampling from the photolysis flow tube and the length of the FAGE cell inlet. Bi-exponential behaviour has also been reported by Sadanaga *et al.* (2004). The authors also could not determine the exact cause of such decay profiles.

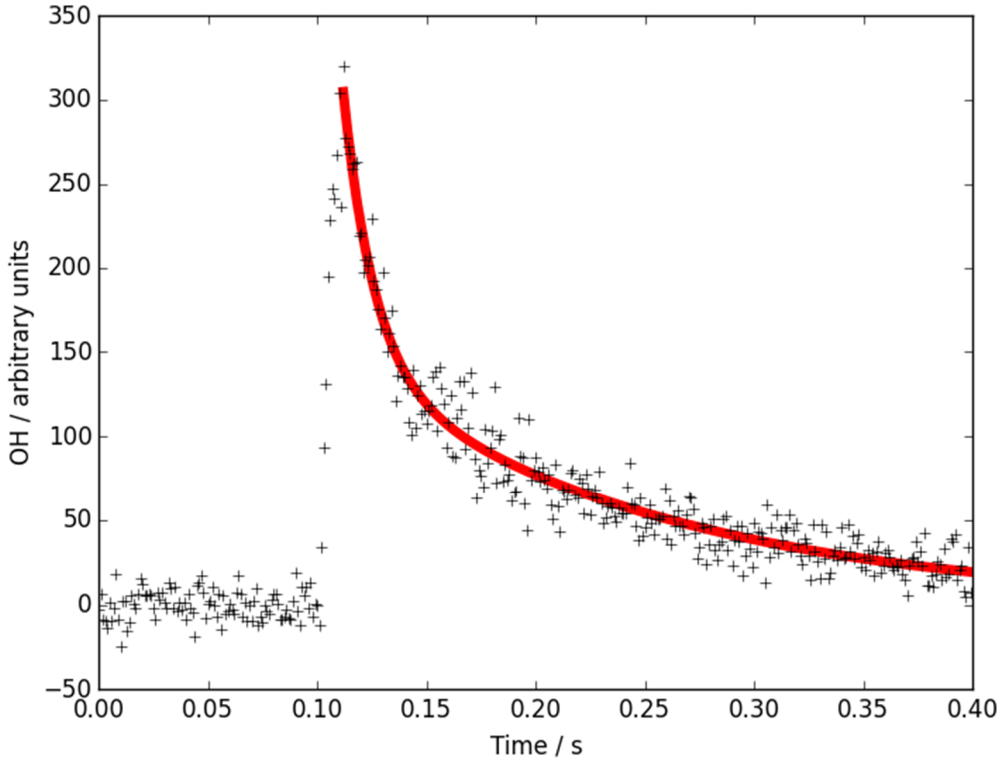

Figure 4-6: Example of bi-exponential OH decay profile as measured using the old inlet configuration. The red line represents the fit to Eq. 4-1, where $k'_{OH(fast)} = 71.8 \pm 6.5\ s^{-1}$ and $k'_{OH(raw)} = 6.9 \pm 0.3\ s^{-1}$.

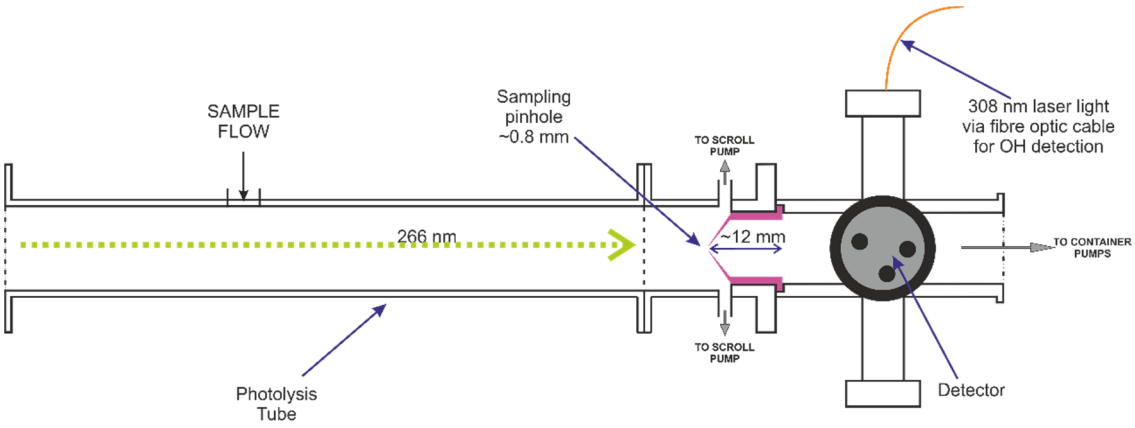

Figure 4-7: Schematic of the new inlet and photolysis flow tube pump-out configuration. Inlet length ~12 mm with radial photolysis flow tube pump-out system.

In combination with the new conical inlet, a new photolysis flow tube pump-out system has been developed. As the pinhole and inlet sit within the photolysis flow tube, the pump-out system has been developed in order to draw the sampled gas flow radially around the FAGE cell inlet, as shown in Figure 4-8.

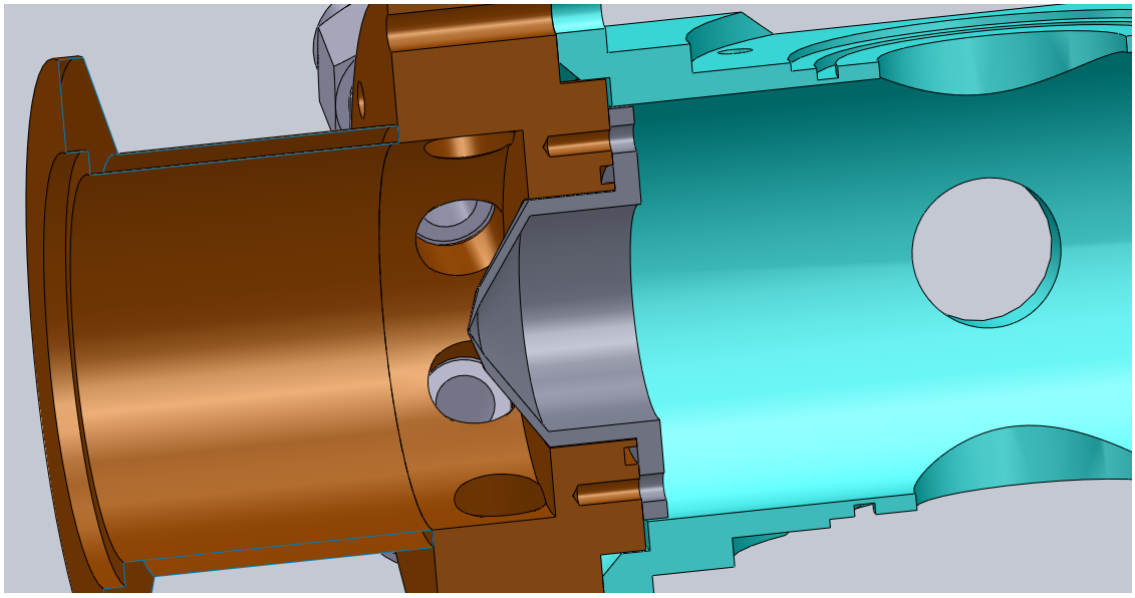

Figure 4-8: Scale diagram of the new sampling inlet and pinhole attached to the FAGE cell of the LFP-LIF OH reactivity instrument. Provided by Dr. Trevor Ingham.

With the new inlet configuration and radial pump-out from the photolysis flow tube, single exponential behaviour of the decays is observed, which can be fitted using Eq. 4-2 in order to return a value of $k'_{OH(raw)}$:

$$\frac{(S_{OH})_t}{(S_{OH})_0} = exp\left(-k'_{OH(raw)}\,t\right) \qquad \text{Eq. 4-2}$$

Examples of single exponential OH decay profiles recorded using the new inlet configuration are shown in Figure 4-9, where the solid red lines represents the fit to

Eq. 4-2. For faster decays, such as that shown in Figure 4-9(b), where the OH signal reaches background levels at earlier times, the fitting programme can be adjusted in order to fit only to the data representative of the actual OH decay. Changing the fitting times in this way ensures that the fit of Eq. 4-2 is representative of the OH decay; background signal once the decay is over, particularly for faster decays such as Figure 4-9(b), is not included in the fit.

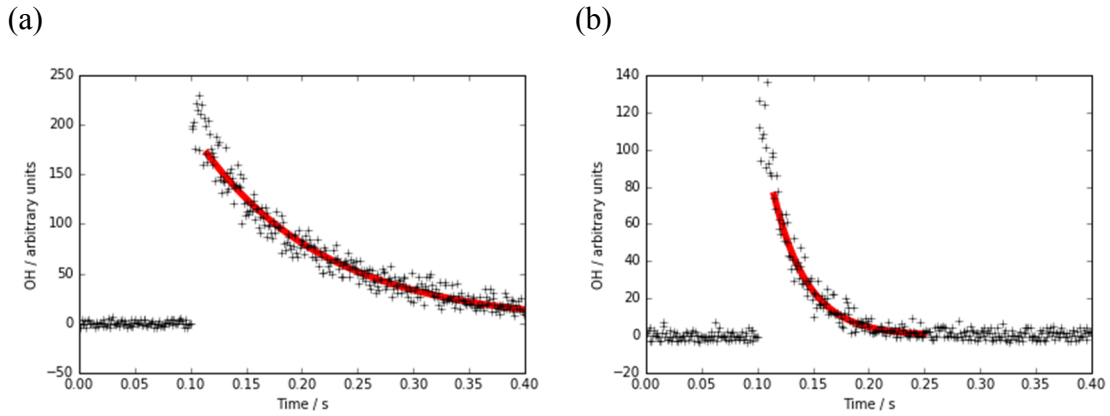

Figure 4-9: Examples of single exponential OH decay profile measured using the new inlet configuration. The red line represents the fit to Eq. 4-2, (a) $k'_{OH(raw)} = 8.82 \pm 0.15\ s^{-1}$ and (b) $k'_{OH(raw)} = 32.74 \pm 1.07\ s^{-1}$.

Characterisation of both the old and the new inlet configurations has been carried out for a range of normal operating parameters; varying O_3 concentration, photolysis flow tube flow rate, photolysis flow tube pressure and FAGE cell pressure. Validation of measurements have been carried out for both inlet configurations by the measurement of bimolecular rate coefficients for hydrocarbons with well-defined rate coefficients in the literature.

A comparison of the measured $k'_{OH(raw)}$ as a function of the total flow rate through the photolysis flow tube is shown in Figure 4-10. For flows of 15 – 16 l min^{-1}, both the old and the new instrument inlet configurations measured ~5.5 s^{-1}. For the new inlet configuration, a decrease of ~2 s^{-1} $k'_{OH(zero)}$ was observed as the total flow rate was increased from 17 l min^{-1} to 27 l min^{-1}; this is attributed to lower wall losses in the photolysis flow tube with shorter residence times at higher flow rates. The high value of ~9 s^{-1} at a total flow rate of 6 l min^{-1} with the old inlet configuration is attributed to the larger residence time leading to the sampled air being irradiated multiple times by the 266 nm photolysis laser beam. Any minor impurities (listed in Table 4-1) within the "zero" air sample may be photolysed, artificially increasing the [OH] within the photolysis flow tube, leading to higher measurement of $k'_{OH(zero)}$. These measurements of

$k'_{OH(zero)}$ show the importance of correctly characterising the instrument for the flow rate during routine operation.

Impurity	**Concentration / ppmv**
CO	<1
CO_2	<300
NO_x	<0.1
VOCs	<0.1

Table 4-1: Impurities stated in synthetic air (BOC, BTCA 178).

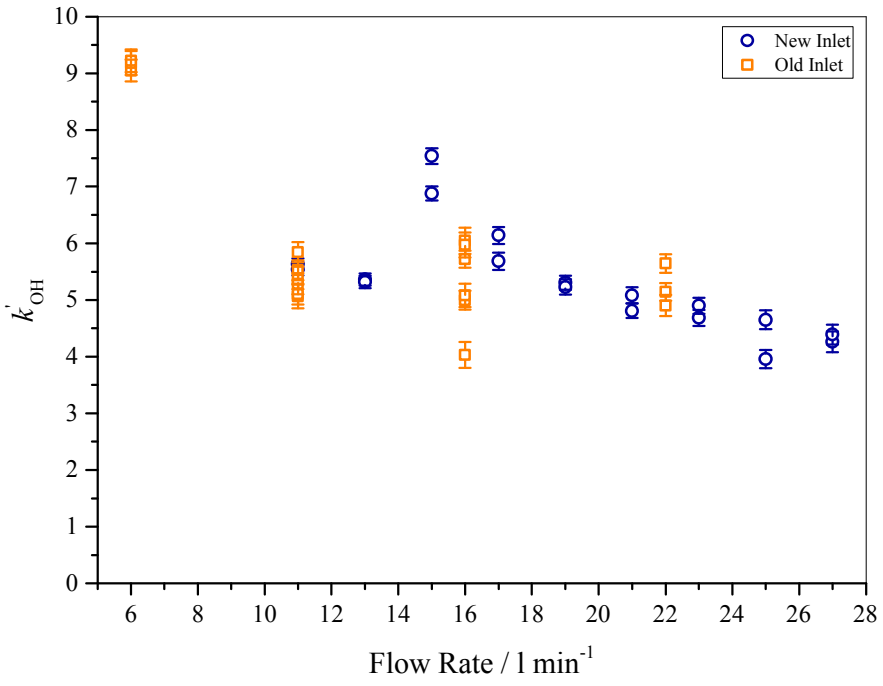

Figure 4-10: Comparison of measured $k'_{OH(zero)}$ as a function of total flow rate through the photolysis flow tube for both the old and new inlet set ups. Error bars represent the 1σ standard error from the fitting procedures; bi-exponential fitting for the old inlet measurements and single exponential fitting for the new inlet measurements.

A comparison of the measurement of $k'_{OH(zero)}$ as a function of photolysis flow tube pressure is shown in Figure 4-11 for both instrument inlet configurations. The solid straight lines represent the linear fit to the data, where the gradient of the line fit to data measured with the old inlet configuration is (-0.005 ± 0.001) s^{-1} Torr^{-1} and the gradient of the line fit to data measured with the new inlet configuration is (-0.003 ± 0.001) s^{-1} Torr^{-1}. The measured value of $k'_{OH(zero)}$ over the pressure range of ~575 Torr to 950 Torr for both

inlet set ups shows no significant dependence on the photolysis flow tube pressure. As measurements of OH reactivity are typically compared to modelled and calculated OH reactivity (from measured sinks of OH), the instrument is routinely run at close to ambient pressure, ~750 Torr. Many species contributing to the overall OH reactivity show a pressure dependence for their reaction with OH radicals, and so it is vital to measure OH reactivity at a photolysis flow tube pressure representative of that recorded for ambient measurements. In order to draw a sample into the LFP-LIF OH reactivity instrument, the instrument is required to run at sub-ambient pressure by ~10 Torr. This, however, would only account for a change in $k'_{OH(zero)}$ of <1%, which is well within the standard uncertainty of the measurements.

The difference observed of ~2 s^{-1} between the measurements taken with the old and new inlet configurations is due to a change in the source of the synthetic air used to make the measurements. Values of k'_{OH} can vary; only upper limits of impurities are provided from BOC (Table 4-1).

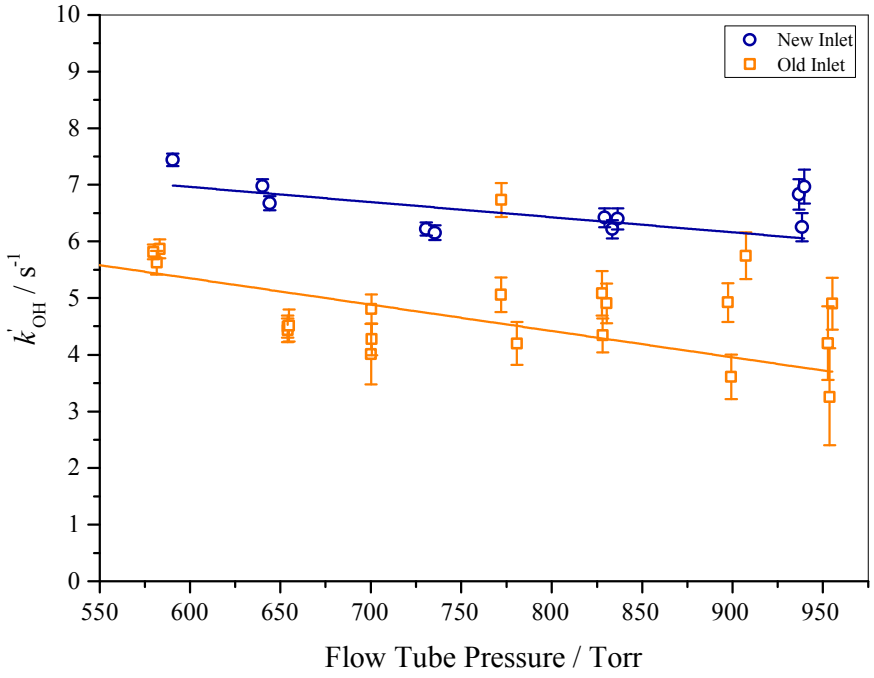

Figure 4-11: Comparison of measured $k'_{OH(zero)}$ as a function of photolysis flow tube pressure for both the old and new inlet set ups. Error bars represent the standard error from the fitting procedures; bi-exponential fitting for the old inlet measurements and single exponential fitting for the new inlet measurements. Linear fit to old inlet data gives a gradient of (-0.005 ± 0.001) s^{-1} $Torr^{-1}$ and to the new inlet data gives a gradient of (-0.003 ± 0.001) $s^{-1}Torr^{-1}$, where the errors are the standard error in the linear least squares fitting procedure.

The measured $k'_{OH(zero)}$ for the old inlet and new inlet configurations as a function of $[O_3]$ in the sampled air flow is shown in Figure 4-12. No discernible dependency is observed over the range of $[O_3]$ shown in Figure 4-12 on the measured values of $k'_{OH(zero)}$; linear fitting to the data gives a gradient of (-0.023 ± 0.017) s^{-1} $ppbv^{-1}$ for the old inlet set up and a gradient of (0.002 ± 0.004) s^{-1} $ppbv^{-1}$ for the new inlet set up. The larger errors associated with the measurement values from the old inlet configuration arise from larger uncertainties from the bi-exponential fitting procedure compared to the single exponential fitting procedure.

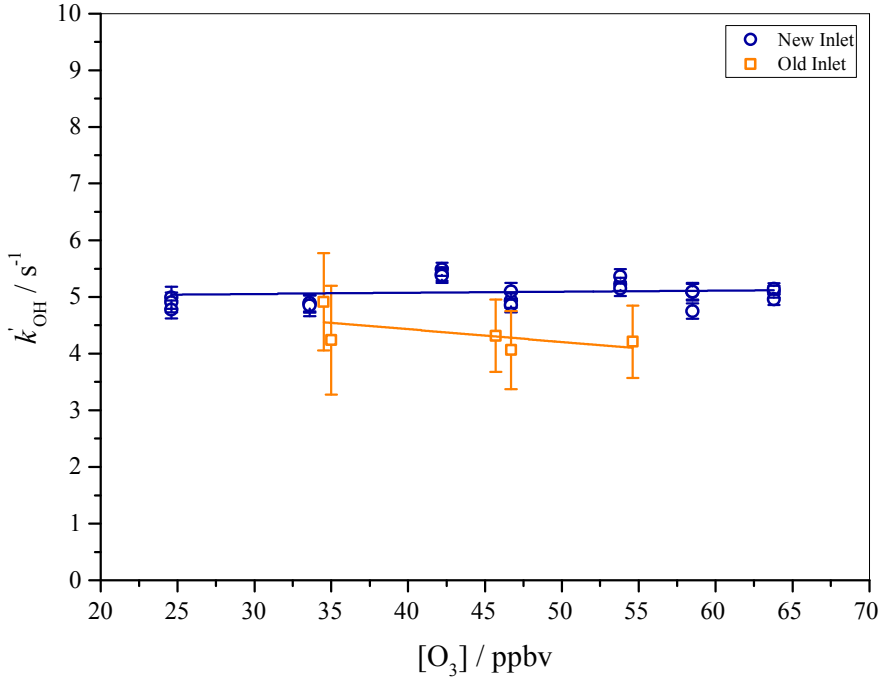

Figure 4-12: Comparison of measured $k'_{OH(zero)}$ as a function of $[O_3]$ in the photolysis flow tube for both the old and new inlet set ups. Error bars represent the standard error from the fitting procedures; bi-exponential fitting for the old inlet measurements and single exponential fitting for the new inlet measurements. Linear fit to old inlet data gives a gradient of -0.023 ± 0.017 s^{-1} $ppbv^{-1}$ and to the new inlet data gives a gradient of 0.002 ± 0.004 s^{-1} $ppbv^{-1}$, where the errors are the standard error in the fitting procedure.

The measured first order decay rate, k'_{OH} against $[CH_4]$ is shown in Figure 4-13 and Figure 4-14 for the old and new inlet configurations, respectively. For both configurations, CH_4 was introduced into the total flow of synthetic air sampled by the OH reactivity instrument; a third MFC was used to control the flow of CH_4 (BOC, CP grade, 99.5% purity)), varying the concentration between (0 – 26) × 10^{15} molecule cm^{-3}. Much higher values, up to ~150 s^{-1}, of k'_{OH} were achieved with the new inlet configuration, however, much greater scatter and error is observed as k'_{OH} reaches values >100 s^{-1}. As

the concentration of CH_4 is increased for the measurements of k'_{OH} >100 s^{-1}, the initial OH signal is reduced and the OH decay is complete over shorter timescales, and hence less data points are used in the fitting procedure, leading to increased error.

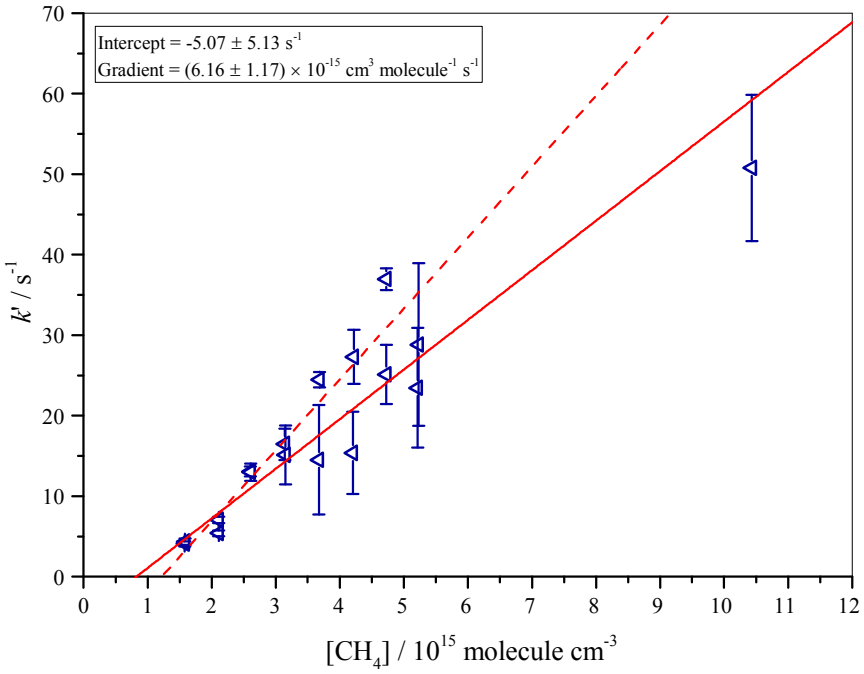

Figure 4-13: Bimolecular plot for the measured k'_{OH} against [CH_4]. Error bars are the standard error in the bi-exponential fitting procedure. Measurements were carried out using the old inlet configuration at a photolysis flow tube pressure of ~760 Torr and FAGE cell pressure of ~2.00 Torr. The solid red line represents the linear least squares fit to the data, where the gradient is equal to the rate coefficient of CH_4 with OH radicals at 298 K, for measurements of k'_{OH} up to 40 s^{-1}. The dashed red line represents the linear least squares fit to the data for all data points, upto k'_{OH} = 51 s^{-1}.

The gradient obtained from the linear least squares fitting procedure for data in Figure 4-13 and Figure 4-14 represents the rate coefficient for the reaction of CH_4 with OH radicals at 298 K. The solid red line shown in Figure 4-13 represents the linear fit to data up to measurements of k'_{OH} = 40 s^{-1} (k_{OH+CH4} = (6.2 ± 1.2) × 10^{-15} cm^3 $molecule^{-1}$ s^{-1}), and the dashed red line represents the linear fit to all of the measurements of k'_{OH} (k_{OH+CH4} = (8.81 ± 0.75) × 10^{-15} cm^3 $molecule^{-1}$ s^{-1}). The linear least squares fit to the data in Figure 4-14 gives a gradient of (6.41 ± 0.18) × 10^{15} cm^3 $molecule^{-1}$ s^{-1}. All errors in gradients are the standard error from the linear least squares fitting procedure. When compared to the literature, the IUPAC recommended rate coefficient of CH_4 with OH radicals at 298 K is (6.4 ± 0.9) × 10^{-15} cm^3 $molecule^{-1}$ s^{-1} (Atkinson *et al.* 2006). Excellent agreement was observed between the IUPAC recommended rate coefficient and that determined from measurements with the new inlet configuration, validating the measurement procedure for values of k'_{OH} up to ~150 s^{-1}. Beyond k'_{OH} = 150 s^{-1},

considerable scatter and larger errors were observed for measurements. Good agreement was observed with the literature for measurements carried out with the old inlet configuration for values of k'_{OH} up to ~40 s^{-1}. The determined rate coefficient for the reaction of CH_4 with OH radicals at 298 K when measurements up to k'_{OH} = 51 s^{-1} were included falls outside of the IUPAC recommended value, and it is concluded that only measurements of k'_{OH} up to ~40 s^{-1} can be used with confidence for the old inlet configuration.

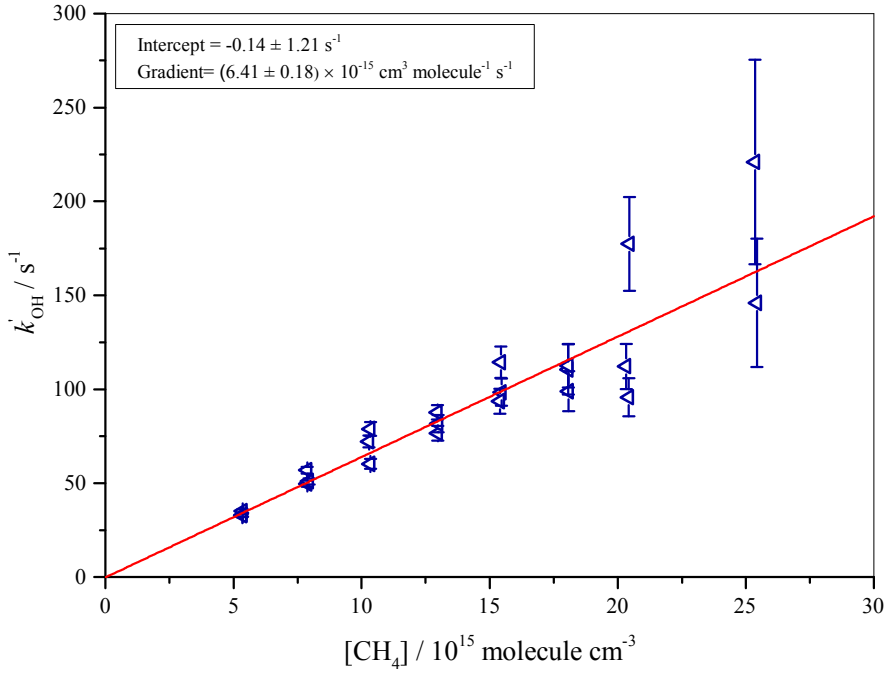

Figure 4-14: Bimolecular plot for the measured k'_{OH} against [CH_4]. Error bars are the standard error in the single exponential fitting procedure. Measurements were carried out using the new inlet configuration at a photolysis flow tube pressure of ~730 Torr and FAGE cell pressure of ~1.95 Torr. The solid red line represents the linear least squares fit to the data, where the gradient is equal to the rate coefficient of CH_4 with OH radicals at 298 K.

Measurements of $k'_{OH(zero)}$ as a function of the integration time, are shown in Figure 4-15. Measurements were successfully carried out at an averaging time of 10 s; measurements at integration times <30 s all show increased scatter as the integration time is reduced, and increased error in the measurements. The ability to measure OH reactivities at short integration times shows the potential for improved time resolution for measurements in the future, allowing for more accurate measurements of rapid changes in OH reactivity, such as may occur in field measurements.

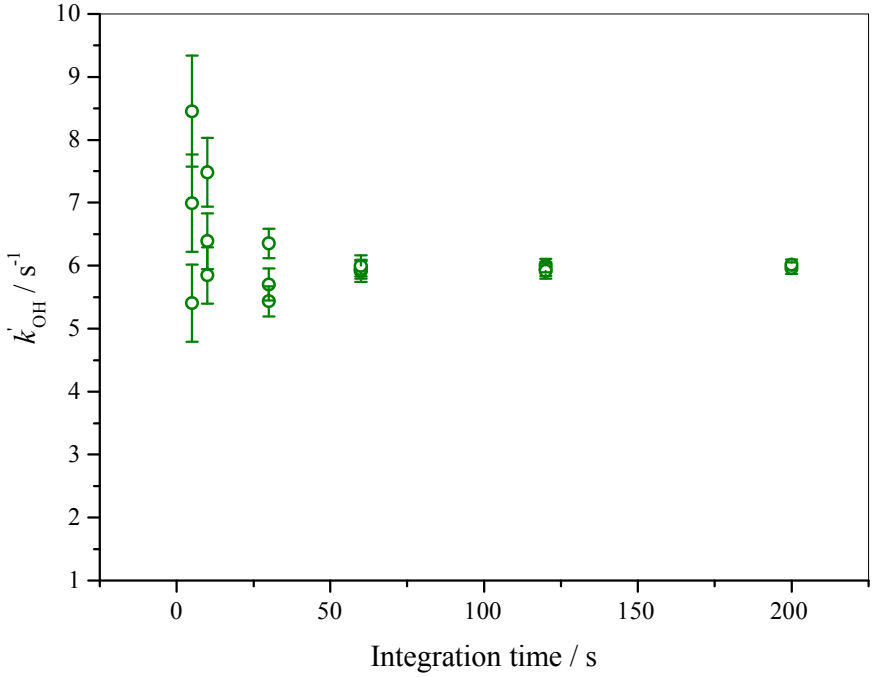

Figure 4-15: Measured k'_{OH} as a function of integration time, determined for the new inlet configuration. Measurements were taken using 13 mW 308 nm probe laser power at a cell pressure of ~1.95 Torr and a photolysis flow tube pressure of 725 Torr. 9 l min^{-1} of humidified air was mixed with 6 l min^{-1} of synthetic air and 1 l min^{-1} of air passed over a mercury pen ray lamp for the production of O_3. Error bars represent the standard error in the single exponential fitting procedure.

The development of a new inlet and photolysis flow tube pump-out system has been shown to have no discernible dependencies observed for any of the parameters investigated over the typical range of atmospherically relevant conditions (photolysis flow tube pressure = 720 – 780 Torr and $[O_3]$ = 25 – 65 ppbv). Validation experiments with both inlet configurations show the suitability of the LFP-LIF instrument for the measurement of OH reactivities up to 40 s^{-1} with the old inlet configuration and up to 150 s^{-1} with the new inlet configuration.

4.4 Coupling to the HIRAC chamber

Few studies have been presented in the literature on OH reactivity measurements from atmospheric simulation chambers (Nakashima *et al.* 2012, Fuchs *et al.* 2013, Nehr *et al.* 2014, Nölscher *et al.* 2014). The LFP-LIF OH reactivity instrument has recently been modified in order to interface the instrument with the HIRAC chamber, as shown in Figure 4-16. A number of considerations were required to be taken into account for the set-up of the instrument with HIRAC, which are detailed here.

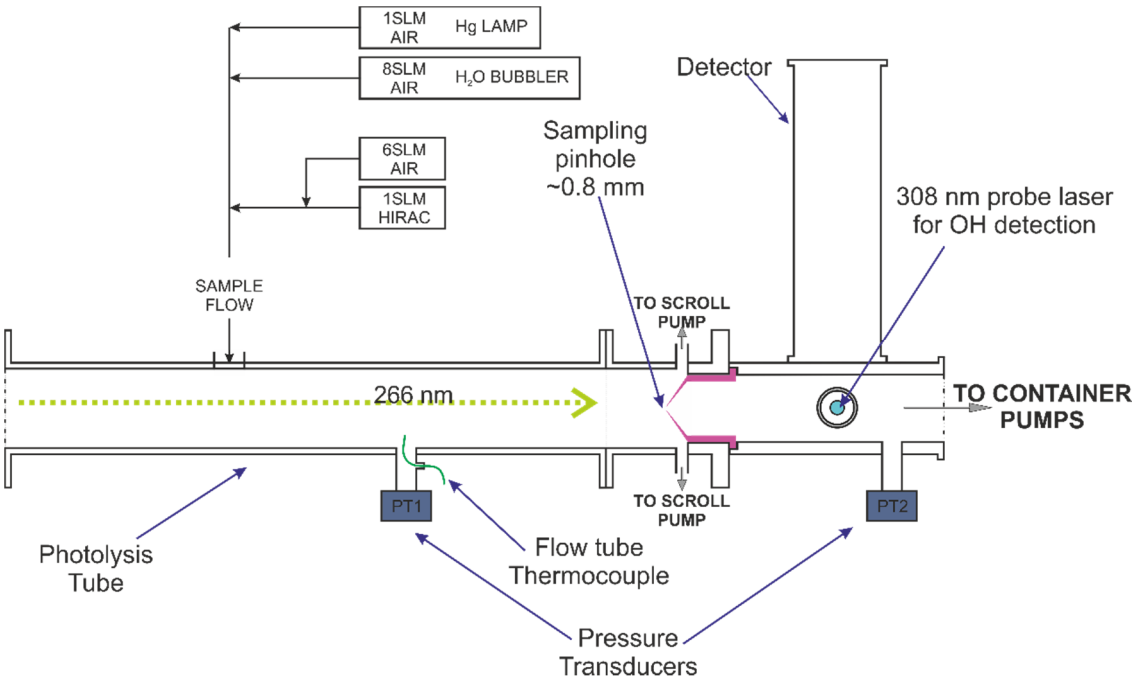

Figure 4-16: Schematic showing the LFP-LIF OH reactivity instrument coupling with the HIRAC chamber.

During field measurements of OH reactivity by LFP-LIF, OH radicals in the photolysis flow tube are produced from O_3 and water vapour present in the ambient air being sampled. As HIRAC is potentially a very dry and clean atmospheric chamber, the addition of O_3 and water vapour is required in order to generate sufficient [OH] within the photolysis flow tube of the instrument for an observable decay, described by reactions R 4-1 to R 4-6. Photolysis of O_2 from passing a flow of synthetic air over a mercury pen ray lamp produces O_3 (~60 ppbv for a lamp current of ~20 mA) following R 4-5 and R 4-6. As in ambient OH reactivity measurements, the O_3 is then photolysed following R 4-1 to produce the electronically excited oxygen atom, $O(^1D)$, which then reacts with water vapour to produce two OH radicals via R 4-2.

$$O_2 + h\nu_{(\lambda = 184.9\ nm)} \rightarrow 2O(^3P) \qquad \text{R 4-5}$$

$$O(^3P) + O_2 \rightarrow O_3 \qquad \text{R 4-6}$$

The OH reactivity instrument typically takes a flow rate of ~16 l min^{-1} for ambient measurements; such a large flow taken entirely from HIRAC would lead to evacuation of the chamber in ~2.3 hours. Sampling by numerous other analytical instruments (GCs, O_3 analyser, NO_x analyser, FAGE) simultaneously alongside OH reactivity measurements would increase the total sample outflow from the chamber considerably. This large sample outflow would require a large counter flow into the chamber in order to maintain the required chamber pressure (~1000 mbar for OH reactivity studies in this work) which

would rapidly dilute the contents of the chamber. A dilution of the OH reactivity sample (BOC, BTCA 178) is used to overcome this, and avoids measurements of high OH reactivities that would be present due to large concentrations of OH reactive species in the chamber; taking 1 l min^{-1} sample from HIRAC, diluted to the total flow of 16 l min^{-1}. The dilution flow of air is set using mass flow controllers (MFCs), controlled via in-house LabVIEW software written by D. R. Cryer.

Figure 4-17 shows a schematic of the flow set up for HIRAC OH measurements, indicating the dilution flows, the HIRAC sample flow, the photolysis flow tube flow and the FAGE cell and scroll pump flows. A portion of the dilution flow (typically 5 l min^{-1} at flow 2 in Figure 4-17) is added to the HIRAC sample flow (flow 1 in Figure 4-17) directly as the sample exits the chamber, with a further 9 l min^{-1} passed through a water bubbler (flow 3 in Figure 4-17) and 1 l min^{-1} passed over a mercury pen ray lamp to generate O_3 (flow 4 in Figure 4-17). All flows are combined to give a total flow of ~16 l min^{-1} which is sampled by the OH reactivity instrument. Space requirements in the laboratory dictated that the sample line was required to be >5 m in length in order to couple the OH reactivity instrument to the HIRAC chamber, and so introducing a portion of the dilution flow directly to the sample as it is drawn from the chamber, reduces the possible losses of reactive species on the sample line by reducing the residence time in the sample line. For a 10 m, ½" (O.D) diameter Teflon sample line, the residence time would be 12.7 s for a flow rate of 6 l min^{-1}, and 1.3 min for a flow rate of 1 l min^{-1}. Tests with different length sample lines showed no discernible effect when measuring k'_{OH} of known concentrations of *iso*-butanol.

These flows are all combined into a 1 m length of ½" (O.D) Teflon tubing which is sampled by the instrument photolysis flow tube (flow 5 in Figure 4-17). The total sampled flow rate from HIRAC is monitored and recorded in the instrument software by a mass flow meter (MFM); careful adjustment of a butterfly valve connected to the scroll pump allows for the flow rate to be finely tuned. The MFM can be coupled to the sample in a number of positions; directly after the sample exits HIRAC (flow 1 in Figure 4-17), connected to the entrance to the photolysis flow tube (flow 5 in Figure 4-17), or connected to the exit from the photolysis flow tube (flow 8 in Figure 4-17), positioned before the valve connected to the scroll pump line. Experiments carried out coupled to the HIRAC chamber have been performed with the MFM coupled directly to the sample line as it exits HIRAC in order to closely monitor the exact sample being taken from the chamber. Connecting the MFM in line either directly measuring the HIRAC sample flow rate or to

measure the total flow into the photolysis flow tube adds a restriction and the potential for pressure build up as the flow goes from ½" (O.D) Teflon tubing to ¼" (O.D) through the MFM, and back to ½" Teflon tubing again. Passing the sample through the MFM also introduces additional stainless steel surfaces which could add to possible losses of reactive species, and provide an additional surface for reactions to occur on. Positioning the MFM to measure flow 8 in Figure 4-17 would allow for indirect measurement of the sample taken from HIRAC as the flow would be calculated from the known flows 2, 3, 4 and 7 in Figure 4-17. The dilution of the sample from HIRAC can then be calculated from these known flow rates in order to adjust the measured $k'_{OH(raw)}$ to the true value of k'_{OH} within HIRAC.

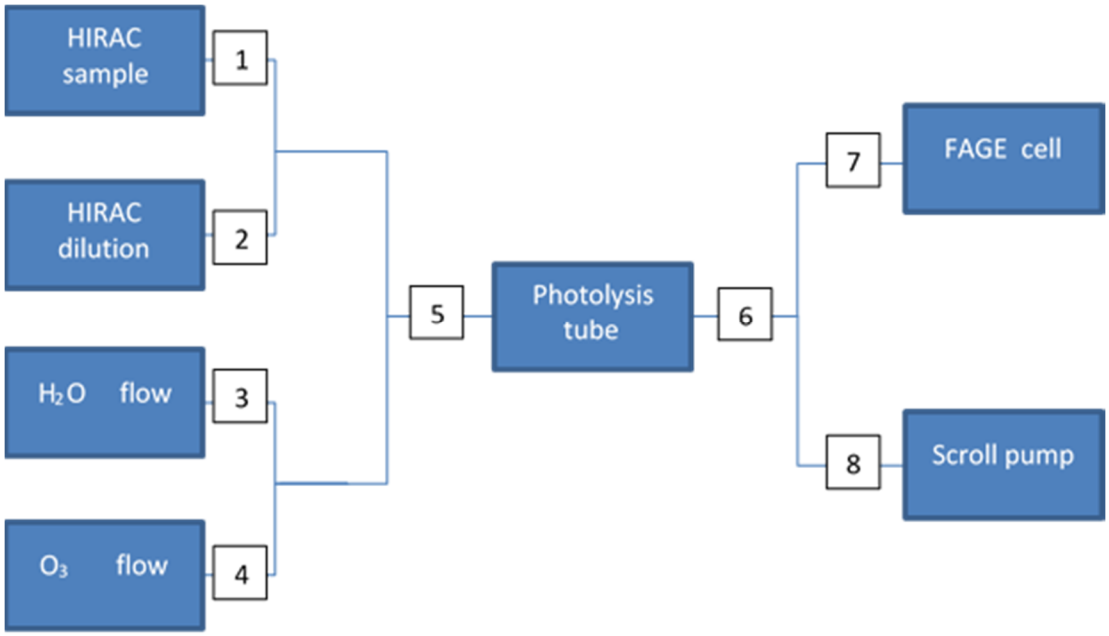

Figure 4-17: Schematic of flow set up for HIRAC OH reactivity measurements. HIRAC sample = 1 l min^{-1}, HIRAC dilution = 5 l min^{-1}, H_2O flow = 9 l min^{-1}, O_3 flow = 1 l min^{-1}, photolysis flow tube flow = 16 l min^{-1}, FAGE cell flow = 3.6 l min^{-1}, scroll pump flow = 12.4 l min^{-1}.

Initial studies with the recently coupled LFP-LIF OH reactivity instrument have been carried out in order to determine optimum operating conditions, and are discussed here. Validation of measurements taken whilst sampling from the HIRAC chamber were carried out for *n*-butanol with the new inlet configuration, shown in Figure 4-18. *N*-butanol was chosen for instrument validation experiments as the chemistry of butanols was to be studied in the HIRAC chamber as part of this thesis (Chapter 6, Chapter 7 and Chapter 8). The gradient obtained from the best fit line to a bimolecular plot is equal to the rate coefficient for the reaction of *n*-butanol with OH radicals. Excellent agreement is observed between the measured $k_{OH + n\text{-butanol}} = (8.24 \pm 0.50) \times 10^{-12}$ cm^3 $molecule^{-1}$ s^{-1},

with the IUPAC recommended rate coefficient $k_{OH + n\text{-butanol}} = (8.5 \pm 3.0) \times 10^{-12}$ cm^3 molecule^{-1} s^{-1} (Atkinson *et al.* 2006).

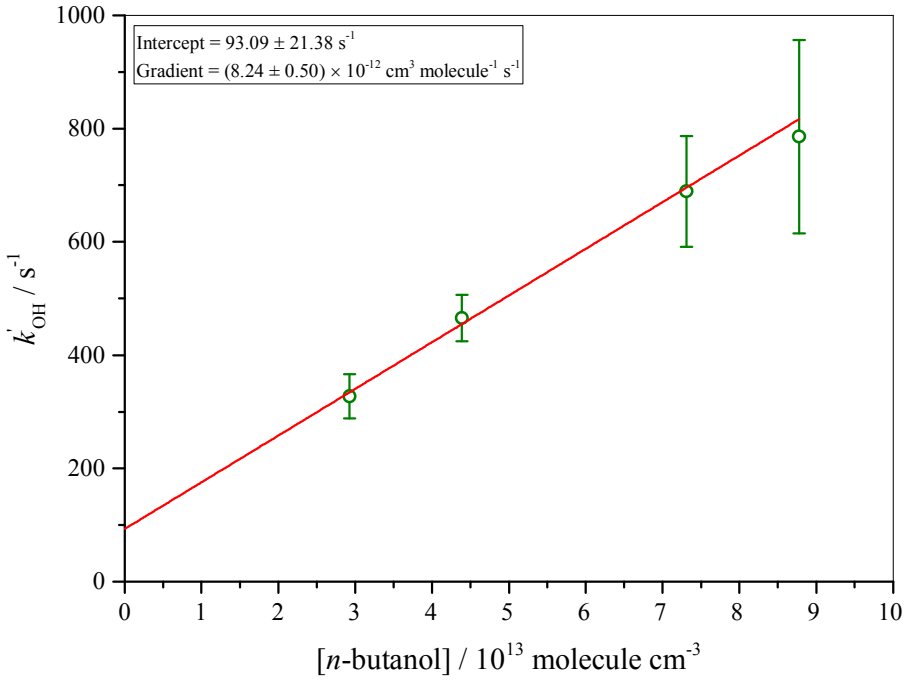

Figure 4-18: Bimolecular plot for the measured k'_{OH} against [*n*-butanol]. Each data point is the average of several k'_{OH} measurements, where the measurements have been corrected for dilution of the sample taken from HIRAC. Error bars are the standard deviation from the average values. Measurements were carried out using the new inlet configuration whilst sampling from the HIRAC chamber, at a photolysis flow tube pressure of ~740 Torr and FAGE cell pressure of ~1.95 Torr. The solid red line represents the linear least squares fit to the data, where the gradient is equal to the rate coefficient of *n*-butanol with OH radicals at 298 K.

Measurements of k'_{OH} whilst sampling from the HIRAC chamber are corrected for the dilution of the sample taken from the chamber. Typically, a dilution factor of 1:16 is used to correct measured values of k'_{OH} for the dilution, giving a value of $k'_{OH(HIRAC)}$ equal to that of the OH reactive species present in the chamber, exact dilution factors are determined from the recorded sample flow taken from HIRAC. The dilution flow avoids measurement of high OH reactivities which are present in the HIRAC chamber due to the large concentrations of compounds required for chamber experiments, and avoids sampling a large volume from the chamber which would require a large counter flow in order to maintain a constant chamber pressure.

The LFP-LIF OH reactivity instrument has been successfully coupled to the HIRAC chamber, with validation of measurements carried out by the measurement of the

bimolecular rate coefficient of *n*-butanol with OH radicals. Excellent agreement with the literature was seen for the measurement of $k'_{OH + n\text{-butanol}}$.

4.5 Conclusions and Future Work

OH reactivity measurements provide valuable information on the HO_x budget in a specific environment where the measurements are being carried out. Coupling of OH reactivity instrumentation to an atmospheric simulation chamber allows for specific reactions to be assessed in isolation in order to obtain further information on chemical mechanisms and rate coefficients.

A LFP-LIF OH reactivity instrument has successfully been coupled to the HIRAC chamber. Validation of the instrument, where known concentrations of hydrocarbons were sampled from HIRAC, showed good agreement with the literature for measured rate coefficients for their reaction with OH radicals. Modifications of the LFP-LIF OH reactivity instrument have shown improved measurements to higher values of k'_{OH} through reducing the FAGE cell inlet length and a new radial pump-out system from the photolysis flow tube, obtaining single exponential OH decay profiles. Comparisons of both the old and new inlet configurations over a range of different operating parameters has shown similar dependencies on the photolysis flow tube pressure, total photolysis flow tube flow and $[O_3]$ concentration.

Measurements of $k'_{OH(zero)}$ as a function of integration time shows the potential for future measurements to be carried out at higher time resolution; the use of a FAGE cell detector with improved sensitivity to that of the CPM, as described in this work, would help to facilitate such measurements in the future.

A description of the LPF-LIF OH reactivity instrument coupled with the HIRAC chamber has been given, in addition to a number of important parameters which required characterisation in order to validate the measurement method for HIRAC experiments. Validation of the measurement system was carried out, where the measured rate coefficient values were in good agreement with literature values.

Validation of the measurements over a range of different types of VOCs would further the knowledge of any potential interferences and losses whilst measuring from the HIRAC chamber. The greatest source of such errors in measurements likely arises due to laboratory space requirements dictating the need for a long sampling line connecting HIRAC to the instrument. A reduction in this sample line would reduce the potential for loss of any species sampled to the walls of the sampling line, and also reduce the potential

for any further reactions to occur through the sample line before the sample reaches the photolysis flow tube of the instrument. It is also suggested that alternative sampling lines should be investigated whilst sampling a range of VOCs from the HIRAC chamber in order to determine the most appropriate for minimising such effects.

Measurements of OH reactivity from an instrument intercomparison carried out at the SAPHIR chamber in Jülich, Germany are given in Chapter 5, where comparisons are made between measurements from three types of instrument, for a range of VOC mixtures within the SAPHIR chamber. Measurements of k'_{OH} with the LFP-LIF instrument whilst sampling from the HIRAC chamber through the course of complex reaction systems are given in Chapter 6, where measurements are compared with OH reactivity calculated from measured species within the chamber. Discussion is given where agreement and discrepancies between the measured and calculated OH reactivity is observed with suggestions given as to the sources of any discrepancies.

4.6 References

Atkinson, R., Baulch, D. L., Cox, R. A., Crowley, J. N., Hampson, R. F., Hynes, R. G., Jenkin, M. E., Rossi, M. J., Troe, J. and Subcommittee, I. (2006). "Evaluated kinetic and photochemical data for atmospheric chemistry: Volume II - gas phase reactions of organic species." Atmospheric Chemistry and Physics **6**(11): 3625-4055.

Cryer, D. R. (2016). Measurements of hydroxyl radical reactivity and formaldehyde in the atmosphere. PhD, Leeds.

Edwards, P. M. (2011). Tropospheric oxidation from the Tropics to the Poles. PhD., Leeds.

Fuchs, H., Hofzumahaus, A., Rohrer, F., Bohn, B., Brauers, T., Dorn, H. P., Haseler, R., Holland, F., Kaminski, M., Li, X., Lu, K., Nehr, S., Tillmann, R., Wegener, R. and Wahner, A. (2013). "Experimental evidence for efficient hydroxyl radical regeneration in isoprene oxidation." Nature Geoscience **6**(12): 1023-1026.

Ingham, T., Goddard, A., Whalley, L. K., Furneaux, K. L., Edwards, P. M., Seal, C. P., Self, D. E., Johnson, G. P., Read, K. A., Lee, J. D. and Heard, D. E. (2009). "A flow-tube based laser-induced fluorescence instrument to measure OH reactivity in the troposphere." Atmospheric Measurement Techniques **2**(2): 465-477.

Nakashima, Y., Tsurumaru, H., Imamura, T., Bejan, I., Wenger, J. C. and Kajii, Y. (2012). "Total OH reactivity measurements in laboratory studies of the photooxidation of isoprene." Atmospheric Environment **62**: 243-247.

Nehr, S., Bohn, B., Dorn, H. P., Fuchs, H., Häseler, R., Hofzumahaus, A., Li, X., Rohrer, F., Tillmann, R. and Wahner, A. (2014). "Atmospheric photochemistry of aromatic hydrocarbons: OH budgets during SAPHIR chamber experiments." Atmospheric Chemistry and Physics **14**(13): 6941-6952.

Nölscher, A. C., Butler, T., Auld, J., Veres, P., Muñoz, A., Taraborrelli, D., Vereecken, L., Lelieveld, J. and Williams, J. (2014). "Using total OH reactivity to assess isoprene photooxidation via measurement and model." Atmospheric Environment **89**(0): 453-463.

Sadanaga, Y., Yoshino, A., Watanabe, K., Yoshioka, A., Wakazono, Y., Kanaya, Y. and Kajii, Y. (2004). "Development of a measurement system of OH reactivity in the atmosphere by using a laser-induced pump and probe technique." Review of Scientific Instruments **75**(8): 2648-2655.

Stone, D., Whalley, L. K., Ingham, T., Edwards, P. M., Cryer, D. R., Brumby, C. A., Seakins, P. W. and Heard, D. E. (2016). "Measurement of OH reactivity by laser flash photolysis coupled with laser-induced fluorescence spectroscopy." Atmospheric Measurement Techniques **9**(7): 2827-2844.

Chapter 5. OH Reactivity Instrument Intercomparison

5.1 Introduction to OH Reactivity Intercomparison

Three techniques are described in the literature for the measurement of OH reactivity; laser flash photolysis coupled with laser induced fluorescence (LFP-LIF), total OH loss rate measurement (TOHLM) and the comparative reactivity method (CRM), these have been described in detail in Chapter 1 with a critical review of the three measurement techniques. A number of comparisons have been reported in the literature for the measurement of OH reactivity. One such is that presented by Zannoni *et al.* (2015) where two CRM OH reactivity instruments were deployed for measurements in the Mediterranean basin. Good agreement was observed between the two instruments in the low NO_x, terpene rich environment. Both of the CRM instruments deployed for this study are based on that described by Sinha *et al.* (2008). Intercomparison of OH reactivity measurements allow for the performance of different measurement methods to be assessed. Intercomparisons of OH reactivity measurements have been reported by Hansen *et al.* (2015) for measurements taken with one LFP-LIF instrument and one CRM instrument in a NO_x rich, urban environment, where the measurements of OH reactivity from the CRM instrument typically lead to an underestimation of OH reactivity as compared to those from the LFP-LIF instrument, due to the photolysis of OH reactive species in the glass reactor of the CRM instrument. An underestimation of ~2 s^{-1} was also observed for measurements carried out with the LFP-LIF instrument, which was attributed to impurities present in the air used to measure the instrumental physical losses, $k'_{OH(physical)}$, highlighting the importance of correct characterisation of $k'_{OH(physical)}$ for LFP-LIF OH reactivity instrumentation. A more detailed review of OH reactivity measurement comparisons has been given in Chapter 1. Instrument comparison studies currently in the literature for OH reactivity measurements have only been carried out for the measurements of ambient air; in these scenarios, it is difficult to ensure instruments are all sampling air with the exact same composition. The use of atmospheric simulation chambers for instrument intercomparisons ensures all instruments are sampling air with the same chemical composition, and experiments can be carried out for a wide range of

atmospherically relevant scenarios. The use of such chambers also allows for measurements of OH reactivity where the absolute OH reactivity can be known from the known concentrations of compounds added to the chamber. A number of different instrument comparison studies have been carried out previously at the SAPHIR chamber (e.g. Schlosser *et al.* (2007), Fuchs *et al.* (2010)).

An informal intercomparison of all OH reactivity measurement techniques was initially proposed at the OH Reactivity Specialists Unity Meeting (ORSUM) in October 2014 (Williams and Brune 2015), where it was decided that the study would take place at the Simulation of Atmospheric Photochemistry In a large Reaction (SAPHIR) chamber in Jülich, Germany. The deployment of as many instruments as possible would allow for the most comprehensive intercomparison of OH reactivity instrumentation to date.

Nine OH reactivity instruments were deployed for the intercomparison study, provided and run by eight research institutions; one TOHLM instrument, four LFP-LIF instruments and four CRM instruments, with the aim to compare all instruments over a range of characterisation experiments and more complex systems sampling mixtures of VOCs, characteristic to those measured in both biogenic and urban environments.

Results from five of these experiments that were the responsibility of the author, will be summarised in this chapter: characterisation measurements for varying H_2O and NO concentrations within SAPHIR, and measurements of OH reactivity sampling mixtures of VOCs typical of an urban environment, under varying NO_x conditions. Results from three other experiments carried out during the OH reactivity instrument intercomparison campaign have been discussed by Cryer (2016), and results from all experiments will form the basis of future publications. A brief overview of results discussed by Cryer (2016) will be given in Section 5.4.

5.2 Introduction to the SAPHIR Chamber

SAPHIR is a 270 m^3 outdoor FEP-Teflon atmospheric simulation chamber based at the Jülich Forschungszentrum, Germany. The chamber is cylindrical in shape, constructed from double-walled Teflon foil which allows for the transmission of sunlight through the chamber walls in order to initiate photochemical reaction processes. The SAPHIR chamber has been designed and constructed in order to allow for multiple shipping containers, housing instrumentation, to be positioned beneath it; Figure 5-1 shows an image of SAPHIR with several shipping containers positioned beneath it, the positioning

of the Leeds FAGE shipping container during the OH reactivity intercomparison is indicated.

Figure 5-1: The SAPHIR chamber at the Jülich Forschungszentrum, Germany. The positioning of the Leeds FAGE shipping container during the OH reactivity instrument intercomparison campaign is labelled.

A louvre roof system, which can be opened or closed within 60 seconds, allows the contents of the chamber to be obscured from, or exposed to, sunlight, allowing for dark reactions and photochemical reactions, initiated by the sunlight, to be investigated. Figure 5-2 shows an image of SAPHIR with the roof shutters open, exposing the chamber contents to sunlight.

Figure 5-2: Image showing the SAPHIR chamber with the roof open to expose the chamber to sunlight for the initiation of oxidation reactions.

Five inlet port panels in the chamber floor allow for numerous analytical instruments to be simultaneously coupled to SAPHIR. Many analytical instruments are housed within shipping containers permanently positioned beneath the chamber. Ancillary measurements made using such instrumentation, alongside OH reactivity measurements during the intercomparison are listed in Table 5-1. Two mixing fans allow for a total mixing time of 60 s within SAPHIR, (one fan is shown in Figure 5-3), and were in operation continuously through all experiments of the intercomparison.

Figure 5-3: Image showing the inside of SAPHIR chamber with the roof system open. One of the two mixing fans and two of the five inlet port panels are labelled.

Species	Instrument
CO	Picarro CRDS
NO	Chemiluminescence
NO_2	Chemiluminescence
VOCs	PTR-TOF-MS
VOCs	GC-FID
Isoprene	GC-FID, PTR-TOF-MS
Toluene	GC-FID, PTR-TOF-MS
HCHO	Hantzsch
o-xylene	GC-FID, PTR-TOF-MS
Acetaldehyde	GC-FID, PTR-TOF-MS
MVK & MACR	PTR-TOF-MS
MVK	GC-FID
MACR	GC-FID
H_2O	CRDS
O_3	UV absorption

Table 5-1: List of instruments used for measurements of species used in the calculation of OH reactivity during the intercomparison. Measurements of VOCs were taken as PTR-TOF-MS data if available at the time when calculations were made. CO = carbon monoxide, NO = nitric oxide, NO_2 = nitrogen dioxide, VOCs = volatile organic compounds, HCHO = formaldehyde, MVK = methyl vinyl ketone, MACR = methacrolein, CRDS = cavity ring down spectroscopy, PTR-TOF-MS = proton transfer - time of flight - mass spectrometer, GC-FID = gas chromatography with flame ionisation detector, UV = ultra violet.

Full details of the construction and measurement techniques employed within SAPHIR have been described previously (Karl *et al.* 2004, Bohn *et al.* 2005, Bohn and Zilken 2005, Rohrer *et al.* 2005). The Teflon construction material of SAPHIR allows it to only

be operated at ambient temperatures, and the chamber is operated at ~50 Pa above ambient pressure.

5.3 OH Reactivity Instrumentation

Nine instruments were used for the measurement of OH reactivity during the OH reactivity intercomparison in October 2015. Details of these instruments are provided in Table 5-2, with the type of measurement technique and relevant references for the specific instrumentation.

Institution	Instrument	Reference
Le Laboratoire des Sciences du Climat et de l'Environment (LSCE) (France)	CRM	Zannoni *et al.* (2016)
University of Lille (France)	LFP-LIF	Hansen *et al.* (2015)
University of Leeds (UK)	LFP-LIF	Stone *et al.* (2016)
Max-Planck Institute for Chemistry (MPIC) (Germany)	CRM	Sinha *et al.* (2008)
Finnish Meteorological Institute (FMI) (Finland)	CRM	Not Available
Mines Douai National Graduate School of Engineering (France)	CRM	Michoud *et al.* (2015)
Jülich Forschingszentrum (FZJ) (Germany)	LFP-LIF	Lou *et al.* (2010)
Jülich Forschingszentrum (FZJ) (Germany)	LFP-LIF	Fuchs *et al.* (2017)
Pennsylvania State University (PSU) (USA)	TOHLM	Kovacs and Brune (2001)

Table 5-2: Details of the institutions involved in the OH reactivity intercomparison at the SAPHIR chamber and the measurement technique used for the measurement of OH reactivity, with relevant references on the specific instrumentation.

All nine OH reactivity instruments were housed within shipping containers beneath the SAPHIR chamber, shown in Figure 5-4. The red shaded container space labelled "Leeds" is where the Leeds FAGE shipping container was positioned throughout the course of this study, housing the LFP-LIF OH reactivity instrument, used in the new inlet configuration as described in Chapter 4. The Lille LFP-LIF instrument was housed in a permanent

shipping container positioned directly opposite the Leeds FAGE shipping container, and both instruments sampled from SAPHIR via the same inlet port in the roof of the chamber. Three CRM OH reactivity instruments were housed in a shipping container to one side of the Leeds FAGE shipping container, all sharing one inlet port. To the other side of the Leeds FAGE shipping container was a temporary shipping container housing the TOHLM OH reactivity instrument from PSU which shared an inlet port with the two LFP-LIF instruments from FZJ, which were housed in a permanent shipping container directly opposite. The LSCE CRM OH reactivity instrument was housed within a permanent shipping container, also housing instrumentation for the measurement of NO_x, to one end of the chamber.

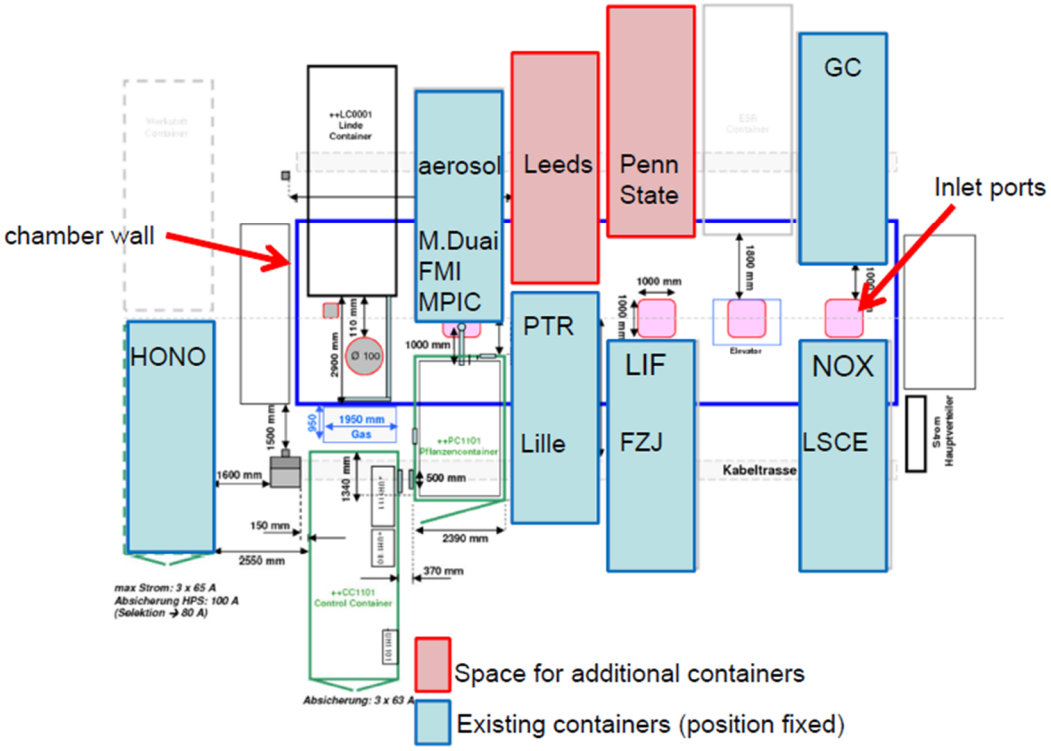

Figure 5-4: Schematic showing the positioning of shipping containers and the instrumentation housed within them during the course of the OH reactivity intercomparison campaign during October 2015. Containers shaded blue are permanently positioned at SAPHIR, containers shaded red are positioned only for the purpose of this work. Provided by Dr. Hendrik Fuchs.

Due to a number of technical problems during the intercomparison, FMI were not able to obtain reliable data. Throughout the work discussed in this chapter, "LIF 4" refers to the Leeds LFP-LIF OH reactivity instrument. All data from the remaining seven OH reactivity instruments are anonymised in the following sections; the identity of the

instruments responsible for each set of measurements will be revealed in future publications.

5.4 Experimental Details

A total of ten experiments were carried out during the OH reactivity intercomparison at the SAPHIR chamber in October 2015, a number of which have been discussed by Cryer (2016), focussing on a comparison the Leeds LFP-LIF OH reactivity measurements with measurements from other instrumentation involved in the measurement study, details of which are given in Table 5-3. The following sections of this chapter will focus on five experiments; 2, 3, 6, 7 and 9.

	Experimental Details	**Reference**
Experiment 1	Linearity test of CO	Cryer (2016)
Experiment 2	Test of H_2O with CO / CH_4	This work
Experiment 3	Test of NO with CO / CH_4	This work
Experiment 4	Monoterpene Mix	Cryer (2016)
Experiment 5	Linearity test of CO / Isoprene	Not Available*
Experiment 6	Urban mixture with NO_x variations	This work
Experiment 7	Urban mixture with NO_x	This work
Experiment 8	Plant chamber emissions	Cryer (2016)
Experiment 9	CO with NO_x	This work
Experiment 10	Sesquiterpene (beta caryophyllene) and OVOCs	Not Available*

Table 5-3: List of experiments carried out during the OH reactivity intercomparison at SAPHIR in October 2015. Five of which are discussed in this work; test of H_2O with CO/CH_4, test of NO with CO/CH_4, urban mixture with NO_x variations, urban mixture with NO_x and CO with NO_x. Results from all experiments will be discussed in future publications with the identity of each instrument being revealed. *Results from these experiments have yet to be interpreted for comparison.

Between each experiment, SAPHIR was flushed with high purity synthetic air (total ~2200 m^3 synthetic air used) in order to clean the chamber so that trace gases were below their instrument detection limits. All LIF instruments require H_2O in order to generate

OH radicals, and so in all experiments, unless otherwise stated, SAPHIR was initially flushed with humidified synthetic air to reach a relative humidity of ~75%. Following this, a period of ~1 hour elapsed for instruments to measure a "chamber zero" before the addition of any OH reactive species.

Results from experiment 1, reported by Cryer (2016), showed that all OH reactivity instruments tracked the calculated OH reactivity from CO well, with more scatter being observed, particularly for lower values of k'_{OH}, for measurements by CRM instruments, which is attributed to the small changes in pyrrole concentration being observed for such k'_{OH} values. Two more complex experiments (4 and 8) were also described by the author; representative of VOC mixtures expected to be sampled in air highly influenced by biogenic emissions. Again, all OH reactivity instruments tracked the calculated OH reactivity well, with more scatter observed from CRM instrument measurements, with a tendency to under predict the calculated OH reactivity. In both of these experiments, ozone was added to the chamber in order to initiate ozonolysis reactions; following this, all instruments tracked the calculated OH reactivity well, however, greater deviations from the calculated OH reactivity were observed. This deviation following the ozonolysis reactions was attributed to unmeasured OH reactive ozonolysis products.

5.4.1 Addition of H_2O with CO / CH_4

OH reactivity measurements that are carried out in the field, do so over a wide range of humidities. Correct characterisation of OH reactivity instrumentation under atmospherically relevant variations in [H_2O] present in the gas sample is vital in order to determine whether any instrument shows a dependence or any interferences from [H_2O]. Throughout the course of this experiment, the roof shutters remained closed, keeping the contents of the chamber in the dark. Following humidification, O_3 (~80 ppbv) was added to the SAPHIR chamber to allow LIF instruments to produce OH within the flow tube of the instruments. A zero measurement period of ~1 hour passed before the addition of CO and CH_4, to give a total OH reactivity of ~20 s^{-1}. Humidification and the addition of CO and CH_4 (to maintain a total reactivity of ~20 s^{-1}) to SAPHIR was repeated a further three times, reaching a final relative humidity of ~83%. An addition of NO_2 (~10 ppbv) was also made at the end of the experiment at ~15:20:00.

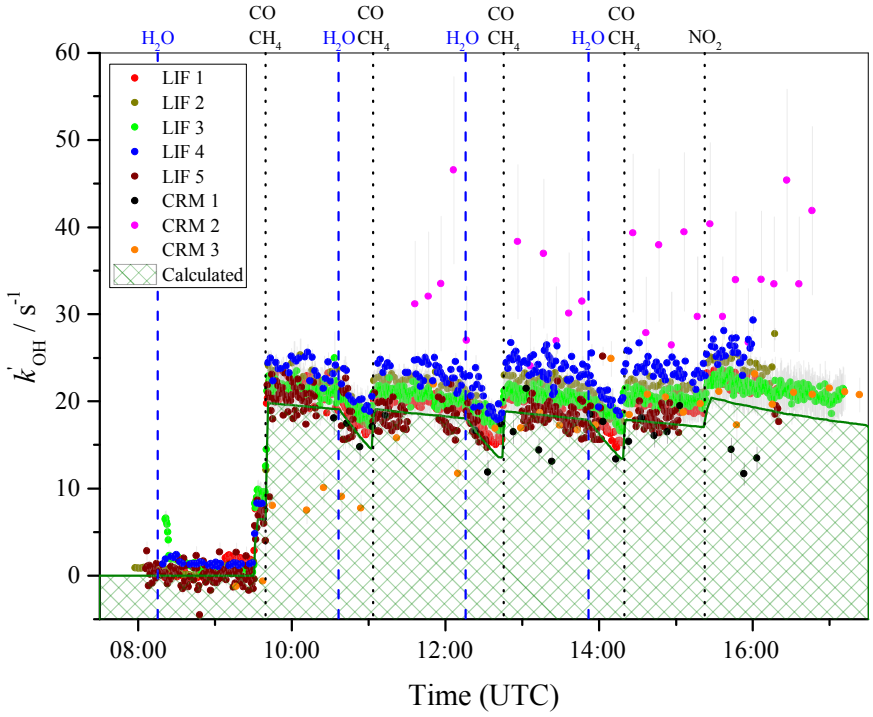

Figure 5-5: Time series of the measurement of k'_{OH} by eight instruments in the SAPHIR chamber. Water was added to SAPHIR in four stages to increase the humidity from ~20%, reaching a final relative humidity of ~83%. CO and CH_4 were also added to SAPHIR following humidification in order to give a calculated OH reactivity of ~20 s^{-1} to allow for all instruments to measure well above their LODs. The green hatched area represents the calculated OH reactivity attributed to the CO, CH_4 and NO_2 added to SAPHIR, as well as measured contributions from NO and HCHO. Measurements labelled "LIF 4" were made using the Leeds LFP-LIF OH reactivity instrument.

All instruments followed the time profile of the calculated OH reactivity well, with greater scatter observed for measurements from the three CRM instruments. Agreement is particularly good between LIF instruments. Measurements from CRM instruments are generally more scattered, with CRM 1 and CRM 2 being generally lower than the measurements from the LIF instruments, and CRM 2 being higher than the LIF instrument measurements and calculated OH reactivity. Measurements with the LIF 4 (Leeds) instrument are in good agreement with the calculated OH reactivity and other LIF instruments, however, there is an offset of ~2 s^{-1} above measurements from other LIF instruments. This offset is also seen in the "zero" measurement period (~08:00 – 09:30, where only H_2O and O_3 were present in SAPHIR), and it is concluded to be due to residual species present in the sampling line and minor leaks within the instrument. The results from this experiment show that, especially for the LIF instruments, that no dependence on relative humidity of OH reactivity measurements is observed.

The Leeds LFP-LIF (LIF 4) instrument shows very good agreement with other LIF instruments and the calculated OH reactivity. This agreement, and absence of any dependence on the water concentration, shows the reliability of the measurements from the Leeds LFP-LIF instrument for a range of environments, including field measurements and chamber measurements, such as those that are discussed in Chapter 8, where the relative humidity in HIRAC can vary considerably depending on the chemical reactions under investigation.

5.4.2 Addition of NO with CO / CH_4

OH reactivity measurements are often carried out in urban areas where levels of NO_x can vary greatly, with some environments having extremely high levels of NO_x; concentrations of up to 200 ppbv have been reported from measurement sites in London (Jenkin 2014) . As has been discussed in Chapter 4, for LIF instruments, increased levels of NO present in the gas being sampled, may lead to recycled OH within the flow tube of the instruments, artificially enhancing the [OH] and affecting the measurement of OH reactivity. This experiment aimed to test the influence of varying NO concentrations on the measured OH reactivity from all instruments. The chamber was initially flushed with humidified synthetic air. As high concentrations of NO were to be investigated for this experiment, no O_3 was added to the chamber, and so O_3 was required to be added directly into the LIF instruments in order to facilitate the production of OH radicals within the flow tube of the instruments. For the Leeds LFP-LIF instrument (LIF 4), 1 l min^{-1} synthetic air was passed over a mercury pen ray lamp and combined with a 15 l min^{-1} sample drawn from SAPHIR, giving ~60 ppbv O_3 in the total gas sampled by the instrument. A correction was made to account for this dilution in the analysis process. Following the humidification of SAPHIR, no further additions were made for ~1 hour in order to allow for a "zero" measurement period. CO and CH_4 were then added to SAPHIR to reach ~20 s^{-1} OH reactivity. A further ~1 hour period passed before NO was added to SAPHIR. Three further NO additions were made to SAPHIR; following which, CO and CH_4 were added in order to maintain an OH reactivity of ~20 s^{-1}. A further three NO injections were made following this. The time series of the measurements of OH reactivity from seven instruments is shown in Figure 5-6 for this experiment. Due to technical problems with the instrument, CRM 1 was unable to make reliable OH reactivity measurements during this experiment.

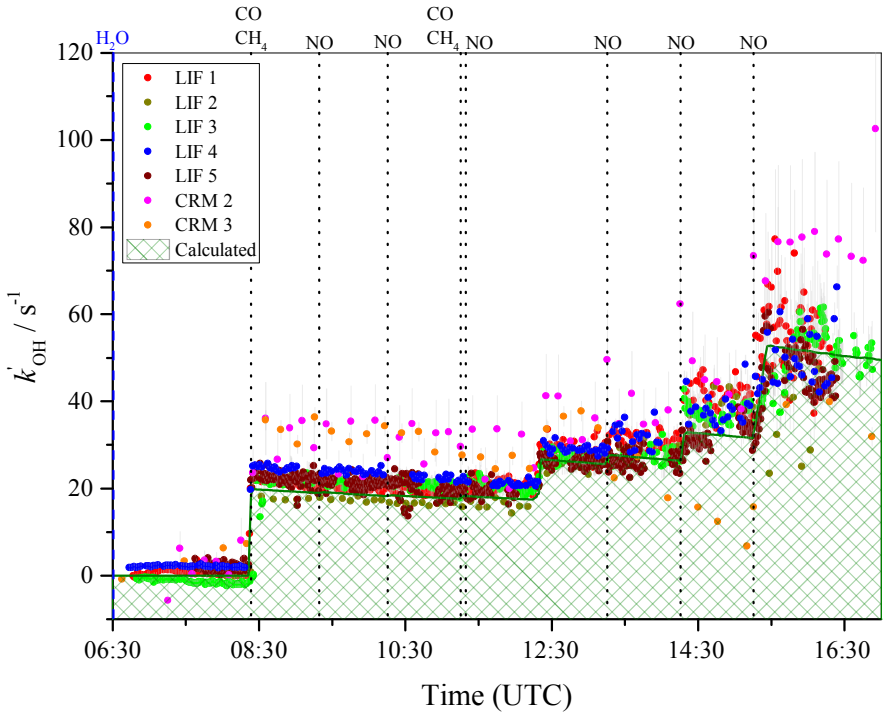

Figure 5-6: Time series of the measurement of k'_{OH} by seven instruments in the SAPHIR chamber. Seven additions of NO were made to SAPHIR, with two additions of CO/CH_4 to give a reactivity of ~20 s^{-1}. The green hatched area represents the calculated OH reactivity attributed to the CO, CH_4 and NO_2 added to SAPHIR, as well as measured contributions from NO and HCHO. Measurements labelled "LIF 4" were made using the Leeds LFP-LIF OH reactivity instrument. Dashed blue vertical line represents when SAPHIR was humidified and dotted black vertical lines represent the times at which species were added to SAPHIR.

Again, all instruments track the profile of the calculated OH reactivity well, with the LIF 4 (Leeds) instrument showing particularly good agreement with the profiles of the other LIF instruments. Following the fifth addition of NO to SAPHIR, resulting in a total [NO] ~ 15 ppbv, greater deviation from the calculated OH reactivity was observed for all instruments.

Measurements of OH reactivity made by LIF instruments are prone to the influence from OH recycling by NO in the flow tube of the instruments at high concentrations of NO_x present in the sampled gas. LIF type instruments where OH radicals are produced by water photolysis (TOHLM) produce high concentrations of HO_2 within the flow tube under normal operating conditions:

$H_2O + h\nu_{(184.9\,nm)} \rightarrow OH + H$ R 5-1

$H + O_2 + M \rightarrow HO_2 + M$ R 5-2

and so simultaneous measurements of ambient NO concentrations are made in order to correct for the formation of OH within the flow tube following:

$HO_2 + NO \rightarrow OH + NO_2$ R 5-3

LFP-LIF instruments do not produce high concentrations of HO_2 in the flow tube under normal operating conditions, however, under certain conditions, production of HO_2 or RO_2 within the flow tube of the instrument may lead to the formation of OH by reaction with NO:

$CO + OH \rightarrow H + CO_2$ R 5-4

$H + O_2 + M \rightarrow HO_2 + M$ R 5-5

$CH_4 + OH + O_2 \rightarrow CH_3O_2 + H_2O$ R 5-6

$CH_3O_2 + NO \rightarrow CH_3O + NO_2$ R 5-7

$CH_3O + O_2 \rightarrow HO_2 + HCHO$ R 5-8

$HO_2 + NO \rightarrow OH + NO_2$ R 5-9

In the experiment described here, the recycling of NO to produce OH in the flow tube of the Leeds LFP-LIF instrument was observed by bi-exponential OH decay profiles, following a total NO concentration >15 ppbv in SAPHIR. This is shown in Figure 5-7 where the data have been fitted with a single exponential fitting function (a) and a bi-exponential fitting function (b). Figure 5-8 shows a comparison of data fitted with a single exponential function, and where data has been fitted with a bi-exponential function for [NO] > 15 ppbv in SAPHIR, against the calculated OH reactivity. The measured OH reactivity follows the same time profile as the calculated OH reactivity when k'_{OH} has been extracted using a bi-exponential fitting fuction. Model simulations carried out by Stone *et al.* (2016) for similar experimental conditions where CO, CH_4 and NO are present showed that neither the single exponential or the bi-exponential fitting functon

returned the true value of k'_{OH}, however, at values of [NO] > 15 ppbv, the bi-expoential fitting function returns a value closer to that of the true value.

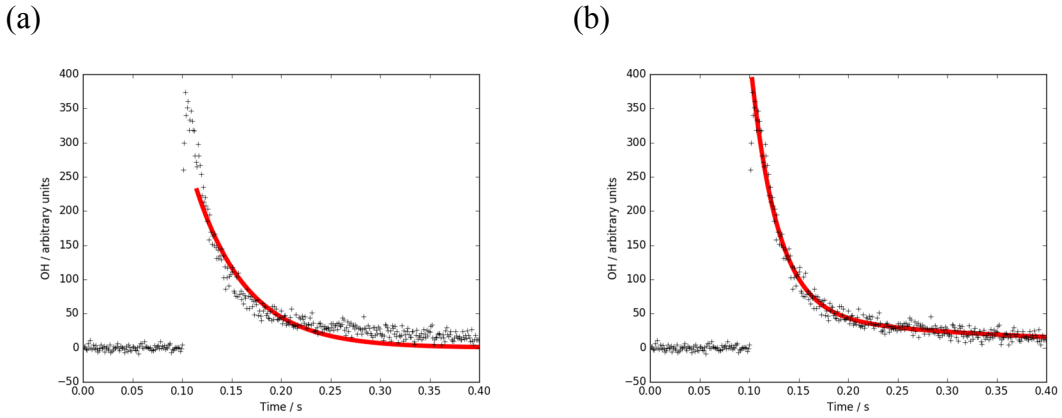

Figure 5-7: Example bi-exponential decay profile as obseverved at high NO_x concentrations (NO = 40 ppbv for data shown). (a) data fitted with single exponential function, resulting in a value of $k'_{OH(raw)}$ = 19.22 ± 0.58 s^{-1}. (b) data fitting with bi-exponential function, resulting in a value of $k'_{OH(raw)}$ = 37.2 ± 1.1 s^{-1}, where the fast component of the decay is used as an estimation for the measured value of k'_{OH}.

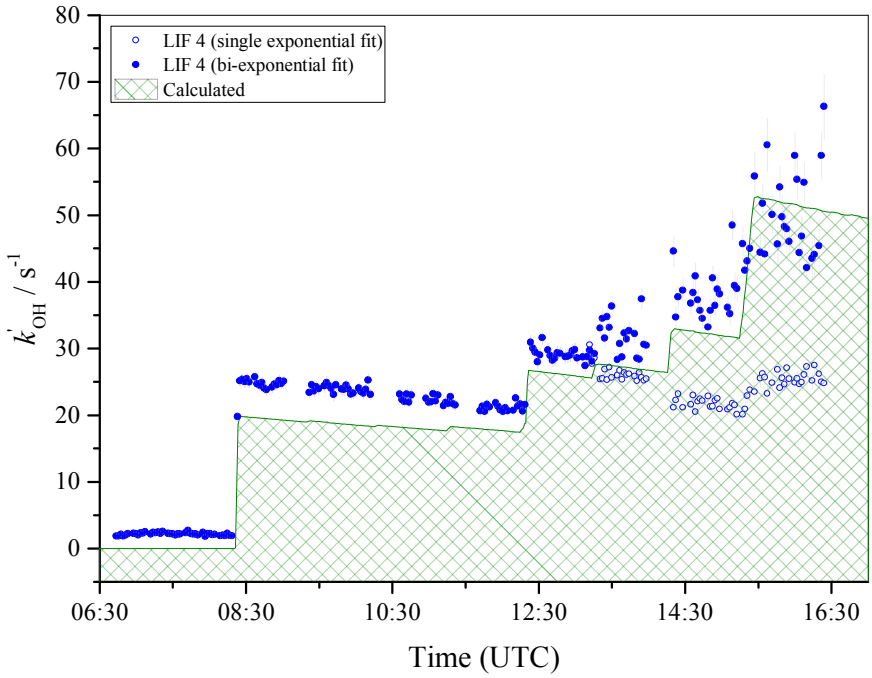

Figure 5-8: Time series of k'_{OH} as measured by the Leeds LFP-LIF (LIF 4) instrument compared to the calculated OH reactivity. Open blue circles represent data fitted with a single exponential function and filled blue circles represent data fitted with a bi-exponential function to extract a value of k'_{OH}.

As OH radicals are produced within the flow tube of the LIF instruments following reactions R 5-4 to R 5-9, this would be observed as an artificial growth in OH to a

maximum, which then decays. When this artificially enhanced OH production and decay is combined with relatively fast OH decay from the true OH reactivity measurement, this is observed as a bi-exponential decay profile. The artificially produced OH decay occurs on a relatively long time scale as compared to the true OH decay, at longer times, the generated OH has a greater influence on the true OH decay.

5.4.3 CO with NO_x

A third experiment was carried out where OH reactivity measurements from SAPHIR were taken in the presence of CO and NO_x. Following a chamber "zero" measurement period of ~1 hour, three additions of CO were made to the chamber. Two injections of 2,3-dimethylbutene were made to SAPHIR in order to quench any O_3 present, observed by two spikes in OH reactivity at ~11:45:00 and ~12:45:00. Following this, O_3 was added directly to the LIF instruments as described above. The time series for this experiment is shown in Figure 5-9. Following the removal of O_3 from SAPHIR by the addition of an alkene, three additions of NO were made.

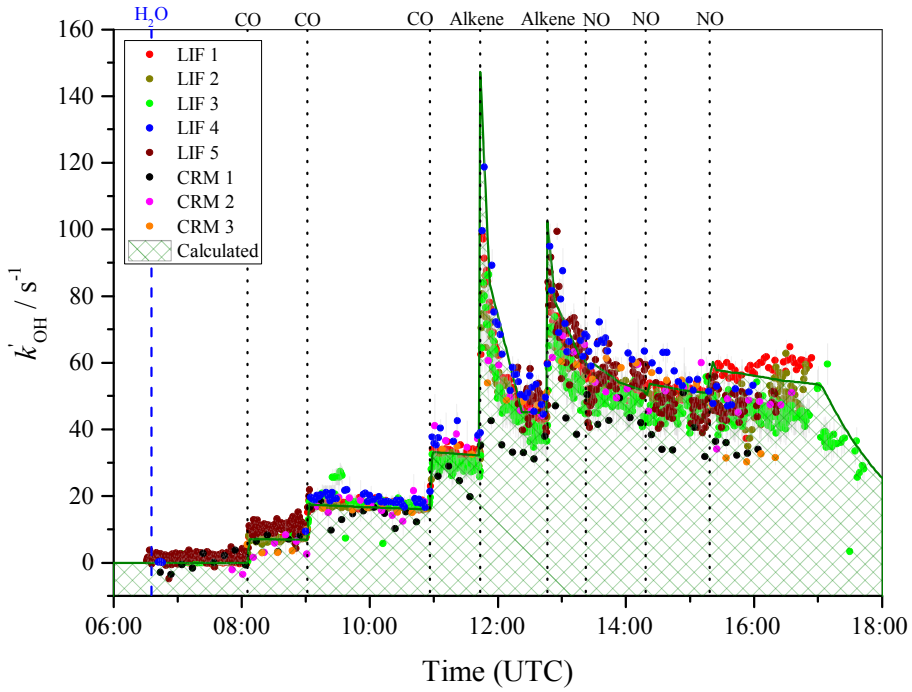

Figure 5-9: Time series of the measurement of k'_{OH} by eight instruments in the SAPHIR chamber. Measurements were carried out sampling from SAPHIR with multiple additions of CO and NO. The green hatched area represents the calculated OH reactivity in SAPHIR. Measurements labelled "LIF 4" were made using the Leeds LFP-LIF OH reactivity instrument. Dashed blue vertical line represents when SAPHIR was humidified and dotted black vertical lines represent the times at which species were added to SAPHIR.

The OH reactivity measurements from all instruments track the time profile of the calculated OH reactivity very well. Due to a loss of power to the Leeds FAGE shipping container, OH reactivity measurements from the LIF 4 instrument were only made from 09:00:00 onwards. A large spike to ~150 s^{-1} OH reactivity was observed following the first injection of 2,3-dimethylbutene to SAPHIR, with a smaller spike to ~100 s^{-1} following the second injection of 2,3-dimethylbutene. At these two spikes, the LIF instruments follow the time profile of the calculated OH reactivity extremely well, showing their excellent time resolution and sensitivity in measurements. The three CRM instrument measurements observe smaller spikes in the OH reactivity measurements; CRM OH reactivity instruments have poorer time resolution (making one OH reactivity measurements every 600 – 900 seconds, compared to one measurement every 30 – 160 seconds for LIF instruments), and so are unable to track such rapid fluctuations in OH reactivity.

Following the addition of 2,3-dimethylbutene to SAPHIR, good agreement between all LIF instruments is observed. Following the second addition of 2,3-dimethylbutene to SAPHIR, measurements by LIF 4 (Leeds) are slightly higher than the calculated OH reactivity, whereas measurements from LIF 1, LIF 2, LIF 3 and LIF 4 are slightly lower than the calculated OH reactivity. As the calculated OH reactivity is only determined from a small number of measured VOCs, this value is likely not the exact OH reactivity within SAPHIR during the experiments. The differences between the measured and calculated OH reactivities, however, indicate the presence of some systematic uncertainties for measurements from the different LIF instruments following the addition of an alkene, likely arising from unmeasured ozonolysis products from the reaction of 2,3-dimethylbutene with O_3.

Measurements of OH reactivity from CRM 1 are seen to be consistently lower than all the other OH reactivity measurements following the addition of 2,3-dimethylbutene to SAPHIR. As suggested for the LIF measurements, this may also arise due to interferences within the instrument following the addition of an alkene into the measured gas and any related ozonolysis products and intermediate species. Measurements from CRM 2 agree very well with the calculated OH reactivity and the majority of other measurements at all times throughout the experiment. Following the final addition of NO to SAPHIR, greater deviation from the calculated OH reactivity was observed for OH reactivity measurements; it is possible that the concentration of NO at this point has reached values

such that OH recycling within the flow tube of the LIF instruments was more significant than expected.

5.4.4 Measurements of an urban VOC mixture in the presence of NO_x

In order to test the performance of the OH reactivity instruments to more complex systems, experiments were carried out with an "urban" mixture of VOCs, characteristic of typical VOC mixtures sampled in urban areas, in the presence of NO_x. The urban mixture consisted of 1-pentene (42% OH reactivity), toluene (14% OH reactivity) and *o*-xylene (44% OH reactivity). For the first of these experiments, shown in Figure 5-10, measurements were carried out with multiple additions of NO_2 to SAPHIR. Following the "zero" chamber measurement period, the urban VOC mixture was injected into the chamber. Approximately 20 minutes following this, the chamber roof was opened to expose the contents of the chamber to sunlight, allowing for the photolysis of NO_2 for the remainder of the experiment, to give an atmospherically relevant ratio of NO_2 : NO. A period of ~1 hour elapsed after opening the chamber roof prior to the first addition of NO_2. Four further NO_2 additions were made before a second addition of the urban VOC mixture was injected into SAPHIR. One final addition of NO_2 was made to SAPHIR ~1 hour following this.

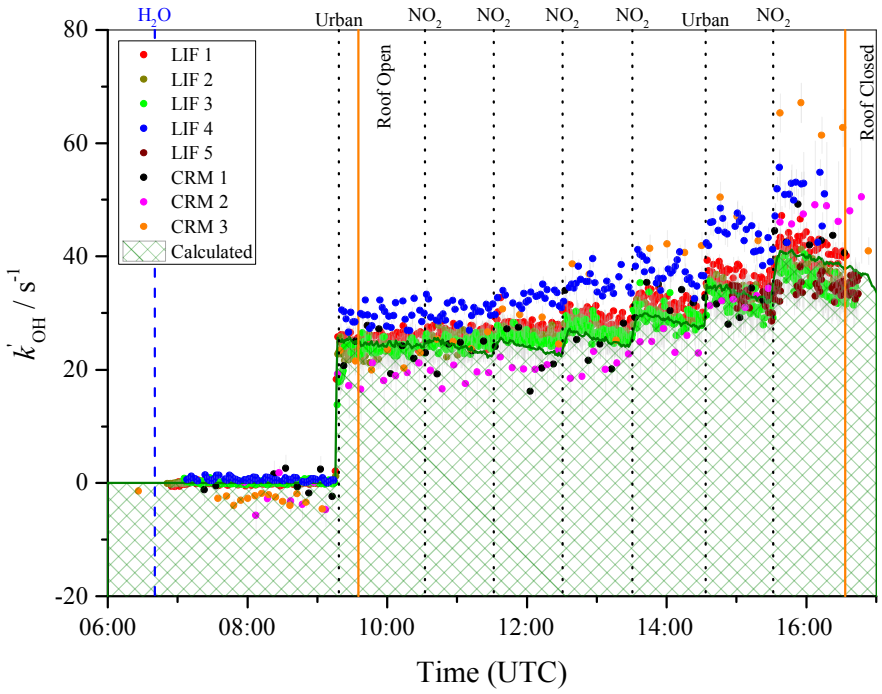

Figure 5-10: Time series of the measurement of k'_{OH} by eight instruments in the SAPHIR chamber. Measurements were carried out sampling an urban VOC mixture from SAPHIR with sequential additions of NO_2. The roof shutters were opened, at 09:35, in order to produce atmospherically relevant ratio of NO_2 : NO within the chamber. The green hatched area represents the calculated OH reactivity in SAPHIR. Measurements labelled "LIF 4" were made using the Leeds LFP-LIF OH reactivity instrument. The dashed blue vertical line shows the time at which SAPHIR was humidified, the dotted black vertical lines represent the times at which reactive species were added to SAPHIR, and the solid orange vertical lines represent the time at which the chamber roof shutters were opened and closed.

A second experiment was carried out with the same urban VOC mixture, where only two additions of NO_2 were made to SAPHIR. Figure 5-11 shows the time series of the OH reactivity measurements from eight instruments, and the calculated OH reactivity. Following a period of ~1 hour for a chamber "zero" measurement, NO_2, CO and an urban VOC mixture were added to SAPHIR. An hour of measurements were taken before a second addition of the urban VOC mixture was made. The SAPHIR roof shutters were opened ~1 hour following this, to allow for the photolysis of NO_2. A further NO_2 injection was added ~1 hour after the chamber roof was opened, and two further additions of the urban VOC mixture were made.

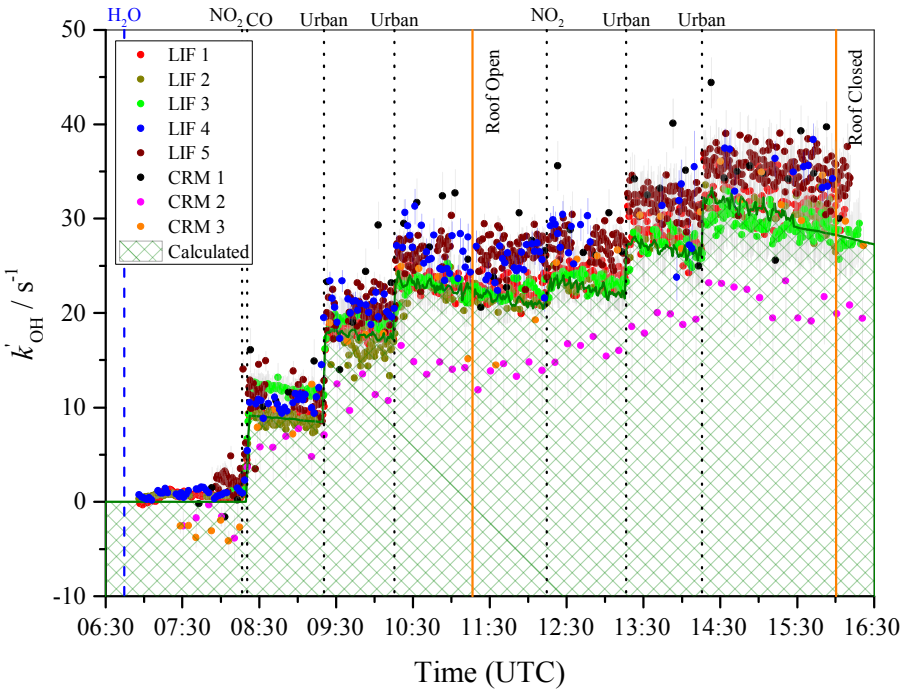

Figure 5-11: Time series of the measurement of k'_{OH} by eight instruments in the SAPHIR chamber. Measurements were carried out sampling from SAPHIR with multiple additions of an urban VOC mixture and two additions of NO_2. The roof shutters were opened, at 11:15, in order to expose the contents of SAPHIR to sunlight and to allow for the photolysis of NO_2 within the reaction mixture. The green hatched area represents the calculated OH reactivity in SAPHIR. Measurements labelled "LIF 4" were made using the Leeds LFP-LIF OH reactivity instrument. The dashed blue vertical line indicates when SAPHIR was humidified, the dotted black vertical lines indicate the times at which reactive species were added to SAPHIR, and the solid orange vertical lines indicate the time at which the roof shutters were opened and closed.

All instrument measurements track the profile of the calculated OH reactivity well. For the first two VOC additions, agreement of measurements from CRM 2 with all other instruments and the calculated OH reactivity is good; following the third step increase in OH reactivity, CRM 2 is no longer in good agreement. Although CRM 2 shows poor agreement following the third step increase in OH reactivity, the measurements from the instrument follow the same time profile in OH reactivity through the following step increases in reactivity to the end of the experiment. The observation here of lower OH reactivity measurements from CRM 2 instrument at higher NO_x concentrations present in SAPHIR is similar to that observed in the previous experiment.

Measurements from the LIF 3 instrument are in excellent agreement with calculated OH reactivity at later times during the experiment; following the third step increase in OH reactivity and onwards. Poorer agreement is seen for measurements from the LIF 3 instrument following the first two step increases in OH reactivity. Excellent agreement is

seen for measurements from the LIF 1 and LIF 2 instruments with calculated OH reactivity throughout the entire experiment. The Leeds LFP-LIF (LIF 4) and LIF 5 instruments are seen to typically measure OH reactivity higher than the measurements from the LIF 1 and LIF 2 instruments, and the calculated OH reactivity. Both the LIF 4 and LIF 5 instruments show a positive offset in OH reactivity measurements as compared to the calculated during the chamber "zero" period at the beginning of the experiment, suggesting that, similar to the experiments discussed in Section 5.4.1, contamination within the sampling lines or small leaks within the instruments may be influencing the OH reactivity measurements from these instruments. Measurements from the LIF 4 (Leeds) instrument are typically more scattered for reactivities $\geq$30 s^{-1}, however, stated errors are typically within errors of the measurements from other LIF instruments.

5.4.5 Correlations

To gain an insight into the performance of all instruments across the entire study, the relationship between the measured OH reactivity, with the calculated OH reactivity is shown in Figure 5-12. In order to give an indication as to the performance of instruments, data only for experiments when CO and CH_4 were present in SAPHIR are shown in these correlations; measurements following oxidation and photolysis reactions are excluded as reaction products are not included in the calculation of k'_{OH} and so the calculated OH reactivity would not be representative of the true OH reactivity within the air being sampled. Very good agreement is observed between all instrument measured OH reactivity and the calculated OH reactivity for all experiments, especially for measurements from the LIF instruments.

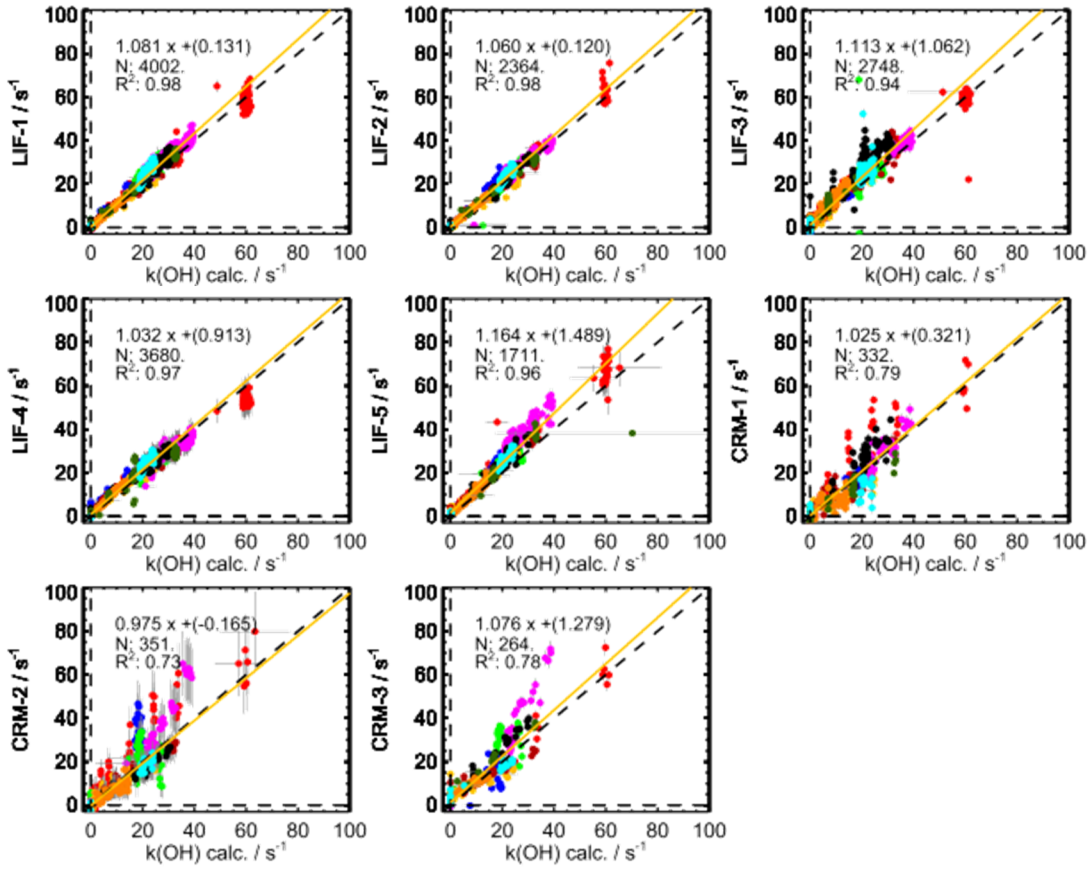

Figure 5-12: Correlation plots showing the relationship between measured OH reactivity from eight instruments with calculated OH reactivity for all ten experiments conducted during the OH reactivity intercomparison in October 2015. Each different colour represents a different experiment. Measurements labelled "LIF 4" are those carried out with the Leeds LFP-LIF OH reactivity instrument. Provided by Dr. Hendrik Fuchs.

Figure 5-13 shows the difference between the measured OH reactivity from seven of the OH reactivity instruments, and the calculated OH reactivity as a function of NO concentration in SAPHIR (due to technical issues with CRM 1 during Experiment 3, data from this instrument has not been included for this comparison).

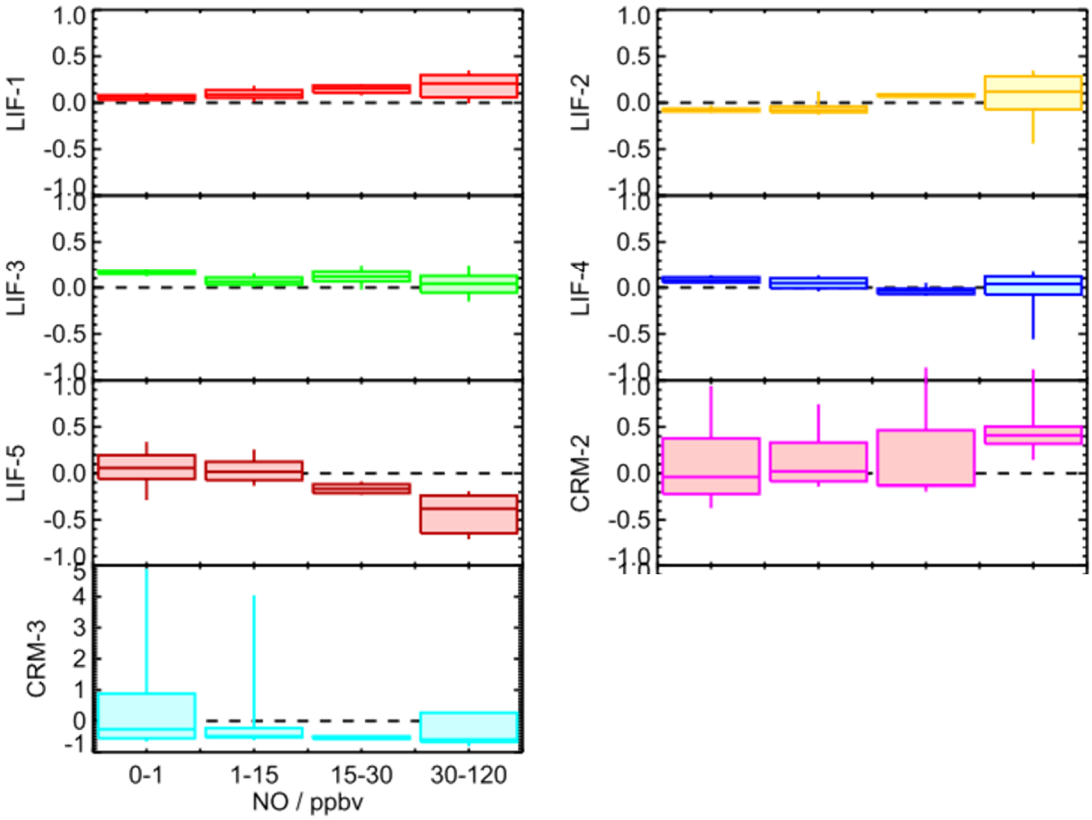

Figure 5-13: Relative differences between measured and calculated OH reactivity for the experiment on the test of NO with CO / CH_4 for measurements of OH reactivity from the seven instruments able to measure during this experiment. LIF 4 refers to measurements from the Leeds LFP-LIF instrument. Provided by Dr. Hendrik Fuchs.

For all LIF type instruments only minor differences were observed between the measured and calculated OH for all NO concentrations, with the difference increasing with NO concentration in the gas sampled from SAPHIR. A greater difference was observed for all of the LIF instruments at the highest NO concentrations; this is attributed to the change in the data analysis procedure. A bi-exponential fitting function has been used in the data analysis for LIF instruments at the highest NO concentrations, which gives only an approximation to the true OH reactivity value, as has been described in Chapter 4. Much greater differences in the measured and calculated OH reactivity for all of the CRM instruments were observed at all NO concentrations, however, no systematic dependence on the NO concertation was observed.

5.5 Conclusions

Overall, all of the OH reactivity instruments performed well for the duration of the intercomparison at SAPHIR in October 2015, with very few unplanned gaps in measurements from a small number of instruments. It should be noted that the results presented and discussed in this chapter are preliminary; further detailed analysis of data

is being carried out by researchers at the Jülich Forschungszentrum, Germany, and will be presented in future publications. Agreement between all instruments and the calculated OH reactivity is generally good, particularly for measurements of "simple" reaction mixtures for measurements where concentrations of species were well known (e.g CO, CH_4, urban VOC mixture). Deviations from the calculated OH reactivity were 3 – 16% for all instruments in the correlations shown in Figure 5-12. The difference between the measured and calculated OH reactivity for all instruments was observed to increase with more complex reaction mixtures such as the initiation of ozonolysis and photolysis reactions within the chamber. The increased difference between measured and calculated OH reactivity in these cases is due to the relatively small number of OH reactive species that were measured; ozonolysis and photolysis reaction intermediates and products were not measured, leading to an underestimation in the calculated OH reactivity.

CRM instruments show more scatter than LIF instruments due to their lower precision and accuracy, especially at low values of OH reactivity due to the large number of corrections required in the data analysis process. LIF instruments all show good precision, however, scatter is seen to increase with increasing values of k'_{OH} due to their reduced accuracy for the measurement of higher OH reactivity values. This was typically seen for measured values of $k'_{OH} > 50$ s^{-1}; values which are generally higher than those measured under ambient conditions. Measurements of high OH reactivity (>50 s^{-1}), however, are useful in chamber studies where VOC concentrations are often required to be higher than in the atmosphere to allow instruments to measure their concentrations reliably above their detection limits and for an appreciable reaction timescale; results from experiments carried out in the HIRAC chamber (given in Chapter 8) are typically 30 – 60 minutes in duration with starting concentrations of VOC ~3×10^{13} molecule cm^{-3}.

A number of significant findings were made for instruments during the OH reactivity intercomparison. The importance of correct characterisation for CRM instruments over a range of normal operating parameters is already known (Michoud *et al.* 2015), however, a previously unknown dependence on O_3 concentrations was observed for one of the CRM instruments during this study, leading to an initial underestimation in the measured OH reactivity prior to corrections being applied to the data for this interference.

Significant influence from NO recycling in LFP-LIF instruments was observed as OH decay profiles changed from single exponential to bi-exponential at [NO] > 15 ppbv. Fitting of a bi-exponential function to this data returns a value of k'_{OH} giving a close estimation to that of the true value of k'_{OH}. Bi-exponential decay profiles have only been

reported once previously for ambient measurements (Lou *et al.* 2010) as a result of NO recycling within the flow tube of the instrument.

5.6 References

Bohn, B., Rohrer, F., Brauers, T. and Wahner, A. (2005). "Actinometric measurements of NO_2 photolysis frequencies in the atmosphere simulation chamber SAPHIR." Atmospheric Chemistry and Physics **5**(2): 493-503.

Bohn, B. and Zilken, H. (2005). "Model-aided radiometric determination of photolysis frequencies in a sunlit atmosphere simulation chamber." Atmospheric Chemistry and Physics **5**(1): 191-206.

Cryer, D. R. (2016). Measurements of hydroxyl radical reactivity and formaldehyde in the atmosphere. PhD, Leeds.

Fuchs, H., Brauers, T., Dorn, H. P., Harder, H., Häseler, R., Hofzumahaus, A., Holland, F., Kanaya, Y., Kajii, Y., Kubistin, D., Lou, S., Martinez, M., Miyamoto, K., Nishida, S., Rudolf, M., Schlosser, E., Wahner, A., Yoshino, A. and Schurath, U. (2010). "Technical Note: Formal blind intercomparison of HO_2 measurements in the atmosphere simulation chamber SAPHIR during the HOxComp campaign." Atmospheric Chemistry and Physics **10**(24): 12233-12250.

Fuchs, H., Tan, Z., Lu, K., Bohn, B., Broch, S., Brown, S. S., Dong, H., Gomm, S., Häseler, R., He, L., Hofzumahaus, A., Holland, F., Li, X., Liu, Y., Lu, S., Min, K. E., Rohrer, F., Shao, M., Wang, B., Wang, M., Wu, Y., Zeng, L., Zhang, Y., Wahner, A. and Zhang, Y. (2017). "OH reactivity at a rural site (Wangdu) in the North China Plain: contributions from OH reactants and experimental OH budget." Atmospheric Chemistry and Physics **17**(1): 645-661.

Hansen, R. F., Blocquet, M., Schoemaecker, C., Léonardis, T., Locoge, N., Fittschen, C., Hanoune, B., Stevens, P. S., Sinha, V. and Dusanter, S. (2015). "Intercomparison of the comparative reactivity method (CRM) and pump–probe technique for measuring total OH reactivity in an urban environment." Atmospheric Measurement Techniques **8**(10): 4243-4264.

Jenkin, M. E. (2014). "Investigation of the impact of short-timescale NO_x variability on annual mean oxidant partitioning at UK sites." Atmospheric Environment **90**: 43-50.

Karl, M., Brauers, T., Dorn, H. P., Holland, F., Komenda, M., Poppe, D., Rohrer, F., Rupp, L., Schaub, A. and Wahner, A. (2004). "Kinetic Study of the OH-isoprene and O_3-isoprene reaction in the atmosphere simulation chamber, SAPHIR." Geophysical Research Letters **31**(5).

Kovacs, T. A. and Brune, W. H. (2001). "Total OH loss rate measurement." Journal of Atmospheric Chemistry **39**(2): 105-122.

Lou, S., Holland, F., Rohrer, F., Lu, K., Bohn, B., Brauers, T., Chang, C. C., Fuchs, H., Häseler, R., Kita, K., Kondo, Y., Li, X., Shao, M., Zeng, L., Wahner, A., Zhang, Y., Wang, W. and Hofzumahaus, A. (2010). "Atmospheric OH reactivities in the Pearl River Delta – China in summer 2006: measurement and model results." Atmospheric Chemistry and Physics **10**(22): 11243-11260.

Michoud, V., Hansen, R. F., Locoge, N., Stevens, P. S. and Dusanter, S. (2015). "Detailed characterizations of the new Mines Douai comparative reactivity method instrument via laboratory experiments and modeling." Atmospheric Measurement Techniques **8**(8): 3537-3553.

Rohrer, F., Bohn, B., Brauers, T., Bruning, D., Johnen, F. J., Wahner, A. and Kleffmann, J. (2005). "Characterisation of the photolytic HONO-source in the atmosphere simulation chamber SAPHIR." Atmospheric Chemistry and Physics **5**: 2189-2201.

Schlosser, E., Bohn, B., Brauers, T., Dorn, H.-P., Fuchs, H., Häseler, R., Hofzumahaus, A., Holland, F., Rohrer, F., Rupp, L., Siese, M., Tillmann, R. and Wahner, A. (2007). "Intercomparison of Two Hydroxyl Radical Measurement Techniques at the Atmosphere Simulation Chamber SAPHIR." Journal of Atmospheric Chemistry **56**(2): 187-205.

Sinha, V., Williams, J., Crowley, J. N. and Lelieveld, J. (2008). "The Comparative Reactivity Method - a new tool to measure total OH Reactivity in ambient air." Atmospheric Chemistry and Physics **8**(8): 2213-2227.

Stone, D., Whalley, L. K., Ingham, T., Edwards, P. M., Cryer, D. R., Brumby, C. A., Seakins, P. W. and Heard, D. E. (2016). "Measurement of OH reactivity by laser flash photolysis coupled with laser-induced fluorescence spectroscopy." Atmospheric Measurement Techniques **9**(7): 2827-2844.

Williams, J. and Brune, W. (2015). "A roadmap for OH reactivity research." Atmospheric Environment **106**: 371-372.

Zannoni, N., Dusanter, S., Gros, V., Sarda Esteve, R., Michoud, V., Sinha, V., Locoge, N. and Bonsang, B. (2015). "Intercomparison of two comparative reactivity method instruments in the Mediterranean basin during summer 2013." Atmospheric Measurement Techniques **8**(9): 3851-3865.

Zannoni, N., Gros, V., Lanza, M., Sarda, R., Bonsang, B., Kalogridis, C., Preunkert, S., Legrand, M., Jambert, C., Boissard, C. and Lathiere, J. (2016). "OH reactivity and concentrations of biogenic volatile organic compounds in a Mediterranean forest of downy oak trees." Atmospheric Chemistry and Physics **16**(3): 1619-1636.

Chapter 6. Temperature Dependent Relative Rate Studies of Butanols with Cl atoms

6.1 Introduction

The relative rate technique is commonly used to measure the rate coefficients of a target compound of interest (Atkinson 1986, Nelson *et al.* 1990, Wu *et al.* 2003, Kaiser and Wallington 2007). The technique relies on measuring the rate of loss of the target compound, relative to that of a reference compound. The ratio of rate coefficients of the target compound and reference compound are reported; the absolute rate coefficient determined will be dependent on the literature rate coefficient chosen for determining the rate coefficient of interest. The importance of chlorine in the atmosphere has been discussed in Chapter 1. Hydrocarbons typically have rates of reaction with Cl atoms orders of magnitude greater than their analogous reactions with the hydroxyl radical, OH. Here, a study is presented on the temperature dependence of the rate of reaction of Cl atoms, with *n*-butanol and *iso*- butanol. Cyclohexane was used as a reference compound for the relative rate technique. The choice of reference compound is important in relative rate studies; it should have a rate coefficient that is well defined in the literature, and also react at a comparable rate to the compound of interest. It should be easily detectable by the analytical method chosen for monitoring the concentration of compounds throughout the course of the experiment. It is also important to know whether the reference reaction kinetics have any pressure or temperature dependencies. Reaction rates can also be determined using absolute methods; pulsed laser photolysis resonance fluorescence (PLP-RF) or discharge flow tube technique.

Chlorine atoms are produced through the photolysis of molecular chlorine, Cl_2, at wavelengths ~360 nm (R 6-1). The chlorine atoms then subsequently react with both the reactant, *n*-butanol or *iso*-butanol, and the reference, cyclohexane, compounds (R 6-2 and R 6-3).

$Cl_2 + h\nu \rightarrow Cl + Cl$ R 6-1

$Cl + \text{reactant} \xrightarrow{k_{\text{reactant}}} \text{products}$ R 6-2

$Cl + \text{reference} \xrightarrow{k_{\text{reference}}} \text{products}$ R 6-3

The rate coefficient of the target reactant compound (*n*-butanol or *iso*- butanol) can then be determined from the known rate coefficient of the reference compound (cyclohexane), following equations Eq. 6-1 to Eq. 6-5. The rate of decay of both the reactant and reference compounds with respect to their reaction with Cl atoms are described by Eq. 6-1 and Eq. 6-2; integrating these two equations gives Eq. 6-3 and Eq. 6-4, which, when combined, gives Eq. 6-5. A plot of Eq. 6-5 should yield a straight line, where the gradient is equal to k_{reactant} / $k_{\text{reference}}$. As the relative rate method relies on the decay of one compound relative to another, the exact concentrations of each compound do not need to be known. In the work presented here, signal from the HIRAC GC-FID, as described in Chapter 2, was used as an indicator of concentration.

$$-\frac{d[\text{reactant}]}{dt} = k_{\text{reactant}}[\text{Cl}][\text{reactant}] \quad \text{Eq. 6-1}$$

$$-\frac{d[\text{reference}]}{dt} = k_{\text{reference}}[\text{Cl}][\text{reference}] \quad \text{Eq. 6-2}$$

$$\ln\left(\frac{[\text{reactant}]_t}{[\text{reactant}]_0}\right) = k_{\text{reactant}}[\text{Cl}] \quad \text{Eq. 6-3}$$

$$\ln\left(\frac{[\text{reference}]_t}{[\text{reference}]_0}\right) = k_{\text{reference}}[\text{Cl}] \quad \text{Eq. 6-4}$$

$$\ln\left(\frac{[\text{reactant}]_t}{[\text{reactant}]_0}\right) = \frac{k_{\text{reactant}}}{k_{\text{reference}}}\left\{\ln\left(\frac{[\text{reference}]_t}{[\text{reference}]_0}\right)\right\} \quad \text{Eq. 6-5}$$

An example of decays of a reactant and reference compound following a relative rate experiment is shown in Figure 6-1(a), with the linear plot described by Eq. 6-5 being illustrated in Figure 6-1(b). The linear fit to Figure 6-1(b), shown by the solid red line, gives the relative rate ratio of k_{reactant} / $k_{\text{reference}}$, from which the rate coefficient for the reaction of the reactant compound with the reactive species (Cl atoms in this case) is determined from the well-defined literature rate coefficient of the reference compound with the reactive species.

(a) (b)

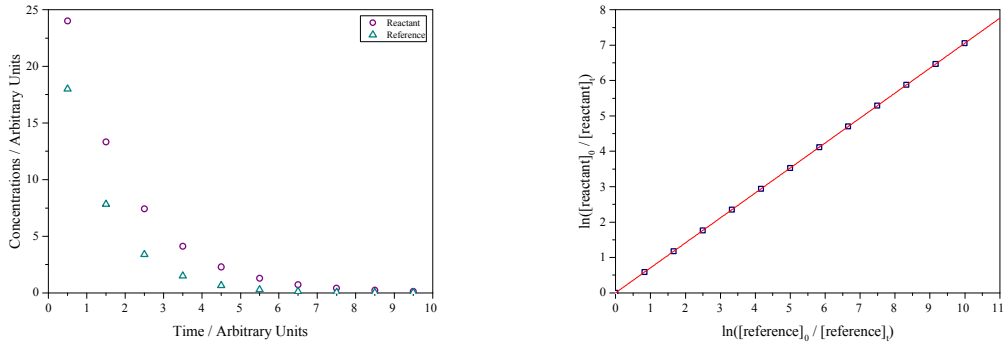

Figure 6-1: (a) example decay as would be produced from a relative rate experiment. (b) example relative rate plot of $\ln([\text{reactant}]_0 / \ln[\text{reactant}]_t)$ vs. $\ln([\text{reference}]_0 / [\text{reference}]_t)$ where the solid red line represents the linear fit to the data, with the gradient giving the ratio of $k_{\text{reactant}} / k_{\text{reference}}$.

The accuracy of the rate coefficients determined by the relative rate method is dependent on the accuracy of the reference rate coefficient; however, the relative rate ratio is reported so that the reference rate coefficients can be updated as more accurate values are reported in the literature.

6.2 Cl + Butanol Temperature Dependent Relative Rate Studies

As discussed in Chapter 1, the isomers of butanol are of particular interest in atmospheric chemistry as they show great potential for use as biofuels. OH is the most abundant oxidising agent in the troposphere, however, Cl atoms also play an important role in VOC oxidation processes under certain conditions in the troposphere (Simpson *et al.* 2015). Cl atoms typically react considerably faster with VOCs as compared to the reaction of OH with VOCs in the troposphere (e.g. $k_{\text{Cl + CH4}} = (1.0 \pm 0.14) \times 10^{-13}$ molecule cm^{-1} s^{-1} compared to $k_{\text{OH + CH4}} = (6.4 \pm 0.89) \times 10^{-15}$ molecule cm^{-1} s^{-1} (Atkinson *et al.* 2006)).

Oxidation reactions and product studies of *iso*-butanol are presented in Chapter 7 and Chapter 8 of this thesis, with comparisons made between OH radical and Cl atom chemistry, and with the analogous, non-substituted alkane; *iso*-butane. Only one previous temperature dependent study of the kinetics of *n*-butanol with Cl atoms has been reported in the literature (Garzón *et al.* 2006); the rate coefficients were measured by an absolute method; pulsed laser photolysis resonance fluorescence (PLP-RF). A number of relative rate studies have been reported for the determination of the room temperature rate coefficient of *n*-butanol with Cl atoms (Nelson *et al.* 1990, Wu *et al.* 2003, Hurley *et al.* 2009). Photolysis of Cl_2 or $COCl_2$ was used as the Cl atom source, and cyclohexane, propane, acetylene, ethene and propene were used as reference compounds. Garzón *et al.*

(2006) reported a value for the room temperature rate coefficient slightly lower, $(1.96 \pm 0.19) \times 10^{-10}$ cm^3 molecule^{-1} s^{-1} at 298 K, than that recommended by IUPAC (Atkinson *et al.* 2006), $(2.21 \pm 0.41) \times 10^{-10}$ cm^3 molecule^{-1} s^{-1} at 298 K, and lower than those presented from relative rate studies. Previous Cl atom rate coefficients measured using the absolute PLP-RF method have been shown to give values more than a factor of two lower than other literature values (Farrugia *et al.* 2015). It was suggested that these lower values are likely due to the reaction of alkyl radicals, R$^{\cdot}$, in the system with the high concentration of Cl_2 present to regenerate Cl atoms, described by R 6-4 to R 6-6.

$$Cl_2 + h\nu \rightarrow Cl + Cl \qquad \text{R 6-4}$$

$$RH + Cl \rightarrow R^{\cdot} + HCl \qquad \text{R 6-5}$$

$$R^{\cdot} + Cl_2 \rightarrow RCl + Cl \qquad \text{R 6-6}$$

The lower value at 298 K reported by Garzón *et al.* (2006) for the rate coefficient for the reaction of Cl atoms with *n*-butanol is within the error of the IUPAC recommended value. Garzón *et al.* (2006) reported a slight negative temperature dependence of the reaction of *n*-butanol with Cl atoms over the range 264 – 382 K. In the study presented here, cyclohexane was used as a reference compound, and experimental relative rate ratios were put on an absolute basis using $k_{(\text{cyclohexane + Cl})} = (3.08 \pm 0.12) \times 10^{-10}$ cm^3 molecule^{-1} s^{-1} (Aschmann and Atkinson 1995).

Cl_2 photolysis is routinely used as a Cl atom source for kinetic and mechanistic studies in the HIRAC chamber, and so this was chosen as the Cl atom source for these experiments. Previous chlorine atom relative rate studies in HIRAC have shown excellent agreement with literature values (Farrugia *et al.* 2015).

6.2.1 Experimental

Experiments were carried out in the HIRAC chamber at an ambient pressure of 1000 mbar over the temperature range 266 – 343 K. The HIRAC chamber temperature control system is described in Chapter 2. Experiments were carried out in 80% N_2 (BOC, 99.998% purity) and 20% O_2 (BOC, 99.999% purity) with all four mixing fans on. HIRAC was evacuated to <1 mbar between experiments in order to clean the chamber. Chlorine atoms were produced from the photolysis of molecular chlorine using UV-B photolysis lamps (Philips TL 40 W/12 RS SLV). Cl_2 (~6 – 9 ppmv, Sigma-Aldrich, ≥99.5%) was introduced into the chamber as a gas via a vacuum line. Hydrocarbons (~2 ppmv) *iso*-butanol (Sigma-Aldrich, ≥99.0%), *n*-butanol (Sigma-Aldrich, ≥99.4%)

and cyclohexane (Fisher Scientific, >99%.) were injected directly into the chamber with a 50 ± 0.5 µl glass syringe.

The decay of the hydrocarbons were monitored by two GC-FIDs. One GC, GC1, was fitted with a DB-WAX polyethylene glycol column (15 m length, 0.25 µm film and 0.32 mm internal diameter). The second GC, GC2, was fitted with a CP-Sil-5CB 100% dimethylpolysiloxane column (50 m length, 0.25 µm film and 0.32 mm internal diameter). For studies of *n*-butanol, the GC1 oven temperature was held at 40 °C and the GC2 oven temperature was held at 100 °C for the duration of the experiments. For studies of *iso*-butanol, the GC1 oven temperature was held at 42 °C and the GC2 oven temperature was held at 90 °C for the duration of the experiments. The sampling system for GC measurements from HIRAC has been described in Chapter 2.

Errors are calculated as the sum in quadrature of the accuracy and precision in the measured rate coefficients. Linear least squares regression analysis of the plots of $\ln([\text{reactant}]_0 / [\text{reactant}]_t)$ vs. $\ln([\text{reference}]_0 / [\text{reference}]_t)$ yield a straight line plot where the gradient is the relative ratio of the two rate coefficients. For each individual experiment (multiple experiments were carried out for each temperature), a rate coefficient was calculated using Eq. 6-6. Error in the calculated k_{reactant} values was propagated from the error in the gradient and the error in the literature reference rate coefficient. Final values quoted are the average calculated k_{reactant} values, with their propagated uncertainties.

$$k_{\text{reactant}} = \text{gradient} \times k_{\text{reference}} \qquad \text{Eq. 6-6}$$

Due to the low vapour pressures of both *n*-butanol (4 mmHg at 20 °C) and *iso*-butanol (8 mmHg at 20 °C), difficulties were encountered in the delivery of these compounds into HIRAC, especially at low temperatures for *iso*-butanol. The concentrations of both *n*-butanol and *iso*-butanol took considerable time to stabilise in HIRAC at ~265 K and ~275 K. Figure 6-2 shows the GC peak heights for both *n*-butanol and cyclohexane during the course of one experiment at ~265 K.

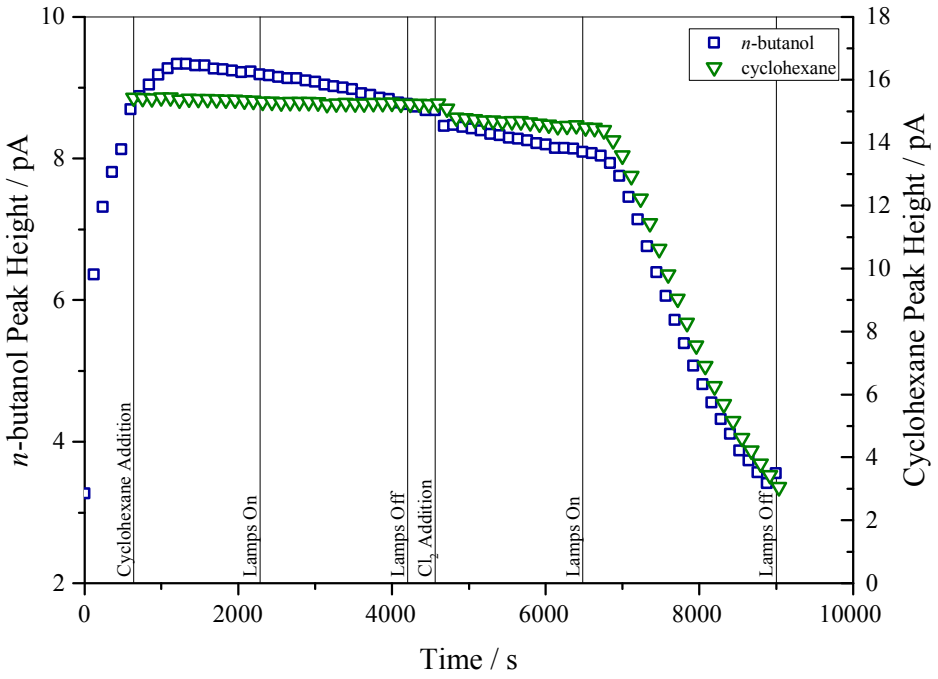

Figure 6-2: Plot to show the stability of *n*-butanol and cyclohexane at ~265 K in HIRAC. Blue squares represent *n*-butanol GC peak heights and green triangles represent cyclohexane GC peak heights. Stability of compounds was tested without Cl_2 present with the photolysis lamps on, and with Cl_2 present with the photolysis lamps off. Vertical lines indicate the times at which the photolysis lamps were switched on and off, and when Cl_2 was added to the chamber.

N-butanol was present in the chamber prior to the first GC injection, and it was observed to take ~1000 s to reach a stable concentration, as recorded from the peak height in the GC chromatogram. Cyclohexane was added to the chamber at 640 s, and its peak height shown in the GC chromatogram was immediately stable. Data points prior to the photolysis lamps being switched on at 2280 s are representative of the wall losses for each compound, which was taken into account during the analysis procedure. A small decrease in the peak heights for both *n*-butanol and cyclohexane can be observed at ~4500 s in Figure 6-2, due to the addition of Cl_2 to HIRAC; a small amount of the total gas mixture was evacuated from HIRAC in order to introduce the Cl_2 gas from the vacuum line. The lamps were switched on at ~ 6500 s, initiating the photolysis of Cl_2 and the resultant decay of *n*-butanol and cyclohexane was used to determine the value of $k_{(n\text{-butanol} + Cl)}$.

Similar wall effects were also observed for *iso*-butanol at temperatures of ~265 K and ~275 K, however, were much more significant than those observed for *n*-butanol at these temperatures. Figure 6-3 shows the peak heights for both *iso*-butanol and cyclohexane during the course of an experiment in HIRAC carried out at ~265 K.

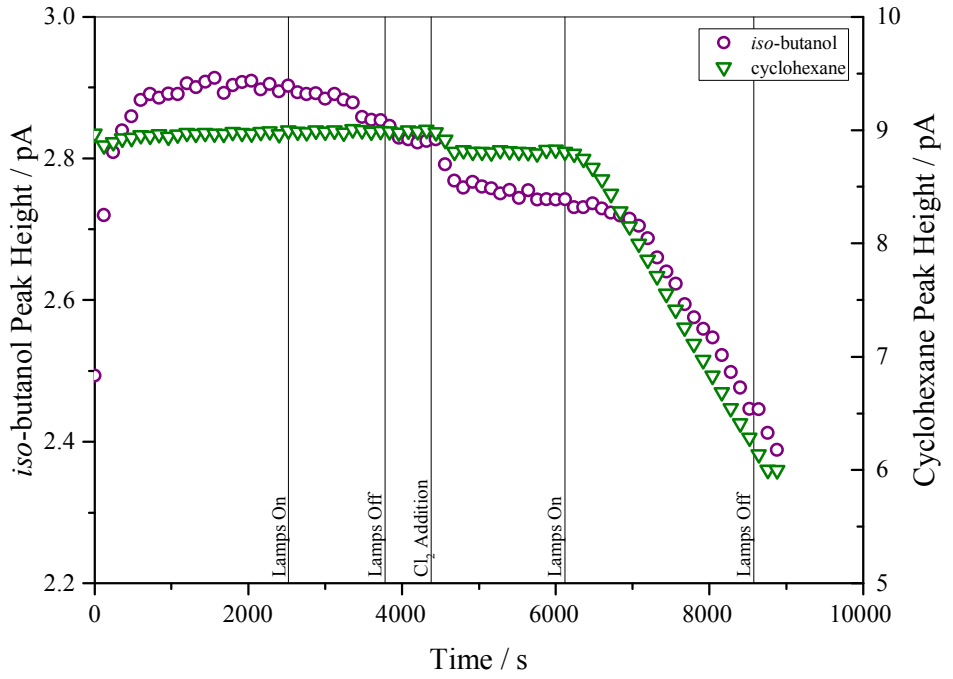

Figure 6-3: Plot to show the stability of *iso*-butanol and cyclohexane at ~275 K in HIRAC. Purple circles represent *iso*-butanol GC peak heights and green triangles represent cyclohexane GC peak heights. Stability was tested with Cl_2 present with the lamps off.

Cyclohexane and *iso*-butanol were both present in the chamber prior to the first GC injection. Similar to that of the *n*-butanol at ~265 K, the concentration of *iso*-butanol following injection into the chamber took a significant time to stabilise as compared to the cyclohexane which stabilised in concentration almost immediately. Again, wall losses were be determined for *iso*-butanol and cyclohexane in the absence of Cl_2 with the photolysis lamps switched on and off. A dip in the peak heights observed at ~4400 s coincided with the addition of Cl_2 to the chamber. The decays of *iso*-butanol and cyclohexane following the photolysis of Cl_2 were used to determine the rate coefficient for the reaction of *iso*-butanol with Cl atoms (6200 - 8580 s).

Considerable difference in the measured apparent wall loss was observed when measured with the lamps off with Cl_2 present, as compared to with the lamps on without Cl_2 present in HIRAC. This indicates that the *iso*-butanol is reacting in some way, however, examination of FTIR spectra for these wall loss periods with the photolysis lamps on showed no evidence of HCl production, which would be expected if the loss was due to reaction with Cl atoms. It is possible that this increased loss rate could be due to reaction with OH radicals on illumination of the chamber; compounds on the walls of the chamber (e.g. nitrates or acids) may be photolysed when the photolysis lamps are turned on,

producing OH radicals which would then react with the *iso*-butanol present. If this were the case, it would be expected that the cyclohexane present in the chamber would also react with any OH radicals present, and a value for $k_{(iso\text{-butanol + OH})}$ could be determined from the relative decays of *iso*-butanol and cyclohexane, however, this was not the case. The wall losses are likely more complex than initially thought; arising from a combination of affects under varying conditions of the chamber.

A significant difference in wall effects was observed with *iso*-butanol, dependent on the cleanliness of HIRAC. The chamber had been previously been cleaned five months prior to the first set of experiments being conducted at ~265 K and ~275 K. During experiments carried out in September of 2016, HIRAC needed to be opened up for the replacement of a broken quartz tube. During this time it was decided to carry out an extensive cleaning procedure for the chamber. Due to the complex nature of the problems encountered at low temperatures with the *iso*-butanol experiments, and the greatly differing $k_{(iso\text{-butanol + Cl})}$ values obtained from these experiments, these results have been excluded from further analysis and discussion in this work. Detailed studies of the wall effects at different temperatures of the isomers of butanol, and other low vapour pressure compounds of interest to study in HIRAC, form the basis of ongoing work within the HIRAC laboratory.

6.2.2 Results and Discussion

Previous measurements of the rate coefficient of *n*-butanol with Cl atoms have been carried out by a number of research groups, using both the relative rate technique and the pulsed laser photolysis – resonance fluorescence technique. A comparison of previous measurements with those obtained in this work is presented in Table 6-1. Only one previous temperature dependence study has been reported for this reaction (Garzón *et al.* 2006), using the pulsed laser photolysis – resonance fluorescence absolute rate method.

The results obtained at room temperature in this work, for the relative ratio of rate coefficients, 0.73 ± 0.03, are in good agreement with the previous values of 0.73 ± 0.03 and 0.66 ± 0.05 reported by Wu *et al.* (2003) and Nelson *et al.* (1990), respectively, where cyclohexane was also used as the reference compound. The slightly lower value of 0.66 ± 0.05 reported by Nelson *et al.* (1990) results in a rate coefficient value of $(2.03 \pm 0.15) \times 10^{-10}$ cm^3 molecule^{-1} s^{-1}, within the error of the IUPAC recommended rate coefficient for the reaction of *n*-butanol with Cl atoms; $(2.2 \pm 0.4) \times 10^{-10}$ cm^3 molecule^{-1} s^{-1}. The room temperature rate coefficients obtained also agree well with those obtained by Wu *et al.* (2003) and Hurley *et al.* (2009), where a range of reference

compounds were used. Garzón *et al.* (2006) carried out a number of studies at room temperature over a range of pressures (20 – 200 Torr), with no pressure dependence being observed. The room temperature rate coefficient obtained in this work agrees, to within the quoted error, with those determined by Garzón *et al.* (2006) over a range of pressures.

The IUPAC recommended rate coefficient for the reaction of *n*-butanol with Cl atoms is $(2.2 \pm 0.4) \times 10^{-10}$ cm^3 molecule^{-1} s^{-1} at 298 K (Atkinson *et al.* 2006), obtained from averaging the rates reported by Garzón *et al.* (2006), Nelson *et al.* (1990) and Wu *et al.* (2003). As the only available temperature dependent study of this reaction is that reported by Garzón *et al.* (2006), the IUPAC recommended temperature dependent rate coefficient is this value, adjusted to return the IUPAC recommended rate coefficient at 298 K.

An example relative rate plot, produced for the reaction of *n*-butanol with Cl atoms at 298 K, using cyclohexane as the reference compound is shown in Figure 6-4, where the straight line represents the relative rate ratio. In this example, a relative rate ratio of 0.71 ± 0.01 was obtained, resulting in a rate coefficient of $k_{n\text{-butanol}} = (2.20 \pm 0.10) \times 10^{-10}$ cm^3 molecule^{-1} s^{-1} when put on an absolute basis using the reference rate coefficient of $k_{\text{cyclohexane}} = (3.08 \pm 0.12) \times 10^{-10}$ cm^3 molecule^{-1} s^{-1} (Aschmann and Atkinson 1995).

Reference Compound	T / K	Pressure / mbar	Method	$k_{butanol}$ / $k_{reference}$	$k_{butanol}$ / 10^{-10} cm^3 molecule^{-1} s^{-1}	Reference
-	266	113	PLP-RF	-	2.41 ± 0.18	Garzón *et al.* (2006)
	283	120			2.30 ± 0.26	
	298	27			1.92 ± 0.10	
		120			2.02 ± 0.10	
		267			1.98 ± 0.14	
	311	127			1.80 ± 0.12	
	330	133			1.60 ± 0.08	
	343	113			1.49 ±0.06	
	354	120			1.47 ± 0.04	
	282	127			1.39 ± 0.10	
Cyclohexane*	295 ± 2	1013	RR	0.73 ± 0.03	2.25 ± 0.09	Wu *et al.* (2003)
Propane†				1.61 ± 0.08	2.11 ± 0.11	
Acetylene‡	296 ± 2	933	RR	4.11 ± 0.41	2.08 ± 0.21	Hurley *et al.* (2009)
Ethene§				2.36 ± 0.34	2.19 ± 0.32	
Propene**				0.89 ± 0.09	2.35 ± 0.24	
Cyclohexane*	298 ± 2	1013	RR	0.66 ± 0.05	2.03 ± 0.15	Nelson *et al.*
Cyclohexane*	266 ± 0.45	1000	RR	0.78 ± 0.12	2.40 ± 0.36	This Work
	275 ± 0.40			0.76 ± 0.08	2.33 ± 0.25	
	298 ± 0.43			0.73 ± 0.03	2.25 ± 0.11	
	313 ± 0.13			0.70 ± 0.05	2.14 ± 0.15	
	331 ± 0.45			0.65 ± 0.06	1.99 ± 0.18	
	343 ± 0.39			0.66 ± 0.07	2.02 ± 0.22	

Table 6-1: Comparison of rate coefficients and relative rate ratios for the reaction of Cl atoms with *n*-butanol. PLP-RF = Pulse laser photolysis resonance fluorescence, RR = Relative rate. $^{*}k_{(cyclohexane + Cl)} = (3.08 \pm 0.12) \times 10^{-10}$ cm^3 molecule^{-1} s^{-1} (Aschmann and Atkinson 1995). $^{\dagger}k_{(propane + Cl)} = 1.31 \times 10^{-10}$ cm^3 molecule^{-1} s^{-1}. $^{\ddagger}k_{(acetylene + Cl)} = 5.07 \times 10^{-11}$ cm^3 molecule^{-1} s^{-1}. $^{\S}k_{(ethane + Cl)} = 9.29 \times 10^{-11}$ cm^3 molecule^{-1} s^{-1}. $^{**}k_{(propene + Cl)} = 2.64 \times 10^{-10}$ cm^3 molecule^{-1} s^{-1}.

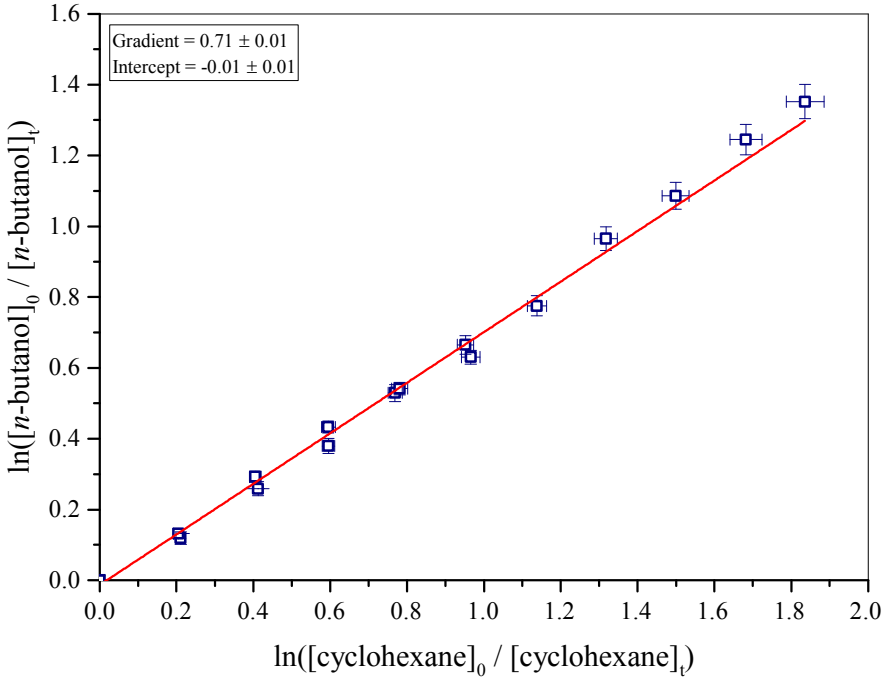

Figure 6-4: Example relative rate data plot for the reaction of *n*-butanol + Cl using cyclohexane as a reference at 298 ± 1 K and 1013 ± 4 mbar. The experiment was carried out in 80:20 N_2:O_2 and the decay of compounds was measured using two GC-FID systems. Error bars represent 1σ errors, propagated from GC measurements. The red line shows the linear least squares regression analysis giving a slope of 0.71 ± 0.01 and an intercept of -0.01 ± 0.01. $k_{n\text{-butanol}}$ = (2.20 ± 0.10) × 10^{-10} cm^3 $molecule^{-1}$ s^{-1}. Error bars represent error in the measurements to 1σ, errors in gradient and intercept are the standard error of the fitting procedure.

Arrhenius plots were obtained for both *n*-butanol and *iso*-butanol by plotting the natural logarithm of the obtained rate coefficients against 1 / temperature, where the gradient is equal to E_a/R and the intercept is equal to lnA, as described by equations Eq. 6-8 and Eq. 6-7. Figure 6-5 and Figure 6-7 show the Arrhenius plots for the reactions of Cl atoms with *n*-butanol and *iso*-butanol, respectively.

$$\ln k = -\frac{E_a}{\mathrm{RT}} + \ln \mathrm{A} \qquad \text{Eq. 6-7}$$

$$\ln k = \text{gradient} \times \frac{1}{\mathrm{T}} + \text{intercept} \qquad \text{Eq. 6-8}$$

$$k = \mathrm{A}\exp^{-E_a/\mathrm{RT}} \qquad \text{Eq. 6-9}$$

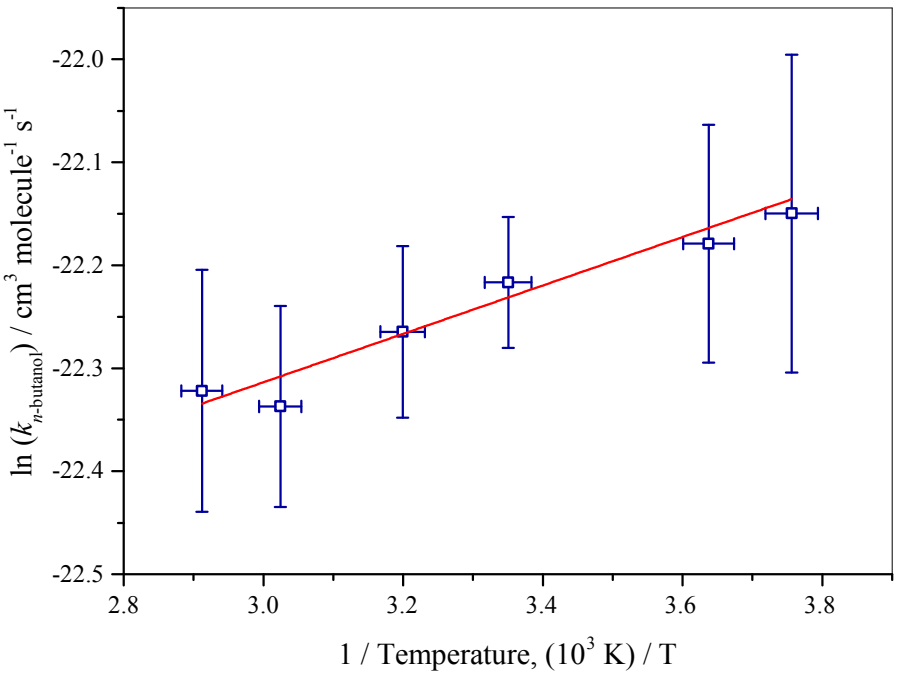

Figure 6-5: Arrhenius plot of the temperature dependent rate coefficient for the reaction of *n*-butanol + Cl over the temperature range 265 – 345 K, determined in the HIRAC chamber at a pressure of ~1000 mbar. The red line represents the linear least squares regression analysis giving a gradient of 235.07 ± 34.45 and an intercept of -23.02 ± 0.11 cm^3 molecule^{-1} s^{-1}. Error bars represent error propagated from the error in the measurements to 1σ, errors in gradient and intercept are the standard error of the fitting procedure.

Table 6-2 gives a comparison of the Arrhenius parameters obtained with those in the literature, where the IUPAC value is based solely on that reported by Garzón *et al.* (2006), for the reaction of *n*-butanol with Cl atoms. The value of E_a obtained from this study was -1.95 ± 0.28 K, which is not in very close agreement with that reported by Garzón *et al.* (2006) (E_a = -4.56 ± 0.54 K) or that recommended by IUPAC; E_a = -4.57 ± 1.66 K (Atkinson *et al.* 2006). Considering the IUPAC recommended value of E_a is based only on the one temperature dependent study reported by Garzón *et al.* (2006), it is difficult to draw conclusions on the agreement of this work to the previous study. The Arrhenius expression determined in this work, for the reaction of *n*-butanol with Cl atoms is given by Eq. 6-10:

$$k = 1.01 \times 10^{-10} \exp((235 \pm 34)/T)\ \text{cm}^3\ \text{molecule}^{-1}\ \text{s}^{-1} \qquad \text{Eq. 6-10}$$

over the temperature range 266 – 343 K.

A / 10^{-10} cm^3 molecule^{-1} s^{-1}	E_a / kJ mol^{-1}	Temperature Range / K	Reference
31.2 ± 0.31	-4.56 ± 0.54	266 – 382	Garzón *et al.* (2006)
35.0	-4.57 ± 1.66	260 – 390	Atkinson *et al.* (2006)*
1.01 ± 0.30	-1.95 ± 0.28	266 – 343	This work

Table 6-2: Comparison of Arrhenius parameters for the temperature dependence for the reaction of *n*-butanol with Cl atoms. *IUPAC recommended value.

Table 6-3 compares the rate coefficients determined in this work for the reaction of *iso*-butanol with Cl atoms over the temperature range of 296 – 344 K, with those previously reported in the literature. No previous temperature dependence for the rate coefficient of the reaction of *iso*-butanol with Cl atoms has been reported in the literature. Only two previous studies on the room temperature rate coefficient have been reported, both using the relative rate method for the determination of $k_{iso\text{-butanol}}$ (Wu *et al.* 2003, Andersen *et al.* 2010). The results obtained in this work were in very good agreement with those reported previously, for the room temperature rate coefficient ($(1.95 \pm 0.14) \times 10^{-10}$ cm^3 molecule^{-1} s^{-1}). Agreement was particularly good when compared to the previous studies where cyclohexane was used as a reference compound; $(1.88 \pm 0.07) \times 10^{-10}$ cm^3 molecule^{-1} s^{-1} reported by Andersen *et al.* (2010) and $(1.95 \pm 0.11) \times 10^{-10}$ cm^3 molecule^{-1} s^{-1} reported by Wu *et al.* (2003). It should be noted that the rate coefficients reported in Table 6-1 and Table 6-3, where cyclohexane was used as the reference compound, have all been put on an absolute basis using the rate coefficient of cyclohexane of $(3.08 \pm 0.12) \times 10^{-10}$ cm^3 molecule^{-1} s^{-1} (Aschmann and Atkinson 1995).

Reference Compound	T / K	Pressure / mbar	Method	$k_{butanol}$ / $k_{reference}$	$k_{butanol}$ / 10^{-10} cm^3 molecule^{-1} s^{-1}	Reference
Cyclohexane*	296	933	RR	0.61 ± 0.07	1.88 ± 0.22	Andersen *et al.* (2010)
Ethene†				2.24 ± 0.16	2.08 ± 0.15	
Cyclohexane*	295 ± 2	1013	RR	0.59	1.82 ± 0.12	Wu *et al.* (2003)
Propane‡				1.50	1.96 ± 0.11	
Cyclohexane*	296 ± 0.79	1000	RR	0.63 ± 0.05	1.95 ± 0.14	This Work
	313 ± 0.35			0.57 ± 0.01	1.76 ± 0.04	
	331 ± 0.25			0.55 ± 0.01	1.70 ± 0.03	
	344 ± 0.41			0.52 ± 0.02	1.60 ± 0.06	

Table 6-3: Comparison of rate coefficients and relative rate ratios for the reaction of Cl atoms with *iso*-butanol. RR = Relative rate. *$k_{(cyclohexane + Cl)}$ = ((3.08 ± 0.12) × 10^{-10} cm^3 molecule^{-1} s^{-1} (Aschmann and Atkinson 1995). †$k_{(ethene + Cl)}$ = 1.31 × 10^{-10} cm^3 molecule^{-1} s^{-1}. ‡$k_{(propane + Cl)}$ = 9.29 × 10^{-11} cm^3 molecule^{-1} s^{-1}.

Figure 6-6 shows an example relative rate plot produced for the determination of the rate coefficient of *iso*-butanol with Cl atoms at 297 K, where cyclohexane was used as a reference compound. The gradient of the linear fit to the data gives the relative rate ratio, in this example a value of 0.64 ± 0.01 was obtained, which, when put on an absolute basis for the literature value of $k_{\text{cyclohexane + Cl}}$ from Aschmann and Atkinson (1995), returns a value of $k_{iso\text{-butanol + Cl}} = (1.98 \pm 0.09) \times 10^{-10}$ cm^3 molecule^{-1} s^{-1}.

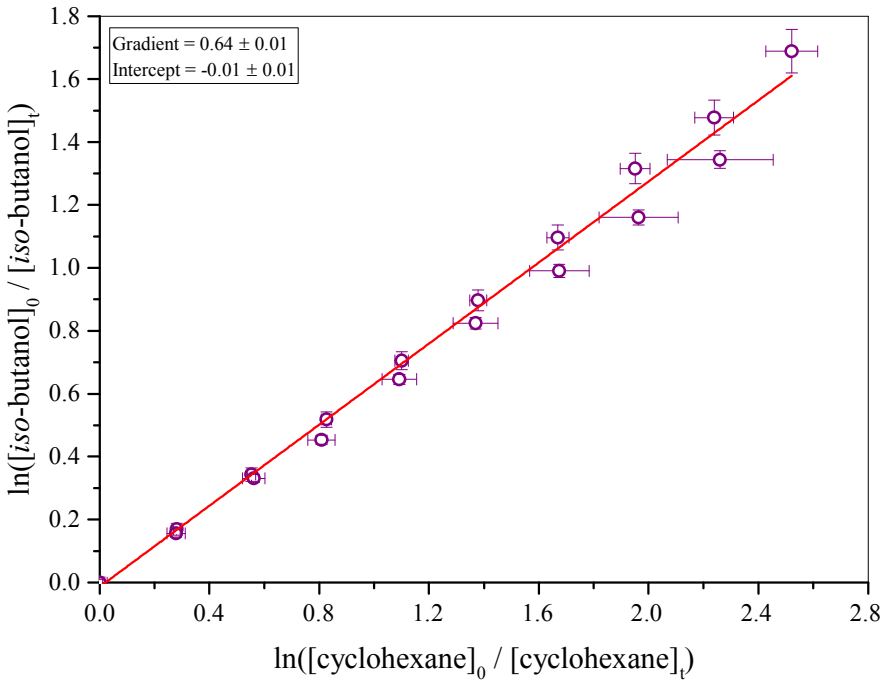

Figure 6-6: Example relative rate data plot for the reaction of *iso*-butanol + Cl using cyclohexane as a reference at 297 ± 1 K and 1011 ± 2 mbar. The experiment was carried out in 80:20 N2:O2 and the decay of compounds was measured using two GC-FID systems. Error bars represent 1σ errors, propagated from GC measurements. The red line shows the linear least squares regression analysis giving a slope of 0.64 ± 0.01 and an intercept of -0.01 ± 0.01. $k_{iso\text{-butanol}}$ + Cl = (1.98 ± 0.09) × 10^{-10} cm^3 molecule^{-1} s^{-1}. Error bars represent error in the measurements to 1σ, errors in gradient and intercept are the standard error of the fitting procedure.

An Arrhenius plot for *iso*-butanol temperature dependence of the rate coefficient for the reaction with Cl atoms is shown in Figure 6-7, which gave an E_a of -3.06 ± 0.63 kJ mol^{-1}. The Arrhenius expression for the reaction of *iso*-butanol with Cl atoms is given by Eq. 6-11:

$$k = 5.53 \times 10^{-11} \exp((367 \pm 76)/T) \text{ cm}^3 \text{ molecule}^{-1} \text{ s}^{-1} \qquad \text{Eq. 6-11}$$

over the temperature range 296 – 344 K.

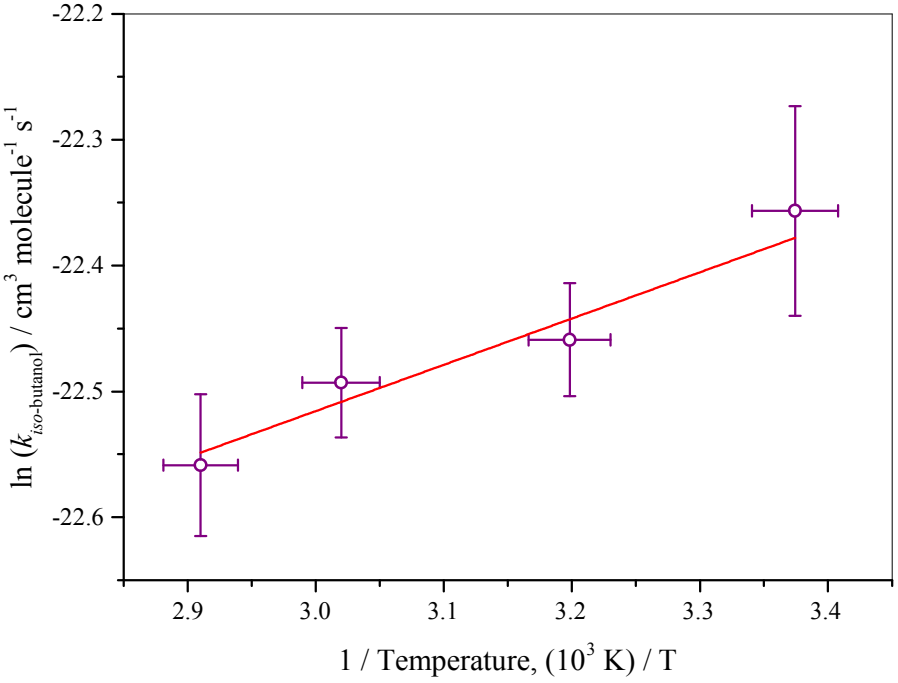

Figure 6-7: Arrhenius plot of the temperature dependent rate coefficient for the reaction of *iso*-butanol + Cl over the temperature range 296 – 344 K, determined in the HIRAC chamber at a pressure of ~1000 mbar. The red line represents the linear least squares regression analysis giving a gradient of 367.67 ± 76.27 and an intercept of -23.62 ± 0.24 cm^3 molecule^{-1} s^{-1}. A = (5.53 ± 1.66) × 10^{-11} cm^3 molecule^{-1} s^{-1}. Error bars represent the propagated error from the error in the measurements to 1σ, errors in gradient and intercept are the standard error of the fitting procedure.

The Arrhenius plots for the reaction of Cl atoms with both *n*-butanol and *iso*-butanol show slight negative temperature dependence. For the reaction of *n*-butanol with Cl atoms, this is in agreement with what has previously been shown by Garzón *et al.* (2006), where they also reported slight negative temperature dependence for other alcohols, including 1-pentanol, 1-propanol and ethanol. They also noted that the rate coefficients of these alcohols with Cl atoms increased with carbon number. The rate coefficients of for the reaction of *n*-butane and *iso*-butane with Cl atoms have also been reported to show slight negative temperature dependence (Sarzynski and Sztuba 2002), however, these studies gave substantial errors, making the activation energy, in effect, zero.

The first relative rate temperature dependence study of the reaction of Cl atoms with *n*-butanol over the temperature range 266 – 343 K is reported here. The rate coefficient obtained in this work for the reaction of *n*-butanol and Cl atoms at 298 K, (2.25 ± 0.11) × 10^{-10} cm^3 molecule^{-1} s^{-1}, is in excellent agreement with the IUPAC recommended value of (2.2 ± 0.41) × 10^{-10} cm^3 molecule^{-1} s^{-1} (Atkinson *et al.* 2006). The value, (1.96 ± 0.19) × 10^{-10} cm^3 molecule^{-1} s^{-1}, reported by Garzón *et al.* (2006) is within

error of the IUPAC recommended value, however, is lower than other literature values using the relative rate technique. Other studies of Cl atom kinetics with hydrocarbons have also shown that PLP-RF studies, often report lower values of rate coefficients than those with the relative rate technique (Farrugia *et al.* 2015). It has been suggested that these lower reported values are due to regeneration of Cl atoms by the reaction of alkyl radicals with high concentrations of Cl_2 present in the system (Kaiser and Wallington 2007, Farrugia *et al.* 2015). Agreement was observed for the temperature dependence of the reaction of *n*-butanol with Cl atoms with that described by Garzón *et al.* (2006), where a slight negative temperature dependence was reported both in this relative rate study and the absolute study in the literature. Here, the Arrhenius expression $k = 1.03 \times 10^{-10} \exp((235 \pm 34)/T)$ cm^3 $molecule^{-1}$ s^{-1} was determined, compared to $3.12 \times 10^{-11} \exp((548 \pm 65)/T)$ cm^3 $molecule^{-1}$ s^{-1} determined by Garzón *et al.* (2006). Further studies into the temperature dependence with different reference compounds would assist in reducing the uncertainty. The relative rate method has been previously shown to give good agreement with literature rate coefficients of hydrocarbons with Cl atoms, such as those reported by Farrugia (2013) on the reaction of Cl atoms with a series of ketones, carried out in the HIRAC chamber. Cl atom regeneration is not expected in the relative rate method for the determination of rate coefficients of compounds with Cl atoms.

Two temperature dependent studies for the reaction of OH radicals with *n*-butanol have been reported in the literature; those by McGillen *et al.* (2013) and by Mellouki *et al.* (2004). The former reported on the temperature dependence between 220 and 380 K where non-Arrhenius behaviour was observed, and the latter between 241 and 373 K where the Arrhenius expression $k = 5.3 \times 10^{-12} \exp[(146 \pm 92)/T]$ was reported. The study by McGillen *et al.* (2013) reports on the temperature dependence for the rate coefficients of all four isomers of butanol with OH radicals over the temperature range 220 – 380 K, where non-Arrhenius behaviour was observed for all compounds, made more apparent when their data was combined with high temperature data available in the literature. McGillen *et al.* (2013) discuss the site specific reactions for the OH attack of the four isomers of butanol; at tropospherically relevant temperatures. Over the same temperature range, 265 – 345 K, as has been studied in this work for the rate coefficient of *n*-butanol and *iso*-butanol with Cl atoms, McGillen *et al.* (2013) also reported a negative temperature dependence for the rate coefficients with OH radicals. Temperature dependence has also been observed for the analogous non-functionalised alkanes;

n-butane and *iso*-butane for their rate coefficients with Cl atoms (Farrugia 2013), however, are not as strongly temperature dependent as the results reported in this work for *n*-butanol and *iso*-butanol.

The first study of the temperature dependence of *iso*-butanol with Cl atoms has been reported here. Excellent agreement was obtained with the literature for the rate coefficient of $k_{(iso\text{-butanol + Cl})}$ at room temperature, were a value of $k = (1.95 \pm 0.14) \times 10^{-10}$ cm^3 molecule^{-1} s^{-1} was determined. Again, a slight negative temperature dependence was observed. Due to the complex nature of the wall effects observed with *iso*-butanol in a metal chamber such as HIRAC, the temperature dependence could not be determined below ~298 K. Work is ongoing into better understanding these wall effects in order to accurately determine the rate coefficient of *iso*-butanol with Cl atoms at lower temperatures. Again, further studies with a range of reference compounds would also assist in reducing any uncertainties in the determination of the temperature dependence for the reaction of Cl atoms with *iso*-butanol.

Tropospheric chlorine chemistry has seen increased interest in recent years; Cl atoms are important oxidising agents in the atmosphere and their precursors are found in a range of environments across the globe including the Arctic, the marine boundary layer and in urban areas (Saiz-Lopez and von Glasow 2012, Faxon and Allen 2013). Fully understanding the kinetics and mechanisms of the butanol isomers is critical in assessing their suitability as biofuels. The reaction of Cl atoms with butanols, in the presence of NO_x, leads to the formation of ozone in the atmosphere. The importance of ozone in the atmosphere has been described in Chapter 1; Chapter 7 reports a detailed study of the products of the atmospheric oxidation of *iso*-butanol with both Cl atoms and OH radicals under a range of [NO_x] concentrations relevant to the urban atmosphere.

The temperature dependence of the site specific reactions of OH radicals with the four isomers of butanol has been reported by McGillen *et al.* (2013); where non-Arrhenius behaviour was observed for all isomers. The analogous rate coefficients with Cl atoms, as has been described in this work, may be expected to follow a similar temperature dependence. Negative temperature dependence has been observed for the rate coefficients of *n*-butanol and *iso*-butanol with OH radicals over a similar temperature range as in this work, 265 – 345 K, with a slightly stronger temperature dependence having been reported in the literature. The attack of Cl atoms is typically less selective than that of OH radicals;

as is deduced from end product studies of *n*-butanol and *iso*-butanol with both Cl atoms and OH radicals.

Garzón *et al.* (2006) studied the rate coefficients for the reaction of Cl atoms with a series of alcohols; methanol, ethanol, *n*-propanol, *n*-butanol and *n*-pentanol. With the exception of methanol, all of the alcohols showed a negative temperature dependence over the temperature range 264 – 382 K, with the temperature dependence becoming more pronounced as the carbon chain was increased from ethanol to *n*-pentanol. This trend in reactivity towards Cl atoms for the series of alcohols has also been reported by Wallington and Kurylo (1987), Wallington *et al.* (1988), Nelson *et al.* (1990) and Wu *et al.* (2003). The study by Garzón *et al.* (2006) concluded the observed temperature dependencies for methanol, ethanol, *n*-propanol, *n*-butanol and *n*-pentanol are indicative of the carbon chain lengths; the positive temperature dependence observed for the reaction of methanol with Cl atoms is characteristic of compounds only containing CH_3 groups, with the presence of CH_2 groups in the other alcohols studied typically resulting in a negative temperature dependence. Similar temperature dependencies have also been reported for a series of ketones and aldehydes with CH_2 groups (Cuevas *et al.* 2004, Cuevas *et al.* 2006).

The Arrhenius expressions for the reaction of Cl atoms with *n*-butanol and *iso*-butanol from this work are compared with those recommended by IUPAC for the reaction of OH radicals with *n*-butanol and *iso*-butanol in Table 6-4. A negative temperature dependence is reported for all four reactions; with the dependence being stronger for the reaction with Cl atoms for *n*-butanol and *iso*-butanol than with OH radicals.

	***n*-butanol**	***iso*-butanol**	**Reference**
$k_{(Cl + butanol)}$ / **cm^3 molecule^{-1} s^{-1}**	$1.10 \times 10^{-10} \exp(235 / T)$	$5.53 \times 10^{-11} \exp(367 / T)$	This Work
Temperature / K	266 – 343	296 - 344	
$k_{(OH + butanol)}$ / **cm^3 molecule^{-1} s^{-1}**	$5.3 \times 10^{-12} \exp(140 / T)$	$2.73 \times 10^{-12} \exp(352 / T)$	Atkinson *et al.* (2006)
Temperature / K	260 - 380	240 - 370	

Table 6-4: Comparison of Arrhenius expressions determined from this work for the rate coefficients of Cl atoms with *n*-butanol and *iso*-butanol and IUPAC recommended Arrhenius expressions for the rate coefficients of OH radicals with *n*-butanol and *iso*-butanol.

An article by Sims (2013) discusses temperature dependencies of chemical reactions, showing how negative temperature dependencies are characteristic of barrierless reactions which proceed via a weakly bound intermediate complex, illustrated by the potential energy surface diagram in Figure 6-8. As the temperature decreases, the intermediate complex is more stabilised, allowing for the reaction to proceed towards the products of the reaction. At higher temperatures, the intermediate complex is less stable, and dissociates back to the reactant species.

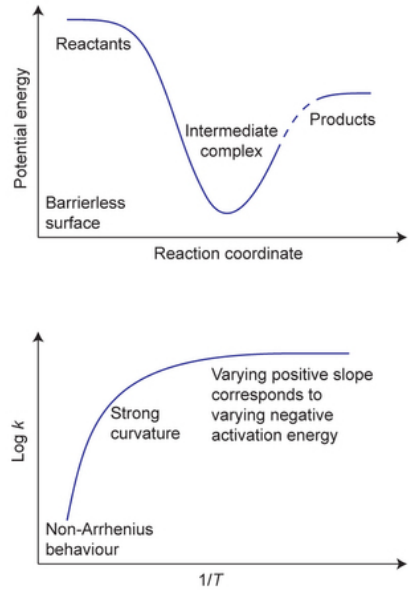

Figure 6-8: The potential energy surface (top) and temperature dependence (bottom) characteristic of reactions with negative temperature dependencies. Adapted from Sims (2013).

As discussed, the negative temperature dependence of straight chain alcohols is related to the number of carbons in the chain, where for the room temperature rate coefficients for their reaction with Cl atom; $k_{(Cl + methanol)} < k_{(Cl + ethanol)} < k_{(Cl + n\text{-propanol})} < k_{(Cl + n\text{-butanol})} < k_{(Cl + n\text{-pentanol})}$, with the reaction of ethanol and Cl atoms having a positive temperature dependence, characteristic of compounds with only a CH_3 group present. The reaction of OH radicals with straight chain alcohols also show a similar trend in their reactivities; $k_{(OH + methanol)} < k_{(OH + ethanol)} < k_{(OH + n\text{-propanol})} < k_{(OH + n\text{-butanol})}$, where the rate coefficient for the reaction of OH radicals with methanol shows a positive temperature dependence and the other alcohols show a negative temperature dependence which becomes more pronounced as the carbon chain is increased. In all alcohol reactions with Cl atoms or OH radicals where a negative temperature dependence is observed, the temperature dependence is more pronounced for the reaction with Cl atoms as compared to OH radicals, and also becomes more pronounced as the carbon chain is increased. The negative temperature dependence reported in this work for the rate coefficient for the

reaction of *iso*-butanol with Cl atoms is only slightly more pronounced than that of the reaction with OH radicals. In contrast, no temperature dependence is observed for the rate coefficient for the reaction of *iso*-propanol with Cl atoms, and a strongly negative temperature dependence is observed for its reaction with OH radicals. The difference in these observations is related to the structures of the compounds (shown in Figure 6-9); negative temperature dependencies are typical of compounds with CH_2 groups, where *n*-propanol, *n*-butanol and *iso*-butanol all have CH_2 groups and *iso*-propanol does not.

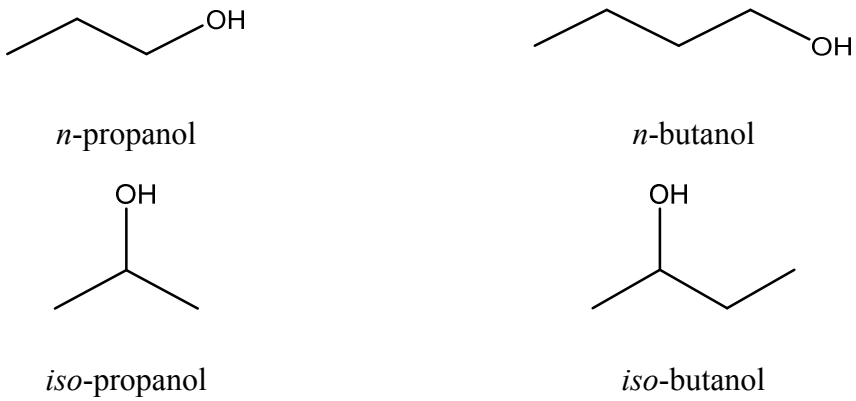

Figure 6-9: Structures of *n*- and *iso*-propanol and *n*- and *iso*-butanol.

Tropospheric concentrations of Cl atoms are typically lower than concentrations of OH radicals, 10^5 molecule cm^{-3} and 10^6 molecule cm^{-3}, respectively. The reaction of *n*-butanol and *iso*-butanol with Cl atoms would become a significant loss pathway in environments where Cl atom concentrations are high, such as in the marine boundary layer and in certain urban areas as has been discussed in Chapter 1. The negative temperature dependencies reported are likely to have a significant impact on the tropospheric production of ozone in such environments.

6.3 References

Andersen, V. F., Wallington, T. J. and Nielsen, O. J. (2010). "Atmospheric Chemistry of *i*-Butanol." The Journal of Physical Chemistry A **114**(47): 12462-12469.

Aschmann, S. M. and Atkinson, R. (1995). "Rate constants for the gas-phase reactions of alkanes with Cl atoms at 296 ± 2 K." International Journal of Chemical Kinetics **27**(6): 613-622.

Atkinson, R. (1986). "Kinetics and mechanisms of the gas-phase reactions of the hydroxyl radical with organic compounds under atmospheric conditions." Chemical Reviews **86**(1): 69-201.

Atkinson, R., Baulch, D. L., Cox, R. A., Crowley, J. N., Hampson, R. F., Hynes, R. G., Jenkin, M. E., Rossi, M. J., Troe, J. and Subcommittee, I. (2006). "Evaluated kinetic and photochemical data for atmospheric chemistry: Volume II - gas phase reactions of organic species." Atmospheric Chemistry and Physics **6**(11): 3625-4055.

Cuevas, C. A., Notario, A., Martinez, E. and Albaladejo, J. (2004). "A kinetic study of the reaction of Cl with a series of linear and ramified ketones as a function of temperature." Physical Chemistry Chemical Physics **6**(9): 2230-2236.

Cuevas, C. A., Notario, A., Martínez, E. and Albaladejo, J. (2006). "Temperature-dependence study of the gas-phase reactions of atmospheric Cl atoms with a series of aliphatic aldehydes." Atmospheric Environment **40**(21): 3845-3854.

Farrugia, L. (2013). Kinetics and mechanistic studies in the HIRAC chamber. PhD, University of Leeds.

Farrugia, L. N., Bejan, I., Smith, S. C., Medeiros, D. J. and Seakins, P. W. (2015). "Revised structure activity parameters derived from new rate coefficient determinations for the reactions of chlorine atoms with a series of seven ketones at 290 K and 1 atm." Chemical Physics Letters **640**: 87-93.

Faxon, C. B. and Allen, D. T. (2013). "Chlorine chemistry in urban atmospheres: a review." Environmental Chemistry **10**(3): 221-233.

Garzón, A., Cuevas, C. A., Ceacero, A. A., Notario, A., Albaladejo, J. and Fernández-Gómez, M. (2006). "Atmospheric reactions $Cl+CH_3–(CH_2)_n–OH(n=0–4)$: A kinetic and theoretical study." The Journal of Chemical Physics **125**(10): 104305.

Hurley, M. D., Wallington, T. J., Laursen, L., Javadi, M. S., Nielsen, O. J., Yamanaka, T. and Kawasaki, M. (2009). "Atmospheric Chemistry of *n*-Butanol: Kinetics, Mechanisms, and Products of Cl Atom and OH Radical Initiated Oxidation in the Presence and Absence of NO_x." The Journal of Physical Chemistry A **113**(25): 7011-7020.

Kaiser, E. W. and Wallington, T. J. (2007). "Rate Constants for the Reaction of Cl with a Series of C4 to C6 Ketones Using the Relative Rate Method." The Journal of Physical Chemistry A **111**(42): 10667-10670.

McGillen, M. R., Baasandorj, M. and Burkholder, J. B. (2013). "Gas-Phase Rate Coefficients for the OH + *n*-, *i*-, *s*-, and *t*-Butanol Reactions Measured Between 220 and 380 K: Non-Arrhenius Behavior and Site-Specific Reactivity." The Journal of Physical Chemistry A **117**(22): 4636-4656.

Mellouki, A., Oussar, F., Lun, X. and Chakir, A. (2004). "Kinetics of the reactions of the OH radical with 2-methyl-1-propanol, 3-methyl-1-butanol and 3-methyl-2-butanol between 241 and 373 K." Physical Chemistry Chemical Physics **6**(11): 2951-2955.

Nelson, L., Rattigan, O., Neavyn, R., Sidebottom, H., Treacy, J. and Nielsen, O. J. (1990). "Absolute and relative rate constants for the reactions of hydroxyl radicals and chlorine atoms with a series of aliphatic alcohols and ethers at 298 K." International Journal of Chemical Kinetics **22**(11): 1111-1126.

Saiz-Lopez, A. and von Glasow, R. (2012). "Reactive halogen chemistry in the troposphere." Chemical Society Reviews **41**(19): 6448-6472.

Sarzynski, D. and Sztuba, B. (2002). "Gas-phase reactions of Cl atoms with propane, *n*-butane, and *iso*-butane." International Journal of Chemical Kinetics **34**(12): 651-658.

Simpson, W. R., Brown, S. S., Saiz-Lopez, A., Thornton, J. A. and Glasow, R. v. (2015). "Tropospheric Halogen Chemistry: Sources, Cycling, and Impacts." Chemical Reviews **115**(10): 4035-4062.

Sims, I. R. (2013). "Low-temperature reactions: Tunnelling in space." Nature Chemistry **5**(9): 734-736.

Wallington, T. J. and Kurylo, M. J. (1987). "The gas phase reactions of hydroxyl radicals with a series of aliphatic alcohols over the temperature range 240–440 K." International Journal of Chemical Kinetics **19**(11): 1015-1023.

Wallington, T. J., Skewes, L. M., Siegl, W. O., Wu, C.-H. and Japar, S. M. (1988). "Gas phase reaction of Cl atoms with a series of oxygenated organic species at 295 K." International Journal of Chemical Kinetics **20**(11): 867-875.

Wu, H., Mu, Y., Zhang, X. and Jiang, G. (2003). "Relative rate constants for the reactions of hydroxyl radicals and chlorine atoms with a series of aliphatic alcohols." International Journal of Chemical Kinetics **35**(2): 81-87.

Chapter 7. Product studies of the oxidation of *iso*-butanol in the presence and absence of NO_x

7.1 Introduction

The use of alcohols as biofuels has been discussed in detail in Chapter 1. The four isomers of butanol demonstrate potential for use as biofuels due to their physical properties being more similar to that of petrol than ethanol or methanol. The production of biofuels will inevitably lead to an increase in their release into the troposphere from fugitive emissions; through direct emission of gaseous fuels or evaporation into the atmosphere. An increase in biofuel oxidation products, primarily carbonyl compounds, would therefore also be expected. Biofuels have been shown to reduce regulated pollutants, however, they are known to produce and increase in unregulated emissions such as carbonyls, which could potentially be more harmful to the atmosphere (Cardone *et al.* 2002, Fontaras *et al.* 2009, He *et al.* 2009, Lin *et al.* 2009, Chai *et al.* 2013). The oxidation of VOCs in the atmosphere is closely linked to the formation of tropospheric ozone and other pollutants. *Iso*-butanol has seen interest as a second generation biofuel as has been discussed in Chapter 1. Before any potential biofuel can be put into use as a vehicle fuel, a detailed understanding of its oxidation processes is required in order to fully assess the atmospheric implications of its oxidation products, including its potential to produce ozone.

As discussed in Chapter 1, OH radicals are the most abundant oxidising agent in the troposphere, and so it is vital to investigate the processes occurring throughout the OH radical initiated oxidation of *iso*-butanol. Cl atoms are also widely employed to investigate kinetics and oxidation processes of tropospherically relevant VOCs under atmospheric conditions. The kinetics of Cl atom initiated reactions are typically 10 – 100 times faster than the analogous OH radical initiated reactions. Cl atoms are typically formed in atmospheric simulation chamber studies following the photolysis of molecular chlorine (Cl_2) or oxalyl choloride, $(COCl)_2$, at wavelengths <300 nm, R 7-1 and R 7-2.

$Cl_2 + h\nu_{(\lambda < 300\ nm)} \rightarrow Cl + Cl$ R 7-1

$(COCl)_2 + h\nu_{(\lambda < 300\ nm)} \rightarrow 2Cl + CO$ R 7-2

OH radicals are typically produced in chamber studies following the photolysis of methyl nitrite, CH_3ONO at wavelengths ≥290 nm, or the photolysis of HONO:

$CH_3ONO + h\nu_{(\lambda \geq 290\ nm)} \rightarrow CH_3O + NO$ R 7-3

$CH_3O + O_2 \rightarrow CH_2O + HO_2$ R 7-4

$HO_2 + NO \rightarrow OH + NO_2$ R 7-5

$HONO + h\nu_{(190\ nm < \lambda < 400\ nm)} \rightarrow OH + NO$ R 7-6

The use of CH_3ONO or HONO as OH radical precursors leads to high concentrations of NO_x being present in the chamber. Peroxides such as hydrogen peroxide (H_2O_2) and *tert*-butyl hydroperoxide (*t*BuOOH) can also be photolysed to produce OH radicals in chamber studies, however, the photolysis of peroxides occurs at much shorter wavelengths, typically photolysis lamps with a maximum output at ~254 nm are used. The use of peroxides as OH precursors allows for OH radical initiated processes to be investigated in the absence of NO_x.

$H_2O_2 + h\nu_{(\lambda > 230\ nm)} \rightarrow OH + OH$ R 7-7

The use of 254 nm lamps for the photolysis of peroxides can lead to some complications arising from the photolysis of oxidation products, influencing product yields. When carrying out investigations into ozone formation under varying NO_x conditions, the sole use of 254 nm photolysis lamps is not sufficient as longer wavelengths ($\lambda > 300$ nm) are required in order to facilitate ozone formation following R 7-8 and R 7-9:

$NO_2 + h\nu_{(\lambda > 300\ nm)} \rightarrow NO + O(^3P)$ R 7-8

$O(^3P) + O_2 \rightarrow O_3$ R 7-9

In this case, two sets of lamps with maximum wavelength output, one at 254 nm and one at 360 nm are used in order to ensure NO_2 is photolysed to NO and $O(^3P)$.

Previous chamber oxidation product studies of VOCs, specifically those of the isomers of butanol, have investigated the OH radical initiated oxidation only in the presence of NO_x (Cavalli *et al.* 2002, Hurley *et al.* 2009, Andersen *et al.* 2010) as CH_3ONO or HONO

were employed as the OH precursor. Cl atom initiated oxidation studies of butanol isomers in the literature have been reported in both the presence and absence of NO_x, (Hurley *et al.* 2009, Andersen *et al.* 2010), however, these studies were carried out in the presence of very high concentrations of NO_x, ~100 ppmv; levels typically not observed in the troposphere.

The studies presented here are the first reported on the products of the OH radical initiated oxidation of *iso*-butanol in the absence of NO_x, employing H_2O_2 as the OH radical precursor. They are also the first reported under varying levels of tropospherically relevant concentrations of NO, allowing for more relevant conclusions to be drawn on the implications of the OH radical initiated oxidation of *iso*-butanol. The Cl atom initiated oxidation process of *iso*-butanol is also reported in the absence of NO_x for comparison with previous literature studies (Andersen *et al.* 2010); and in the presence of varying levels of tropospherically relevant concentrations of NO for comparison with the OH radical initiated oxidation of *iso*-butanol in the presence of varying initial NO concentrations.

Tropospheric ozone is harmful to both plant and animal life (Krupa *et al.* 1998, Felzer *et al.* 2007, Ellingsen *et al.* 2008, Monks 2009); its formation is closely related to VOC oxidation in high NO_x environments. The first measurements of ozone concentrations following the oxidation of *iso*-butanol by either Cl atoms or OH radicals in the absence and presence of varying initial NO concentrations are presented. Comparison is drawn on the ozone formation between the *iso*-butanol oxidation and the oxidation of *iso*-butane. The comparison with *iso*-butane was used as the analogous non-functionalised alkane in order to better understand the impact of the alcohol functional group of potential biofuel compounds.

Measurements of OH reactivity provide valuable information on the total loss rate of OH within the specific environment where measurements are being carried out (Kaiser *et al.* 2016, Whalley *et al.* 2016, Fuchs *et al.* 2017). The ability to measure OH reactivity in chamber studies allows for more in depth investigation into the discrepancies typically observed between measured and calculated OH reactivity from field studies. In chamber studies, chemical reactions can be studied in isolation, with knowledge of exact compounds being inputted into the system. By comparing measured and calculated OH reactivity for such constrained reaction systems, it is possible to gain further insight into our understanding of the chemical processes occurring. The first OH reactivity

measurements following the oxidation of VOCs in the HIRAC chamber are presented in Chapter 8, with comparison to calculated OH reactivity, from measured species, made for the Cl atom and OH radical oxidation of *iso*-butanol and *iso*-butane in the absence and presence of varying initial NO concentrations.

7.2 Experimental

All experiments were carried out in the HIRAC chamber at ambient temperature and pressure of ~298 K and ~1000 mbar. HIRAC was filled to 1000 mbar with 80% N_2 (BOC, 99.998% purity) and 20% O_2 (BOC, 99.999% purity). GC-FID with a CP-Sil 5CB (50 m length, 0.32 mm i.d., 5 µl film thickness) column was used to quantify concentrations of *iso*-butanol, *iso*-butane, *iso*-butyraldehyde and acetone for all of the experiments carried out. FTIR spectra were used to quantify *iso*-butanol, *iso*-butane and formaldehyde for all of the experiments carried out. It was not possible to detect formaldehyde using the GC-FID.

OH and HO_2 radicals were measured using the HIRAC FAGE instrument, as described in Chapter 3 and OH reactivity was measured with the LFP-LIF instrument as described in Chapter 4. OH reactivity measurements are discussed in Chapter 8. O_3 and NO_x (NO and NO_2) were measured using commercial instruments; Thermo Envirnomenal Instruments Inc. Model 49C UV Photometric O_3 Analyzer (LOD = 1 ppbv) and Thermo Environmental Instruments Inc. Model 42C Trace Level Chemiluminescence NO-NO_2-NO_x Analyzer (LOD = 50 pptv).

Iso-butyraldehyde formed in the oxidation reactions with both Cl and OH initiated chemistry, can subsequently react with any Cl atoms or OH radicals present in the chamber:

$$\textit{Iso}\text{-butyraldehyde} + \text{Cl} \xrightarrow{k_{\text{Cl}+\textit{iso}\text{-butyraldehyde}}} \text{products} \qquad \text{R 7-10}$$

$$\textit{Iso}\text{-butyraldehyde} + \text{OH} \xrightarrow{k_{\text{OH}+\textit{iso}\text{-butyraldehyde}}} \text{products} \qquad \text{R 7-11}$$

and it was necessary to take this into account in the product yield analysis. In the OH radical systems, significant loss of *iso*-butyraldehyde due to photolysis also needed to be taken into consideration. *Iso*-butyraldehyde is known to photolyse at wavelengths of 230 - 350 nm (Martinez *et al.* 1992, Chen *et al.* 2002).

Iso-butyraldehyde + $h\nu \xrightarrow{j_{iso\text{-butyraldehyde}}}$ products R 7-12

In all experiments, loss of reactants and products due to dilution of HIRAC by the large total sampling flow of ~8 l min^{-1} was also considered. These losses can be observed by the curvature of the *iso*-butyraldehyde concentration profiles, shown in Section 7.3 and Section 7.4. Knowing the loss processes involved, the product data can be fitted using Eq. 7-1, similar to that described by Meagher *et al.* (1997) and used by Andersen *et al.* (2010) for analysis of *iso*-butanol oxidation product data (see Appendix A for derivation of Eq. 7-1).

$$y = \frac{\alpha/h}{1-\left(\frac{g}{h}\right)}(1-x)\left\{(1-x)^{\left(\frac{g}{h}-1\right)}-1\right\} \quad \text{Eq. 7-1}$$

$$h = \frac{k_{RH}[OH] + k_{dil}}{k_{RH}[OH]} \quad \text{Eq. 7-2}$$

$$g = \frac{k_{prod}[OH] + k_{dil} + j_{prod}}{k_{RH}[OH]} \quad \text{Eq. 7-3}$$

$$y = \frac{[prod]_t}{[RH]_0} \quad \text{Eq. 7-4}$$

$$x = 1 - \frac{[RH]_t}{[RH]_0} \quad \text{Eq. 7-5}$$

where k_{RH} is the rate coefficient for the reaction of the reactant and the oxidising agent (Cl or OH), k_{prod} is the rate coefficient for the reaction of the product (*iso*-butyraldehyde) and the oxidising agent (Cl or OH), k_{dil} is the rate of loss due to dilution in the chamber and j_{prod} is the photolysis rate of the product (*iso*-butyraldehyde) in the chamber. The values of k_{RH} and k_{prod} are taken from the literature, values of k_{dil} are determined for each experiment from counter flow data and/or dilution measurements of the reactant prior to the initiation of the oxidation reaction, and j_{prod} was determined for each measured compound in separate photolysis experiments.

7.2.1 Cl Atom Initiated Oxidation Studies

The photolysis of molecular chlorine was used to produce Cl atoms in the HIRAC chamber at a wavelength of ~360 nm. Cl_2 ((1.24 – 1.69) × 10^{14} molecule cm^{-3}) was added to the chamber via the delivery vessel. *Iso*-butanol (2.90 × 10^{13} molecule cm^{-3}) was injected directly into the chamber using a 50 ± 0.5 µl syringe, over a flow of N_2.

Iso-butane ((3.31 – 4.10) × 10^{13} molecule cm^{-3}) was injected into the chamber via the delivery line (described in Chapter 2) as a gas. All measurements were carried out as described above in Section 7.2. Experiments were typically run for 20 - 30 minutes.

7.2.2 OH Radical Initiated Oxidation Studies

Iso-butanol (2.9 × 10^{13} molecule cm^{-3}) was injected directly into the chamber using a 50 ± 0.5 µl syringe over a flow of N_2. *Iso*-butane was introduced into the chamber via the delivery vessel as described in Chapter 2. H_2O_2 (8.95 × 10^{13} molecule cm^{-3}) was injected directly into the chamber using a 50 ± 0.5 µl syringe over a flow of N_2. OH radical initiated oxidation experiments employed the use of two sets of photolysis lamps; GE G55T8 / OH 7G UVC photolysis lamps with a maximum output at ~254 nm were used to photolyse the OH precursor, and Philips TL-K 40W/05 lamps with a maximum output at ~360 nm were required in order to investigate O_3 formation from the oxidation of the selected hydrocarbons.

7.3 Cl Atom Initiated Oxidation of *Iso*-butanol

7.3.1 Studies in the Presence of NO_x

Mixtures of *iso*-butanol, Cl_2 and NO in 1000 mbar 4:1, N_2:O_2, were irradiated using black lamps with a maximum output at ~360 nm in order to investigate the products of the Cl atom initiated oxidation process of *iso*-butanol in the presence of NO_x. *Iso*-butyraldehyde, acetone and HCHO were observed as major products following the oxidation process in all experiments conducted.

The formation of *iso*-butyraldehyde following the oxidation of *iso*-butanol by Cl atoms, under varying initial NO concentrations, is shown in Figure 7-1. The dashed lines represent the linear least squares fit to the data, with the intercept forced through zero, for <30% consumption of *iso*-butanol, where the gradient represents the initial yield of *iso*-butyraldehyde. These gradients are given in Table 7-1. No clear trend in the initial yield of *iso*-butyraldehyde is observed, indicating that other factors may be influencing the formation of *iso*-butyraldehyde. It would be expected that in cases where the initial NO concentration was similar, such as 61 ppbv and 73 ppbv initial NO, that the initial yield of *iso*-butyraldehyde would also be similar. In fact, this was not observed, with the initial *iso*-butyraldehyde yield with 61 ppbv initial NO being 94%, and 68% with 73 ppbv initial NO. This suggests that the initial yield was influenced by the initial concentrations of other species within HIRAC, such as OH and HO_2 radicals, or NO_2. These species will be discussed later in this section. Under all initial NO concentrations, the

iso-butyraldehyde is observed to go through a maximum and decay towards zero as the *iso*-butanol was consumed. This was expected, as *iso*-butyraldehyde will react with Cl atoms present, at a faster rate than the reaction of *iso*-butanol with Cl atoms ($k_{Cl + iso\text{-butyraldehyde}}$ = (1.37 ± 0.08) × 10^{-10} cm^3 $molecule^{-1}$ s^{-1} and $k_{Cl + iso\text{-butanol}}$ = (2.06 ± 0.40) × 10^{-10} cm^3 $molecule^{-1}$ s^{-1}) (Andersen *et al.* 2010); OH radicals are also formed during the Cl atom initiated oxidation process, with which the *iso*-butyraldehyde can react.

Andersen *et al.* (2010) noted that *iso*-butanol may also be lost through reaction with OH radicals, which is produced in the Cl atom initiated oxidation experiments in the presence of NO_x, however, they observed no significant impact on the *iso*-butyraldehyde yield and concluded that the OH radicals did not play an important role in the chemistry occurring. The authors were able to fit their experimental data using an equation similar to Eq. 7-1, taking into account the loss of *iso*-butyraldehyde from its reaction with Cl atoms.

In the work presented here, initial Cl_2 concentrations were nearly 100 times lower than those used in the study by Andersen *et al.* (2010), (1.24 – 1.69) × 10^{14} molecule cm^{-3} and (4.21 – 8.04) × 10^{15} molecule cm^{-3}. It was not possible to obtain a value for the initial yield of *iso*-butyraldehyde by fitting the experimental data with Eq. 7-1; it is likely that higher initial [OH] present in HIRAC, and the lower initial [Cl_2] lead to OH radicals playing a more significant role in the chemistry occurring than in the work presented by Andersen *et al.* (2010). This result indicates the importance of understanding the chemical processes occurring at varying ratios of Cl:OH in the troposphere; concentrations of OH radicals in the troposphere are typically considerably greater than Cl atoms.

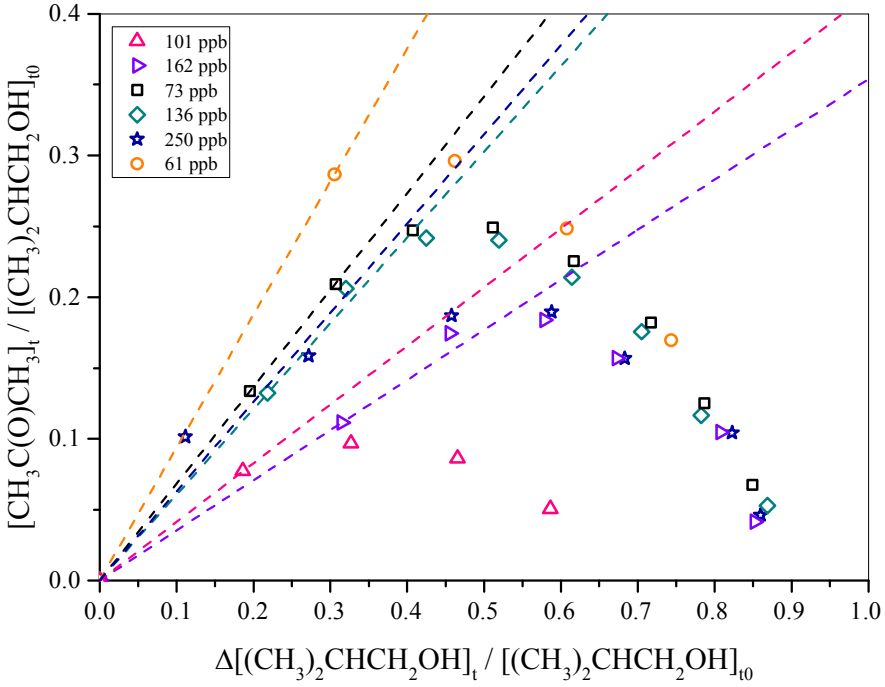

Figure 7-1: Formation of *iso*-butyraldehyde vs. the loss of *iso*-butanol following the Cl atom initiated oxidation of *iso*-butanol in 80:20 mixtures of N_2:O_2 at 298 K and 1000 mbar total pressure in the presence of NO_x. Dashed lines represent linear least squares fit to the data with the intercept fixed through zero at <30% *iso*-butanol consumption.

[NO] / ppbv	Gradient
61	0.94
73	0.68
101	0.41
136	0.61
162	0.35
250	0.57

Table 7-1: *Iso*-butyraldehyde production yields following the Cl atom initiated oxidation of *iso*-butanol in 80:20 mixtures of N_2:O_2 at 298 K and 1000 mbar total pressure in the presence of NO_x. Gradients represent linear least squares fit to the data where the intercept is fixed through zero for *iso*-butanol consumption <30%.

Figure 7-2 shows the formation of acetone vs. the loss of butanol under a range of initial NO concentrations. No curvature is observed in the acetone formation, unlike the *iso*-butyraldehyde formation. The kinetics of the reaction of acetone with Cl atoms are considerably slower ($k_{Cl + acetone} = (2.10 \pm 0.29) \times 10^{-12}$ cm^3 molecule^{-1} s^{-1} (Atkinson *et al.*

2006)) than that of the reaction of Cl atoms with *iso*-butanol ($k_{Cl + iso\text{-butanol}} = (2.06 \pm 0.40) \times 10^{-10}$ cm^3 molecule^{-1} s^{-1}) (Andersen *et al.* 2010), and so no loss of acetone was observed. A general trend is observed in that as the initial [NO] was increased, the yield (taken from the gradient of the linear least squares fit fixed through zero) decreased. Yields determined from the linear least squares fit to the data in Figure 7-2 are given in Table 7-2.

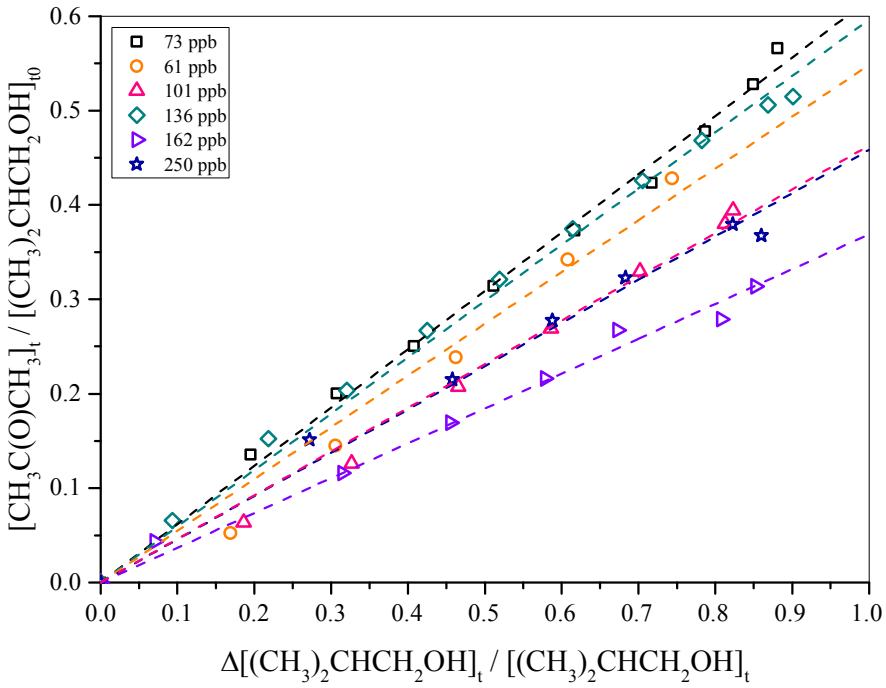

Figure 7-2: Formation of acetone vs. the loss of *iso*-butanol following the Cl atom initiated oxidation of *iso*-butanol in 80:20 mixtures of N_2:O_2 at 298 K and 1000 mbar total pressure in the presence of NO_x. Dashed lines represent linear least squares fit to the data with the intercept fixed through zero. Values reported in the text refer to linear least squares fit to the data without the intercept fixed (see Table 7-2).

Andersen *et al.* (2010) reported an acetone yield of 35 ± 3% following the Cl atom initiated oxidation of *iso*-butanol in the presence of NO_x; this is in good agreement with the yields reported in Table 7-2 for the studies carried out at the highest concentrations of initial NO in HIRAC (36 ± 1% for an initial NO concentration of 162 ppbv and 45 ± 2% for an initial NO concentration of 250 ppbv). These acetone yields, however, should be taken as upper limits as no correction has been made for the formation of acetone following subsequent reactions of *iso*-butyraldehyde within the system.

[NO] / ppbv	Gradient	Intercept
61	0.60 ± 0.03	-0.03 ± 0.01
73	0.61 ± 0.01	0.004 ± 0.009
101	0.49 ± 0.01	-0.02 ± 0.01
136	0.57 ± 0.01	0.02 ± 0.01
162	0.36 ± 0.01	0.01 ± 0.01
250	0.45 ± 0.02	0.01 ± 0.01

Table 7-2: Acetone production yields following the Cl atom initiated oxidation of *iso*-butanol in 80:20 mixtures of N_2:O_2 at 298 K and 1000 mbar total pressure in the presence of NO_x. Gradients represent linear least squares fit to the data where the intercept is not fixed through zero. Errors represent the standard error from the fitting procedure.

The formation of HCHO vs. the loss of *iso*-butanol is shown in Figure 7-3, for varying initial NO concentrations. Again, a general trend is observed; the initial yield of HCHO (represented by the linear least squares fit line to the data for <40% *iso*-butanol consumption with the intercept forced through zero) decreases with increasing initial [NO] to a minimum, and then increased again. Table 7-3 details the initial yields of HCHO, for <40% *iso*-butanol consumption. As the initial [NO] was increased, the potential for OH formation following reaction R 7-13 increased, leading to more OH radicals present in the system to react with the *iso*-butanol and its oxidation products.

$$NO + HO_2 \rightarrow OH + NO_2 \qquad \text{R 7-13}$$

$$NO_2 + h\nu \rightarrow NO + O(^3P) \qquad \text{R 7-14}$$

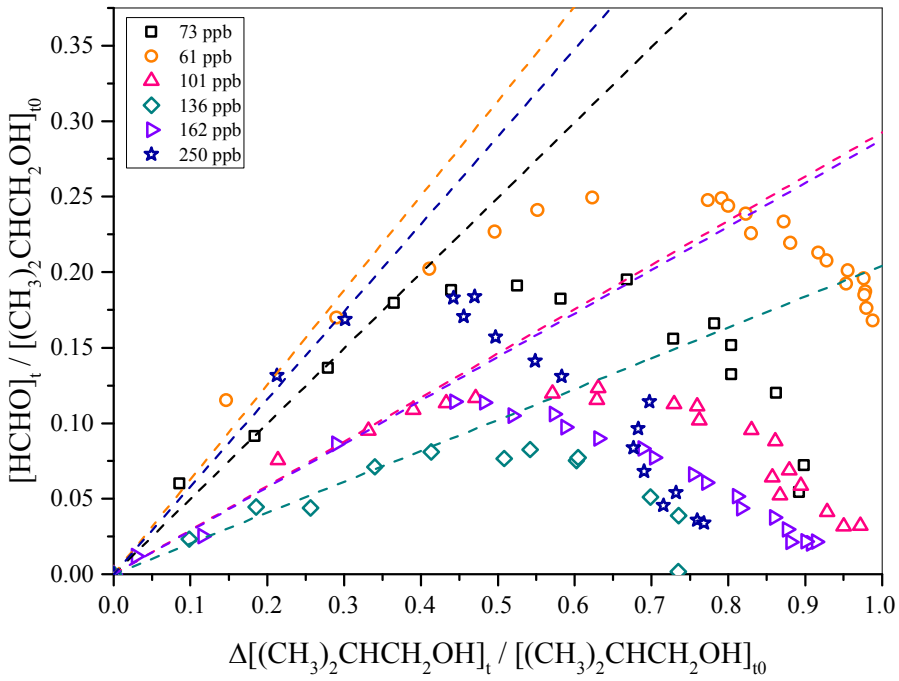

Figure 7-3: Formation of HCHO vs. the loss of *iso*-butanol following the Cl atom initiated oxidation of *iso*-butanol in 80:20 mixtures of N_2:O_2 at 298 K and 1000 mbar total pressure in the presence of NO_x. Dashed lines represent linear least squares fit to the data (for <40% *iso*-butanol consumption) with the intercept fixed through zero. Values reported in the text refer to linear least squares fit to the data without the intercept fixed (see Table 7-3).

[NO] / ppbv	Gradient	Intercept
61	0.59 ± 0.12	0.01 ± 0.02
73	0.47 ± 0.03	0.01 ± 0.01
101	0.28 ± 0.03	0.01 ± 0.01
136	0.20 ± 0.02	0.01 ± 0.01
162	0.29 ± 0.03	-0.001 ± 0.004
250	0.57 ± 0.04	0.002 ± 0.009

Table 7-3: HCHO production yields following the Cl atom initiated oxidation of *iso*-butanol in 80:20 mixtures of N_2:O_2 at 298 K and 1000 mbar total pressure in the presence of NO_x. Gradients represent linear least squares fit to the data (for <40% *iso*-butanol consumption) where the intercept is not fixed through zero. Errors represent the standard error from the fitting procedure.

Curvature is observed in Figure 7-3 for the formation of HCHO vs. the loss of *iso*-butanol, whereas no curvature is observed in the analogous plot for acetone in Figure 7-2. This

difference is attributed to the relative reactivities of acetone and HCHO with Cl atoms and OH radicals. The reaction of acetone with Cl atoms is two orders of magnitude slower than that of *iso*-butanol with Cl atoms, whereas the reaction of HCHO with Cl atoms is comparable with that of *iso*-butanol with Cl atoms.

It is assumed that both *iso*-butanol and acetone are additionally lost due to dilution only, where the gradient obtained from a linear least squares fit gives the yield of acetone. Yields of acetone quoted should be taken as an upper limit; it is known that acetone will also be formed following the reaction of *iso*-butyraldehyde with OH radicals or Cl atoms present in the system, as described by R 7-15 to R 7-21, giving an overestimation of the yield of acetone.

$(CH_3)_2CHCHO + Cl(\text{or } OH) \rightarrow (CH_3)_2CHCO + HCl(\text{or } H_2O)$ R 7-15

$(CH_3)_2CHCO + O_2 \rightarrow (CH_3)_2CHC(O)O_2$ R 7-16

$(CH_3)_2CHC(O)O_2 + RO_2 \rightarrow (CH_3)_2CHC(O)O + RO + O_2$ R 7-17

$(CH_3)_2CHC(O)O \rightarrow (CH_3)_2CH + CO_2$ R 7-18

$(CH_3)_2CH + O_2 \rightarrow (CH_3)_2CHO_2$ R 7-19

$(CH_3)_2CHO_2 + RO_2 \rightarrow (CH_3)_2CHO + RO + O_2$ R 7-20

$(CH_3)_2CHO + O_2 \rightarrow CH_3C(O)CH_3 + HO_2$ R 7-21

In the presence of NO_x, OH radicals are formed during the Cl atom initiated oxidation of *iso*-butanol; Andersen *et al.* (2010) observed no discernible difference in the *iso*-butyraldehyde yield between experiments carried out in the absence and presence of NO_x, implying that OH radical chemistry in the Cl atom initiated oxidation process does not play a significant role in the formation of *iso*-butyraldehyde. It should therefore be possible to use Eq. 7-1 to fit to the product data in order to obtain a value of α for *iso*-butyraldehyde in the Cl atom initiated oxidation of *iso*-butanol, assuming that the OH radical concentration reaches a steady state in a short time period from the initiation of the oxidation reaction. Along with considerably higher concentrations of Cl_2 used by Andersen *et al.* (2010), the authors also used much higher initial concentrations of NO; $(2.1 – 2.7) \times 10^{15}$ molecule cm^{-3} compared to $(1.5 – 6.3) \times 10^{12}$ molecule cm^{-3} used in this work. The results presented in this work suggest that the yields of products in the Cl atom initiated oxidation of *iso*-butanol in the presence of NO_x are affected by the initial concentration of [NO] present in HIRAC. The considerably higher concentrations of Cl_2

used in the experiments by Andersen *et al.* (2010) ensure that OH radicals are insignificant in the chemical processes occurring in the oxidation process; the high concentrations of NO ensure that all peroxy radicals produced in the oxidation process react with NO to directly form the oxidation products. In the work presented here, it is suggested that a competition may exist between the reaction with NO and the reaction with peroxy radicals in the oxidation process, influencing the yields of the oxidation products.

The time series concentration profiles of O_3, OH, HO_2, NO and NO_2 are shown in Figure 7-4 for the Cl atom initiated oxidation of *iso*-butanol in the presence of varying initial NO concentrations. It can be seen from these time series concentration profiles that in the presence of NO_x, the OH concentration reached a steady state within 100 s, except in the case of the highest initial [NO], where the OH reached a steady state within 400 s. In all cases the OH concentration reached a steady state as the NO concentration tends towards zero, showing that the two are closely related. The HO_2 concentration reached a maximum steady state as the NO concentration decreased, following almost an inverse concentration time profile to that of the NO concentrations. As the initial NO concentration was increased, the HO_2 took longer to reach a steady state. The vertical lines in the HO_2 concentration time series indicate the time at which the photolysis lamps were switched off, following which the HO_2 concentration decayed towards zero. In the absence of any other reactive species, this HO_2 decay would be equal to the HO_2 self-reaction, in which the HO_2 decay would be complete in ~90 seconds. The decay of HO_2 observed in Figure 7-4 typically occurs over ~250 seconds; considerably longer timescale than that of the HO_2 self-reaction. This would suggest that there are other dark reactions occurring leading to the formation of HO_2. This HO_2 formation likely arises from any RO species present, following R 7-22:

$$RO + O_2 \rightarrow HO_2 + RCHO \qquad \text{R 7-22}$$

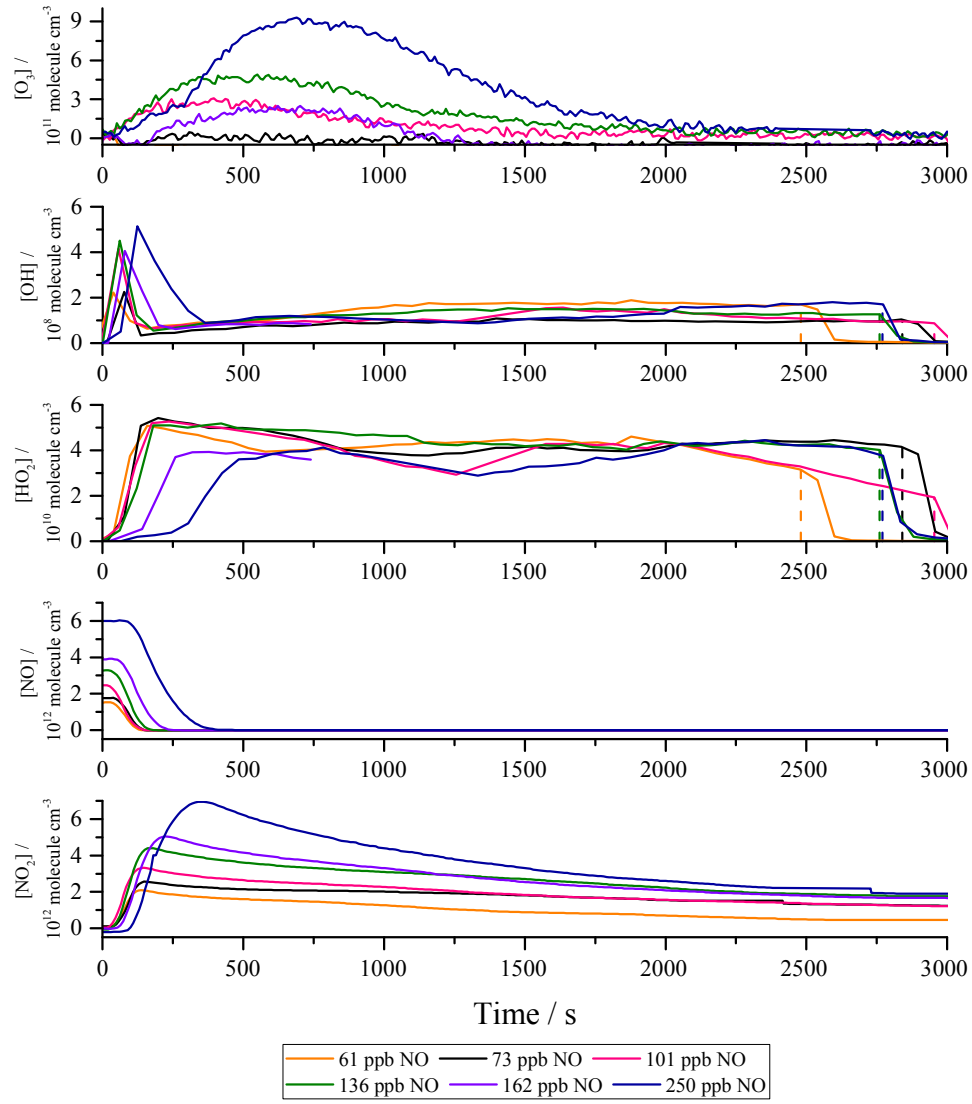

Figure 7-4: Time series of $[O_3]$, [OH], $[HO_2]$, [NO] and $[NO_2]$ for the Cl atom initiated oxidation of *iso*-butanol in the presence of NO_x. Vertical dashed lines in the [OH] and $[HO_2]$ time series indicate the time at which the photolysis lamps were switched off. O_3 analyser LOD = 1 ppbv, NO LOD = 50 pptv (120 second averaging).

Dark formation of HO_2 may also arise from the reaction of OH radicals with O_3 or CO; the OH radical concentration also decayed on a similar timescale to the decay of HO_2 when the photolysis lamps were switched off. The reaction of OH radicals with O_3, however, is unlikely as the $[O_3]$ was approximately zero in all cases at this time in the experiment.

With the exception of the 162 ppbv initial NO concentration case, the peak ozone concentration was observed to increase with increasing initial NO. As the initial NO concentration was increased, greater concentrations of NO_2 were produced, which go on

to produce O_3 following R 7-8 and R 7-9. It is known that the chemiluminescence NO_x analyser used measures any compound that is converted into NO by the molybdenum NO_2 to NO converter, and so the NO_2 concentrations reported should be considered as a total of NO_2 and any NO_y species present in the sample gas. As expected, the peak NO_2 concentrations shown in Figure 7-4 increased with increasing initial [NO]. In all cases, the NO_2 concentration rapidly increased, at shorted times, to a maximum, and then declined. The NO_2 concentration never reached zero, due to the recorded concentration of NO_2 being the sum of NO_2 and NO_y species, and the rapid recycling of NO_2 following R 7-13 and R 7-14.

7.3.2 Studies in the Absence of NO_x

Mixtures of Cl_2 and *iso*-butanol, in 1000 mbar total pressure 4:1 N_2:O_2, were irradiated with black lamps with a maximum output of ~360 nm. In the absence of NO_x; $HO_2 + RO_2$ and $RO_2 + RO_2$ reactions play a significant role in the conversion of the peroxy radicals to alkoxy radicals. In experiments carried out in the absence of NO_x this was observed as it is not possible to use Eq. 7-1 to obtain a value of α for the formation of *iso*-butyraldehyde.

The formation of acetone vs. the loss of *iso*-butanol is shown in Figure 7-5, where the solid red line represents the linear least squares fit to the data without the intercept fixed, and the dashed black line represents the linear least squares fit to the data with the intercept forced through zero. The gradient of the linear least squares fit represents the acetone yield; 72 ± 1%. This yield is relatively high compared to that reported by Andersen *et al.* (2010), where they reported an initial yield of <5% for <20% *iso*-butanol consumption. Here, the higher yield may be attributed to higher background levels of HO_x within HIRAC influencing the acetone yield formation as a primary product in the *iso*-butanol oxidation, and as a secondary product from the oxidation of *iso*-butyraldehyde. Andersen *et al.* (2010) observed significant curvature in their acetone formation (circles in Figure 7-6) from the Cl atom initiated oxidation of *iso*-butanol in the presence of NO_x, indicating that acetone was not a primary product in the oxidation process. As discussed in Section 7.2.1, the higher background [HO_x] combined with lower $[Cl_2]_0$, as compared to Andersen *et al.* (2010), may lead to the OH radicals playing a more significant role in the chemical processes occurring.

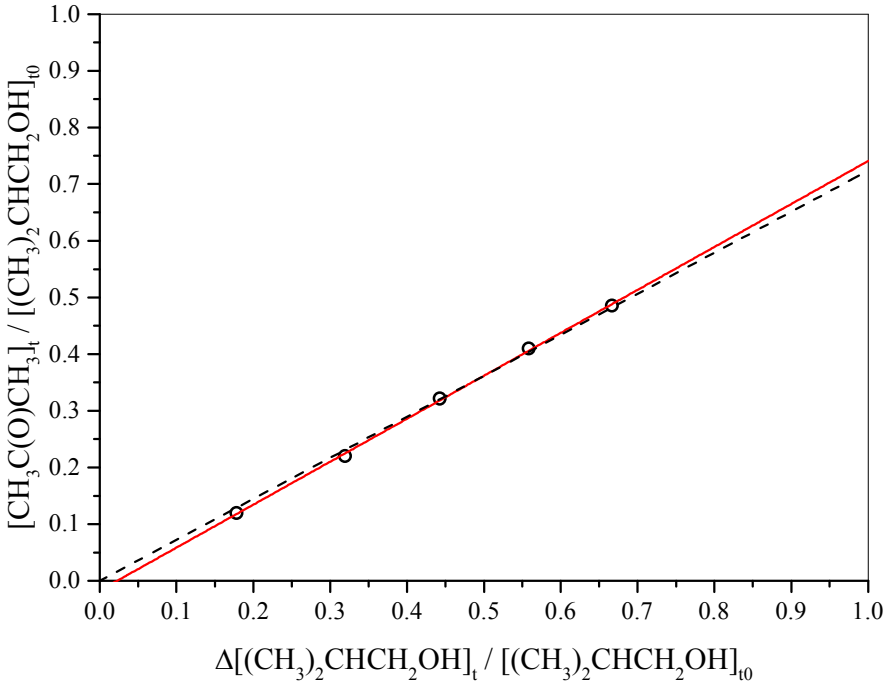

Figure 7-5: Formation of acetone vs. the loss of *iso*-butanol following the Cl atom initiated oxidation of *iso*-butanol in 80:20 mixtures of N_2:O_2 at 298 K and 1000 mbar total pressure in the absence of NO_x. The dashed lines represents linear least squares fit to the data with the intercept fixed at zero. The solid red line represents linear least squares fit to the data without the intercept fixed.

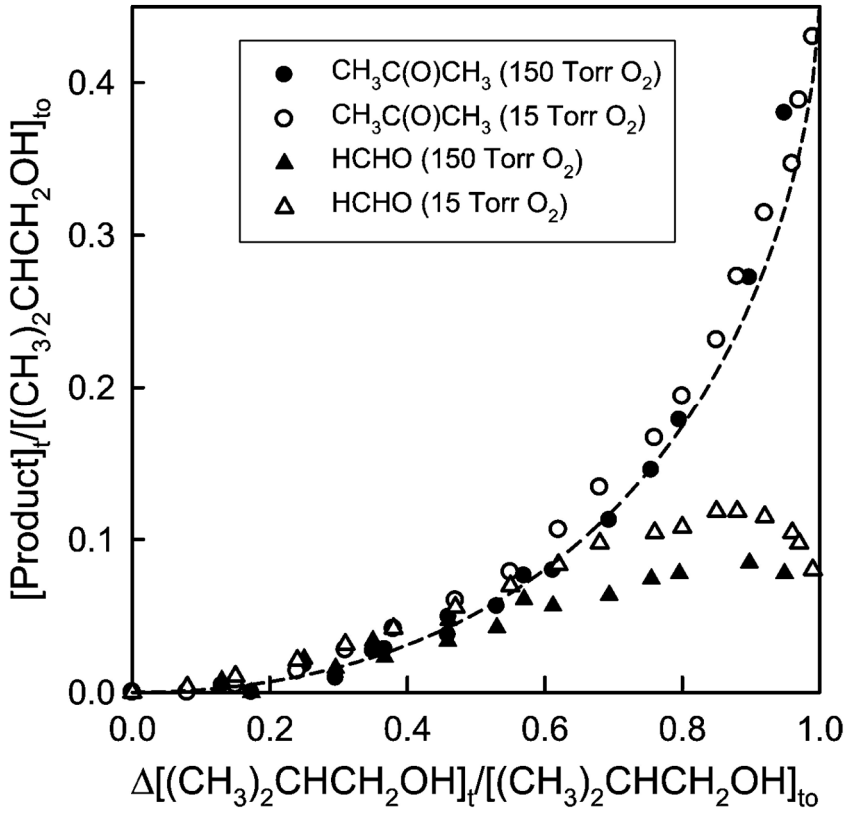

Figure 7-6: Formation of acetone (circles) and HCHO (triangles) vs. the loss of *iso*-butanol following the Cl atom initiated oxidation of *iso*-butanol in the absence of NO_x. Reproduced from Andersen *et al.* (2010).

The formation of HCHO vs. the loss of *iso*-butanol is shown in Figure 7-7. It can be seen that the yield of HCHO increased to a maximum, at *iso*-butanol consumption of >60%, and then declined. This decline in HCHO may arise from a number of contributing factors; reaction with Cl atoms present in the system, reaction with OH radicals present in the system, and loss due to the dilution of HIRAC. The low yield of HCHO reflects the lower concentration of OH radicals produced in the system in the absence of NO; HCHO is formed as a secondary product in the oxidation of *iso*-butanol. Low yields of HCHO from the Cl atom initiated oxidation of *iso*-butanol in the absence of NO_x were also reported by Andersen *et al.* (2010), where they also concluded that HCHO is not formed as a primary product in this oxidation process; formation of HCHO vs. the loss of *iso*-butanol is shown by the triangles in Figure 7-6. Andersen *et al.* (2010) reported yields of HCHO of <5% for <20% *iso*-butanol consumption. Here, slightly higher yield of 10% was observed for <20% *iso*-butanol consumption, likely influenced by higher background levels of OH within HIRAC. Background levels of HO_x within HIRAC can vary from day to day due to the varied use of the chamber; similar to the frequent study of reactions in the presence of NO_x which can lead to higher levels of NO_x containing species on the walls of the chamber, the frequent study involving certain compounds can lead to varying levels of compounds present on the chamber walls that produce HO_x in subsequent experiments. Detailed investigation into the use of different species and their influence on background levels of HO_x has, to date, not been conducted, however, the addition of Cl_2 in 100 – 200 mbar of laboratory N_2, left with the photolysis lamps set to switch on and off repeatedly overnight between experiments has been seen to reduce the levels of background HO_x present in HIRAC. Further investigation into the influence of residual compounds within the chamber is required in order to fully appreciate sources of background HO_x, and would assist in determining the most appropriate cleaning protocols between experiments.

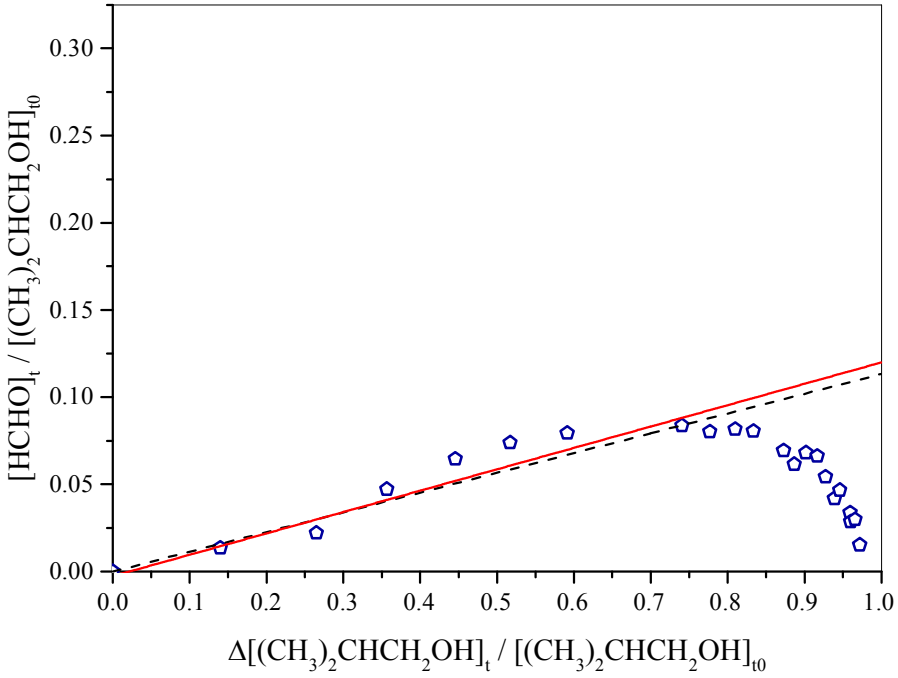

Figure 7-7: Formation of HCHO vs. the loss of *iso*-butanol following the Cl atom initiated oxidation of *iso*-butanol in 80:20 mixtures of N_2:O_2 at 298 K and 1000 mbar total pressure in the absence of NO_x. The dashed line represents linear least squares fit to the data (for <40% *iso*-butanol consumption) with the intercept fixed at zero. The solid red line represents linear least squares fit to the data without the intercept fixed.

Concentration time profiles for O_3, OH, HO_2, NO and NO_2 are shown in Figure 7-8 for the Cl atom initiated oxidation of *iso*-butanol in the absence of NO_x. It can clearly be shown here that the studies are carried out in the absence of NO_x, from the NO concentration time profile. In this case, no ozone formation was observed, which is to be expected in the absence of NO_x as no NO_2 formation is possible in the oxidation process to produce ozone following R 7-8 and R 7-9. The OH concentration peaks to ~8×10^8 molecule cm^{-3} at around 500 s from the initiation of the oxidation reaction. This peak comes at much later times to the peak OH concentration observed for the Cl atom initiated oxidation of *iso*-butanol in the presence of NO_x, is significantly greater in concentration, and remains at a steady concentration for ~300 s; whereas in the presence of NO_x, the OH concentration immediately decayed following its maximum. This lasting peak in OH concentration is likely due to a number of factors; the reaction of the majority of hydrocarbons (and intermediate species) with Cl atoms is significantly faster than their reaction with OH radicals. In the presence of NO_x, OH radicals may also be lost following their reaction with NO_2:

$OH + NO_2 \rightarrow NO + HO_2$ R 7-23

which will not be occurring in the absence of NO_x.

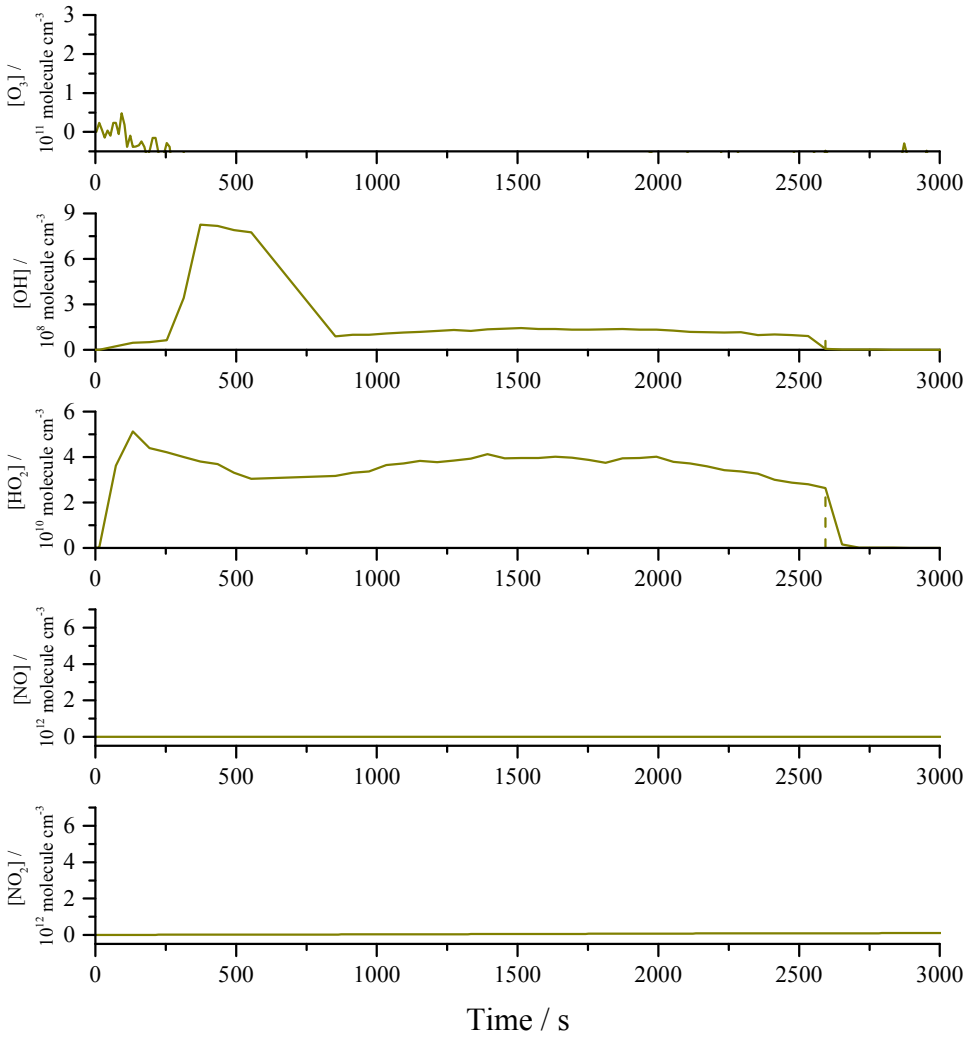

Figure 7-8: Time series comparison of $[O_3]$, [OH], $[HO_2]$, [NO] and $[NO_2]$ for the Cl atom initiated oxidation of *iso*-butanol in the absence of NO_x. The vertical line in the $[HO_2]$ time series indicates the time at which the photolysis lamps were switched off. O_3 analyser LOD = 1 ppbv, NO LOD = 50 pptv (120 second averaging).

7.4 OH Radical Initiated Oxidation of *Iso*-butanol

7.4.1 Studies in the Presence of NO_x

Mixtures of *iso*-butanol, H_2O_2 (50% purity in water) and NO were irradiated with two sets of photolysis lamps; one set with a maximum output at ~254 nm in order to initiate the H_2O_2 photolysis reaction, and a set of black lamps with a maximum output at ~360 nm

in order to photolyse NO_2 produced in the reaction to enable production of O_3 to be observed, following reactions R 7-8 and R 7-9.

The formation of *iso*-butyraldehyde vs. the loss of *iso*-butanol under three different initial [NO] is shown in Figure 7-9, where the dashed lines represent the fit to Eq. 7-1, and the solid lines represent the linear least squares fit to <30% *iso*-butanol consumption to give an initial yield of *iso*-butyraldehyde prior to any significant influence from secondary chemistry in the oxidation reaction. The curvature observed in the formation of *iso*-butyraldehyde represents the loss of *iso*-butyraldehyde due to reaction with OH radicals and loss due to photolysis and dilution within HIRAC. The initial yield of *iso*-butyraldehyde (for <15% *iso*-butanol consumption) increased with increasing initial [NO]. The formation of the alkoxy radical from the peroxy radical is enhanced by the presence of NO, following reaction R 7-24.

$$RO_2 + NO \rightarrow RO + NO_2 \qquad \text{R 7-24}$$

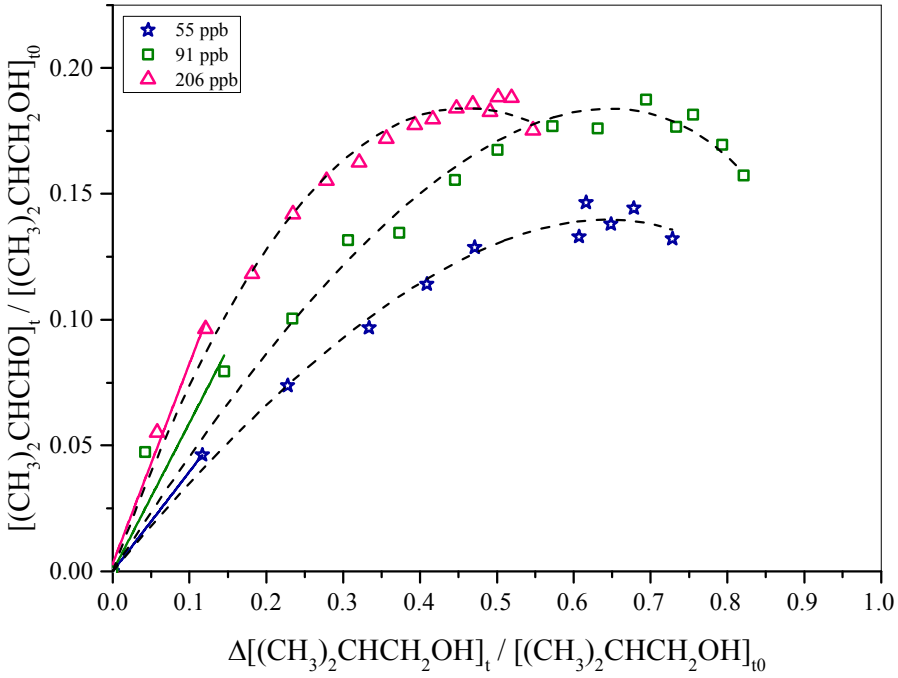

Figure 7-9: Formation of *iso*-butyraldehyde vs. the loss of *iso*-butanol following the OH radical initiated oxidation of *iso*-butanol in 80:20 mixtures of N_2:O_2 at 298 K and 1000 mbar total pressure in the presence of NO_x. The dashed lines represent a fit to Eq. 7-1. The solid lines represent linear least squares fit to the data (for <30% *iso*-butanol consumption) with the intercept fixed at zero.

The initial yields at <30% *iso*-butanol consumption and the final molar yields of *iso*-butyraldehyde are given in Table 7-3. The initial yields for *iso*-butanol consumption increased with increasing initial NO concentration. In contrast, the final molar yield increased and then decreased at the maximum initial NO concentration. As only three different initial NO concentrations were investigated, it is difficult to draw conclusions as to any trend in the yields relating to the initial [NO]. It is suggested that the trend in initial *iso*-butyraldehyde yields, for <30% *iso*-butanol consumption is influenced by the initial concentrations of OH and HO_2 present in HIRAC. The concentration time profiles of O_3, OH, NO and NO_2 are shown in Figure 7-14.

[NO] / ppbv	**Final Molar Yield**	**Initial Yield (<30% *iso*-butanol consumption)**
55	83 ± 14 %	34 ± 2%
91	91 ± 14%	48 ± 6%
206	47 ± 20%	61 ± 4%

Table 7-4: Yields of *iso*-butyraldehyde from the OH radical initiated oxidation of *iso*-butanol in the absence of NO_x. Errors represent the standard error from the fitting procedure.

The formation of acetone vs. the loss of *iso*-butanol is shown in Figure 7-10, where the dashed lines represent the linear least squares lines of best fit, forcing the intercept through zero, in order to obtain a value for the final product yield. For the reaction of *iso*-butanol with OH radicals, the acetone product yield increases as the initial [NO] is increased.

As the initial [NO] was increased, the initial peak concentration of OH also increased, however, the background OH concentration, i.e. $[OH]_0$, decreased. The acetone yield is enhanced by the presence of NO in the system as the peroxy radical formed from the ß-hydrogen abstraction is rapidly converted to the alkoxy radical which rapidly decomposes to form acetone and HCHO. In the absence of NO, the peroxy radical can react with other peroxy radicals or HO_2 radicals to produce acetone and HCHO. The presence of NO provides a more direct route to the formation of acetone, whereas in the absence of NO_x, the peroxy radicals may be lost through reaction with other peroxyl radicals, not resulting in the formation of acetone. The yield of acetone under the highest initial NO concentration studied, 64 ± 1%, is in good agreement with that reported by Andersen *et al.* (2010) for the OH radical initiated oxidation of *iso*-butanol in the presence

of NO_x; 61 ± 4%. As with the acetone yield for the Cl atom initiated oxidation of *iso*-butanol in the presence of NO_x, the yields reported here should be taken as upper limits, due to the formation of acetone following the oxidation of *iso*-butyraldehyde. McGillen *et al.* (2013) constrained the acetone yield closer to 40% for the OH radical initiated oxidation of *iso*-butanol.

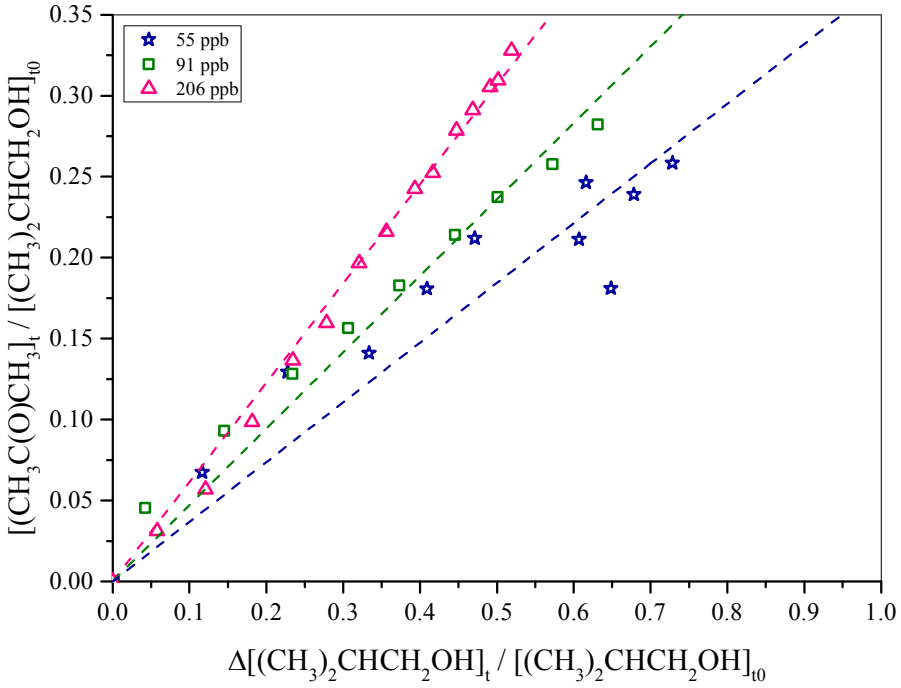

Figure 7-10: Formation of acetone vs. the loss of *iso*-butanol following the OH radical initiated oxidation of *iso*-butanol in 80:20 mixtures of N_2:O_2 at 298 K and 1000 mbar total pressure in the presence of NO_x. The dashed lines represent linear least squares fit to the data with the intercept fixed through zero. Values reported in the text refer to linear least squares fit to the data without the intercept fixed (see Table 7-3).

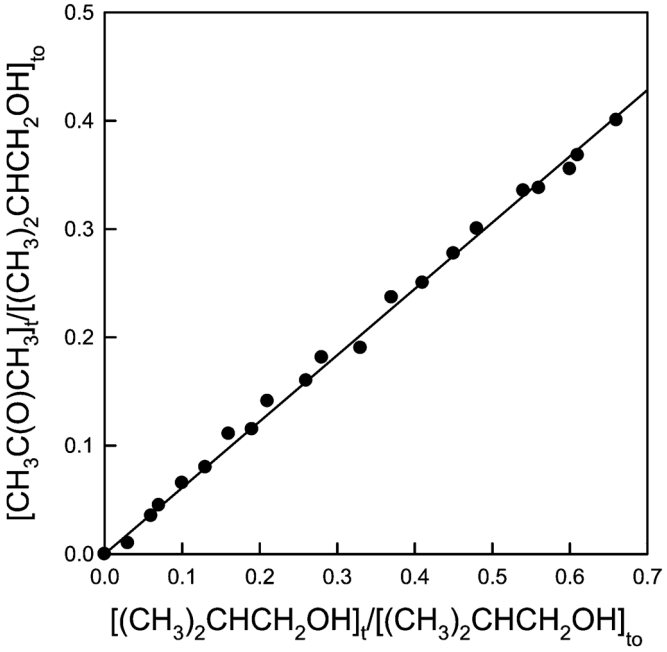

Figure 7-11: Formation of acetone vs. the loss of *iso*-butanol for the OH radical initiated oxidation of *iso*-butanol in the presence of NO_x. Reproduced from Andersen *et al.* (2010).

[NO] / ppbv	Gradient	Intercept
55	0.30 ± 0.04	0.03 ± 0.02
91	0.42 ± 0.02	0.02 ± 0.01
206	0.64 ± 0.01	-0.011 ± 0.003

Table 7-5: Acetone production yields following the OH radical initiated oxidation of *iso*-butanol in 80:20 mixtures of N_2:O_2 at 298 K and 1000 mbar total pressure in the presence of NO_x. Gradients represent linear least squares fit to the data where the intercept is not fixed through zero. Errors represent the standard error from the fitting procedure.

Figure 7-12 shows the formation of HCHO vs. the loss of *iso*-butanol under varying initial [NO]. The dashed lines represent the linear least squares fit to the data for <40% consumption of *iso*-butanol. Upwards curvature of the HCHO production is observed in all three initial [NO] conditions, indicating the formation of HCHO as a secondary product in the OH radical initiated oxidation process of *iso*-butanol in the presence of NO_x. There are numerous sources of HCHO formation in the *iso*-butanol oxidation process from secondary chemistry and so it is not possible to use the HCHO product yield as an indication of attack from one single position of the *iso*-butanol. No yields of HCHO following the OH radical initiated oxidation of *iso*-butanol in the presence of NO_x were reported by Andersen *et al.* (2010).

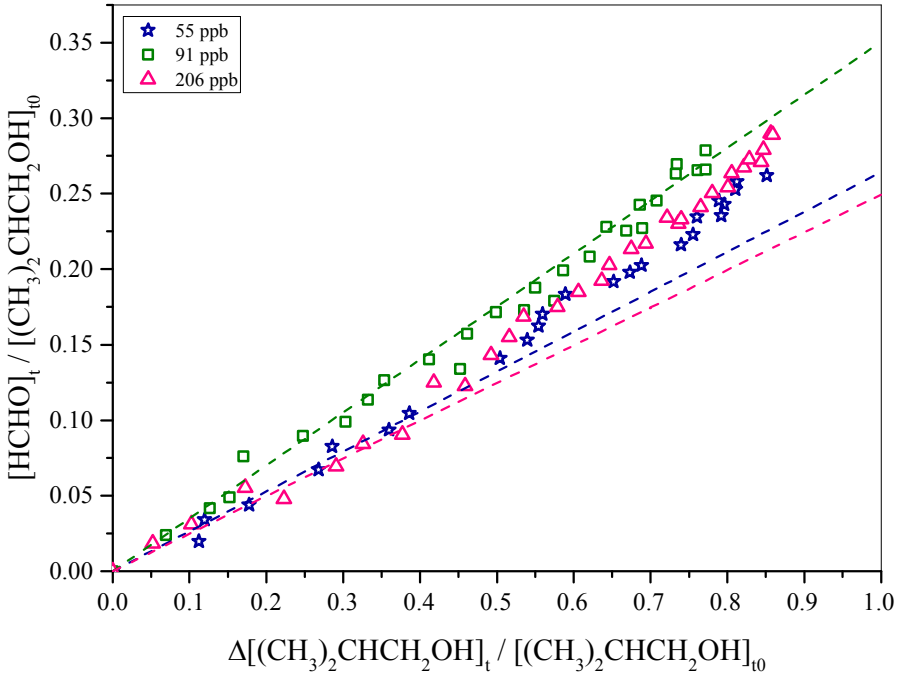

Figure 7-12: Formation of HCHO vs. the loss of *iso*-butanol following the OH radical initiated oxidation of *iso*-butanol in 80:20 mixtures of N_2:O_2 at 298 K and 1000 mbar total pressure in the presence of NO_x. The dashed lines represent linear least squares fit to the data (for <40% *iso*-butanol consumption) with the intercept fixed through zero. Values reported in the text refer to linear least squares fit to the data without the intercept fixed (see Table 7-3).

[NO] / ppbv	Gradient	Intercept
55	0.28 ± 0.01	-0.003 ± 0.004
91	0.34 ± 0.02	0.001 ± 0.005
206	0.23 ± 0.02	0.005 ± 0004

Table 7-6: HCHO production yields following the OH radical initiated oxidation of *iso*-butanol in 80:20 mixtures of N_2:O_2 at 298 K and 1000 mbar total pressure in the presence of NO_x. Gradients represent linear least squares fit to the data (for <40% *iso*-butanol consumption) where the intercept is not fixed through zero. Errors represent the standard error from the fitting procedure.

Concentration time profiles of O_3, OH, HO_2, NO and NO_2 are shown in Figure 7-14 for the OH radical initiated oxidation of *iso*-butanol in the presence of varying initial NO concentrations. Similar to the Cl atom initiated oxidation of *iso*-butanol in the presence of varying initial NO concentrations, following an initial spike, the OH concentration tends towards a steady state. As the initial NO concentration was increased, the maximum of the initial spike in OH concentration decreased in magnitude, and the time for it to reach its maximum increased. The chemistry of HO_x and NO_x are very closely related, as

has been discussed in detail in Chapter 1. A clear trend between the initial NO concentration and maximum O_3 concentration was not observed, however, as with the Cl atom initiated oxidation of *iso*-butanol in the presence of varying initial NO concentrations, the time for the ozone concentration to reach a maximum increased with increasing initial NO concentration. The lack of a correlation between the initial NO concentration and the maximum O_3 concentration indicates a regime change; as the initial *iso*-butanol concentration was kept constant between all experiments, and only the initial [NO] was altered, it is likely that the reaction system has changed between NO_x limiting and VOC limiting conditions. Unlike in the Cl atom initiated oxidation of *iso*-butanol in the presence of NO_x, the NO in the OH radical initiated oxidation of *iso*-butanol decayed over a much greater time period. As the kinetics of Cl atom initiated processes are considerably faster than the kinetics of OH radical initiated processes, products and intermediates are formed on much longer time scales, hence, the NO was consumed over longer time scales.

The difference in kinetics between the OH radical and Cl atom initiated oxidation of *iso*-butanol is displayed by the hydrocarbon concentration time profiles in Figure 7-13. The concentration time profiles in Figure 7-13 (a) and (c) show the OH radical and Cl atom initiated oxidation of *iso*-butanol in the absence of NO_x, respectively. From these plots, the considerably faster kinetics of the Cl atom oxidation process is clearly observable in the profiles of *iso*-butanol, *iso*-butyraldehyde and acetone. Figure 7-13 (b) and (d) show a comparison of the concentration time profiles for the OH radical and Cl atom initiated oxidation of *iso*-butanol in the presence of NO_x, respectively. Again, the difference in kinetics between the OH radical and Cl atom initiated oxidation processes is observed.

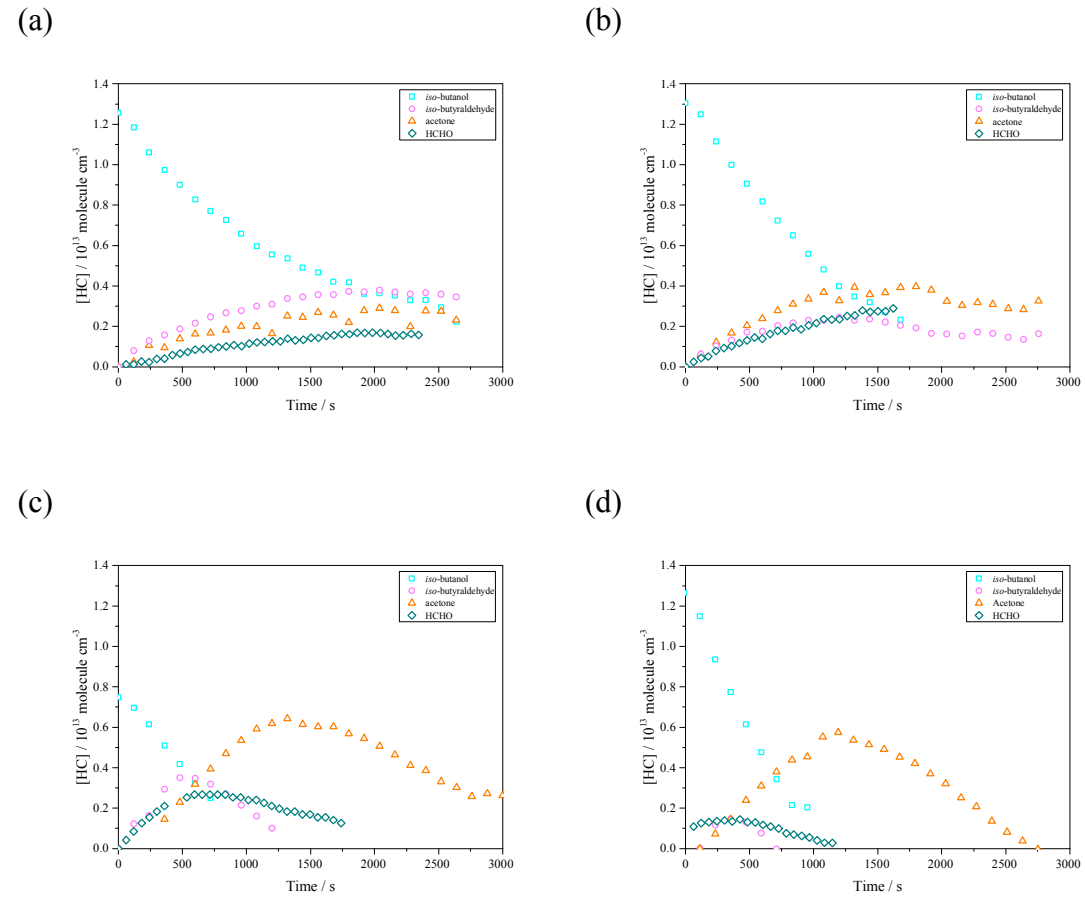

Figure 7-13: Comparison of *iso*-butanol and stable product concentration time profiles. (a) *iso*-butanol + OH in the absence of NO_x (b) *iso*-butanol + OH in the presence of 91 ppbv initial [NO] (c) *iso*-butanol + Cl in the absence of NO_x (d) *iso*-butanol + Cl in the presence of 101 ppbv initial [NO].

A difference in kinetics is also observed between the oxidation processes in the absence of NO_x and in the presence of NO_x for both the OH radical and Cl atom initiated oxidation of *iso*-butanol. This difference is attributed to the greater production of OH radicals in both systems in the presence of NO_x, as has been described by R 7-25 and R 7-26:

$$NO + HO_2 \rightarrow OH + NO_2 \qquad \text{R 7-25}$$

$$NO_2 + h\nu \rightarrow NO + O(^3P) \qquad \text{R 7-26}$$

The $[HO_2]$ and $[O_3]$ for the OH radical initiated oxidation of *iso*-butanol in the presence of varying initial NO concentrations follow very similar time profiles as shown in Figure 7-14. The sharp decay of HO_2 (and decay of O_3) observed from ~1900 s for 91 ppbv initial NO, from ~2800 s for 206 ppbv initial NO and from ~2500 s for 55 ppbv initial NO coincides with the photolysis lamps being switched off, ending the oxidation reaction. As has been discussed in Section 7.3, the observed HO_2 decay is on a much longer time scale than would be expected if the decay was solely due to the HO_2

self-reaction; it is concluded that a number of dark reactions leading to the formation of HO_2 are influencing the HO_2 decay once the photolysis lamps are switched off. The slow growth of HO_2 radicals in the 206 ppbv initial NO case corresponds with the decay of NO, as the [NO] tends towards zero at ~2000 s, the HO_2 concentration reached a maximum steady state also coinciding with the maximum [O_3]. This was also the case for the growth of HO_2 radicals in the 90 ppbv initial NO and 55 ppbv initial NO.

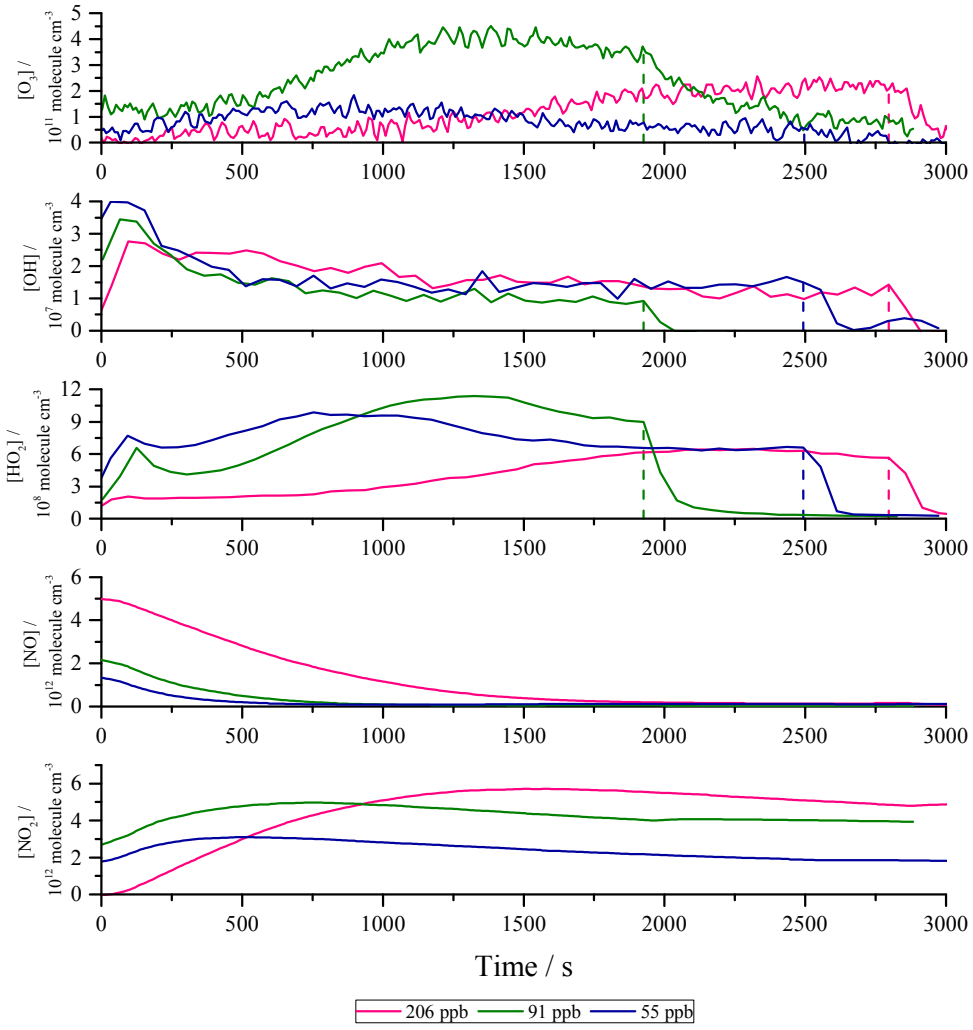

Figure 7-14: Time series comparison of [O_3], [OH], [HO_2], [NO] and [NO_2] for the OH radical initiated oxidation of *iso*-butanol in the presence of NO_x. Vertical lines in the [O_3], [OH] and [HO_2] plots indicate the time at which the photolysis lamps were switched off. O_3 analyser LOD = 1 ppbv, NO LOD = 50 pptv (120 second averaging).

The observed steady state concentrations of OH radicals indicates some mechanism for OH recycling within the system, which would be expected in the presence of HO_2, NO_x

and O_3. It is possible that O_3 photolysis may play a significant role in the production of OH radicals following:

$$O_3 + h\nu_{(220\ nm < \lambda < 305\ nm)} \rightarrow O(^1D) + O_2 \qquad \text{R 7-27}$$

$$O(^1D) + H_2O \rightarrow OH + OH \qquad \text{R 7-28}$$

Investigation into the formation of OH radicals from O_3 photolysis within HIRAC would help elucidate the OH production following such oxidation processes.

7.4.2 Studies in the Absence of NO_x

Mixtures of H_2O_2 and *iso*-butanol were irradiated using two sets of photolysis lamps; four lamps with a maximum output at ~254 nm in order to initiate H_2O_2 photolysis, and four lamps with a maximum output at ~360 nm. The use of the black lamps in the absence of NO_x allows for more direct comparison of product yields, as they are likely influence by photolysis from these lamps.

The formation of *iso*-butyraldehyde vs. the loss of *iso*-butanol is shown in Figure 7-15, where the solid straight line represents the linear least squares best fit line to the data for <20% *iso*-butanol consumption, and the dashed line represents the linear least squares best fit line to the data for <50% *iso*-butanol consumption. It can be seen that the production of *iso*-butyraldehyde was linear until ~50% consumption of *iso*-butanol. The absence of NO_x here reduces any secondary OH radical formation, which was observed in reactions in the presence of NO_x, preventing the *iso*-butyraldehyde from being lost to secondary chemistry by the reaction with OH radicals. The yields obtained from the linear least squares fitting to the data (given in Table 7-7) may be reported as a lower limit; it is known that *iso*-butyraldehyde photolyses in the wavelength region 230 - 350 nm with a maximum at 294 nm (Martinez *et al.* 1992). *Iso*-butyraldehyde produced in the oxidation process of *iso*-butanol will therefore go on to photolyse when the chamber is irradiated with both sets of photolysis lamps. The linearity observed for the production of *iso*-butyraldehyde vs. the loss of *iso*-butanol indicates that loss of *iso*-butyraldehyde due to photolysis was not significant. Investigation into the photolysis of *iso*-butyraldehyde with the two sets of photolysis lamps switched on yielded a photolysis rate of 2.6×10^{-4} s^{-1}. Further investigation into photolysis of *iso*-butyraldehyde, and other similar carbonyl compounds, would be beneficial in determining their product yields, enabling a better understanding of the impact of photolysis processes in such experiments. The initial yield of *iso*-butyraldehyde at *iso*-butanol consumption of <20% was 80%, indicating that

the primary abstraction site for the OH radical initiated attack of *iso*-butanol is at the α position. No previous yields of *iso*-butyraldehyde have been reported for the OH initiated oxidation of *iso*-butanol in the absence of NO_x.

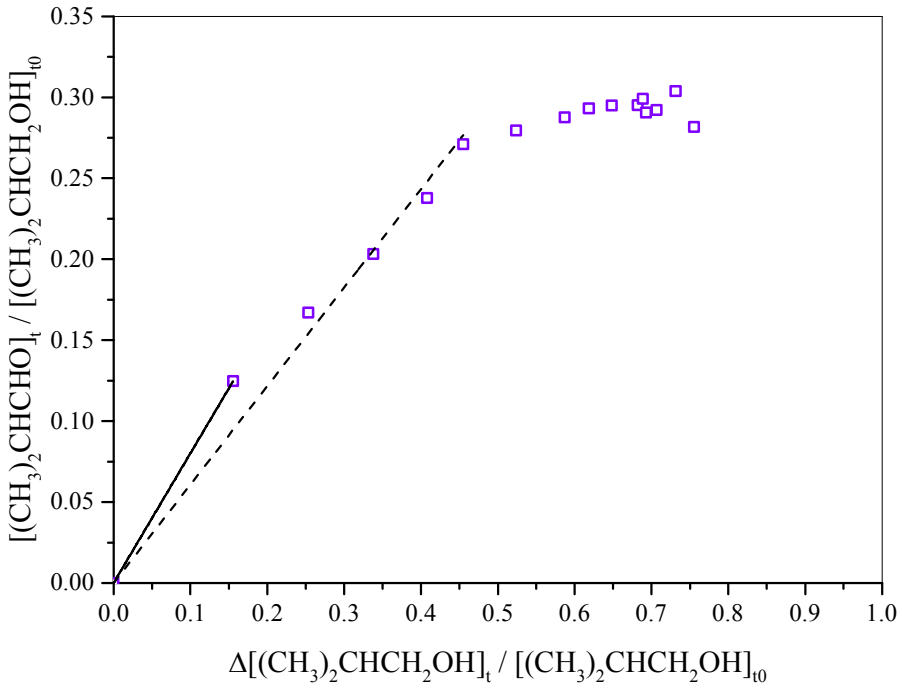

Figure 7-15: Formation of *iso*-butyraldehyde vs. the loss of *iso*-butanol following the OH radical initiated oxidation of *iso*-butanol in 80:20 mixtures of N_2:O_2 at 298 K and 1000 mbar total pressure in the absence of NO_x. The dashed line represents linear least squares fit to the data (for <50% *iso*-butanol consumption) with the intercept fixed through zero. The solid line represents linear least squares fit to the data (for <20% *iso*-butanol consumption) with the intercept fixed through zero. Values reported in the text refer to linear least squares fit to the data without the intercept fixed (see Table 7-3).

% *iso*-butanol consumption	**Gradient**	**Intercept**
<50	0.56 ± 0.04	0.02 ± 0.01
<20	0.80	0

Table 7-7: *iso*-butyraldehyde production yields following the OH radical initiated oxidation of *iso*-butanol in 80:20 mixtures of N_2:O_2 at 298 K and 1000 mbar total pressure in the absence of NO_x. Gradients represent linear least squares fit to the data (for <50% and <20% *iso*-butanol consumption) where the intercept is not fixed through zero. Errors represent the standard error from the fitting procedure.

The formation of acetone vs. loss of *iso*-butanol for the OH radical initiated oxidation of *iso*-butanol in the absence of NO_x is shown in Figure 7-16, where the solid red line represents the linear least squares fit to the data, and the dashed black line represents the

linear least squares fit to the data with the intercept forced through zero. Yields obtained from these fits to the data are 27 ± 3 % and 30 ± 1 %, respectively. As discussed for the production of acetone following the Cl atom initiated oxidation of *iso*-butanol, here the formation yield of acetone should also be considered as an upper limit as its formation following R 7-15 to R 7-21 has not been accounted for in the analysis procedure. The linearity also indicates that little acetone was lost through reaction with OH radicals; this is not surprising when considering the relative rates of reaction for acetone ($(1.8 \pm 0.3) \times 10^{-13}$ cm^3 $molecule^{-1}$ s^{-1} (Atkinson *et al.* 2006)) and *iso*-butanol ($(8.9 \pm 1.7) \times 10^{-12}$ cm^3 $molecule^{-1}$ s^{-1} (Atkinson *et al.* 2006)) with OH radicals. The reaction of acetone with OH radicals is over an order of magnitude slower than the reaction of *iso*-butanol with OH radicals. Similar to *iso*-butyraldehyde, it is known that acetone photolyses in the region of 210 – 340 nm; the linearity of the production of acetone vs. loss of *iso*-butanol indicates that acetone photolysis does not play a significant role in the loss of acetone during this reaction. It may also be the case that the linearity observed in the formation yield of acetone arises due to the loss of acetone being balanced by the formation of acetone.

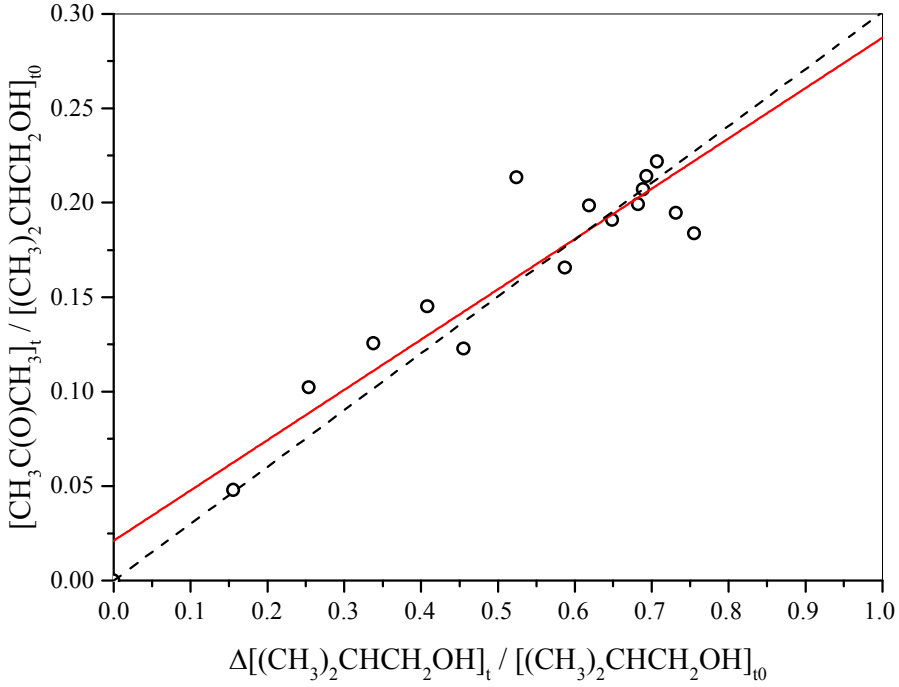

Figure 7-16: Formation of acetone vs. the loss of *iso*-butanol following the OH radical initiated oxidation of *iso*-butanol in 80:20 mixtures of N_2:O_2 at 298 K and 1000 mbar total pressure in the absence of NO_x. The dashed line represents linear least squares fit to the data with the intercept fixed through zero (gradient = 0.30 ± 0.01). The solid red line represents linear least squares fit to the data without the intercept fixed through zero (gradient = 0.27 ± 0.03, intercept = 0.02 ± 0.01).

Figure 7-17 shows the formation of HCHO vs. the loss of *iso*-butanol following the OH radical initiated oxidation of *iso*-butanol in the absence of NO_x. The dashed black line represents the linear least squares fit to the data for <40% *iso*-butanol consumption, and the solid red line represents the linear least squares fit to the data for <40% *iso*-butanol consumption with the intercept forced through zero. The yields of HCHO obtained from these fits are 19 ± 2 % and 20 ± 1%, respectively. There are many sources of HCHO production following the OH initiated oxidation of *iso*-butanol in the absence of NO_x.

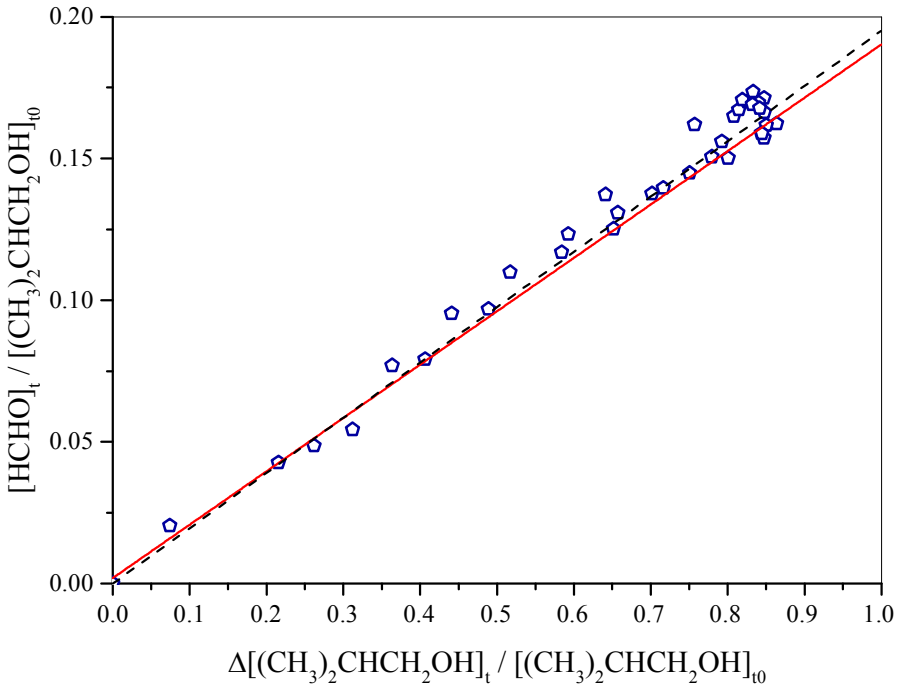

Figure 7-17: Formation of HCHO vs. the loss of *iso*-butanol following the OH radical initiated oxidation of *iso*-butanol in 80:20 mixtures of N_2:O_2 at 298 K and 1000 mbar total pressure in the absence of NO_x. The dashed black line represents linear least squares fit to the data (for <40% *iso*-butanol consumption) with the intercept fixed through zero (gradient = 0.20 ± 0.01). The solid red line represents linear least squares fit to the data (for <40% *iso*-butanol consumption) without the intercept fixed through zero (gradient = 0.19 ± 0.02, intercept = 0.001 ± 0.004).

The concentration time profiles shown in Figure 7-18 are of the measured O_3, OH, HO_2, NO and NO_2 for the OH radical initiated oxidation of *iso*-butanol in the absence of NO. As with the Cl atom initiated oxidation of *iso*-butanol in the absence of NO, this can also be shown to be truly in the absence of any NO from its concentration time profile. No ozone formation was observed; as no NO was present in the system, no NO_2 formation can occur to facilitate the production of ozone. An initial OH peak was observed to a maximum of ~1.0 × 10^8 molecule cm^{-3} which then decayed towards a steady concentration of ~1.0 × 10^7 molecule cm^{-3}. The initial spike in OH concentration was primarily due to photolysis of H_2O_2 (R 7-7). The HO_2 was also seen to peak at ~100s and decay to roughly a steady concentration, following a similar profile to the [OH].

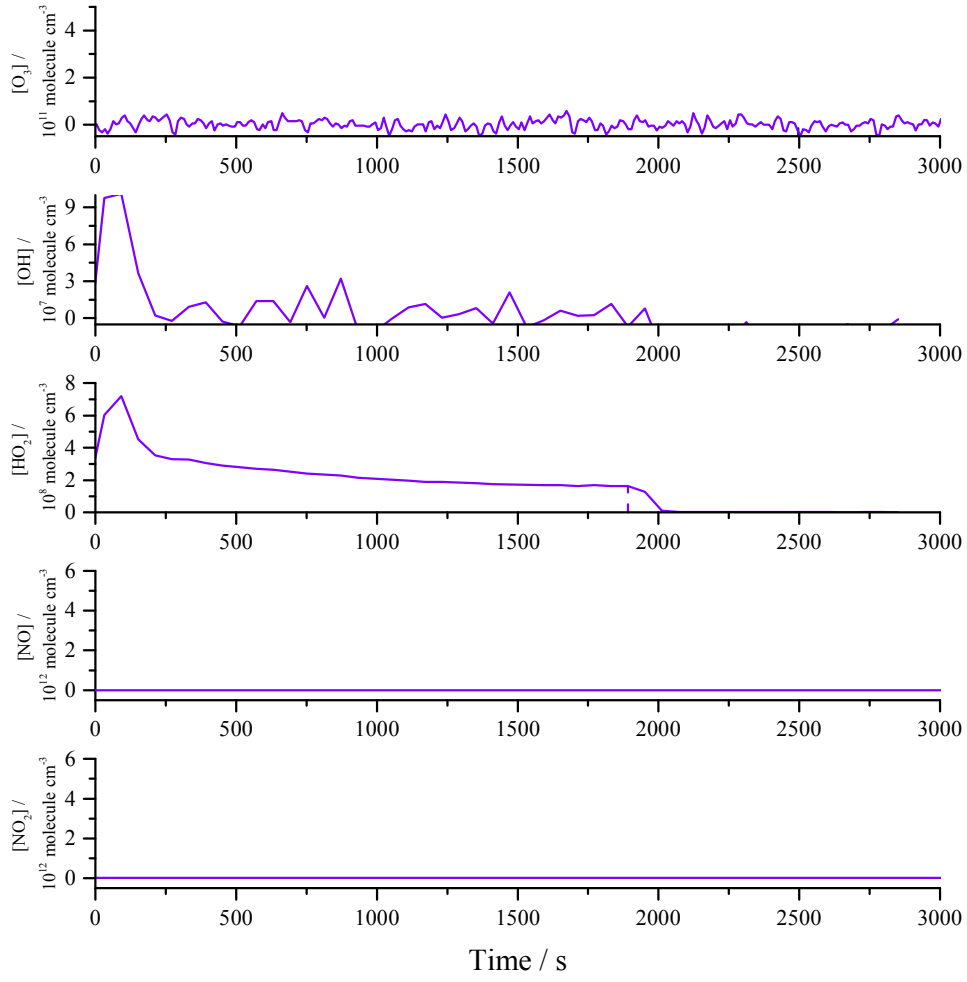

Figure 7-18: Time series comparison of $[O_3]$, [OH], $[HO_2]$, [NO] and $[NO_2]$ for the OH radical initiated oxidation of *iso*-butanol in the absence of NO_x. The vertical line in the $[HO_2]$ plot indicates the time at which the photolysis lamps are switched off. O_3 analyser LOD = 1 ppbv, NO LOD = 50 pptv (120 second averaging).

7.5 Comparison of Product Formation

7.5.1 Comparison of the Oxidation of *Iso*-butanol by OH Radicals and Cl Atoms in the Absence of NO_x

A comparison of the formation of acetone vs. the loss of *iso*-butanol for the oxidation of *iso*-butanol in the absence of NO_x, initiated by Cl atoms and OH radicals is given in Figure 7-19. The final production yield of acetone from the OH radical initiated oxidation was ~30%, whereas for the analogous reaction with Cl atoms, the final production yield was ~75%. The difference in acetone product yields between the Cl atom and OH radical initiated oxidation of *iso*-butanol is primarily due to difference in kinetics between OH radical and Cl atom initiated oxidation; as *iso*-butyraldehyde was formed rapidly in the

Cl atom initiated oxidation, it was also seen to rapidly decay, predominantly through further oxidation with Cl atoms (and OH radicals), leading to greater concentrations of acetone being produced. The presence of OH radicals (produced during the oxidation reaction) in the Cl atom initiated oxidation reactions will also play a role in the increased yield of acetone from Cl atom initiated oxidation.

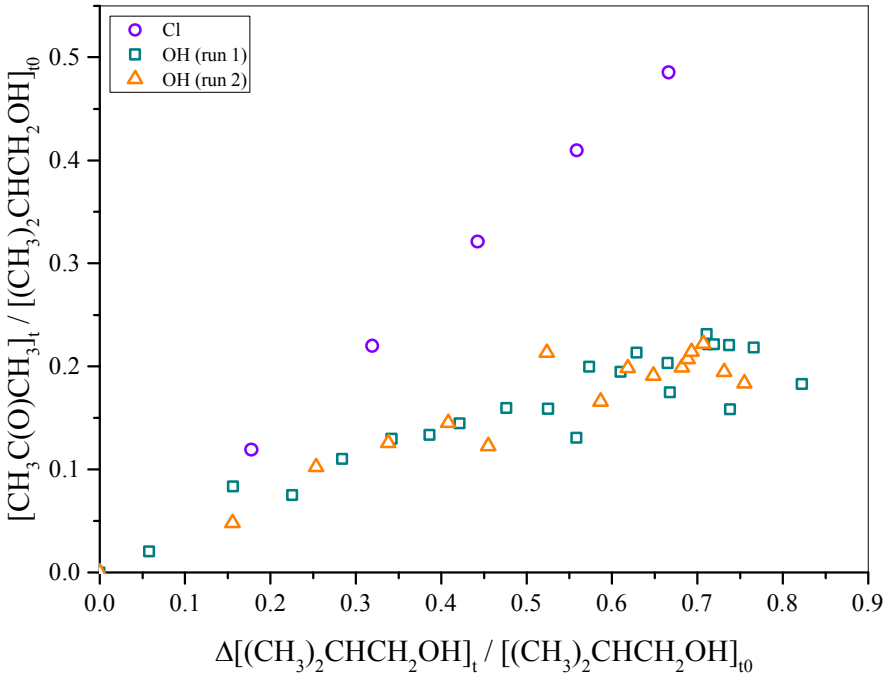

Figure 7-19: Formation of acetone vs. the loss of *iso*-butanol following the oxidation of *iso*-butanol in 80:20 mixtures of N_2:O_2 at 298 K and 1000 mbar total pressure in the absence of NO_x. Purple circles represent Cl atom initiated oxidation, green squares and orange triangles represent OH radical initiated oxidation.

The formation profile of HCHO vs. the loss of *iso*-butanol is shown in Figure 7-20 for both the OH radical and Cl atom initiated oxidation reactions in the absence of NO_x. There is a distinct difference in the profiles between the two systems; in the Cl atom initiated oxidation, the HCHO increased to a maximum at ~70% *iso*-butanol consumption and then decayed. In marked contrast, the HCHO formation continued to increase with *iso*-butanol consumption in the OH radical initiated oxidation process. In the Cl atom initiated oxidation, OH radicals are also formed throughout the oxidation process, the HCHO produced can be lost through secondary chemistry with either Cl atoms or OH radicals present in the system. In the OH radical initiated oxidation, only OH radicals are present for reaction with species present in the chamber. The reaction of HCHO with OH radicals is an order of magnitude lower, $k_{OH + HCHO} = (8.5 \pm 1.6) \times 10^{-12}$ cm^3 molecule^{-1} s^{-1}

(Atkinson *et al.* 2006), than that of the reaction with Cl atoms, $k_{Cl + HCHO} = (7.2 \pm 1.0) \times 10^{-11}$ cm^3 molecule^{-1} s^{-1} (Atkinson et al. 2006), and so it should be expected that HCHO is lost at later times in the oxidation process. In the absence of NO_x, Andersen *et al.* (2010) observed a similar HCHO formation profile for the Cl atom initiated oxidation study, with yields <5% being reported for *iso*-butanol consumption <20%. HCHO is formed from numerous pathways in the oxidation process, and increased photolysis of products in the OH radical oxidation system, due the wavelength of lamps required for the photolysis of H_2O_2 to produce OH, will increase the formation of HCHO throughout the oxidation process as both *iso*-butyraldehyde and acetone are photolysed in the wavelength region irradiating the chamber. At ~50% *iso*-butanol consumption, both systems showed similar HCHO production yields of ~15%. The similarity of the HCHO production between the two systems confirms that HCHO was formed from numerous secondary reactions of other oxidation products with Cl atoms, OH radicals and photolysis.

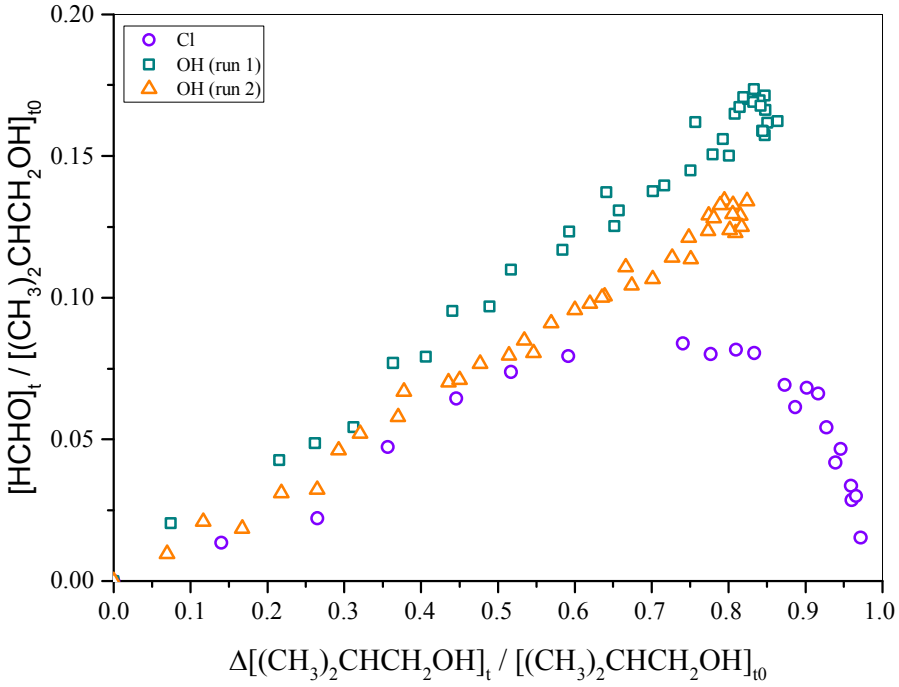

Figure 7-20: Formation of HCHO vs. the loss of *iso*-butanol following the oxidation of *iso*-butanol in 80:20 mixtures of N_2:O_2 at 298 K and 1000 mbar total pressure in the absence of NO_x. Purple circles represent Cl atom initiated oxidation, green squares and orange triangles represent OH radical initiated oxidation.

7.5.2 Comparison of the OH Radical Initiated Oxidation of *Iso*-butanol in the Presence and Absence of NO_x

Figure 7-21 shows a comparison of the formation of *iso*-butyraldehyde vs. the loss of *iso*-butanol for the OH radical initiated oxidation of *iso*-butanol in the absence and

presence of NO_x. The solid lines represent the initial *iso*-butyraldehyde production yields for <20% *iso*-butanol consumption. There is a marked difference in the observed initial yields for *iso*-butyraldehyde in the presence and absence of NO_x; the initial yields are compared in Table 7-8. The initial production yield of *iso*-butyraldehyde in the absence of NO_x, 80%, was much greater than in the presence of NO_x. As the initial [NO] was increased, the initial production yield of *iso*-butyraldehyde increased towards that of the initial production yield in the absence of NO_x. Andersen et al. (2010) did not report any yields for *iso*-butyraldehyde for the OH radical initiated oxidation of *iso*-butanol in the presence of NO_x due to IR features of CH_3ONO obscuring those from *iso*-butyraldehyde. In this study, *iso*-butyraldehyde was measured using GC-FID, and could also be observed in the FTIR spectra as H_2O_2 was used as the OH radical precursor.

(a) (b)

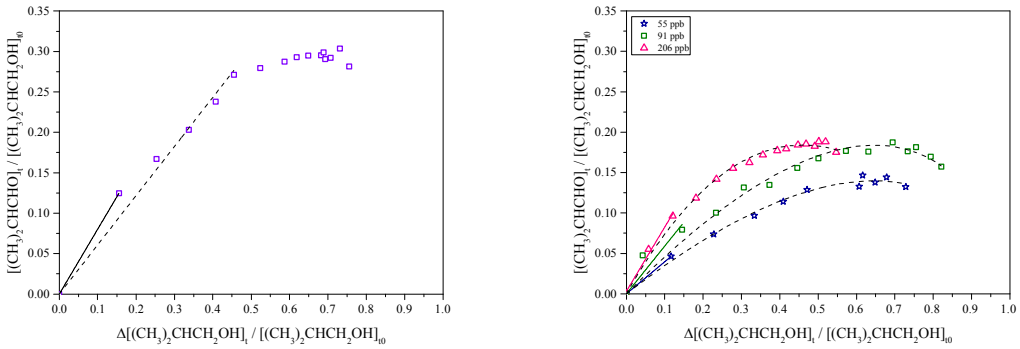

Figure 7-21: Comparison of formation of *iso*-butyraldehyde vs. the loss of *iso*-butanol following the oxidation of *iso*-butanol in 80:20 mixtures of N_2:O_2 at 298 K and 1000 mbar total pressure in (a) the absence and (b) the presence of NO_x. Solid lines represent linear least squares fit to the data for *iso*-butanol consumption <20% with the intercept forced through zero.

Initial [NO] / ppbv	Gradient
Low	0.80
55	0.40
91	0.59 ± 0.11
206	0.79 ± 0.08

Table 7-8: Comparison of initial *iso*-butyraldehyde formation yields for the OH initiated oxidation of *iso*-butanol in the presence and absence of NO_x. Gradients are those fitted to the data in Figure 7-21 for *iso*-butanol consumption <20%. Errors represent the standard error in the fitting procedure.

A comparison of the formation of acetone vs. the loss of *iso*-butanol in the absence and presence of NO_x for the OH radical initiated *iso*-butanol oxidation is given in Figure 7-22.

The dashed lines represent the linear least squares fit of the data with the intercept forced through zero. Table 7-9 details the gradients for the linear least squares fit to the data in Figure 7-22. As the initial [NO] was increased, the product yield of acetone from the OH initiated oxidation of *iso*-butanol increased. Under high [NO_x] conditions, Andersen *et al.* (2010) reported that 61 ± 4% of the reaction of OH radicals with *iso*-butanol occurred at the ß position; the results reported here, at the highest initial [NO] in the system, agree well, with 64 ± 1% of the reaction occurring at the ß position to produce acetone. Andersen *et al.* (2010) did not account for any production from the secondary reaction of *iso*-butyraldehyde with OH radicals present in the system. The formation of acetone from the ß position is shown in Figure 7-23. In the absence of NO_x, the peroxy radical formed in the second step of the mechanism shown in Figure 7-23 would react with HO_2 or RO_2 radicals present which would not form the alkoxy radical.

(a) (b)

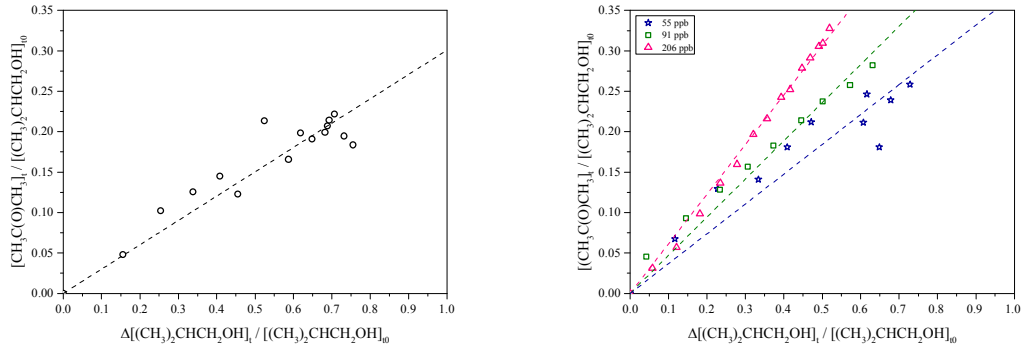

Figure 7-22: Comparison of formation of acetone vs. the loss of *iso*-butanol following the oxidation of *iso*-butanol in 80:20 mixtures of N_2:O_2 at 298 K and 1000 mbar total pressure in (a) the absence and (b) the presence of NO_x. Dashed lines represent linear least squares fit to the data with the intercept forced through zero.

Initial [NO]	Gradient	Intercept
Low	0.27 ± 0.03	0.02 ± 0.01
55	0.30 ± 0.04	0.03 ± 0.02
91	0.42 ± 0.02	0.02 ± 0.01
206	0.64 ± 0.01	-0.011 ± 0.003

Table 7-9: Comparison of initial acetone formation yields for the OH initiated oxidation of *iso*-butanol in the presence and absence of NO_x. Gradients are those fitted to the data in Figure 7-22. Errors represent the standard error in the fitting procedure.

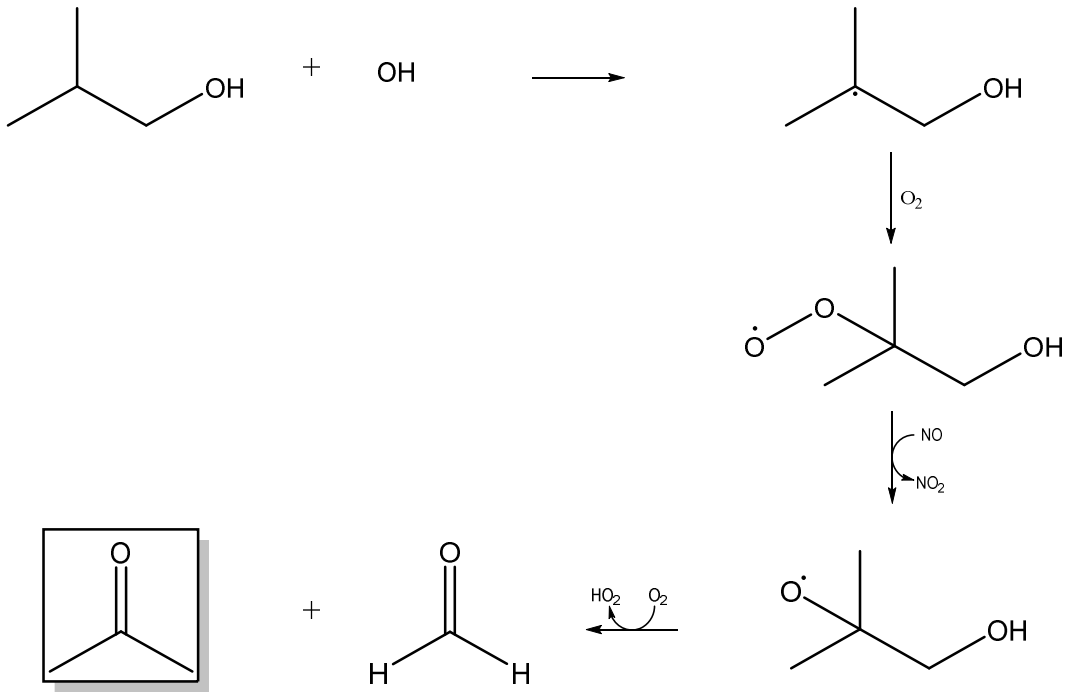

Figure 7-23: Mechanism for the formation of acetone from the ß-hydrogen abstraction in the OH radical initiated oxidation of *iso*-butanol in the presence of NO_x.

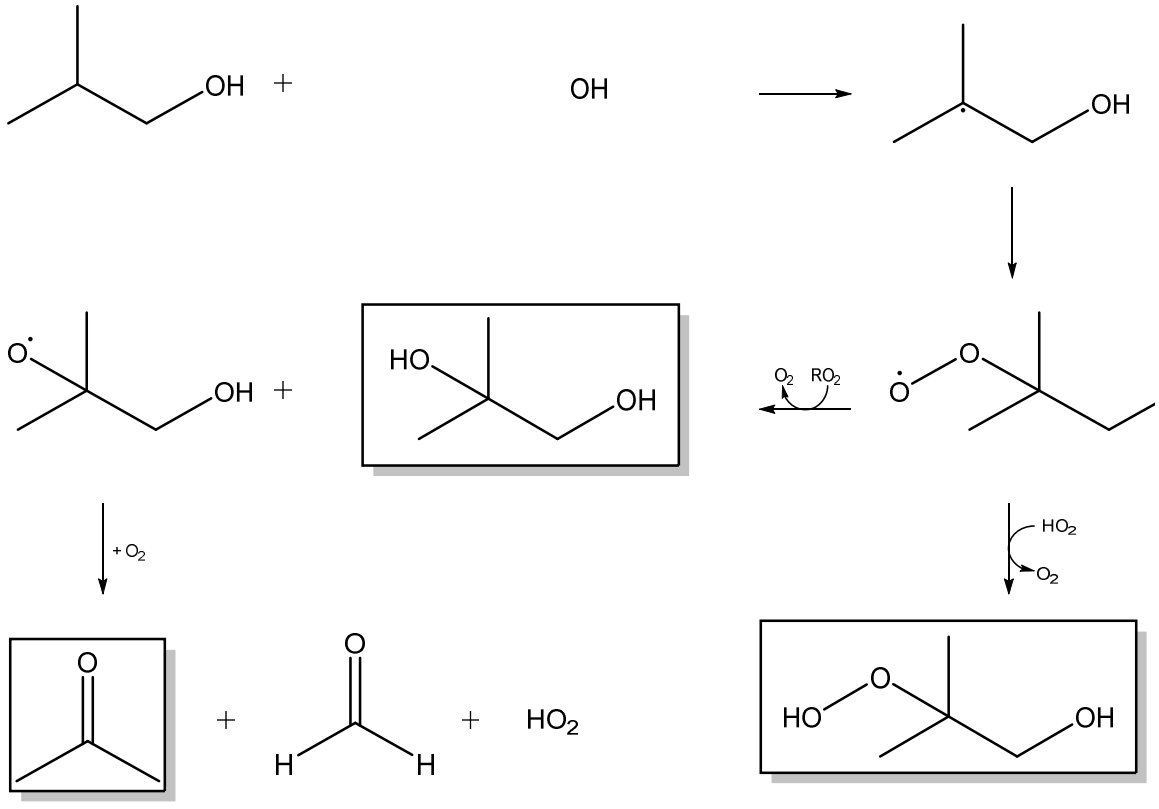

Figure 7-24: Mechanism for the formation of acetone from the ß-hydrogen abstraction in the OH radical initiated oxidation of *iso*-butanol in the absence of NO_x.

A comparison of the formation of HCHO vs. the loss of *iso*-butanol for the OH radical initiated oxidation of *iso*-butanol in the absence and presence of NO_x is shown in Figure 7-25, where the dashed lines represent the linear least squares fit to the data with

the intercept forced through zero. The gradients from the linear least squares fit to the data are given in Table 7-10, where the gradient represents the product yield fit to <40% *iso*-butanol consumption. An increase in HCHO yield at <40% *iso*-butanol consumption was observed as the initial [NO] increased, until a maximum when the HCHO product yield then decreased. As the initial [NO] increased, more OH was formed via R 7-13. As this reaction increased the [OH] produced, more OH radicals were available for reaction with HCHO.

This observation of initial HCHO formation yields also corresponds to the initial formation yields of *iso*-butyraldehyde under varying NO concentrations. As the initial yield of *iso*-butyraldehyde increased and decreased with increasing initial [NO], the formation of HCHO, either from photolysis or secondary reaction of *iso*-butyraldehyde with OH radicals, increased through a maximum and the decreased. Due to the relative reactivities of *iso*-butyraldehyde and acetone with OH radicals, it is likely that the HCHO formation observed primarily arises from the degradation of *iso*-butyraldehyde than from the degradation of acetone.

(a) (b)

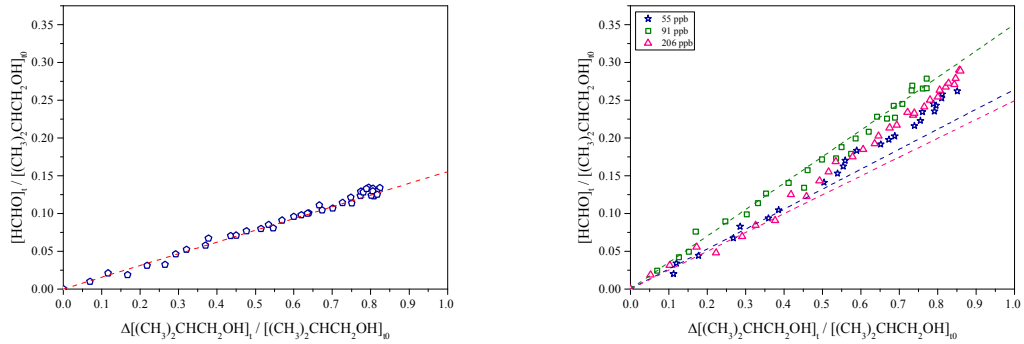

Figure 7-25: Comparison of formation of HCHO vs. the loss of *iso*-butanol following the oxidation of *iso*-butanol in 80:20 mixtures of N_2:O_2 at 298 K and 1000 mbar total pressure in the absence (a) and presence (b) of NO_x. Dashed lines represent linear least squares fit to the data for <40% *iso*-butanol consumption, with the intercept forced through zero.

Initial [NO]	Gradient	Intercept
Low	0.19 ± 0.02	0.001 ± 0.004
55	0.28 ± 0.01	-0.003 ± 0.004
91	0.34 ± 0.02	0.001 ± 0.005
206	0.23 ± 0.02	0.005 ± 0004

Table 7-10: Comparison of initial HCHO formation yields for the OH initiated oxidation of *iso*-butanol in the presence and absence of NO_x. Gradients are those fitted to the data in Figure 7-25 for <40% *iso*-butanol consumption. Errors represent the standard error in the fitting procedure.

7.5.3 Comparison with preliminary modelling results

As described in Chapter 1, the use of chemical models are extremely useful for comparisons with both field measurements and laboratory based studies, such as the atmospheric simulation chamber studies reported in this work. The chemical simulation software, Kintecus V.5.50, was used with the tropospheric degradation mechanism for *iso*-butanol taken form the MCM v3.3.1 to conduct a preliminary study into the formation of ozone under varying initial NO concentrations for the OH radical and Cl atom initiated oxidation of *iso*-butanol (Jenkin *et al.* 2003, Bloss *et al.* 2005, Ianni 2014). For the Cl atom initiated oxidation modelling study, Cl atom chemistry was added to the MCM mechanism, taken from IUPAC (Atkinson *et al.* 2006) and Andersen *et al.* (2010).

Initial concentrations of *iso*-butanol, NO, NO_2, O_3, OH, HO_2, H_2O_2 and Cl_2 were taken directly from experimental measurements, with $j(Cl_2)$ and $j(H_2O_2)$ being determined for each experiment from fitting a simplified oxidation model to the measured decay of *iso*-butanol, and j(*iso*-butyraldehyde) and j(acetone) determined experimentally for each set of photolysis lamps. All model runs were carried out at 298 K and 1000 mbar and were run for a total time of 30 minutes. Results presented below should be considered as preliminary comparisons of trends in ozone formation. Dilution, wall losses and photolysis of other products or intermediate species were considered to be zero for the purposes of the modelling study; experimental measurements will be influenced by all of these factors.

A comparison of the measured and modelled ozone formation following the Cl atom initiated oxidation of *iso*-butanol in the presence of varying initial NO concentrations is shown in Figure 7-26. Due to the differences in conditions described above between the experimental conditions and the preliminary modelling conditions, it is only possible to

currently draw qualitative comparisons between the two sets of results. Experimental results observed ozone concentrations approximately ten times greater than those from the modelling study; this difference most likely occurs due to photolysis rates not being accurately described in the model mechanism.

(a) (b)

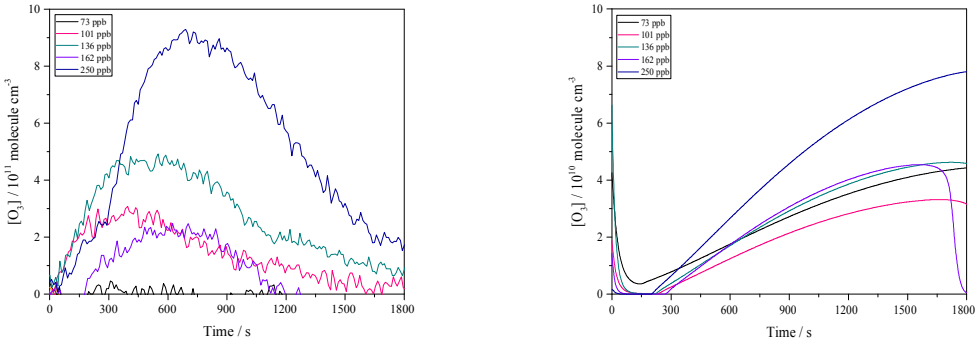

Figure 7-26: Comparison of ozone formation for the Cl atom initiated oxidation of *iso*-butanol under varying initial NO concentrations. (a) experimental results (b) preliminary MCM modelling study using experimental initial concentrations.

A similar trend in ozone formation was observed from both the experimental measurements and the modelled ozone; the greatest ozone formation was observed with the highest initial concentration of NO present in the system, with the peak ozone generally increasing with the initial NO concentration. The absence of any direct correlation between the initial NO concentration and the peak ozone concentration observed in both the experimental results and the modelled ozone, indicates that the initial concentrations of other species present in the system (primarily OH, HO_2 and NO_2) play an important role in the formation of ozone during the oxidation process.

The ozone formation following the OH radical initiated oxidation of *iso*-butanol under varying initial NO concentrations is shown in Figure 7-27 for experimental data and modelled results. Again, the experimental ozone concentrations are approximately a factor of ten greater than those predicted through model simulations. The trend in peak ozone concentration measured was not replicated through the modelling study.

(a) (b)

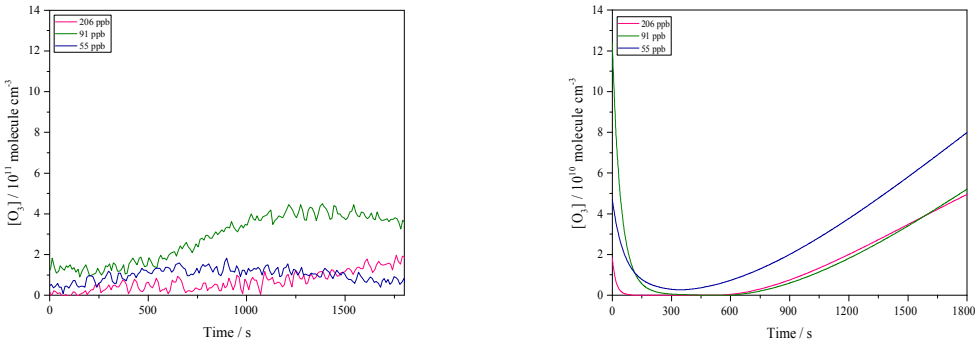

Figure 7-27: Comparison of ozone formation for the OH radical initiated oxidation of *iso*-butanol under varying initial NO concentrations. (a) experimental results (b) preliminary MCM modelling study using experimental initial concentrations.

The preliminary modelling results described here, and compared with measurements of ozone concentrations following the Cl atom and OH radical initiated oxidation processes of *iso*-butanol under varying initial NO concentrations, show the importance of accurately representing all processes occurring within atmospheric simulation chamber studies. Full characterisation of the output of the photolysis lamps used in such chamber studies is essential to accurately model oxidation processes. The agreement in the trend observed in ozone formation following the Cl atom initiated oxidation of *iso*-butanol indicates that the mechanism employed is appropriate; the lack of agreement for the OH radical initiated oxidation of *iso*-butanol may be improved with the inclusion of comparisons over a larger range of initial NO concentrations, as for the Cl atom initiated study.

Further work is required into the modelling of the *iso*-butanol oxidation processes, with full characterisation of chamber specific processes such as the photolysis of products and intermediate species. The photolysis lamps used in HIRAC are typically thought of for their photolysis at the maximum wavelength output, however, as can be seen in Figure 7-28, each of the different photolysis lamps has varying output at numerous wavelengths. Careful consideration of the absorption cross sections of species present, and experimental investigation into their photolysis with different photolysis lamps, in the chamber is required in order to correctly describe the photolysis rates of species present in the oxidation processes. The lamps used in this study were a set of Philips TL-K 40W/05 with a maximum wavelength output at ~360 nm for the Cl atom initiated oxidation processes, and a combination of these lamps and a set of GE G55T8 / OH 7G UVC lamps with a maximum wavelength output at ~254 nm for the OH radical initiated oxidation processes.

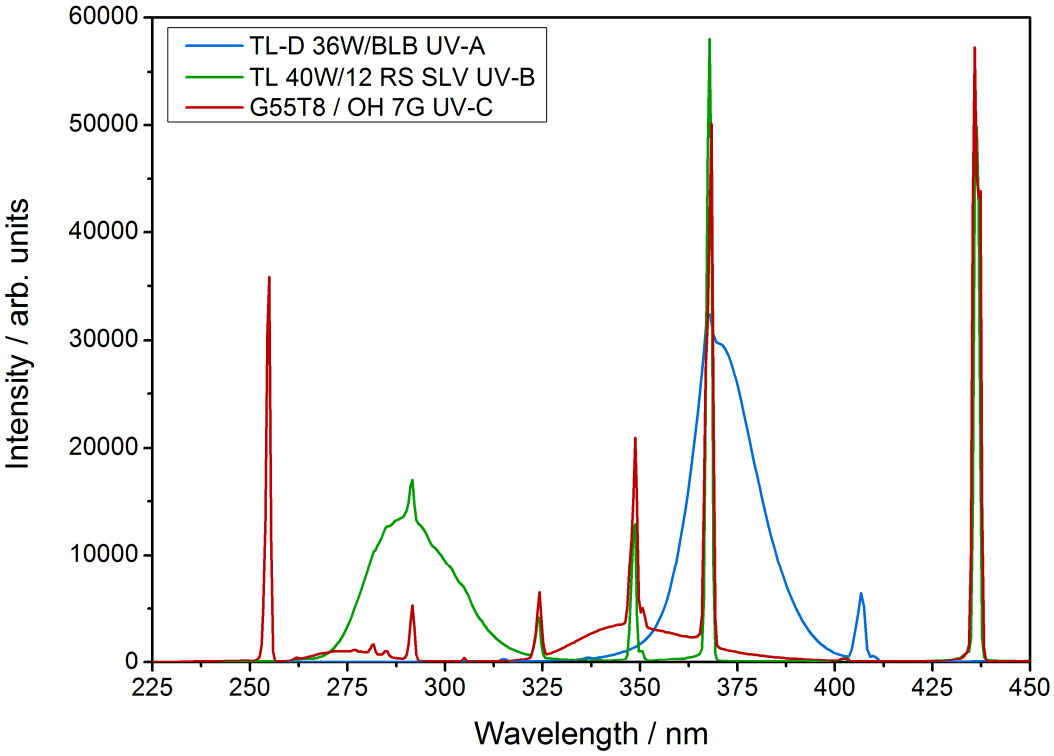

Figure 7-28: Emission spectra of the three different photolysis lamps available for use within HIRAC. Reproduced from Winiberg (2014).

As can be seen from the emissions spectra, the lamps used for the photolysis of H_2O_2 (GE G55T8 / OH 7G UVC) have multiple sharp, strong emissions; at ~290 nm, ~325 nm, ~350 nm, ~ 370 nm and 435 nm, all of which may play significant role in the photolysis of a number of products and intermediate species formed throughout the oxidation process. The lamps used for the photolysis of Cl_2 (Philips TL-K 40W/05) have a very broad emission band ranging from 350 nm to 400 nm, with a maximum output at ~360 nm. This broad emission band is also likely to influence the photolysis of products and intermediate species.

7.6 Comparison with a non-functionalised alkane, *iso*-butane

The alcohol functional group of *iso*-butanol gives this functionalised alkane different reactivity towards OH radicals and Cl atoms as compared to its analogous, non-functionalised alkane, *iso*-butane. In order to investigate the potential benefit to the use of alcohols as biofuels as compared to their analogous non-functionalised alkanes, studies of the OH radical and Cl atom initiated oxidation of *iso*-butane under varying initial NO_x conditions were carried out. Here, a comparison of ozone formation for the oxidation of *iso*-butanol and *iso*-butane under varying NO_x conditions for both the OH radical and Cl atom initiated oxidation processes, is presented. The structures of

iso-butanol and *iso*-butane are given in Figure 7-29, where the different hydrogen positions are numbered.

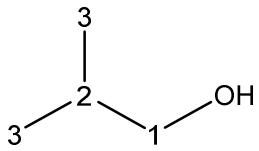

Iso-butanol

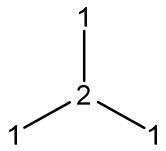

Iso-butane

Figure 7-29: Structures of *iso*-butanol and *iso*-butane, numbered with different hydrogen atoms.

7.6.1 Ozone Formation from the Cl Atom Initiated Oxidation of *iso*-butanol and *iso*-butane in the Presence and Absence of NO_x

Figure 7-30 shows a comparison of the measured O_3 formation throughout the Cl atom initiated oxidation of *iso*-butanol and *iso*-butane under varying initial [NO]. The trend observed in both cases, shows that an increase in the initial [NO] leads to greater [O_3] throughout the oxidation process. A significant difference was observed between the *iso*-butanol and the *iso*-butane systems in that considerably greater concentrations of ozone were produced in the *iso*-butane oxidation process as compared to the *iso*-butanol oxidation process for similar initial NO concentrations. This is of importance in determining appropriate alternative biofuels for use in motor vehicles, as ozone is a pollutant and harmful to human, animal and plant health, it is important to reduce the potential for fuels to produce ozone in the troposphere. As Cl is not the most dominant oxidising agent in the troposphere, it is therefore important to investigate the potential for ozone production from potential biofuels from their OH radical initiated oxidation process under similar NO_x environments. Nitrogen oxides also play a significant role in controlling the concentration of ozone in the troposphere:

$$O_3 + h\nu \rightarrow O_2 + O \qquad \text{R 7-29}$$

$$NO + O_3 \rightarrow NO_2 + O_2 \qquad \text{R 7-30}$$

(a) (b)

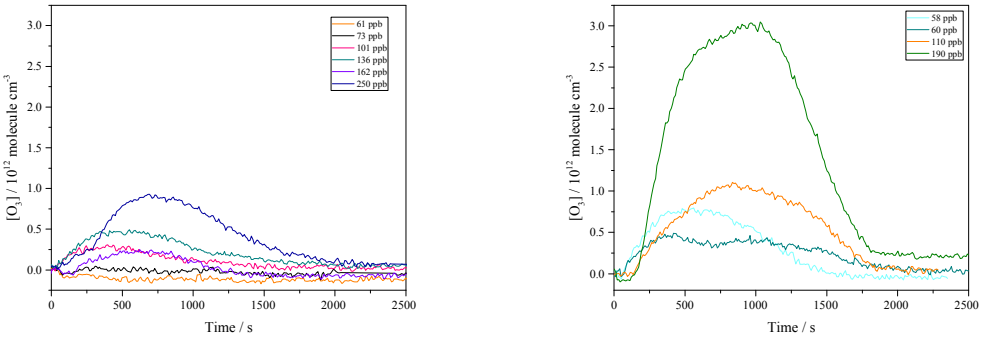

Figure 7-30: Comparison of measured O_3 for the Cl atom initiated oxidation of *iso*-butanol (a) vs. *iso*-butane (b) in the presence of NO_x.

Table 7-11 shows the peak ozone concentrations and the time from the beginning of the oxidation process at which it occurs for the Cl atom initiated oxidation of *iso*-butanol and *iso*-butane in the presence of varying initial [NO]. Under all comparable initial NO concentrations, the peak ozone concentration is reached at much longer times in the *iso*-butane oxidation as compared to the *iso*-butanol oxidation process. The peak ozone concentration also corresponds to significantly lower hydrocarbon consumption for the *iso*-butanol oxidation as compared to the iso-butane oxidation; with the hydrocarbon consumption increasing with increasing $[NO]_0$ for both compounds.

***Iso*-butanol**				***Iso*-butane**			
$[NO]_0$ / ppbv	**$[O_3]_{max}$ / ppbv**	**Time / s**	***Iso*-butanol consumption**	**$[NO]_0$ / ppbv**	**$[O_3]_{max}$ / ppbv**	**Time / s**	***Iso*-butane consumption**
61	1	28	10%	58	33	561	75%
73	2	308	20%	60	20	419	50%
101	13	396	40%	110	45	835	80%
136	20	550	40%	190	125	1032	95%
162	10	623	60%				
250	38	690	75%				

Table 7-11: Percentage hydrocarbon consumption at peak ozone concentrations for the Cl atom initiated oxidation of *iso*-butanol and *iso*-butane under varying initial NO concentrations.

The rate coefficients for the reaction of Cl atoms with *iso*-butanol and *iso*-butane are not significantly different; *iso*-butanol ($(2.06 \pm 0.40) \times 10^{-10}$ cm^3 $molecule^{-1}$ s^{-1} (Atkinson *et*

al. 2006)) being 50% greater than that of *iso*-butane ($(1.25 \pm 0.04) \times 10^{-10}$ cm^3 $molecule^{-1}$ s^{-1}) (Choi *et al.* 2006)). The presence of the OH functional group in *iso*-butanol plays a significant role as it influences the reactivity of the α-hydrogen towards Cl atoms, leading to there being three different hydrogen atoms present in *iso*-butanol, whereas there are only two different hydrogens in *iso*-butane, as indicated in Figure 7-29. The faster kinetics of *iso*-butanol with Cl atoms leads to the peak ozone concentration occurring at shorter times due to the more rapid production of NO_2 which subsequently produces O_3. The α-peroxy radical produced following the oxidation of *iso*-butanol rapidly decomposes to produce *iso*-butyraldehyde, whereas the corresponding α-peroxy radical produced from *iso*-butane reacts with NO to produce the alkyl radical which subsequently decomposes to *iso*-butyraldehyde. The NO_2 produced goes on to form O_3.

7.6.2 Ozone Formation from the OH Radical Initiated Oxidation of *iso*-butanol and *iso*-butane in the Presence and Absence of NO_x

As discussed in Chapter 1, ozone in the troposphere is toxic to plant and animal health. The potential for compounds to produce ozone throughout their oxidation process is, therefore, of great importance to determine, in order to fully assess their impact on air quality and the environment. OH radicals are the primary oxidising agent in the troposphere. Whilst studies involving Cl atoms are valuable for investigating overall trends, studies of OH radical initiated oxidation processes provide more relevant information on the influence of VOC oxidation in the troposphere.

The concentration of ozone in time following the OH radical initiated oxidation of *iso*-butanol and *iso*-butane under varying initial [NO] conditions is shown in Figure 7-31. In both cases, as the initial [NO] was increased, the time at which the observed ozone reaches a maximum is also increased. In contrast to the Cl atom initiated oxidation of *iso*-butane under varying initial [NO], the maximum ozone observed for the OH radical initiated oxidation decreased with increasing NO.

(a) (b)

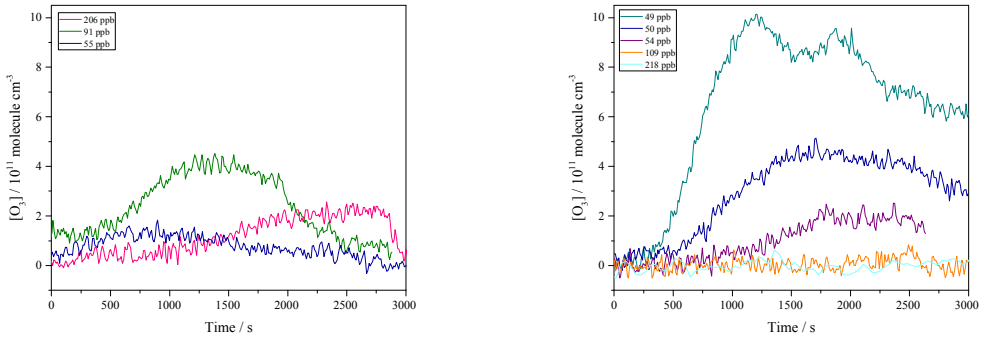

Figure 7-31: Comparison of ozone formation for the OH radical initiated oxidation of *iso*-butanol (a) and *iso*-butane in the presence of NO_x (b).

For both compounds, the ozone production was significantly lower than that of the Cl atom initiated oxidation process. The relative kinetics of the OH radical versus Cl atom initiated oxidation of both compounds are over two orders of magnitude slower. It is concluded that slower formation of peroxy radicals in the OH oxidation processes leads to the lower measured O_3 concentrations. Again, the peak ozone concentrations at the time at which it occurs are compared in Table 7-12, with the total hydrocarbon consumption also given. As with the Cl atom initiated oxidation processes, the time at which the peak ozone was reach was later for the *iso*-butane oxidation process as compared to the *iso*-butanol oxidation process, and the *iso*-butanol consumption was significantly greater at the peak ozone concentration.

***Iso*-butanol**				***Iso*-butane**			
$[NO]_0$ / ppbv	**$[O_3]_{max}$ / ppbv**	**Time / s**	***Iso*-butanol consumption**	**$[NO]_0$ / ppbv**	**$[O_3]_{max}$ / ppbv**	**Time / s**	***Iso*-butane consumption**
55	8	898	60%	49	42	1200	20%
91	19	1384	75%	50	21	1708	30%
206	11	2330	90%	54	10	1365	35%
				109	3	2492	55%
				218	2	2884	50%

Table 7-12: Percentage hydrocarbon consumption at peak ozone concentrations for the Cl atom initiated oxidation of *iso*-butanol and *iso*-butane under varying initial NO concentrations.

The ozone concentration time profiles for the OH radical initiated oxidation of *iso*-butanol and *iso*-butane under low NO_x conditions is shown in Figure 7-32. In both cases, no ozone

formation was observed under low NO_x conditions, owing to the lack of NO_2 being produced in the system, which reduces the amount of $O(^3P)$ available to react with O_2 present and form O_3 (see R 7-8 and R 7-9).

(a) (b)

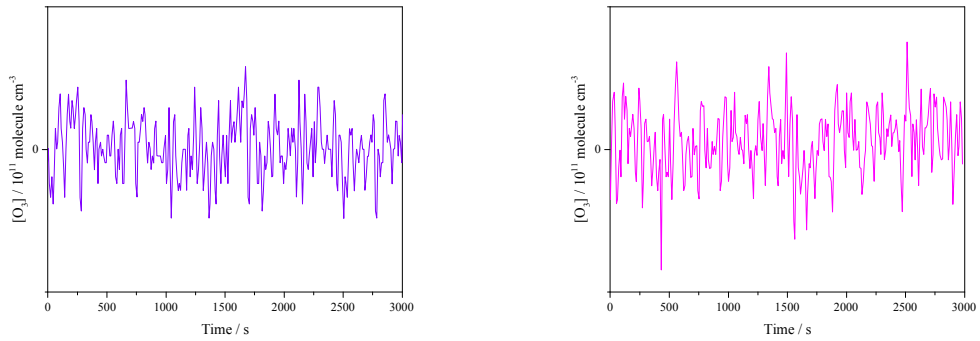

Figure 7-32: Comparison of ozone formation for the OH radical initiated oxidation of *iso*-butanol (a) and *iso*-butane (b) in the absence of NO_x.

Little is available in the literature on the ozone formation from Cl atom initiated oxidation of VOCs; a modelling study by Chang and Allen (2006) investigated the enhancement of ozone formation due to Cl atoms in an urban environment. The authors reported that ozone enhancement could be up to 70 ppbv for a one hour average, in localised areas during the morning, with the peak ozone (typically observed in the later hours of the day) showing an enhancement of <10 ppbv due to chlorine. This study highlights the importance of Cl atom chemistry in early hours of the day, when chlorine containing species are rapidly photolysed to produce Cl atoms. They also noted an influence on the VOC and NO_x emissions on the production of ozone. It is possible that the observed differences in ozone production presented in this work between the OH radical and Cl atom initiated oxidation processes, arise from any differences in photolysis rates of H_2O_2 to produce OH radicals and Cl_2 to produce Cl atoms. Further study into the photolysis rates and yields of OH radicals and Cl atoms is required in order to gain a further insight into this. From the POCP values alone, 37.5 and 30.7 for *iso*-butanol and *iso*-butane, respectively, it would be expected that *iso*-butanol would lead to the formation of greater concentrations of ozone.

7.7 Summary and Conclusions

This chapter has described a comprehensive study into the oxidation processes of *iso*-butanol and *iso*-butane, initiated by Cl atoms or OH radicals in the absence and presence of varying initial NO concentrations. This is the first study of the OH radical initiated oxidation of *iso*-butanol in the absence of NO_x, and under varying,

tropospherically relevant NO concentrations. The products of the Cl atom and OH radical initiated oxidation of *iso*-butanol in the absence and presence of varying initial [NO] have been discussed and, where appropriate, comparisons with previous literature studies have been drawn. The ozone formation following the Cl atom and OH radical initiated oxidation of *iso*-butanol in the absence and presence of NO_x has been reported, with comparison made to the analogous, non-functionalised alkane; *iso*-butane.

In a previous study reported by Andersen *et al.* (2010), no discernible difference was observed in the *iso*-butyraldehyde yields for the Cl atom initiated oxidation of *iso*-butanol in the absence or presence of NO_x. The authors reported an initial yield of 48 ± 3% in the absence of NO_x and 46 ± 3% in the presence of NO_x. In this study, a clear trend was observed in the initial *iso*-butyraldehyde yields; when the initial NO concentration was increased, the initial *iso*-butyraldehyde yield decreased through a minimum and increased again at the maximum initial [NO]. The initial yield of *iso*-butyraldehyde of 57 ± 15% for Cl atom initiated oxidation of *iso*-butanol in the presence of 250 ppbv initial NO is in good agreement with that reported by Andersen *et al.* (2010) in the presence of NO_x. The yields of *iso*-butyraldehyde observed under varying initial NO concentrations indicate that they are highly dependent on the exact initial [NO] present.

Products in the oxidation process of VOCs play a significant role in their ozone production following the oxidation process. The ozone formation is, however, more complex as it is also closely linked with the concentrations of NO_x and HO_x present in the system. For the OH radical initiated oxidation of *iso*-butanol, peak ozone formation increased with increasing initial [NO], however, the ozone formation in the OH radical initiated oxidation of *iso*-butanol peaked at ~4.5×10^{11} molecule cm^{-3} for an initial NO concentration of 91 ppbv and decreased to ~2×10^{11} molecule cm^{-3} for 206 ppbv initial NO. For the Cl atom initiated oxidation of *iso*-butane under varying initial [NO], the peak ozone formation also increased with increasing initial [NO]. The peak ozone concentration measured for the Cl atom initiated oxidation of *iso*-butane under varying initial [NO] was considerably higher, $(0.5 – 3.0) \times 10^{12}$ molecule cm^{-3} for initial [NO] in the range 58 – 190 ppbv, than the peak measured for the Cl atom initiated oxidation of *iso*-butanol under varying initial [NO]; $(0.05 – 0.8) \times 10^{12}$ molecule cm^{-3}. This difference in maximum ozone formation demonstrates the potential benefit, in terms of ozone formation, for the use of alcohols as fuels over alkanes.

In the troposphere, VOCs are predominantly oxidised by OH radicals rather than Cl atoms, as they are in far greater abundance. The peak ozone formation for the OH radical initiated oxidation of *iso*-butanol in the presence of 91 ppbv initial NO was at ~4.5 × 10^{11} molecule cm^{-3}, decreasing to ~2 × 10^{11} molecule cm^{-3} for 206 ppbv initial NO. This trend in peak ozone formation was also observed for the OH radical initiated oxidation of *iso*-butane in the presence of NO_x; with the maximum ozone formation peak at 10 × 10^{11} molecule cm^3 for 49 ppbv initial NO, and decreasing towards zero for 190 and 218 ppbv initial [NO]. Although the ozone formation tends towards zero for the OH radical initiated oxidation of *iso*-butane at 109 ppbv initial NO, with an ozone concentration of ~2 × 10^{11} molecule cm^{-3}, for the *iso*-butanol oxidation, the range of O_3 concentrations under varying initial [NO] was much lower, (1.8 – 4.5) × 10^{11} molecule cm^{-3} for 91 - 206 ppbv initial NO, as compared to (0 – 10) × 10^{11} molecule cm^{-3} for 49 - 218 ppbv initial NO. The lower range of peak ozone formation from the OH radical initiated oxidation of *iso*-butanol shows the potential benefit of the use of alcohols as fuels, over alkanes, in varying NO_x environments.

The difference in trends observed in the ozone formation between the Cl atom initiated oxidation and the OH radical initiated oxidation is attributed to the differences in OH and HO_2 concentrations in the two different systems. Preliminary results of ozone formation from a model simulation of the OH radical and Cl atom initiated oxidation of *iso*-butanol in the presence of varying initial NO concentrations have been presented, and compared to measured ozone concentrations. A similar trend to that of the measured peak ozone concentrations, was observed in the simulation of Cl atom initiated oxidation of *iso*-butanol in the presence of varying initial NO concentrations, where the peak ozone concentration increased with increasing initial NO concentration. The trend observed in the measured peak ozone concentrations from the OH radical initiated oxidation of *iso*-butanol in the presence of varying NO was not replicated through simulations, however, fewer initial NO concentrations were investigated for the OH radical oxidation process. Comparison of a greater range of initial NO concentrations for this oxidation process would assist in verifying these results. The MCM is a complex chemical mechanism describing the tropospheric degradation of VOCs; with 338 reactions and 90 species included in the tropospheric degradation process of *iso*-butanol. Further investigation into the chemical mechanism used in the simulation is required in order to ascertain whether the inclusion of all such reactions are required in simulating the oxidation processes as occurring in HIRAC. It is also necessary to fully characterise the

photolysis of all species included within the chemical model to accurately represent their loss processes. Detailed characterisation of processes occurring in HIRAC, for a wide range of species, is ongoing work within the laboratory in order to gain further understanding of reactions occurring within the chamber that would not occur in the troposphere. Further in depth examination of the reactions included in the chemical model would allow for the relative importance of each reaction in the ozone formation to be considered, and for determination of potentially simplifying the reaction mechanism to more directly describe the oxidation processes occurring. As the MCM has been primarily produced to simulate chemical processes occurring in the troposphere, only a small number of reactions involving chlorine chemistry are included. Chlorine is routinely used in atmospheric simulation chambers as a low NO_x precursor for reactions, it is photolysed at long wavelengths; the inclusion of more detailed chlorine chemistry in the MCM would allow for more accurate comparisons to be made with results from chamber experiments.

In summary, the use of *iso*-butanol as a potential biofuel shows potential in terms of reduced ozone emissions when compared to its analogous non-functionalised alkane, *iso*-butane. Product yields from the Cl atom initiated oxidation of *iso*-butanol in the presence and absence of NO_x are shown to be in reasonable agreement with those in the literature, with any differences primarily attributed to background chemistry within HIRAC. Product yields from the OH radical initiated oxidation of *iso*-butanol in the presence and absence of NO_x have also been reported, with the yield of acetone being in excellent agreement with that reported by Andersen *et al.* (2010). Yields of *iso*-butyraldehyde and HCHO were also reported. Measurements of the OH radical initiated oxidation of *iso*-butanol in the presence of NO_x employing CH_3ONO as the OH radical precursor would allow for more direct comparison to those measurements reported by Andersen *et al.* (2010), however, this would lead to very high levels of NO_x not normally found in tropospheric environments.

7.8 References

Andersen, V. F., Wallington, T. J. and Nielsen, O. J. (2010). "Atmospheric Chemistry of *i*-Butanol." The Journal of Physical Chemistry A **114**(47): 12462-12469.

Atkinson, R., Baulch, D. L., Cox, R. A., Crowley, J. N., Hampson, R. F., Hynes, R. G., Jenkin, M. E., Rossi, M. J., Troe, J. and Subcommittee, I. (2006). "Evaluated kinetic and photochemical data for atmospheric chemistry: Volume II - gas phase reactions of organic species." Atmospheric Chemistry and Physics **6**(11): 3625-4055.

Bloss, C., Wagner, V., Jenkin, M. E., Volkamer, R., Bloss, W. J., Lee, J. D., Heard, D. E., Wirtz, K., Martin-Reviejo, M., Rea, G., Wenger, J. C. and Pilling, M. J. (2005). "Development

of a detailed chemical mechanism (MCMv3.1) for the atmospheric oxidation of aromatic hydrocarbons." Atmospheric Chemistry and Physics **5**(3): 641-664.

Cardone, M., Prati, M. V., Rocco, V., Seggiani, M., Senatore, A. and Vitolo, S. (2002). "Brassica carinata as an Alternative Oil Crop for the Production of Biodiesel in Italy: Engine Performance and Regulated and Unregulated Exhaust Emissions." Environmental Science & Technology **36**(21): 4656-4662.

Cavalli, F., Geiger, H., Barnes, I. and Becker, K. H. (2002). "FTIR Kinetic, Product, and Modeling Study of the OH-Initiated Oxidation of 1-Butanol in Air." Environmental Science & Technology **36**(6): 1263-1270.

Chai, M., Lu, M., Liang, F., Tzillah, A., Dendramis, N. and Watson, L. (2013). "The use of biodiesel blends on a non-road generator and its impacts on ozone formation potentials based on carbonyl emissions." Environmental Pollution **178**(0): 159-165.

Chang, S. and Allen, D. T. (2006). "Atmospheric Chlorine Chemistry in Southeast Texas: Impacts on Ozone Formation and Control." Environmental Science & Technology **40**: 251.

Chen, Y., Zhu, L. and Francisco, J. S. (2002). "Wavelength-Dependent Photolysis of *n*-Butyraldehyde and *i*-Butyraldehyde in the 280−330-nm Region." The Journal of Physical Chemistry A **106**(34): 7755-7763.

Choi, N., Pilling, M. J., Seakins, P. W. and Wang, L. (2006). "Studies of site selective hydrogen atom abstractions by Cl atoms from isobutane and propane by laser flash photolysis/IR diode laser spectroscopy." Physical Chemistry Chemical Physics **8**(18): 2172-2178.

Ellingsen, K., Gauss, M., Van Dingenen, R., Dentener, F. J., Emberson, L., Fiore, A. M., Schultz, M. G., Stevenson, D. S., Ashmore, M. R., Atherton, C. S., Bergmann, D. J., Bey, I., Butler, T., Drevet, J., Eskes, H., Hauglustaine, D. A., Isaksen, I. S. A., Horowitz, L. W., Krol, M., Lamarque, J. F., Lawrence, M. G., van Noije, T., Pyle, J., Rast, S., Rodriguez, J., Savage, N., Strahan, S., Sudo, K., Szopa, S. and Wild, O. (2008). "Global ozone and air quality: a multi-model assessment of risks to human health and crops." Atmospheric Chemistry and Physics Discussions **2008**: 2163-2223.

Felzer, B. S., Cronin, T., Reilly, J. M., Melillo, J. M. and Wang, X. (2007). "Impacts of ozone on trees and crops." Comptes Rendus Geoscience **339**(11–12): 784-798.

Fontaras, G., Karavalakis, G., Kousoulidou, M., Tzamkiozis, T., Ntziachristos, L., Bakeas, E., Stournas, S. and Samaras, Z. (2009). "Effects of biodiesel on passenger car fuel consumption, regulated and non-regulated pollutant emissions over legislated and real-world driving cycles." Fuel **88**(9): 1608-1617.

Fuchs, H., Tan, Z., Lu, K., Bohn, B., Broch, S., Brown, S. S., Dong, H., Gomm, S., Häseler, R., He, L., Hofzumahaus, A., Holland, F., Li, X., Liu, Y., Lu, S., Min, K. E., Rohrer, F., Shao, M., Wang, B., Wang, M., Wu, Y., Zeng, L., Zhang, Y., Wahner, A. and Zhang, Y. (2017). "OH reactivity at a rural site (Wangdu) in the North China Plain: contributions from OH reactants and experimental OH budget." Atmospheric Chemistry and Physics **17**(1): 645-661.

He, C., Ge, Y., Tan, J., You, K., Han, X., Wang, J., You, Q. and Shah, A. N. (2009). "Comparison of carbonyl compounds emissions from diesel engine fueled with biodiesel and diesel." Atmospheric Environment **43**(24): 3657-3661.

Hurley, M. D., Wallington, T. J., Laursen, L., Javadi, M. S., Nielsen, O. J., Yamanaka, T. and Kawasaki, M. (2009). "Atmospheric Chemistry of *n*-Butanol: Kinetics, Mechanisms, and Products of Cl Atom and OH Radical Initiated Oxidation in the Presence and Absence of NO_x." The Journal of Physical Chemistry A **113**(25): 7011-7020.

Ianni, J. C. (2014). "Kintecus, Windows Version 5.00, 2014, www.kintecus.com." from www.kintecus.com.

Jenkin, M. E., Saunders, S. M., Wagner, V. and Pilling, M. J. (2003). "Protocol for the development of the Master Chemical Mechanism, MCM v3 (Part B): tropospheric

degradation of aromatic volatile organic compounds." Atmos. Chem. Phys. **3**(1): 181-193.

Kaiser, J., Skog, K. M., Baumann, K., Bertman, S. B., Brown, S. B., Brune, W. H., Crounse, J. D., De Gouw, J. A., Edgerton, E. S., Feiner, P. A., Goldstein, A. H., Koss, A., Misztal, P. K., Nguyen, T. B., Olson, K. F., St Clair, J. M., Teng, A. P., Toma, S., Wennberg, P. O., Wild, R. J., Zhang, L. and Keutsch, F. N. (2016). "Speciation of OH reactivity above the canopy of an isoprene-dominated forest." Atmospheric Chemistry and Physics **16**(14): 9349-9359.

Krupa, S. V., Nosal, M. and Legge, A. H. (1998). "A numerical analysis of the combined open-top chamber data from the USA and Europe on ambient ozone and negative crop responses." Environmental Pollution **101**(1): 157-160.

Lin, Y.-C., Wu, T.-Y., Ou-Yang, W.-C. and Chen, C.-B. (2009). "Reducing emissions of carbonyl compounds and regulated harmful matters from a heavy-duty diesel engine fueled with paraffinic/biodiesel blends at one low load steady-state condition." Atmospheric Environment **43**(16): 2642-2647.

Martinez, R. D., Buitrago, A. A., Howell, N. W., Hearn, C. H. and Joens, J. A. (1992). "The near U.V. absorption spectra of several aliphatic aldehydes and ketones at 300 K." Atmospheric Environment. Part A. General Topics **26**(5): 785-792.

McGillen, M. R., Baasandorj, M. and Burkholder, J. B. (2013). "Gas-Phase Rate Coefficients for the OH + *n*-, *i*-, *s*-, and *t*-Butanol Reactions Measured Between 220 and 380 K: Non-Arrhenius Behavior and Site-Specific Reactivity." The Journal of Physical Chemistry A **117**(22): 4636-4656.

Meagher, R. J., McIntosh, M. E., Hurley, M. D. and Wallington, T. J. (1997). "A kinetic study of the reaction of chlorine and fluorine atoms with HC(O)F at 295±2 K." International Journal of Chemical Kinetics **29**(8): 619-625.

Monks, P. (2009). "Atmospheric Composition Change—Global and Regional Air Quality." Atmospheric Environment **43**: 5268.

Whalley, L. K., Stone, D., Bandy, B., Dunmore, R., Hamilton, J. F., Hopkins, J., Lee, J. D., Lewis, A. C. and Heard, D. E. (2016). "Atmospheric OH reactivity in central London: observations, model predictions and estimates of in situ ozone production." Atmospheric Chemistry and Physics **16**(4): 2109-2122.

Winiberg, F. (2014). Characterisation of FAGE apparatus for HO_x detection and application in an environmental chamber. PhD, University of Leeds.

Chapter 8. OH reactivity measurements following the oxidation of *iso*-butanol and *iso*-butane in the presence and absence of NO_x

8.1 Introduction

As discussed in Chapter 1, measurements of OH reactivity are an extremely useful tool in understanding the oxidation potential of specific environments of the troposphere. The ability to measure OH reactivity in chamber studies allows for discrepancies between calculated, modelled and measured OH reactivity to be investigated more thoroughly; it is possible to study oxidation processes of individual compounds in isolation. With these chamber measurements of OH reactivity, comparisons with calculated OH reactivity from measurable species and comparisons with model simulations can provide useful information on our current level of understanding of the chemical processes occurring. A laser flash photolysis coupled with laser induced fluorescence (LFP-LIF) instrument for the measurement of OH reactivity has been described in Chapter 4, with details on recent development for the improvement of the measurement capability and for measurements with the HIRAC chamber. Results from a comprehensive comparison of instruments for the measurement of OH reactivity have been described in Chapter 5, where all LFP-LIF instruments employed were shown to be in very good agreement with each other, and for simple systems, to be in good agreement with calculated OH reactivity over a range of VOC mixtures.

Few studies of OH reactivity measurements from atmospheric simulation chambers have been previously reported in the literature (Nakashima *et al.* 2012, Fuchs *et al.* 2013, Nehr *et al.* 2014, Nölscher *et al.* 2014). Three of these studies investigated the oxidation of isoprene and compare measurements with results from modelling studies (Nakashima *et al.* 2012, Fuchs *et al.* 2013, Nölscher *et al.* 2014), with the fourth investigating the oxidation of aromatic hydrocarbons (Nehr *et al.* 2014). The three studies into the oxidation of isoprene all showed discrepancies between measured and modelled OH reactivity, with a general under prediction observed from the modelled OH reactivity.

These studies show the value of OH reactivity measurements in chamber studies, enabling the finer details of VOC oxidation processes to be investigated. As described in Chapter 1, the incorporation of modelled intermediates in the modelling of OH reactivity has been shown to reduce the gap between modelled and measured OH reactivity (Whalley *et al.* 2016). Comparison of measurements of OH reactivity with both calculated and modelled OH reactivity for a range of VOCs under different conditions will assist in increasing the depth of knowledge into these oxidation processes, and enable specific areas to be identified that require more detailed investigation.

The importance of investigating both OH radical and Cl atom initiated oxidation processes has been discussed in Chapter 1. Here, OH reactivity measurements are compared with calculated OH reactivity from the OH radical and Cl atom initiated oxidation processes of *iso*-butanol and *iso*-butane in the presence and absence of NO_x. Discrepancies between measured and calculated OH reactivity are discussed, with conclusions being drawn based on the compounds used in the calculation of OH reactivity and the measurement techniques.

8.2 Experimental

All experiments were carried out as described previously in Chapter 7. A LFP-LIF instrument was used for the measurement of OH reactivity from the HIRAC chamber. The OH reactivity measurement procedure from HIRAC has been outlined in Chapter 4. For the measurements reported here, approximately 1 l min^{-1} was sampled from the chamber during all experiments, and the measured OH reactivity, k'_{raw}, was corrected to account for the dilution into the instrument and for the instrument zero ($k'_{OH(physical)}$, discussed in Chapter 4), in order to obtain a value of k'_{OH} representative of the true OH reactivity within the chamber.

OH reactivity was calculated from the measured species within HIRAC for each experiment. This included [HO_2] measured with the FAGE instrument; [*iso*-butanol], [*iso*-butane], [*iso*-butyraldehyde] and [acetone] measured by GC-FID using a CP-Sil 5CB column (50 m length, 0.32 mm i.d., 5 μl film thickness); [HCHO] measured by FTIR; [O_3] measured with a commercial UV photometric analyser (Thermo Electron Corporation, Model 49C, LOD = 1.0 ppbv); and [NO] and [NO_2] measured with a commercial chemiluminescence NO_x analyser (Thermo Environmental Instruments Inc., Model 42C, LOD = 50 pptv at 120 s averaging time). The rate coefficients for the reactions with OH for each of the species mentioned here, and used for the calculation of

OH reactivity, are given in Table 8-1. OH reactivity was calculated at 298 K and 1000 mbar, as these were the conditions during the experiments.

Species	$k_{OH + species}$ / cm^3 molecule^{-1} s^{-1}	Reference
HO_2	1.10×10^{-10}	Atkinson *et al.* (2004)
iso-butanol	8.90×10^{-12}	Atkinson *et al.* (2006)
iso-butane	2.12×10^{-12}	Atkinson (2003)
iso-butyraldehyde	2.60×10^{-12}	Atkinson *et al.* (2006)
Acetone	1.80×10^{-13}	Atkinson *et al.* (2006)
HCHO	8.50×10^{-12}	Atkinson *et al.* (2006)
O_3	7.30×10^{-14}	Atkinson *et al.* (2004)
NO	1.00×10^{-11}	Atkinson *et al.* (2004)
NO_2	1.12×10^{-11}	Atkinson *et al.* (2004)

Table 8-1: Rate coefficients used in the calculation of OH reactivity.

8.3 OH Reactivity Measurements following the Cl Atom Initiated Oxidation of *iso*-butanol and *iso*-butane in the Presence and Absence of NO_x

The measured OH reactivity and calculated contributions to the total calculated OH reactivity for the Cl atom initiated oxidation of *iso*-butanol in the absence of NO_x and in the presence of 101 ppbv and 250 ppbv initial NO are shown in Figure 8-1, Figure 8-2 and Figure 8-3, respectively. In the absence of NO_x, the measured OH reactivity prior to the initiation of the oxidation reaction was in excellent agreement with the calculated OH reactivity, solely from *iso*-butanol present in the chamber. As the oxidation process proceeds, a discrepancy was evident between the measured and calculated OH reactivity; at early times (0 – 900 s), the calculated OH reactivity overestimates that of the measured OH reactivity, and at later times (900 – 3000 s), the calculated OH reactivity considerably underestimates the measured OH reactivity. The measured OH reactivity has errors typically of ~10%, propagated from the error in the OH reactivity measurements and the error in the dilution of the sample taken from HIRAC. Discrepancies between measured and calculated OH reactivity at shorter times are likely due to losses of *iso*-butyraldehyde

within the sampling line into the OH reactivity instrument, whereas discrepancies at later times, where the calculated OH reactivity was underestimating the measured OH reactivity, are more likely due to numerous unmeasured minor products and intermediate species formed throughout the oxidation process.

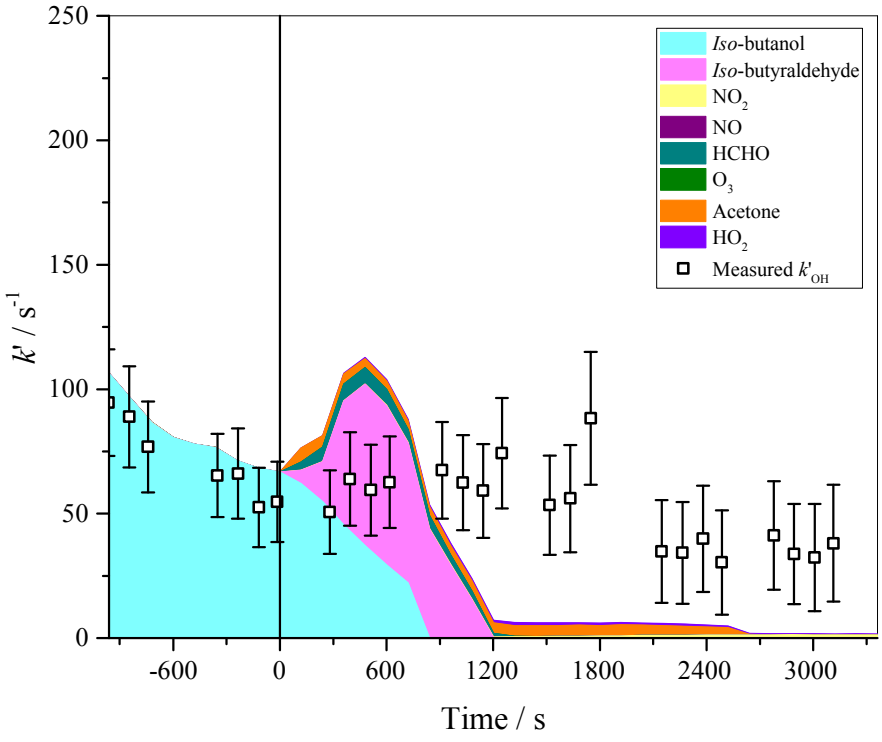

Figure 8-1: Stacked area plot to show the contribution to k'_{OH} from measured species in comparison with measured k'_{OH} for the Cl atom initiated oxidation of *iso*-butanol under low NO_x conditions. The vertical line at time = 0 shows the start of the oxidation process. Error bars represent 1σ propagated uncertainties in the measurements.

As the initial NO concentration was increased, a discrepancy between the measured and calculated OH reactivity prior to the initiation of the oxidation process was observed, and was seen to increase with increasing initial [NO] from 101 ppbv to 250 ppbv, Figure 8-2 and Figure 8-3, respectively. Again, the measured and calculated OH reactivities show similar discrepancies at shorter and longer times for the Cl atom initiated oxidation of *iso*-butanol in the presence of 101 ppbv initial NO, Figure 8-2. The overestimation of the OH reactivity observed in the presence of NO_x prior to the initiation of the oxidation process may in fact be an underestimation of the measured OH reactivity due to OH recycling within the flow tube of the OH reactivity instrument. As discussed in Chapter 5, this has been seen in similar VOC/NO_x chamber studies with the measurement of OH reactivity of a CO/CH_4 mixture in the presence of NO_x. In this case, the measured OH

reactivity may be underestimating the OH reactivity as OH is formed in the flow tube following the reaction of NO with HO_2 present in the flow tube:

Iso-butanol + OH → products + HO_2 R 8-1

HO_2 + NO → OH + NO_2 R 8-2

Further details on how this would lead to an underestimation in measured OH reactivity have been discussed in Chapter 5. For the Cl atom initiated oxidation of *iso*-butanol in the presence of 101 ppbv initial NO, the measured and calculated OH reactivity both follow a similar time profile; an initial sharp increase in OH reactivity, followed by a rapid decay up to ~1000 s and then a more gentle decay from ~1000 s to ~3000 s. The initial sharp increase in OH reactivity is attributed to the rapid production of *iso*-butyraldehyde following the attack of Cl atoms at the α-hydrogen position of *iso*-butanol. As previously discussed, the measured NO_2 is in fact the sum of all NO_2 containing species. At some experimental time points, the calculated contribution to the total calculated OH reactivity from NO_2 may be an overestimation, dependent on the real identity of the species being measured as NO_2. In order to determine the true contribution of NO_2 to the total calculated OH reactivity, NO_2 concentrations should be determined by other measurement techniques where this interference does not occur. At the time of experiments and analysis, no NO_2 reference spectrum was available to determine exact NO_2 concentrations from the FTIR spectra, however, NO_2 was observable in the experimental spectra recorded. If the NO_2 contribution were to be excluded entirely from the total calculated OH reactivity, better agreement would be observed between the measured and calculated OH reactivity at shorter times (0 – 1000 s), however, at later times (1000 – 3000 s) agreement would be poorer.

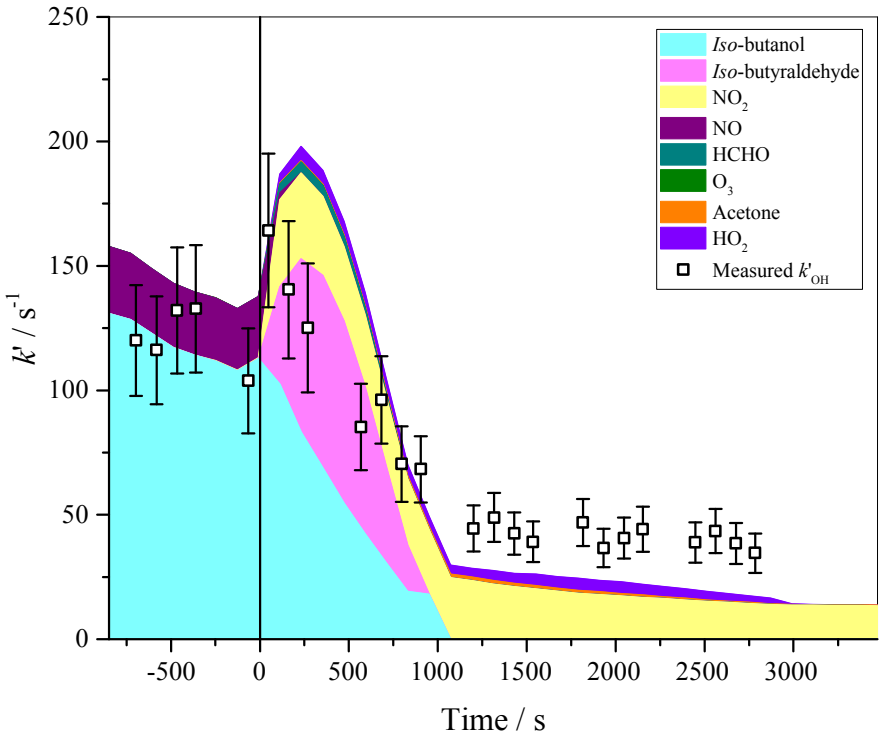

Figure 8-2: Stacked area plot to show the contribution to k'_{OH} from measured species in comparison with measured k'_{OH} for the Cl atom initiated oxidation of *iso*-butanol under an initial [NO] of 101 ppbv. The vertical line at time = 0 shows the start of the oxidation process. Error bars represent 1σ propagated uncertainties in the measurements.

Similar to Figure 8-2, Figure 8-3 shows a significant discrepancy between the measured and calculated OH reactivity prior to the initiation of the oxidation reaction, again attributed to OH recycling from the reaction of NO with HO_2 radicals within the flow tube of the OH reactivity instrument. Overestimation of the calculated OH reactivity was also observed at shorter times (0 – 1200 s), where, in this higher initial [NO] system, if the contribution to the calculated OH reactivity from NO_2 were to be excluded, excellent agreement between the measured and calculated OH reactivity would be observed.

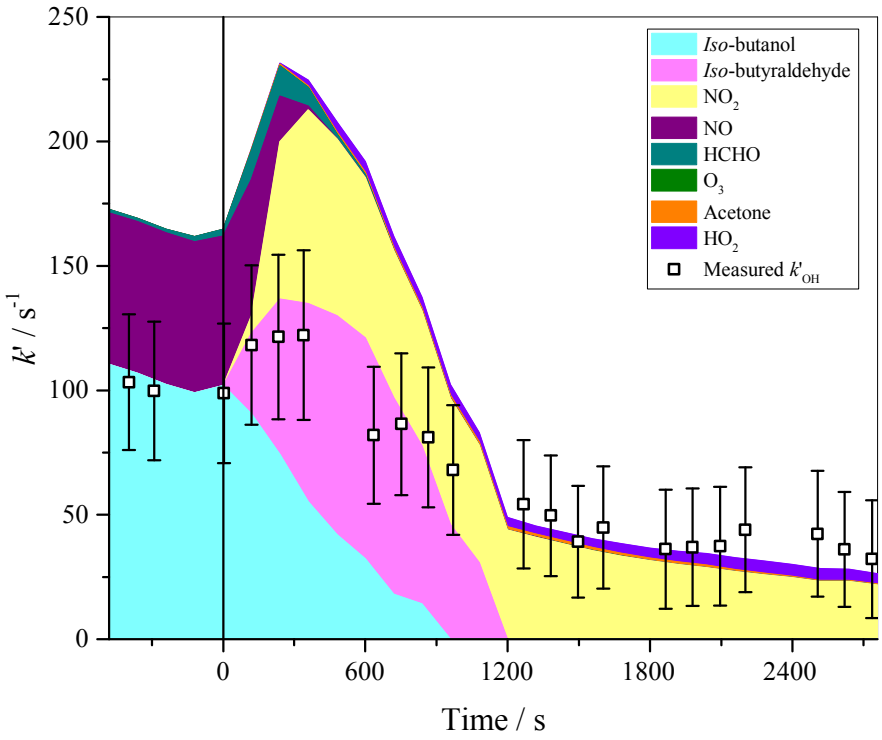

Figure 8-3: Stacked area plot to show the contribution to k'_{OH} from measured species in comparison with measured k'_{OH} for the Cl atom initiated oxidation of *iso*-butanol under an initial [NO] of 250 ppbv. The vertical line at time = 0 shows the start of the oxidation process. Error bars represent 1σ propagated uncertainties in the measurements.

Figure 8-4 shows the calculated contributions to the total calculated OH reactivity for the Cl atom initiated oxidation of *iso*-butanol under low NO_x, 101 ppbv NO and 250 ppbv NO at 600 second time intervals throughout the oxidation process. The calculated contributions to the total calculated OH reactivity for the Cl atom initiated oxidation of *iso*-butane under low NO_x, 110 ppbv NO and 190 ppbv NO are shown in Figure 8-8. As would be expected, the contribution the total calculated OH reactivity from NO at time zero increased with the increase in the initial [NO] present in HIRAC. The contribution to the total calculated OH reactivity from NO_2, more unexpectedly, was observed to increase with increasing time under low NO_x conditions for both the *iso*-butanol and *iso*-butane Cl atom initiated oxidation systems. This is attributed to any residual nitrate compounds present on the chamber walls which will be photolysed when the lamps are switched on, to produce NO_2. Nitrates coming from walls throughout the course of the experiments, which when measuring with a commercial NO_x analyser, are all measured as "NO_2". The contribution from NO_2 to the total calculated OH reactivity, in both the *iso*-butanol and *iso*-butane Cl atom initiated oxidation, increased with increasing initial [NO] for each 600 second time point.

The percentage contributions from measured species to the total calculated OH reactivity at 600 s time intervals for the Cl atom initiated oxidation of *iso*-butanol in the presence and absence of NO_x are given in Table 8-2, with a graphical representation shown in Figure 8-4. As would be expected, as the initial NO concentration was increased, the percentage contribution to the total calculated OH reactivity from NO also increased, from <0.1% in the absence of NO, to 17.8% at 101 ppbv initial NO and 36.7% at 250 ppbv initial NO. With the increasing initial [NO], the contribution to the total calculated OH reactivity from NO_2 also increased at each time point. Slightly unexpected was the contribution to the total calculated OH reactivity from NO_2 in the Cl atom oxidation of *iso*-butanol in the absence of NO_x, eventually dominating the total calculated OH reactivity by the end of the experiment, at 3000 s. NO_2 has previously been observed upon irradiation of HIRAC in 80:20 N_2:O_2; due to the stainless steel construction material of the chamber certain compounds are more prone to sticking to the chamber walls, particularly nitrate compounds, which can then photolyse to produce NO_2 upon irradiation of the chamber, or come off the walls upon irradiation due to surface reactions and temperature changes within the chamber, making them available for reaction with other species present. The more the chamber is used daily, and the more NO_x reactions are investigated, the more NO and NO_2 containing compounds remain on the chamber walls. The contribution to the total calculated OH reactivity from NO_2 is attributed to NO_2 containing compounds coming from the walls of HIRAC.

The contribution to the total calculated OH reactivity from HO_2 was seen to be significantly greater at longer times in the absence of NO_x as compared to in the presence of NO_x, however, the actual concentration of HO_2 at later times was not significantly different between the differing initial [NO]; $[HO_2] = \sim 4 \times 10^{10}$ molecule cm^{-3} for all initial levels of NO at 1800 s. The difference in percentage contribution to the total calculated OH reactivity from HO_2 at 1800 s under varying levels of initial NO is attributed to the greater concentration of NO_x contributing to the total measured OH reactivity under higher initial NO conditions.

$[NO]_{t=0}$	Contributing Species	0 s	600 s	1200 s	1800 s	2400 s
Low NO_x	*Iso*-butanol	99.9	28.3	<0.1	<0.1	<0.1
	Iso-butyraldehyde	<0.1	61.5	78.5	<0.1	<0.1
	Acetone	<0.1	0.6	3.5	17.3	13.7
	NO_2	0.1	0.2	1.4	13.3	21.4
	O_3	<0.1	<0.1	<0.1	<0.1	<0.1
	NO	<0.1	<0.1	<0.1	<0.1	<0.1
	HO_2	<0.1	3.2	12.4	69.5	64.9
	HCHO	<0.1	6.2	4.3	0.1	<0.1
	$\Delta k'_{OH}$	19.6	49.4	76.0	174.8	180.3
101 ppbv	*Iso*-butanol	81.1	30.5	<0.1	<0.1	<0.1
	Iso-butyraldehyde	<0.1	42.5	<0.1	<0.1	<0.1
	Acetone	<0.1	0.7	5.1	4.8	3.2
	NO_2	0.3	20.6	83.0	75.9	78.2
	O_3	<0.1	<0.1	<0.1	<0.1	<0.1
	NO	17.8	<0.1	<0.1	<0.1	<0.1
	HO_2	<0.1	3.7	11.9	19.3	18.5
	HCHO	<0.1	2.0	<0.1	<0.1	<0.1
	$\Delta k'_{OH}$	2.6	42.1	44.2	63.3	63.5
250 ppbv	*Iso*-butanol	61.8	16.8	<0.1	<0.1	<0.1
	Iso-butyraldehyde	<0.1	46.2	<0.1	<0.1	<0.1
	Acetone	<0.1	0.5	2.5	2.9	2.1
	NO_2	<0.1	33.6	89.8	86.3	82.3
	O_3	<0.1	<0.1	0.1	<0.1	<0.1
	NO	36.7	<0.1	<0.1	<0.1	<0.1
	HO_2	<0.1	2.2	7.5	10.8	15.6
	HCHO	1.7	0.5	<0.1	<0.1	<0.1
	$\Delta k'_{OH}$	50.0	80.3	22.2	0.9	36.0

Table 8-2: Percentage contributions of measured species to total calculated OH reactivity for the Cl atom initiated oxidation of *iso*-butanol under low, 101 ppbv and 250 ppbv initial [NO] conditions at 600 s time intervals.

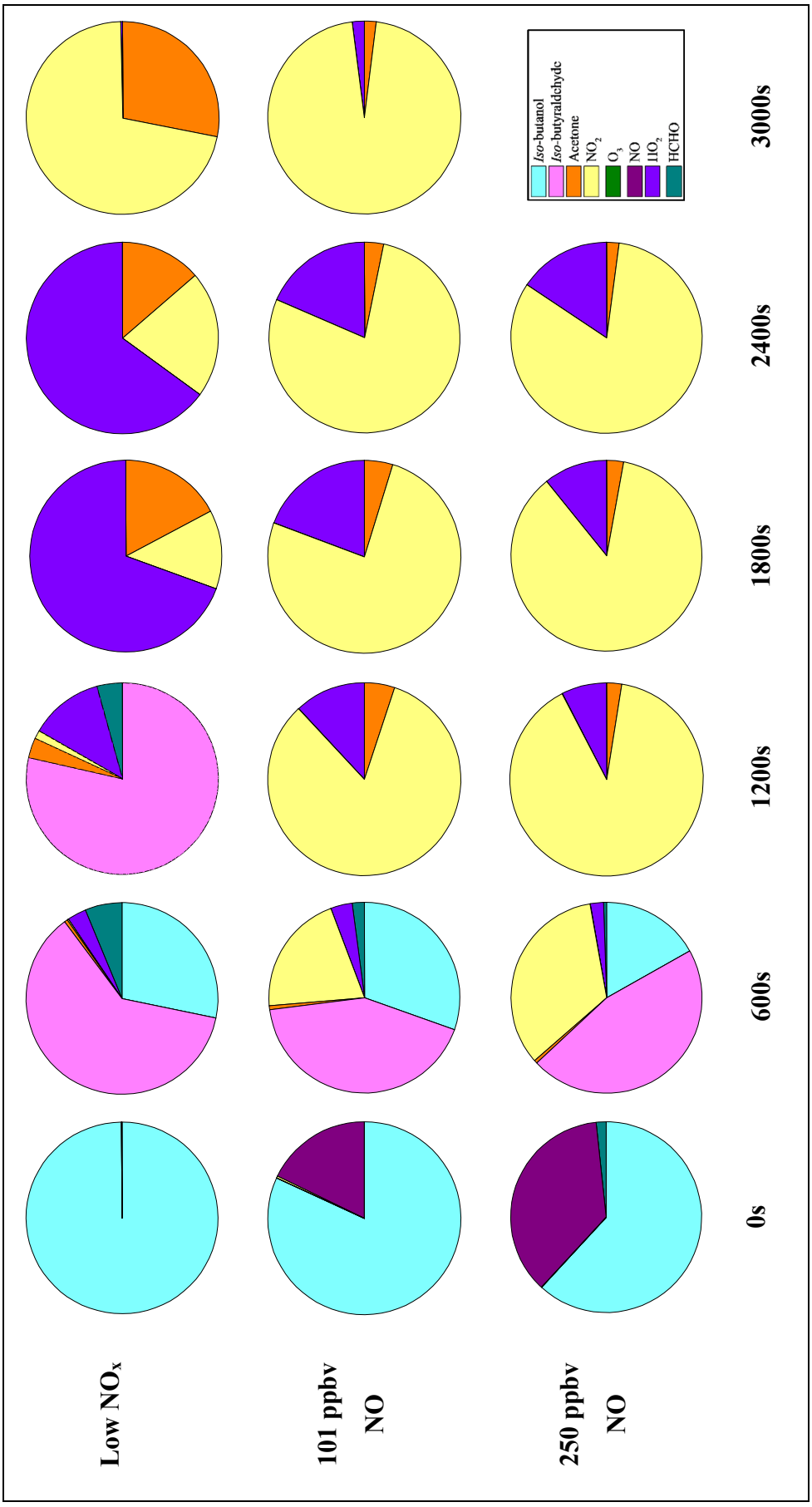

Figure 8-4: Contribution to calculated k'_{OH} at 600s time intervals for the Cl atom initiated oxidation of *iso*-butanol under varying initial [NO] conditions. Light cyan: *iso*-butanol, light magenta: *iso*-butyraldehyde, orange: acetone, light yellow: NO_2, green: O_3, purple: NO, violet: HO_2, dark cyan: HCHO.

A comparison of the measured OH reactivity and the calculated OH reactivity from measured species for the Cl atom initiated oxidation of *iso*-butane in the absence of NO_x, and in the presence of 110 ppbv initial NO and 190 ppbv initial NO are given in Figure 8-5, Figure 8-6 and Figure 8-7, respectively.

Again, good agreement was observed between the measured and calculated OH reactivity for the Cl atom initiated oxidation of *iso*-butane in the absence of NO_x prior to the initiation of the oxidation reaction; when only *iso*-butane was present in the system. Following the initiation of the oxidation reaction, the calculated OH reactivity overestimates the measured OH reactivity at shorter times (0 – 1000 s) and underestimates the measured OH reactivity at later times (1000 – 2400 s). As with the *iso*-butanol oxidation, the primary product of *iso*-butane oxidation is *iso*-butyraldehyde, which was likely lost to the walls of the sampling line into the OH reactivity instrument, resulting in the OH reactivity being undermeasured for high concentrations of *iso*-butyraldehyde. Discrepancies between the calculated OH reactivity at later times (1000 – 2400 s) may arise from a number of unmeasured products and intermediates species.

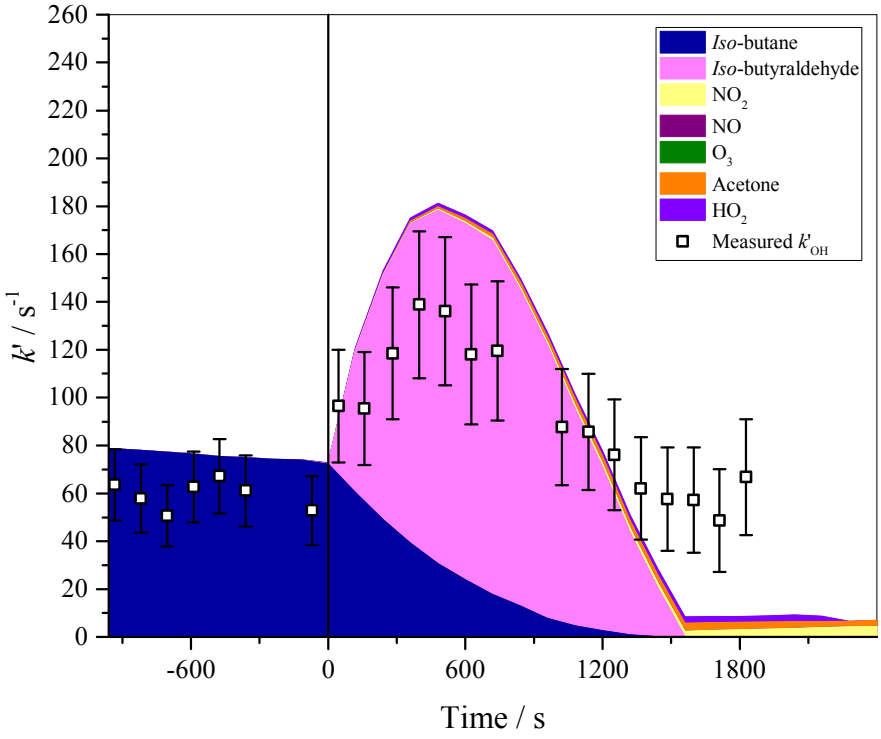

Figure 8-5: Stacked area plot to show the contribution to k'_{OH} from measured species in comparison with measured k'_{OH} for the Cl atom initiated oxidation of *iso*-butane in the absence of NO_x. The vertical line at time = 0 shows the start of the oxidation process. Error bars represent 1σ propagated uncertainties in the measurements.

Discrepancies between measured and calculated OH reactivity for the Cl atom initiated oxidation of *iso*-butane in the presence of NO_x were smaller compared to the discrepancies observed in the absence of NO_x; with the majority of the observed discrepancies being an underestimation of the calculated OH reactivity as compared to the measured OH reactivity. In both 110 ppbv initial NO and 190 ppbv initial NO, the time profiles of the measured and calculated OH reactivity show very good agreement.

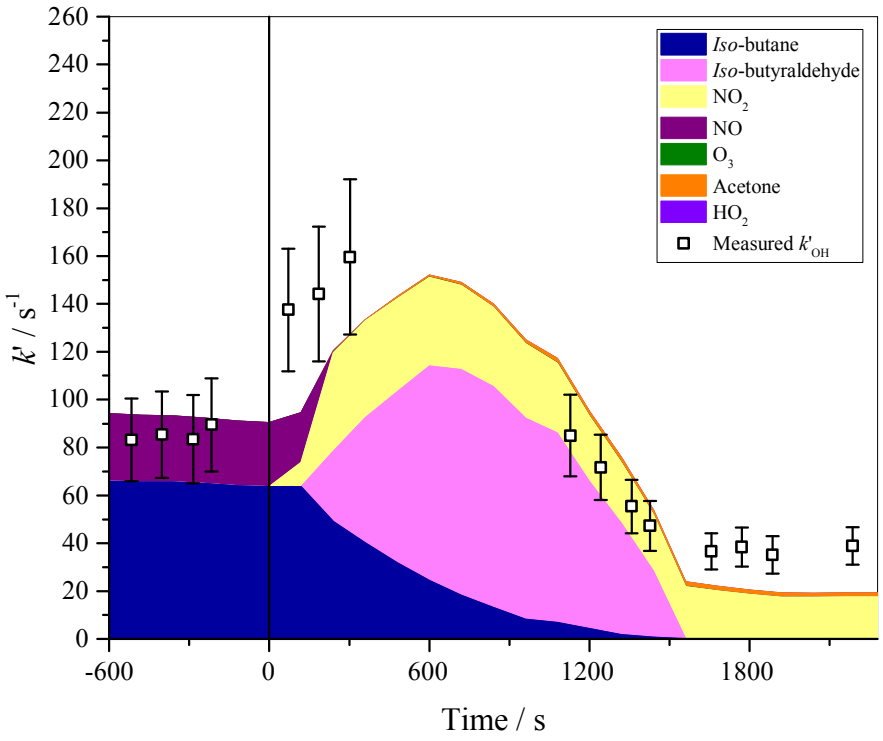

Figure 8-6: Stacked area plot to show the contribution to k'_{OH} from measured species in comparison with measured k'_{OH} for the Cl atom initiated oxidation of *iso*-butane under an initial [NO] of 110 ppbv. The vertical line at time = 0 shows the start of the oxidation process. Error bars represent 1σ propagated uncertainties in the measurements. Missing measured k'_{OH} data points were due to technical issues with the OH reactivity instrument.

The calculated and measured OH reactivity for the Cl atom initiated oxidation of *iso*-butane in the presence of 190 ppbv initial NO are in good agreement, shown in Figure 8-7. Unlike the situations discussed so far, for oxidation processes in the presence of NO_x, here the calculated OH reactivity underestimates the measured OH reactivity. This discrepancy may arise for a number of reasons, including greater concentrations of residual contaminants within HIRAC which are not included in the calculation, or greater concentrations of contaminants within the dilution gas supplied to the OH reactivity instrument. A slight discrepancy was observed at ~1250 s, where the calculated OH reactivity underestimates the measured OH reactivity. A sharp change in gradient was seen at this time in the calculated OH reactivity as the *iso*-butyraldehyde concentration decreased towards zero, whereas the measured OH reactivity shows a much gentler change in gradient as the *iso*-butyraldehyde was consumed. It is likely that the discrepancy observed here was due to the detection limit of the GC-FID for the measurement of *iso*-butyraldehyde. Following this, towards longer times

(1500 – 2400 s), a small discrepancy was observed between the measured and calculated OH reactivity; attributed to the sum of unmeasured products and intermediate species.

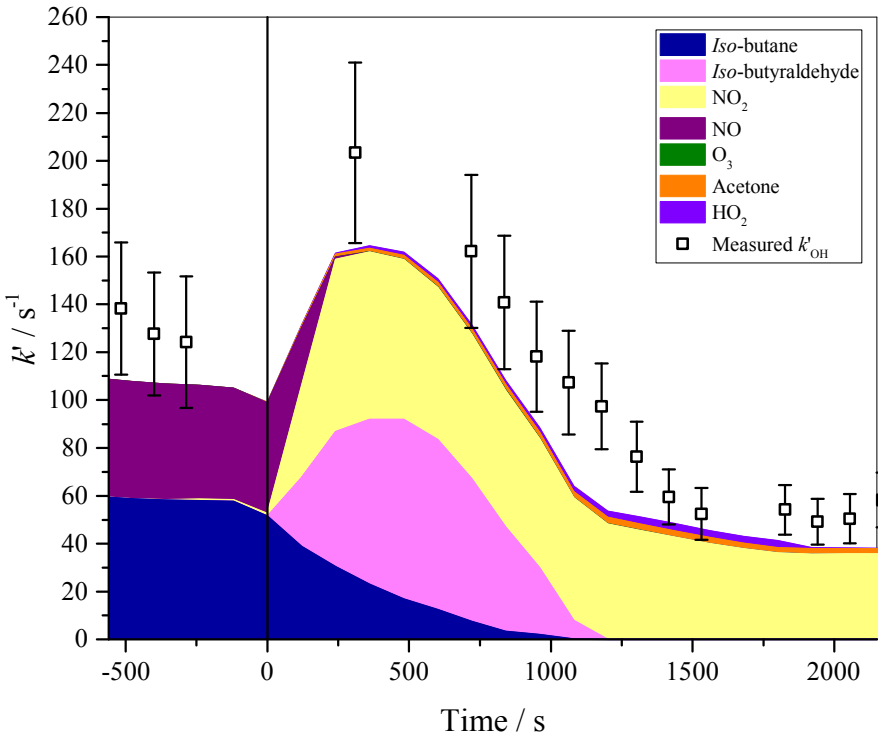

Figure 8-7: Stacked area plot to show the contribution to k'_{OH} from measured species in comparison with measured k'_{OH} for the Cl atom initiated oxidation of *iso*-butane under an initial [NO] of 190 ppbv. The vertical line at time = 0 shows the start of the oxidation process. Error bars represent 1σ propagated uncertainties in the measurements. Missing measured k'_{OH} data points were due to technical issues with the OH reactivity instrument.

Percentage contributions to the total calculated OH reactivity from measured species for the Cl atom initiated oxidation of *iso*-butane in the presence and absence of NO_x at 600 s time intervals throughout the oxidation process are given in Table 8-3, and depicted in Figure 8-8. Again, the percentage contribution from NO to the total calculated OH reactivity for the Cl atom initiated oxidation of *iso*-butane increased as the initial NO concentration increased, from <0.1% in the absence of NO_x to 29.5% at 110 ppbv initial [NO] and 46.7% at 190 ppbv initial [NO].

Similar to observations from in the Cl atom initiated oxidation of *iso*-butanol in the absence of NO_x, a contribution to the total calculated OH reactivity from NO_2 was observed at later times in the oxidation of *iso*-butane in the absence of NO_x; attributed to NO_2 containing species present on the walls of the chamber.

The percentage contribution to the total calculated OH reactivity from *iso*-butyraldehyde decreased at 600 s and 1200 s as the initial [NO] was increased; decreasing from 84.5% in the absence of NO_x, to 59.0% in 110 ppbv initial NO and 47.3% in 190 ppbv initial NO. At 1200 s, the percentage contribution from *iso*-butyraldehyde to the total calculated OH reactivity increased in both the absence of NO_x and in 110 ppbv initial NO from the percentage contribution at 600 s. The *iso*-butyraldehyde was completely consumed by 1200 s in the presence of 190 ppbv initial NO; the peak [OH] in fact decreased from 110 ppbv initial NO to 190 ppbv initial NO, however, the maximum [OH] was considerably longer lived in the 190 ppbv initial NO, remaining for ~100 s before decaying at a relatively slow rate as compared to the much faster instant decay of OH radicals in the 110 ppbv initial NO. This longer lived [OH] enables the *iso*-butyraldehyde to be consumed by both Cl atoms and OH radicals present in the system.

The percentage contribution to the total calculated OH reactivity from acetone was observed to increase throughout the oxidation process for all initial NO concentrations. The rate of reaction of acetone with Cl atoms is considerably slower, $k_{Cl + acetone} = (2.10 \pm 0.29) \times 10^{-12}$ cm^3 molecule^{-1} s^{-1} (Atkinson et al. 2006), than the rate of reaction of *iso*-butyraldehyde, $k_{Cl + iso\text{-butyraldehyde}} = (1.37 \pm 0.08) \times 10^{-10}$ cm^3 molecule^{-1} s^{-1} (Andersen et al. 2010), and so little to none of the acetone produced from the *iso*-butanol oxidation was consumed by Cl atoms. An increase in the percentage contribution to the total OH reactivity from acetone was observed in the absence of NO_x throughout the oxidation; from <0.1% at 0 s to 0.8% at 600 s, 3.8% at 1200 s, 36.2% at 1800 s and 36.1% at 2400 s. The large percentage contribution from acetone at later times (1800 s and 2400 s) arises as acetone was also produced following the oxidation and photolysis of *iso*-butyraldehyde, and other products in the oxidation process have been consumed by reaction with Cl atoms and OH radicals.

Ozone does not have a significant influence on the total calculated OH reactivity; remaining ≤0.1% at all times throughout the oxidation of *iso*-butane for all initial NO concentrations, with the exception of 190 ppbv initial NO at 1200 s where the percentage contribution from ozone reaches 0.4%. As shown in Chapter 7, the concentration of ozone produced following the Cl atom initiated oxidation of *iso*-butane in the presence of NO_x was significantly larger than concentrations from the Cl atom initiated oxidation of *iso*-butanol in the presence of NO_x, however, the slow kinetics of O_3 with OH radicals ($k_{OH + O3} = (7.30 \pm 2.57) \times 10^{-14}$ cm^3 molecule^{-1} s^{-1} (Atkinson et al. 2004)) lead to ozone having very little to no impact on the total calculated OH reactivity.

$[NO]_{t=0}$	Contributing Species	0 s	600 s	1200 s	1800 s	2400 s
Low NO_x	*Iso*-butane	99.2	13.5	3.1	<0.1	<0.1
	Iso-butyraldehyde	<0.1	84.5	88.4	<0.1	<0.1
	Acetone	<0.1	0.8	3.8	36.2	36.1
	NO_2	0.2	0.4	2.1	36.0	63.8
	O_3	<0.1	<0.1	<0.1	0.1	0.1
	NO	<0.1	<0.1	<0.1	<0.1	<0.1
	HO_2	0.6	0.9	2.5	27.8	<0.1
	$\Delta k'_{OH}$	2.6	39.5	4.1	155.4	200
110 ppbv	*Iso*-butane	70.5	16.0	4.0	<0.1	
	Iso-butyraldehyde	<0.1	59.0	65.0	<0.1	
	Acetone	<0.1	0.6	2.0	8.7	
	NO_2	<0.1	24.4	29.0	91.2	
	O_3	<0.1	<0.1	<0.1	0.1	
	NO	29.5	<0.1	<0.1	<0.1	
	HO_2	<0.1	<0.1	<0.1	<0.1	
	$\Delta k'_{OH}$	0.8	21.7	28.1	61.4	
190 ppbv	*Iso*-butane	52.2	8.3	<0.1	<0.1	
	Iso-butyraldehyde	<0.1	47.3	<0.1	<0.1	
	Acetone	<0.1	1.1	4.2	4.5	
	NO_2	1.1	42.2	90.5	88.6	
	O_3	<0.1	0.1	0.4	0.1	
	NO	46.7	<0.1	<0.1	<0.1	
	HO_2	<0.1	1.0	4.9	6.9	
	$\Delta k'_{OH}$	-	7.6	58.7	28.0	

Table 8-3: Percentage contributions of measured species to total calculated OH reactivity for the Cl atom initiated oxidation of *iso*-butane under low, 110 ppbv and 190 ppbv initial [NO] conditions at 600 s time intervals

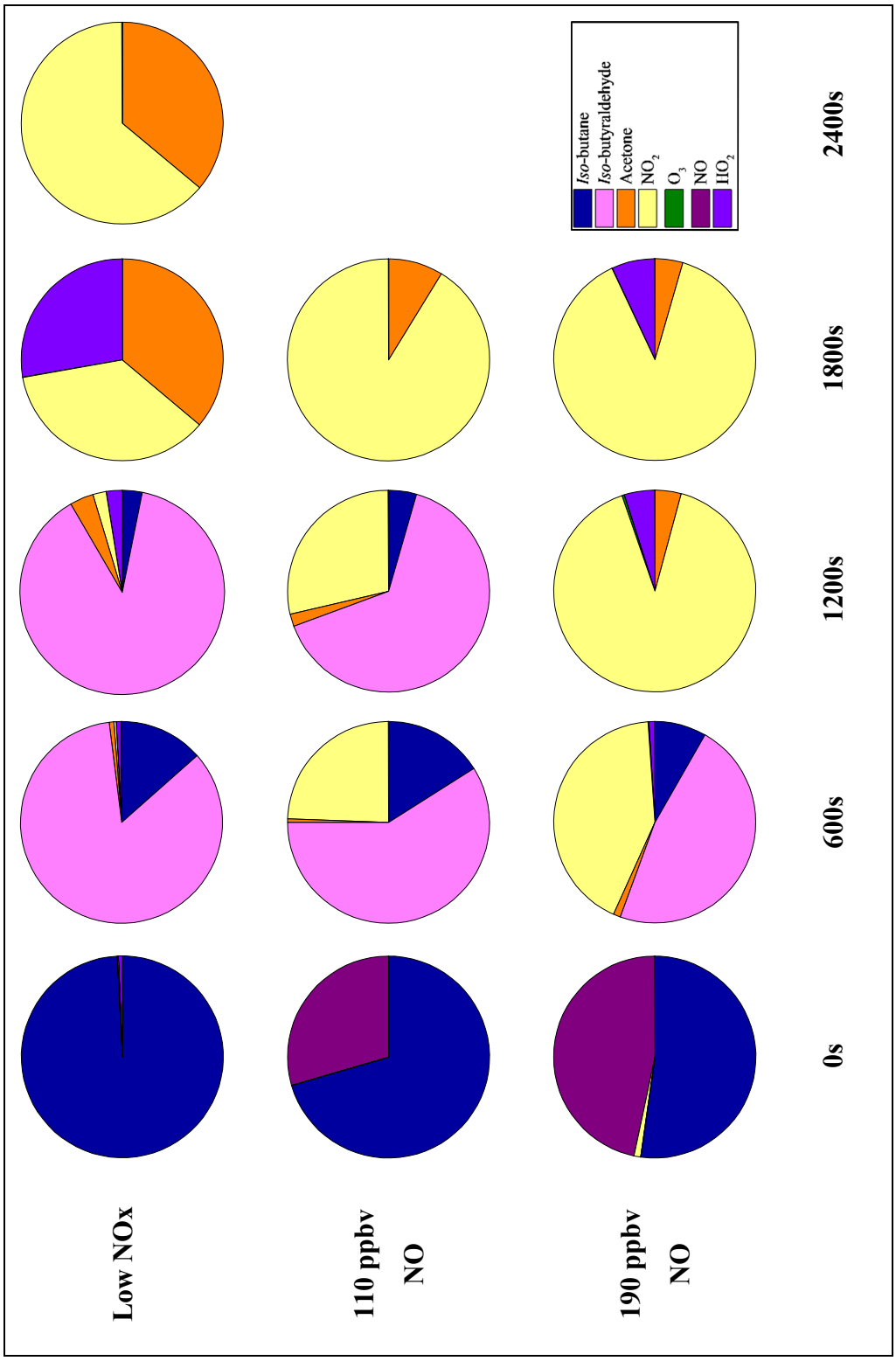

Figure 8-8: Contribution to calculated k'_{OH} at 600s time intervals for the Cl atom initiated oxidation of *iso*-butane with varying initial [NO]. Blue: *iso*-butane, light magenta: *iso*-butyraldehyde, orange: acetone, light yellow: NO_2, green: O_3, purple: NO, violet: HO_2.

8.4 OH Reactivity Measurements following the OH Radical Initiated Oxidation of *Iso*-butanol and *Iso*-butane in the Presence and Absence of NO_x

The OH radical initiated oxidation of *iso*-butanol in the absence and presence of NO_x is compared to that of the OH radical initiated oxidation of *iso*-butane in the absence and presence of NO_x, in order to investigate the influence of the alcohol functional group on OH reactivity measurements. Comparison with the Cl atom initiated oxidation processes will be given in Section 8.5.

Figure 8-9, Figure 8-10 and Figure 8-11 show the calculated contributions to the total calculated OH reactivity compared to the measured OH reactivity for the OH radical initiated oxidation of *iso*-butanol in the absence of NO_x, in the presence of 91 ppbv initial NO and in the presence of 206 ppbv initial NO, respectively. In Figure 8-9, the measured and calculated OH reactivity are seen to be in good agreement prior to the initiation of the oxidation reaction. Following the initiation of the oxidation reaction, discrepancies were observed between the calculated and measured OH reactivity. *Iso*-butyraldehyde is the primary oxidation product following attack by OH radicals at the α-hydrogen position of *iso*-butanol. It is likely that lower values of the measured OH reactivity, compared to the calculated values, arise due to losses in the sampling line into the OH reactivity instrument. Unlike in the Cl atom initiated oxidation of *iso*-butanol, the *iso*-butyraldehyde was not completely consumed within the ~30 minutes of the reaction; the kinetics of *iso*-butyraldehyde with OH radicals are ~10 times slower ($k_{OH + iso\text{-butyraldehyde}} = (2.60 \pm 0.60) \times 10^{-11}$ cm^3 molecule^{-1} s^{-1} (Atkinson *et al.* 2006)) than the kinetics with Cl atoms ($k_{Cl + iso\text{-butyraldehyde}} = (1.37 \pm 0.08) \times 10^{-10}$ cm^3 molecule^{-1} s^{-1} (Andersen *et al.* 2010)).

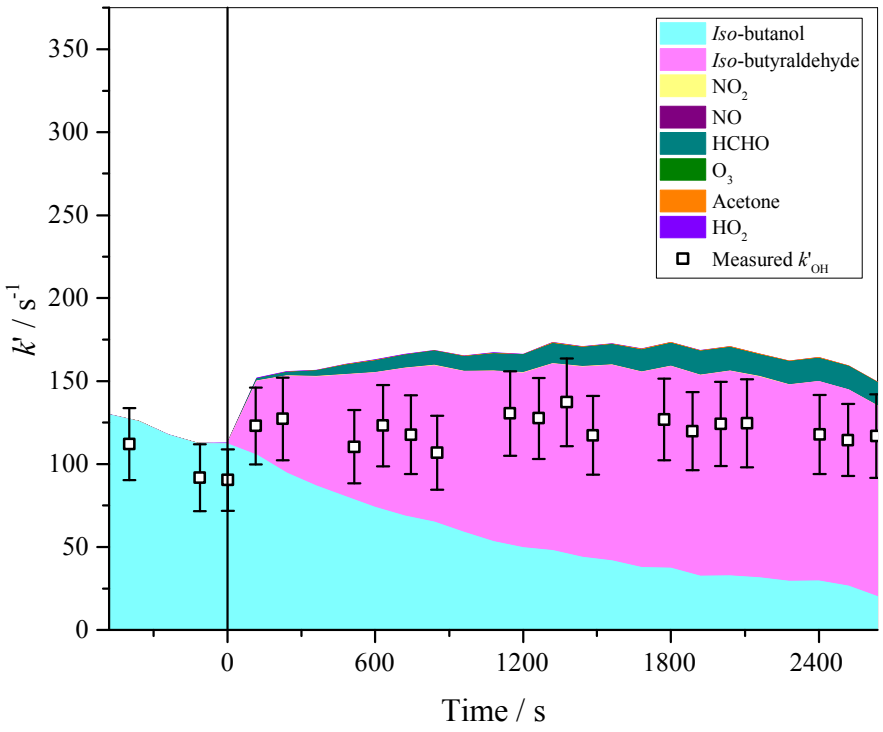

Figure 8-9: Stacked area plot to show the contribution to k'_{OH} from measured species in comparison with measured k'_{OH} for the OH radical initiated oxidation of *iso*-butanol under low NO_x conditions. The vertical line at time = 0 shows the start of the oxidation process. Error bars represent 1σ propagated uncertainties in the measurements.

In the presence of 91 ppbv initial NO, a discrepancy was observed between the measured and calculated OH reactivity prior to the initiation of the oxidation reaction; the calculated OH reactivity was greater than the measured OH reactivity. This discrepancy is attributed to the analysis process for the OH reactivity measurements, resulting in lower values due to recycling of OH within the flow tube of the instrument. At shorter times following the initiation of the oxidation reaction (0 – 500 s), the calculated OH reactivity underestimates the measured OH reactivity. Another significant factor in the underestimation of OH reactivity as compared to measured OH reactivity may be losses of species to the walls of the sampling line into the instrument.

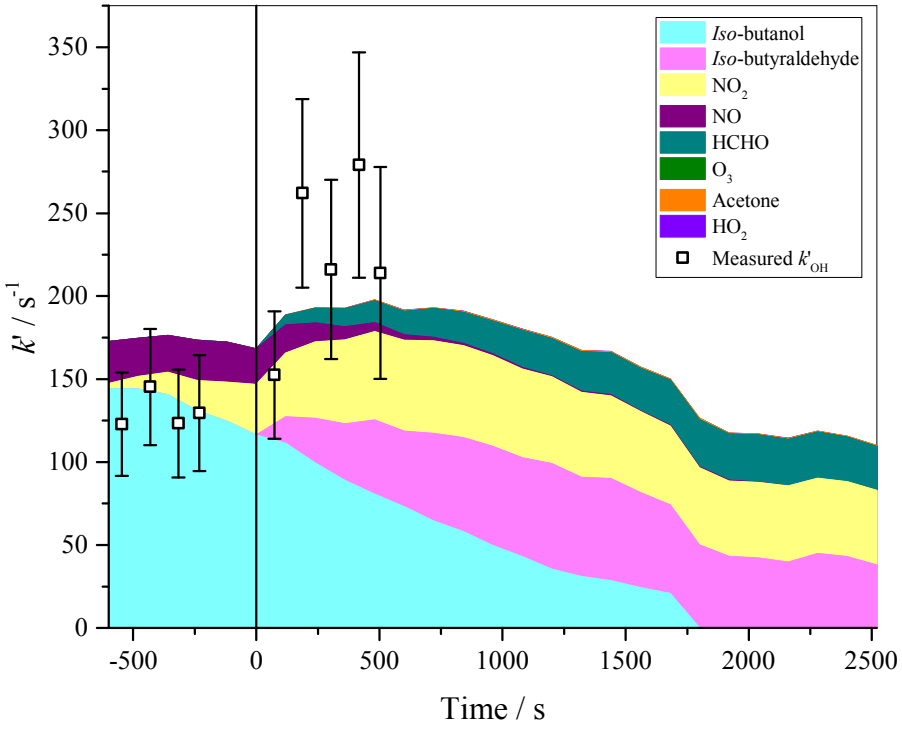

Figure 8-10: Stacked area plot to show the contribution to k'_{OH} from measured species in comparison with measured k'_{OH} for the OH radical initiated oxidation of *iso*-butanol under an initial [NO] of 91 ppbv. The vertical line at time = 0 shows the start of the oxidation process. Error bars represent 1σ propagated uncertainties in the measurements. Missing measured k'_{OH} data points were due to technical issues with the OH reactivity instrument.

The measured and calculated OH reactivity for the OH radical initiated oxidation of *iso*-butanol in the presence of 206 ppbv initial NO is shown in Figure 8-11. Again, a discrepancy between the measured and calculated OH reactivity was observed at times prior to the initiation of the oxidation reaction, when only *iso*-butanol and NO are present in the chamber.

As with the other systems described previously for the Cl atom initiated oxidation of *iso*-butanol in the presence of NO_x, the measured OH reactivity was much lower than the calculated OH reactivity at short reaction times (0 – 600 s); likely due to influences as previously explained from measurements of NO_2 and wall losses.

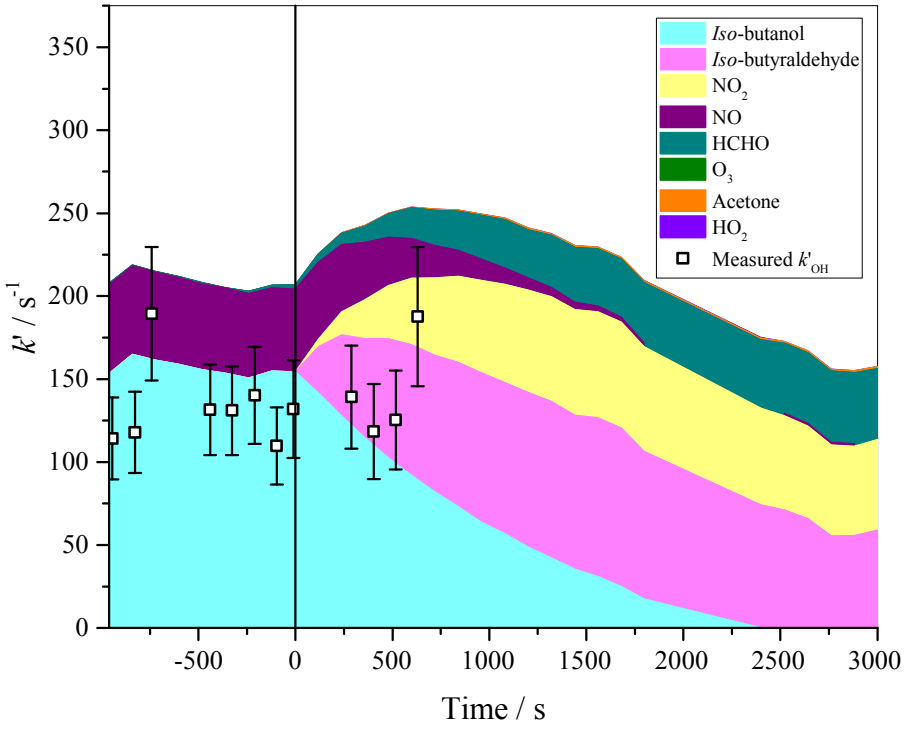

Figure 8-11: Stacked area plot to show the contribution to k'_{OH} from measured species in comparison with measured k'_{OH} for the OH radical initiated oxidation of *iso*-butanol under an initial [NO] of 206 ppbv. The vertical line at time = 0 shows the start of the oxidation process. Error bars represent 1σ propagated uncertainties in the measurements. Missing measured k'_{OH} data points were due to technical issues with the OH reactivity instrument.

Percentage contributions to the total calculated OH reactivity from measured species at 600 s time intervals are given in Table 8-4, and graphically displayed in Figure 8-12. As expected, as the initial NO concentration was increased, the contribution to the total calculated OH reactivity at 0 s from NO increased; from <0.1% in the absence of NO_x, to 12.8% at 91 ppbv initial NO and 24.4% at 206 ppbv initial NO.

Under all three initial NO conditions, the contribution to the calculate OH reactivity from *iso*-butyraldehyde increased throughout the oxidation process; in the absence of NO_x the *iso*-butyraldehyde percentage contribution increased from <0.1% at 0 s, to 49.8% at 600 s, 63.1% at 1200 s, 70.2% at 1800 s and 73.2% at 2400 s. No contribution to the total calculated OH reactivity was observed from NO_2 for the OH radical initiated oxidation of *iso*-butanol in the absence of NO_x. The NO_2 formation and measurement upon irradiating the chamber in the absence of any NO_x is highly dependent on the condition of the chamber walls; influenced by the previous experiments carried out in HIRAC. The contribution from NO_2 to the total calculated OH reactivity was observed to increase

throughout the oxidation process for both the 91 ppbv initial NO and 206 ppbv initial NO.

Under all initial NO concentrations, the contribution to the total calculated OH reactivity from HCHO was observed to increase with time; in the absence of NO_x, HCHO increased from <0.1% at 0 s, to 4.4% at 600 s, 6.5% at 1200 s, 7.9% at 1800s and 8.5% at 2400 s. The HCHO contribution to the total calculated OH reactivity at different time intervals generally increased with increasing initial NO concentration. For an initial NO concentration of 91 ppbv, the HCHO contribution at 0 s was <0.1%, increasing to 6.2% at 600 s, 11.6% at 1200 s, 21.2% at 1800 s and 12.7% at 2400 s. Increasing the initial NO concentration again to 206 ppbv, the contribution to the total calculated OH reactivity increased from <0.1% at 0 s to 7.3% at 600 s, 12.0% at 1200 s, 17.4% at 1800 s and 23.5% at 2400 s. HCHO is a secondary product formed in the oxidation of *iso*-butanol; as the primary products, *iso*-butyraldehyde and acetone, are formed, they go on to form HCHO in their subsequent reactions with OH radicals present and from photolysis. As the initial NO concentration was increased from low NO_x through 91 ppbv to 206 ppbv, the potential for OH recycling increased, increasing the OH radicals available for *iso*-butyraldehyde and acetone to react with and subsequently forming HCHO; this was observed as the contribution to the total calculated OH reactivity from HCHO increased for each 600 s time interval as the initial NO concentration was increased.

The contribution to the total OH reactivity from O_3 was very low throughout all time points for all concentrations of initial NO_x, typically being ≤0.1%. As has been previously discussed in Chapter 7, the formation of ozone from the OH radical initiated oxidation of *iso*-butanol was observed in the presence of NO_x, however, the kinetics of the reaction of ozone with OH radicals are very slow as compared to the kinetics of the other species used in calculating OH reactivity, $k_{OH + O3} = (7.30 \pm 2.57) \times 10^{-14}$ cm^3 molecule^{-1} s^{-1} (Atkinson *et al.* 2004), compared to $(110 - 8.9) \times 10^{-12}$ cm^3 molecule^{-1} s^{-1} for other species included in calculating OH reactivity (excluding acetone).

The kinetics of acetone with OH radicals are also considerably slower than those of other measured species used in calculating total OH reactivity, $k_{OH + acetone} = (1.80 \pm 0.33) \times 10^{-13}$ cm^3 molecule^{-1} s^{-1} (Atkinson *et al.* 2004). Acetone was observed as a primary product for the OH radical initiated oxidation of *iso*-butanol in the presence and absence of NO_x (Chapter 7); however, the contribution from acetone to the

total calculated OH reactivity was observed to be insignificant, contributing <1% under all initial NO_x conditions at all times throughout the oxidation process.

$[NO]_{t=0}$	Contributing Species	0 s	600 s	1200 s	1800 s	2400 s	3000 s
Low NO_x	*Iso*-butanol	99.5	45.3	29.9	21.5	17.9	
	Iso-butyraldehyde	<0.1	49.8	63.1	70.2	73.2	
	Acetone	<0.1	0.2	0.2	0.2	0.3	
	NO_2	0.2	0.1	0.1	0.1	0.1	
	O_3	<0.1	<0.1	<0.1	<0.1	<0.1	
	NO	<0.1	<0.1	<0.1	<0.1	<0.1	
	HO_2	0.4	0.2	0.1	0.1	<0.1	
	HCHO	<0.1	4.4	6.5	7.9	8.5	
	$\Delta k'_{OH}$	21.9	27.6	23.3	30.9	32.7	
91 ppbv	*Iso*-butanol	69.1	38.5	20.5	<0.1	<0.1	
	Iso-butyraldehyde	<0.1	24.1	36.8	40.4	63.8	
	Acetone	<0.1	0.2	0.3	0.6	0.3	
	NO_2	18.1	29.0	30.3	37.4	23.3	
	O_3	<0.1	<0.1	<0.1	<0.1	<0.1	
	NO	12.8	1.8	0.4	0.5	<0.1	
	HO_2	<0.1	<0.1	0.1	0.1	<0.1	
	HCHO	0	6.2	11.6	21.1	12.7	
	$\Delta k'_{OH}$	9.7	43.6	-	-	-	
206 ppbv	*Iso*-butanol	75.6	36.2	20.2	8.3	<0.1	<0.1
	Iso-butyraldehyde	<0.1	31.2	38.8	42.5	42.1	37.2
	Acetone	<0.1	0.2	0.4	0.5	0.6	0.7
	NO_2	<0.1	15.7	25.5	30.1	32.9	34.6
	O_3	<0.1	<0.1	<0.1	<0.1	<0.1	<0.1
	NO	24.4	9.4	3.1	1.1	0.8	0.6
	HO_2	<0.1	<0.1	<0.1	<0.1	<0.1	<0.1
	HCHO	<0.1	7.3	12.0	17.4	23.5	27.0
	$\Delta k'_{OH}$	43.0	30.0	-	-	-	-

Table 8-4: Percentage contributions of measured species to total calculated OH reactivity for the OH radical initiated oxidation of *iso*-butanol under low, 91 ppbv and 206 ppbv initial [NO] conditions at 600 s time intervals.

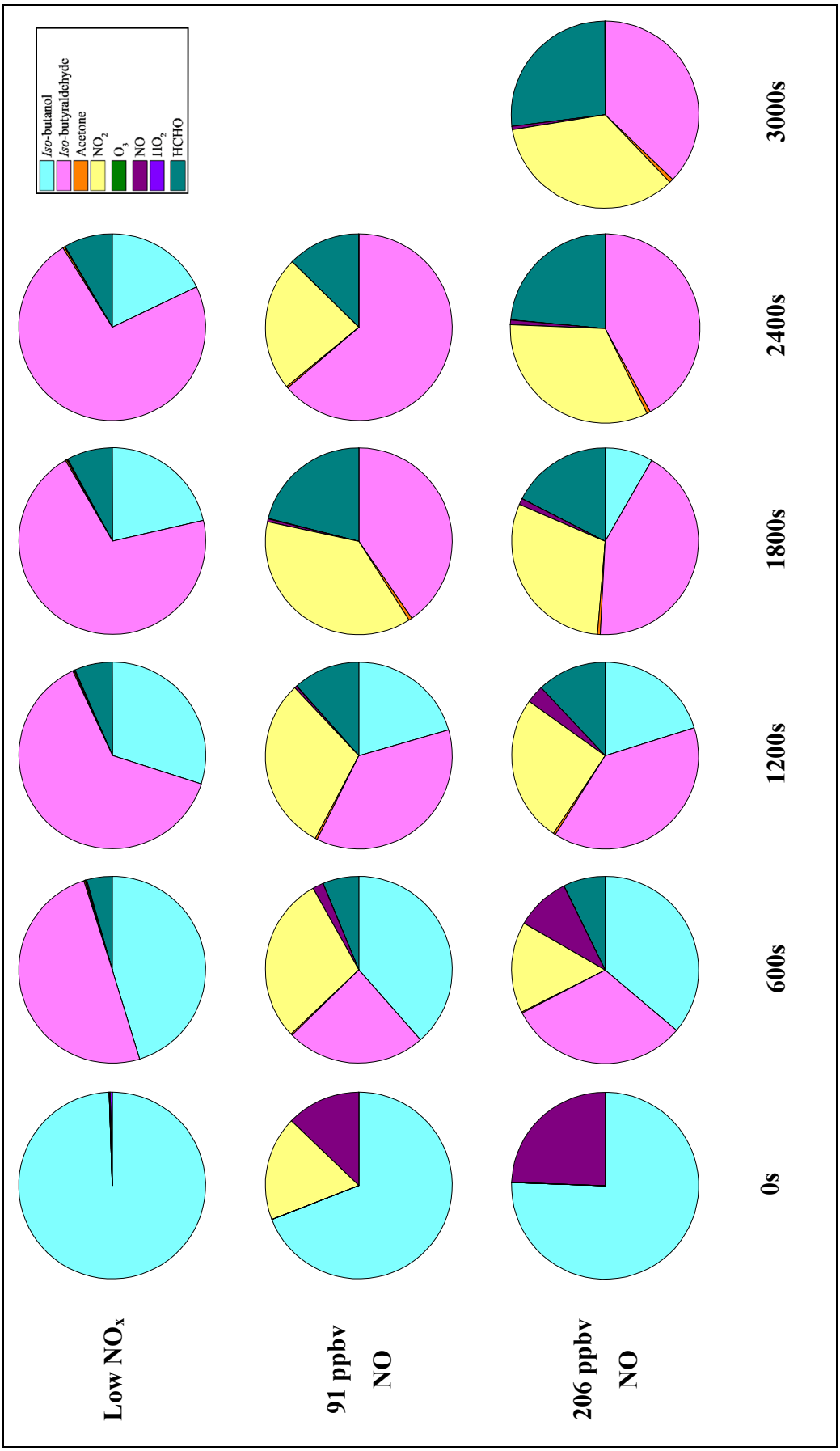

Figure 8-12: Contribution to calculated k'_{OH} at 600s time intervals for the OH radical initiated oxidation of *iso*-butanol under varying initial [NO] conditions. Light cyan: *iso*-butanol, light magenta: *iso*-butyraldehyde, orange: acetone, light yellow: NO_2, green: O_3, purple: NO, violet: HO_2, dark cyan: HCHO.

The stacked area contributions to the calculated OH reactivity comapared to the measured OH reactivity for the OH radical initiated oxidation of *iso*-butane under 109 ppbv initial NO and 218 ppbv intial NO are shown in Figure 8-13 and Figure 8-14, respectively. As with the Cl atom initiated oxidation of *iso*-butane in the presence of NO_x, the calculated OH reactivity underestimates the measured OH reactivity for the OH radical initiated oxidation of *iso*-butane in the presence of NO_x. Prior to the initiation of the oxidation process, the calculated OH reactivity underestimated the measured OH reactivity by ~15 s^{-1} for the oxidation in the presence of 109 ppbv initial NO when only *iso*-butane was present, with this discrepancy increasing to ~60 s^{-1} upon the addition of NO to the system. In the presence of 218 ppbv initial NO, the calcualted and measured OH reactiivty are in excellent agreement prior to the initiation of the oxidation process when only *iso*-butane was present, however, a discrepancy of ~50 s^{-1} between the caclualted and measured OH reactivity was observed as NO was introduced. The discrepancy observed between the calculated and measured OH reactivity with 109 ppbv initial NO when only *iso*-butane was present is likely due to impurities in the bath gas used, dilution gases and residual compounds within the chamber from previous experiments. As discussed previously for the oxidation of *iso*-butanol by OH radicals or Cl atoms, in the presence of NO_x, the discrepancy observed prior to the intiaition of the oxidation process showed an over exestimation of the calcualted OH reactivity comapred to the measured OH reactivity (or under measurement of the OH reactiivty due to OH recycling within the flow tube of the instrument). This was not the case here for the OH radical initiated oxidation of *iso*-butane in the presnece of NO_x as the calculated OH reacitivty was significantly underestimating that of the calculated OH reactivity. In both the 109 ppbv initial NO and 218 ppbv initial NO situations, the contribution to the calculated OH reactivty becomes dominated by NO_x following the initiation of the oxidation process.

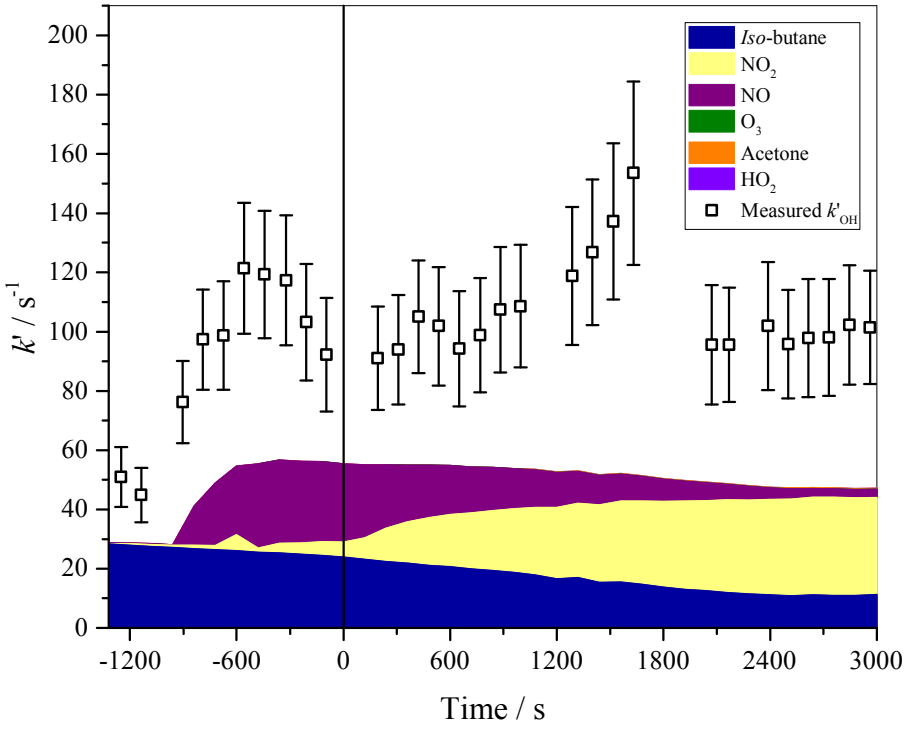

Figure 8-13: Stacked area plot to show the contribution to k'_{OH} from measured species in comparison with measured k'_{OH} for the OH radical initiated oxidation of *iso*-butane under an initial [NO] of 109 ppbv. The vertical line at time = 0 shows the start of the oxidation process. Error bars represent 1σ propagated uncertainties in the measurements. Missing measured k'_{OH} data points were due to technical issues with the OH reactivity instrument.

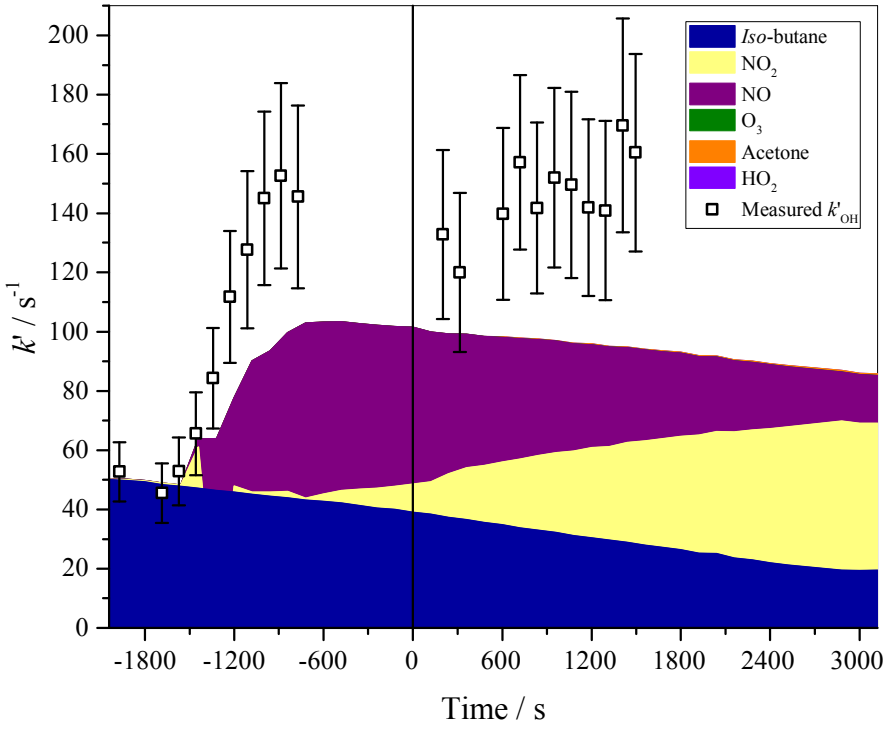

Figure 8-14: Stacked area plot to show the contribution to k'_{OH} from measured species in comparison with measured k'_{OH} for the OH radical oxidation of *iso*-butane under an initial [NO] of 218 ppbv. The vertical line at time = 0 shows the start of the oxidation process. Error bars represent 1σ propagated uncertainties in the measurements. Missing measured k'_{OH} data points were due to technical issues with the OH reactivity instrument.

Table 8-5 gives the percentage contributions to the total calculated OH reactivity from measured species for the OH radical initiated oxidation of *iso*-butane under varying initial NO concentrations, displayed graphically in Figure 8-15. As with all systems discussed so far, the percentage contribution to the total calculated OH reactivity from NO increased with increasing initial NO for time = 0 s; 47.6% at 109 ppbv initial NO and 52.2% at 218 ppbv NO. The contribution from NO to the total calculated OH reactivity then decreased throughout the course of the oxidation process, although still remaining as a significant contribution throughout all time intervals for 218 ppbv initial NO than 109 ppbv initial NO.

As the *iso*-butane was consumed through its oxidation process, the contribution to the total calculated OH reactivity from *iso*-butane decreased; for 109 ppbv initial NO the *iso*-butane contribution decreased from 43.0% at 0 s to 37.6% at 600 s, 31.5% at 1200 s, 27.3% at 1800 s, 23.2% at 2400 s and 23.8% at 3000 s. For 218 ppbv initial NO the percentage contribution to the total calculated OH reactivity from *iso*-butane decreased

from 38.5% at 0 s, to 35.4% at 600 s, 31.8% at 1200 s, 28.4% at 1800 s, 24.6% at 2400 s and 22.5% at 3000 s.

No *iso*-butyraldehyde was observed for the OH radical initiated oxidation of *iso*-butane in the presence of NO_x, it is possible that due to the NO present, any *iso*-butyraldehyde formed was immediately consumed following further oxidation by OH radicals present in the system, however, the absence of any HCHO present would suggest that this may not be the case. Another possible reason for the absence of *iso*-butyraldehyde and HCHO observed is the large dilution required to maintain a constant pressure within HIRAC; any small concentrations of *iso*-butyraldehyde or HCHO formed could be immediately removed due to dilution and wall losses. It would be expected that *iso*-butyraldehyde and HCHO would be observed as the attack of OH radicals at the α carbon of the *iso*-butane would primarily form *iso*-butyraldehyde, which subsequently produce HCHO as a secondary product following its own oxidation by OH radicals present. In comparison, in the Cl atom initiated oxidation of *iso*-butane in the presence of NO_x, both *iso*-butyraldehyde and HCHO were observed, owing to the faster kinetics of *iso*-butane with Cl radicals ($k_{Cl + iso\text{-butane}} = (1.40 \pm 0.08) \times 10^{-10}$ cm^3 molecule^{-1} s^{-1} (Beichert *et al.* 1995)) than with OH radicals ($k_{OH + iso\text{-butane}} = (2.12 \pm 0.42) \times 10^{-12}$ cm^3 molecule^{-1} s^{-1} (Atkinson 2003)).

As with the oxidation systems in the presence of NO_x previously described, despite the high concentrations of ozone observed, the contribution to the total calculated OH reactivity from ozone was <0.1% at all times throughout the oxidation process under all initial NO concentrations, due to its slow rate of reaction with OH radicals.

Acetone was also observed as a primary product in the OH radical initiated oxidation of *iso*-butane in the presence of NO_x, similarly to ozone, owing to its relatively slow kinetics with OH radicals ($k_{OH + acetone} = (1.8 \pm 0.30) \times 10^{-13}$ cm^3 molecule^{-1} s^{-1} (Atkinson *et al.* 2006)), acetone contributed only a very small amount, <1% for all initial NO concentrations and at all times throughout the oxidation process, to the total calculated OH reactivity.

The contribution from NO_2 to the total calculated OH reactivity was observed to increase throughout the oxidation process for both the 109 ppbv initial NO and 218 ppbv initial NO; at 109 ppbv initial NO the NO_2 percentage contribution increased from 9.3% at 0 s to 32.2% at 600 s, 46.0% at 1200 s, 57.4% at 1800 s, 67.8% at 2400 s and 69.7% at 3000 s. At 218 ppbv initial NO, the NO_2 percentage contribution to the total calculated

OH reactivity increased from 9.4% at 0 s to 21.6% at 600 s, 31.8% at 1200 s, 41.1% at 1800 s, 50.7% at 2400 s and 58.0% at 3000 s. The difference in percentage contribution to the total calculated OH reactivity between the 109 ppbv initial NO and the 218 ppbv initial NO is likely due to varying wall conditions within the chamber. As with the Cl atom initiated oxidation of *iso*-butane in the presence of NO, little to no significant influence on the total calculated OH reactivity comes from the presence of HO_2, being <0.1% at all time intervals for both the 109 ppbv initial NO and 218 ppbv initial NO situations.

$[NO]_{t=0}$	Contributing Species	0 s	600 s	1200 s	1800 s	2400 s	3000 s
109 ppbv	*Iso*-butane	43.0	37.6	31.5	27.3	23.2	23.8
	Iso-butyraldehyde	<0.1	<0.1	<0.1	<0.1	<0.1	<0.1
	Acetone	<0.1	<0.1	0.3	0.5	0.6	0.7
	NO_2	9.3	32.2	46.0	57.4	67.8	69.7
	O_3	<0.1	<0.1	<0.1	<0.1	<0.1	<0.1
	NO	47.6	30.1	22.2	14.8	8.3	5.9
	HO_2	<0.1	<0.1	<0.1	<0.1	<0.1	<0.1
	$\Delta k'_{OH}$	50.0	53.0	77.3	84.8	72.7	73.2
218 ppbv	*Iso*-butane	38.5	35.4	31.8	28.4	24.6	22.5
	Iso-butyraldehyde	<0.1	<0.1	<0.1	<0.1	<0.1	<0.1
	Acetone	<0.1	0.2	0.3	0.4	0.5	0.6
	NO_2	9.4	21.6	31.8	41.1	50.7	58.0
	O_3	<0.1	<0.1	<0.1	<0.1	<0.1	<0.1
	NO	52.2	42.8	36.2	30.2	24.2	19.0
	HO_2	<0.1	<0.1	<0.1	<0.1	<0.1	<0.1
	$\Delta k'_{OH}$	35.7	35.0	38.8	-	-	-

Table 8-5: Percentage contributions of measured species to total calculated OH reactivity for the OH radical initiated oxidation of *iso*-butane under 109 ppbv and 218 ppbv initial [NO] conditions at 600 s time intervals.

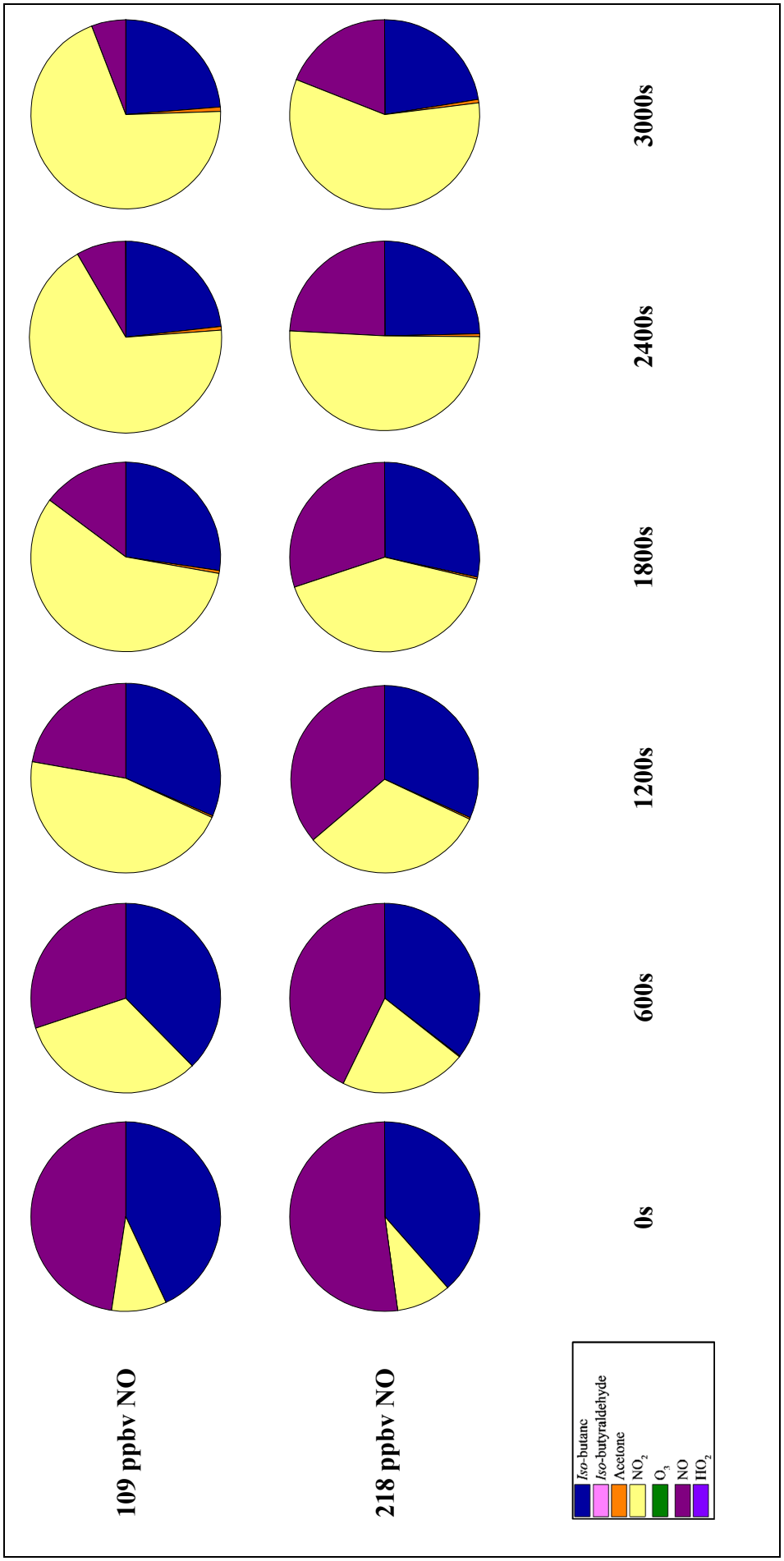

Figure 8-15: Contribution to calculated k'OH at 600s time intervals for the OH radical initiated oxidation of *iso*-butane with varying initial [NO]. Blue: *iso*-butane, light magenta: iso-butyraldehyde, orange: acetone, light yellow: NO_2, green: O_3, purple: NO, violet: HO_2.

8.5 Summary and Conclusions

OH reactivity provides valuable information on the total VOCs within an environment. The ability to measure OH reactivity in chamber studies allows for the oxidation processes of compounds to be investigated in isolation. If all species present throughout such processes are measured, and their rate coefficients for reaction with OH radicals are known, then the measured and calculated OH reactivities should show perfect agreement. Discrepancies were observed between the measured and calculated OH reactivity for the Cl atom and OH radical initiated oxidation of both *iso*-butanol and *iso*-butane under varying initial NO concentrations. The development of the OH reactivity instrument, and its coupling to the HIRAC chamber has been described in Chapter 4. Few previous studies have been reported on OH reactivity measurements from atmospheric simulation chambers. A major source of discrepancies between measured and calculated OH reactivity for field measurements are typically attributed to unmeasured intermediate species. In the chamber studies presented here, discrepancies between measured and calculated OH reactivity may arise for other factors as well as unmeasured intermediate species. A comprehensive set of OH reactivity measurements has been described here following the oxidation processes of *iso*-butanol and *iso*-butane in the presence and absence of NO_x. Both the Cl atom and OH radical initiated oxidation processes have been studied.

In nearly all cases presented, the calculated OH reactivity, prior to the initiation of the oxidation reaction, in the presence of NO_x, was greater than the measured OH reactivity. It is concluded that this discrepancy observed in the presence of NO_x was due to recycling within the flow tube (as has been described in Chapter 4), where fitting the data at these time points with a bi-exponential fitting function may yield a value of k'_{OH} closer to the true value of the OH reactivity. Further work into the analysis of data from these time points would determine whether the discrepancy is due to recycling or from losses of NO in the sampled gas in the sampling line into the instrument. Measurements of the NO concentration in the OH reactivity instrument, taking a small portion of the sampled gas close to the input into the instrument, for measurement with a NO_x analyser would allow for any wall losses to be accounted for. Measurements of NO concentrations in this way, for varying levels of NO and VOCs within HIRAC would aid interpretation of results and indicate if any modifications are required in the sampling procedure for HIRAC measurements.

In the absence of NO_x, in the time periods prior to the initiation of the oxidation process, very good agreement was observed between the measured and calculated OH reactivity, indicating that there are no significant losses of *iso*-butanol or *iso*-butane within the sampling line into the instrument. Further studies into a range of VOCs, such as the carbonyl products observed in the oxidation processes studied in this work, would determine whether this is the case for all of these compounds; it is likely that some compounds are prone to more significant losses within the sampling line. Such losses could be reduced in a number of ways; reducing the residence time in the sampling line by reducing the length of the sampling line or increasing the sample flow rate from HIRAC into the instrument; or the use of a sampling line made from different material.

A general trend in the difference between the measured and calculated OH reactivity was observed; in the OH radical initiated oxidation processes, the average percentage difference increased for all initial NO concentrations as the experiment proceeds, indicating that at later times, unmeasured species become more significant to the total OH reactivity. As the initial NO concentration was increased in the OH radical oxidation processes, the average percentage difference between the measured and calculated OH reactivity decreased; the presence of NO provides a more direct route for the peroxy radicals to the final carbonyl products, whereas in the absence of NO, the peroxy radicals can react with other peroxy radicals, resulting in the formation of numerous other products. The greater difference observed in the absence of NO_x is attributable to numerous unmeasured minor products and intermediate species.

Measurements of OH reactivity following the OH radical initiated oxidation of *iso*-butanol in the presence of varying initial NO concentrations increase with increasing initial [NO]. NO containing species contribute significantly to the OH reactivity; NO and NO_2 contributed 55% and 10%, respectively, to the calculated OH reactivity for the MEGAPOLI winter campaign (Dolgorouky *et al.* 2012) which was carried out in the urban environment of Paris where high levels of NO_x would be expected. In contrast, only 18% of the total calculated OH reactivity came from NO and NO_2 for measurements carried out at a coastal site in North Norfolk (Lee *et al.* 2009).

Overall, the time profiles of the measured and calculated OH reactivity are in better agreement for the Cl atom and OH radical initiated oxidation process of *iso*-butane under varying initial NO concentrations than for the oxidation processes of *iso*-butanol. This better agreement most likely arises due to differences in site specific reactivity between *iso*-butane and *iso*-butanol. There are two different hydrogen types present in *iso*-butane

(one tertiary hydrogen and nine primary hydrogens), whereas there are four different hydrogen types in *iso*-butanol (one –OH group, two α-hydrogens, one β-hydrogen and six γ-hydrogens).The –OH group influences the reactivity of the α-hydrogens, making them more reactive towards attack from both OH radicals and Cl atoms, than the β-hydrogens or the primary hydrogens of *iso*-butane.

The measurements of OH reactivity in the studies presented in this work demonstrates their usefulness in atmospheric simulation chamber studies. These are the first measurements of OH reactivity for relatively complex systems within the HIRAC chamber, and comparison with the calculated OH reactivity has highlighted a number of areas for further characterisation of such measurements. These include systematic investigation into the influence of varying concentrations of NO with a range of VOCs in order to elucidate any OH recycling within the flow tube of the instrument. It is suggested that a wide range of VOCs are to be studied in order to establish the transfer efficiency of different categories of compounds into the instrument in order to determine whether an alternative sampling line is required.

The effects of OH recycling within the flow tube of the instrument could also be investigated with the use of deuterated water or $H_2{}^{18}O$. If deuterated water (D_2O) were to be used instead of H_2O in the bubbler, OD could be produced following R 8-3 and R 8-4:

$$O_3 + h\nu \rightarrow O(^1D) + O_2 \qquad \text{R 8-3}$$

$$O(^1D) + D_2O \rightarrow OD + OD \qquad \text{R 8-4}$$

Rate coefficients of VOCs and other reactive species with OD will be different to those with OH radicals. The total loss rate of OD with reactive species can be monitored in real time, as would be done for the measurement of OH reactivity, in which any OH radicals produced following reactions such as R 8-5 to R 8-8 would not influence the OD decay.

$RO_2 + NO \rightarrow RO + NO_2$ R 8-5

$RO + O_2 \rightarrow HO_2 + RCHO$ R 8-6

$HO_2 + NO \rightarrow OH + NO$ R 8-7

$OH + VOC \rightarrow loss$ R 8-8

$OD + VOC \rightarrow loss$ R 8-9

Similarly, the use of $H_2{}^{18}O$ would produce ^{18}OH, the decay of which could be recorded following its reaction with reactive species present in the sampled gas.

8.6 References

Andersen, V. F., Wallington, T. J. and Nielsen, O. J. (2010). "Atmospheric Chemistry of *i*-Butanol." The Journal of Physical Chemistry A **114**(47): 12462-12469.

Atkinson, R. (2003). "Kinetics of the gas-phase reactions of OH radicals with alkanes and cycloalkanes." Atmospheric Chemistry and Physics **3**(6): 2233-2307.

Atkinson, R., Baulch, D. L., Cox, R. A., Crowley, J. N., Hampson, R. F., Hynes, R. G., Jenkin, M. E., Rossi, M. J. and Troe, J. (2004). "Evaluated kinetic and photochemical data for atmospheric chemistry: Volume I - gas phase reactions of O_x, HO_x, NO_x and SO_x species." Atmospheric Chemistry and Physics **4**(6): 1461-1738.

Atkinson, R., Baulch, D. L., Cox, R. A., Crowley, J. N., Hampson, R. F., Hynes, R. G., Jenkin, M. E., Rossi, M. J., Troe, J. and Subcommittee, I. (2006). "Evaluated kinetic and photochemical data for atmospheric chemistry: Volume II - gas phase reactions of organic species." Atmospheric Chemistry and Physics **6**(11): 3625-4055.

Beichert, P., Wingen, L., Lee, J., Vogt, R., Ezell, M. J., Ragains, M., Neavyn, R. and Finlayson-Pitts, B. J. (1995). "Rate Constants for the Reactions of Chlorine Atoms with Some Simple Alkanes at 298 K: Measurement of a Self-Consistent Set Using Both Absolute and Relative Rate Methods." The Journal of Physical Chemistry **99**(35): 13156-13162.

Dolgorouky, C., Gros, V., Sarda-Esteve, R., Sinha, V., Williams, J., Marchand, N., Sauvage, S., Poulain, L., Sciare, J. and Bonsang, B. (2012). "Total OH reactivity measurements in Paris during the 2010 MEGAPOLI winter campaign." Atmospheric Chemistry and Physics **12**(20): 9593-9612.

Fuchs, H., Hofzumahaus, A., Rohrer, F., Bohn, B., Brauers, T., Dorn, H. P., Haseler, R., Holland, F., Kaminski, M., Li, X., Lu, K., Nehr, S., Tillmann, R., Wegener, R. and Wahner, A. (2013). "Experimental evidence for efficient hydroxyl radical regeneration in isoprene oxidation." Nature Geoscience **6**(12): 1023-1026.

Lee, J. D., Young, J. C., Read, K. A., Hamilton, J. F., Hopkins, J. R., Lewis, A. C., Bandy, B. J., Davey, J., Edwards, P., Ingham, T., Self, D. E., Smith, S. C., Pilling, M. J. and Heard, D. E. (2009). "Measurement and calculation of OH reactivity at a United Kingdom coastal site." Journal of Atmospheric Chemistry **64**(1): 53-76.

Nakashima, Y., Tsurumaru, H., Imamura, T., Bejan, I., Wenger, J. C. and Kajii, Y. (2012). "Total OH reactivity measurements in laboratory studies of the photooxidation of isoprene." Atmospheric Environment **62**: 243-247.

Nehr, S., Bohn, B., Dorn, H. P., Fuchs, H., Häseler, R., Hofzumahaus, A., Li, X., Rohrer, F., Tillmann, R. and Wahner, A. (2014). "Atmospheric photochemistry of aromatic

hydrocarbons: OH budgets during SAPHIR chamber experiments." Atmospheric Chemistry and Physics **14**(13): 6941-6952.

Nölscher, A. C., Butler, T., Auld, J., Veres, P., Muñoz, A., Taraborrelli, D., Vereecken, L., Lelieveld, J. and Williams, J. (2014). "Using total OH reactivity to assess isoprene photooxidation via measurement and model." Atmospheric Environment **89**(0): 453-463.

Whalley, L. K., Stone, D., Bandy, B., Dunmore, R., Hamilton, J. F., Hopkins, J., Lee, J. D., Lewis, A. C. and Heard, D. E. (2016). "Atmospheric OH reactivity in central London: observations, model predictions and estimates of in situ ozone production." Atmospheric Chemistry and Physics **16**(4): 2109-2122.

Chapter 9. Summary, Conclusions and Future Work

The development and characterisation of instrumentation used in the investigation of chemical reactions in atmospheric simulation chambers is extremely important. The work in this thesis has described the development and characterisation of two instruments for their measurements with the HIRAC chamber. Measurements with both of these instruments, utilising the HIRAC chamber, have been reported following the oxidation of processes of *iso*-butanol, a potential biofuel, and the analogous non-functionalised alkane, *iso*-butane. This chapter summarises the work and conclusions that have been presented in this thesis, with suggestions being made on important future work which would allow for further improvements of measurements from the HIRAC chamber.

The HIRAC chamber has been described in Chapter 2, with details of the commercially available analytical instrumentation available for measurements, including GC-FID, FTIR and commercial O_3 and NO_x analysers. The HIRAC FAGE instrument is described in Chapter 3, with a focus on the development of calibration techniques. The conventional "wand" method for FAGE calibration has been discussed, focussing on the N_2O actinometry experiment for the determination of the lamp flux, $F_{184.9\,nm}$. Numerous apparatus has been compared for determining the $F_{184.9\,nm}$, where no discernible differences were observed. Monte Carlo error propagation has been carried out in order to better assess the systematic uncertainty associated with the N_2O actinometry method for the determination of $F_{184.9\,nm}$. From this, it was observed that the variation in the concentration of NO has the most significant influence on the variation in the determined value of $F_{184.9\,nm}$, 46 – 99%. The error in the measured NO concentrations is dependent on the error in the calibration of the chemiluminescence NO_x analysers used in the experiments; it is suggested that a different technique for the measurement of NO concentrations is investigated, in order to reduce the errors associated with these measurements. Low concentrations of NO (<1 ppbv) are typically measured in the N_2O actinometry experiment, close to the detection limit (50 pptv) of the chemiluminescence NO_x analysers, and so a measurement technique capable of measuring lower NO concentrations is likely to reduce contribution of the measured NO to the variation in the determined value of $F_{184.9\,nm}$. The simulation was run twice with different values for the

rate coefficients; the contribution to the variation in $F_{184.9\ nm}$ was observed to increase with increasing lamp current, with the IUPAC rate coefficient values always showing a greater contribution to the variation in $F_{184.9\ nm}$ than the JPL rate coefficient values, correlating to the IUPAC rate coefficients having higher uncertainties associated with them (Atkinson *et al.* 2004, Sander *et al.* 2011). As the Monte Carlo error simulation has only been carried out for one set of experimental data, it is suggested that further investigation into the errors associated with the N_2O method for the determination of $F_{184.9\ nm}$ is carried out.

An alternative method for the calibration of the FAGE instrument HO_2 cell has been described, with results presented on the sensitivity of the HO_2 cell as a function of temperature, determined following the HO_2 self-reaction within the HIRAC chamber. Measurements were carried out over the temperature range 273 – 343 K. Good agreement between the alternative HIRAC method and the previously reported conventional "wand" method for determining the HO_2 cell sensitivity as a function of temperature was observed ($\Delta C_{HO2(HIRAC)}$ = (0.34 ± 0.19) % and $\Delta C_{HO2("wand")}$ = (0.29 ± 0.42) % increase per Kelvin, respectively) (Winiberg 2014). Further work into the temperature profile within the FAGE instrument whilst sampling from HIRAC over a range of temperatures would assist in validating the alternative method. Work is ongoing into the determination of the OH cell sensitivity as a function of temperature following alternative HIRAC calibration methods, and will be presented in a future publication.

The development of a LFP-LIF instrument for the measurement of OH reactivity has been described in Chapter 4, in order to improve the measurement system and to enable measurements of OH reactivity from the HIRAC chamber. A new FAGE inlet and photolysis flow tube pump out system have been described, with validation experiments being carried out for the determination of the rate coefficient of CH_4 with OH. Excellent agreement was obtained as compared to the IUPAC recommended rate coefficient; $(6.41 \pm 0.18) \times 10^{-15}$ cm^3 $molecule^{-1}$ s^{-1} compared to $(6.4 \pm 0.9) \times 10^{-15}$ cm^3 $molecule^{-1}$ s^{-1} (Atkinson *et al.* 2006), with measurements of OH reactivities up to ~150 s^{-1} being reported. A number of characterisation experiments have been reported for comparison between the old and new instrument inlet systems, with no discernible differences being observed over a range of $[O_3]$, flow tube flow rates, flow tube pressures and FAGE cell pressures. The instrument has been successfully coupled to the HIRAC chamber for measurements, and validation of the sampling set up has been carried out through the determination of the bimolecular rate coefficient of *n*-butanol with OH; a

value of (8.21 ± 0.37) × 10^{-12} cm^3 $molecule^{-1}$ s^{-1} was obtained, in excellent agreement with the IUPAC recommended value of (8.5 ± 3.0) × 10^{-12} cm^3 $molecule^{-1}$ s^{-1} (Atkinson *et al.* 2006). Measurements sampling from HIRAC for a range of VOCs, such as the carbonyl product compounds measured during the oxidation studies presented in Chapter 7 and Chapter 8 would help validate the measurement set up. Investigating the use of different sampling lines such as heated lines or lines made from a different material, would assist in determining the optimum sampling method whilst carrying out measurements from the HIRAC chamber.

An OH reactivity instrument intercomparison was carried out at the SAPHIR chamber at the Forschungszentrum in Jülich, Germany in October 2015. Some of the results from this study have been presented in Chapter 5, with measurements from the Leeds LFP-LIF OH reactivity instrument being indicated. Good agreement was observed for the Leeds LFP-LIF instrument with the calculated OH reactivity in all experiments reported; a slight positive offset (typically of ~2 s^{-1}) was observed in the majority of the experiments for the Leeds LFP-LIF instrument, which is attributed to contaminants within the instrument or minor leaks in the sampling line. Measurements from all other instruments have been anonymised, with their identities to be revealed in future publications. In general, all instruments showed good agreement in the time profiles between the measured and calculated OH reactivity; CRM instruments showed greater discrepancies to the calculated OH reactivity, and increased scatter, due to their poorer time resolution and accuracy, particularly at lower OH reactivities.

The temperature dependence of the reactions of Cl atoms with *n*-butanol and *iso*-butanol have been studied by the relative rate method in the HIRAC chamber. The first relative rate study of the temperature dependence of the rate of reaction of *n*-butanol with Cl atoms has been described in Chapter 6 over the temperature range 266 – 343 K, where a negative temperature dependence was observed ($k = 1.01 \times 10^{-10} \exp((235 \pm 34) / T)$ cm^3 $molecule^{-1}$ s^{-1}) . This is in agreement with the negative temperature dependence previously reported in the literature (Garzón *et al.* 2006), and excellent agreements was observed for the room temperature rate coefficient ($k_{298K} = (2.25 \pm 0.11) \times 10^{-10}$ cm^3 $molecule^{-1}$ s^{-1}) with the IUPAC recommended value ($k_{298\ K} = (2.2 \pm 0.4) \times 10^{-10}$ cm^3 $molecule^{-1}$ s^{-1}, (Atkinson *et al.* 2006)). Garzón *et al.* (2006) reported a slightly greater temperature dependence than has been determined in this work; it is likely that the absolute measurements of $k_{OH + n\text{-butanol}}$ are influenced by Cl atom regeneration, which has not been accounted for in the analysis. The first temperature dependent study of the

reaction of Cl atoms with *iso*-butanol has been reported in Chapter 6, over the temperature range 296 – 344 K, where the Arrhenius expression $k = 5.53 \times 10^{-11} \exp((367 \pm 76) / T)$ cm^3 molecule^{-1} s^{-1}, is reported. Very good agreement was observed for the rate coefficient at room temperature, $(1.95 \pm 0.14) \times^{-10}$ cm^3 molecule^{-1} s^{-1}, with values in the literature, particularly for those determined with the same reference compound, cyclohexane; Andersen *et al.* (2010) reported a value of $(1.88 \pm 0.22) \times 10^{-10}$ cm^3 molecule^{-1} s^{-1} and Wu *et al.* (2003) reported a value of $(1.82 \pm 0.12) \times 10^{-10}$ cm^3 molecule^{-1} s^{-1}. To further verify the temperature dependence of the rate of Cl atoms with both *n*-butanol and *iso*-butanol, it is suggested that further investigations are carried out with a range of reference compounds. Due to complex wall effects, it was not possible to extract values for the rate coefficient of the reaction of Cl atoms with *iso*-butanol at temperatures below 296 K; further investigation into low temperature experiments is required in order to determine low temperature rate coefficients.

Alcohols are showing increased interest as potential biofuels in replacing traditional fossil fuels (Sarathy *et al.* 2014). A comprehensive study of the products from the Cl atom and OH radical initiated oxidation of *iso*-butanol in the presence of varying initial NO concentrations is presented in Chapter 7. Previous literature into the oxidation processes of *iso*-butanol have reported on the oxidation products of the Cl atom initiated oxidation in the presence and absence of NO_x, and the OH radical initiated oxidation in the presence of NO_x. The studies in the presence of NO_x have been carried out previously in the presence of extremely high concentrations (Andersen *et al.* 2010). Work presented in Chapter 7 aimed to investigate the oxidation processes in the presence of tropospherically relevant concentrations of NO_x, with comparisons being drawn to the previous literature results. The yield of *iso*-butyraldehyde was observed to decrease through a minimum and then increase again as the NO concentration was increased. The yield of acetone, reported as an upper limit, was seen to increase with increasing NO concentration; this is likely due to chemical activation in the presence of NO, where the alkoxy radical is formed from the peroxy radical, through a high energy intermediate species, leading to rapid decomposition of the alkoxy radical. A high yield of acetone was determined for the Cl atom initiated oxidation of *iso*-butanol in the absence of NO_x (72 ± 1%), as compared to <5% reported by Andersen *et al.* (2010); this discrepancy is attributed to high conversion of the *iso*-butyraldehyde product to acetone following subsequent reactions with Cl atoms and OH radicals present in the system.

In the OH radical initiated oxidation of *iso*-butanol, the yield of *iso*-butyraldehyde was observed to increase with increasing initial [NO], attributed to chemical activation of the intermediate radicals in the presence of NO_x. The yield of acetone was also observed to increase with increasing [NO], with good agreement at the highest [NO], 64 ± 1%, with that reported by Andersen *et al.* (2010), 61 ± 4%. Upward curvature was observed in the HCHO yields; HCHO is formed through many reactions in the oxidation process, and through subsequent reactions of initial products with Cl atoms present in the chamber. Ozone formation following the Cl atom and OH radical initiated oxidation of *iso*-butanol in the presence of varying initial [NO] has been compared to that of the analogous alkane, *iso*-butane. Overall the ozone formation was observed to be higher in all scenarios for the Cl atom initiated oxidation processes than the OH radical initiated oxidation processes; previous studies have shown enhanced ozone formation in the presence of Cl in NO_x polluted environments. Peak ozone was observed to be higher for the *iso*-butane oxidation reactions than the *iso*-butanol oxidation reactions, however, the peak ozone occurred at later times for the *iso*-butane oxidation. Further detailed modelling studies into the oxidation processes that have been described will assist in verifying the understanding of the chemical processes occurring. The MCM only has limited Cl atom chemistry, however, Cl atom initiated oxidation processes have been shown to be of importance in enhancements of tropospheric ozone formation. The addition of detailed Cl atom chemistry to the MCM for modelling studies will help in understanding the potential impact of Cl atom initiated oxidation processes on the formation of tropospheric ozone. Chlorine is routinely used as a precursor in atmospheric simulation chamber investigations; inclusion of more detailed chlorine chemistry in the MCM would allow for more direct comparisons with results from chamber based experiments to be made.

The first measurements of OH reactivity from the HIRAC chamber following relatively complex oxidation systems of the Cl atom and OH radical initiated oxidation of *iso*-butanol and *iso*-butane in the presence of varying initial NO concentrations, have been presented in Chapter 8. Comparisons have been made between the measured OH reactivity and the calculated OH reactivity from measureable species within HIRAC. A number of discrepancies were observed between the measured and calculated OH reactivities in nearly all scenarios described. Discrepancies prior to the initiation of the oxidation reactions are typically seen as the calculated OH reactivity is greater than the measured in the presence of NO_x. This discrepancy is attributed to the presence of NO_x in the flow tube of the instrument leading to OH recycling, and higher values of OH

reactivity being reported. Further investigation into the influence of varying concentrations of NO_x sampled by the OH reactivity instrument for a range of VOCs would verify whether the recycling of OH need be accounted for in the data analysis procedure. The time profiles for the measured OH reactivity are in better agreement for the *iso*-butane oxidation processes than the *iso*-butanol oxidation processes. Further work is suggested on the analysis of FTIR data from the oxidation processes described in order to determine whether any, currently unaccounted for, products have any significant influence on the measured and calculated OH reactivity.

1.1 References

Andersen, V. F., Wallington, T. J. and Nielsen, O. J. (2010). "Atmospheric Chemistry of *i*-Butanol." The Journal of Physical Chemistry A **114**(47): 12462-12469.

Atkinson, R., Baulch, D. L., Cox, R. A., Crowley, J. N., Hampson, R. F., Hynes, R. G., Jenkin, M. E., Rossi, M. J. and Troe, J. (2004). "Evaluated kinetic and photochemical data for atmospheric chemistry: Volume I - gas phase reactions of O_x, HO_x, NO_x and SO_x species." Atmospheric Chemistry and Physics **4**(6): 1461-1738.

Atkinson, R., Baulch, D. L., Cox, R. A., Crowley, J. N., Hampson, R. F., Hynes, R. G., Jenkin, M. E., Rossi, M. J., Troe, J. and Subcommittee, I. (2006). "Evaluated kinetic and photochemical data for atmospheric chemistry: Volume II - gas phase reactions of organic species." Atmospheric Chemistry and Physics **6**(11): 3625-4055.

Garzón, A., Cuevas, C. A., Ceacero, A. A., Notario, A., Albaladejo, J. and Fernández-Gómez, M. (2006). "Atmospheric reactions $Cl+CH_3–(CH_2)_n–OH(n=0–4)$: A kinetic and theoretical study." The Journal of Chemical Physics **125**(10): 104305.

Sander, S. P., Friedl, R. R., Abbatt, J. P. D., Barker, J., Golden, D. M., Kolb, C. E., Kurylo, M. J., Moortgat, G. K., Wine, P. H., Huie, R. E. and Orkin, V. L. (2011). Chemical kinetics and photochemical data for use in atmospheric studies - Evaluation 17. Pasadena CA, Jet Propulsion Laboratory. **17**.

Sarathy, S. M., Oßwald, P., Hansen, N. and Kohse-Höinghaus, K. (2014). "Alcohol combustion chemistry." Progress in Energy and Combustion Science **44**: 40-102.

Winiberg, F. (2014). Characterisation of FAGE apparatus for HO_x detection and application in an environmental chamber. PhD, University of Leeds.

Wu, H., Mu, Y., Zhang, X. and Jiang, G. (2003). "Relative rate constants for the reactions of hydroxyl radicals and chlorine atoms with a series of aliphatic alcohols." International Journal of Chemical Kinetics **35**(2): 81-87.

Appendix A

For the reactions, where A is the reactant (*iso*-butanol), B is the product (*iso*-butyraldehyde) and Z is the oxidising species (OH or Cl):

$$A + Z \xrightarrow{k_A} \alpha B + \text{prod.} \qquad \text{Eq. A- 1}$$

$$B + Z \xrightarrow{k_B} \text{prod} \qquad \text{Eq. A- 2}$$

$$A \xrightarrow{k_{wall}} \text{loss} \qquad \text{Eq. A- 3}$$

$$B \xrightarrow{k_{wall}} \text{loss} \qquad \text{Eq. A- 4}$$

$$B \xrightarrow{j} \text{loss} \qquad \text{Eq. A- 5}$$

Where Eq. A-4 and Eq. A-5 can be combined to give:

$$B \xrightarrow{k_{wall+j}} \text{loss} \qquad \text{Eq. A- 6}$$

The following rate expressions can be written:

$$\frac{d[A]}{dt} = -k_A[A][Z] - k_{wall}[A] \qquad \text{Eq. A- 7}$$

$$\frac{d[B]}{dt} = \alpha k_A[A][Z] - k_B[B][Z] - \left(k_{wall+j}\right)[B] \qquad \text{Eq. A- 8}$$

Eq. A-7 is rearranged to give:

$$dt = \frac{d[A]}{-k_A[A][Z] - k_{wall}[A]} \qquad \text{Eq. A- 9}$$

Substituting *dt* into Eq. A-8 gives:

$$\frac{d[B]}{d[A]}\left(-k_A[A][Z] - k_{wall}[A]\right) = \alpha k_A[A][Z] - k_B[B][Z] - \left(k_{wall+j}\right)[B] \qquad \text{Eq. A- 10}$$

x is equal to the conversion of A and y is the ratio of B to the maximum possible concentration of B (the initial concentration of A):

$$x \equiv 1 - \frac{[A]_t}{[A]_0}$$ Eq. A- 11

$$y \equiv \frac{[B]_t}{[A]_0}$$ Eq. A- 12

Eq. A-11 and Eq. A-12 can be differentiated to give *d*[A] and *d*[B] in terms of *dx* and *dy*:

$$d[A] = -[A]_0 dx$$ Eq. A- 13

$$d[B] = [A]_0 dy$$ Eq. A- 14

Eq. A-13 and Eq. A-14 are substituted into Eq. A-10 to yield:

$$\frac{dy}{dx}\left(k_A \frac{[A]_t}{[A]_0}[Z] + k_{wall}\frac{[A]_t}{[A]_0}\right) = \alpha k_A \frac{[A]_t}{[A]_0}[Z] - k_B \frac{[B]_t}{[A]_0}[Z] - \left(k_{wall+j}\right)\frac{[B]_t}{[A]_0}$$ Eq. A- 15

Substituting the definitions of *x* and *y* from Eq. A-11 and Eq. A-12:

$$\frac{dy}{dx} = \frac{\alpha k_A(1-x)[Z] - k_B y[Z] - \left(k_{wall+j}\right)y}{k_A(1-x)[Z] + k_{wall}(1-x)}$$ Eq. A- 16

Rearranging for α:

$$\alpha = \frac{\frac{dy}{dx}(k_A[Z] + k_{wall})}{k_A[Z]} + \frac{y\left(k_B[Z] + \left(k_{wall+j}\right)\right)}{(1-x)k_A[Z]}$$ Eq. A- 17

Simplifying for α:

$$\alpha = \frac{dy}{dx}h + \left(\frac{y}{(1-x)}g\right)$$ Eq. A- 18

Defining h and g:

$$h = \frac{k_A[Z] + k_{wall}}{k_A[Z]} \quad \text{Eq. A- 19}$$

$$g = \frac{k_B[Z] + \left(k_{wall+j}\right)}{k_A[Z]} \quad \text{Eq. A- 20}$$

$$\frac{\alpha}{h} = \frac{dy}{dx} + y\frac{1}{(1-x)}\frac{g}{h} \quad \text{Eq. A- 21}$$

$$y = \frac{\alpha/_h}{1 - \left(\frac{g}{h}\right)}(1-x)\left\{(1-x)^{\left(\frac{g}{h}-1\right)} - 1\right\} \quad \text{Eq. A- 22}$$